DESIGN AND FABRICATION OF A NOVEL SPINNING FLUIDISED BED (REKABENTUK DAN FABRIKASI LAPISAN TERBENDALIR BERPUTAR NOVEL)

MOHD ROZAINEE BIN TAIB

RESEARCH VOT NO:
72225

Jabatan Kimia
Fakulti Kejuruteraan Kimia & Kejuruteraan Sumber Asli
Universiti Teknologi Malaysia

2003

ACKNOWLEDGEMENTS

The project team wishes to acknowledge the IRPA (Intensification Research on Priority Areas) Grant through Vot No. 72225 for sponsoring this research. Also, we would like to express our most sincere gratitude to BERNAS and Syarikat KIARA Sdn. Bhd., the fabricator of the prototype, for the successful development of the spinning fluidised bed system. We are also grateful to the CFD Research (S) Pte Ltd in Singapore for their technical support during our computational fluid dynamics modelling works.

Our special thanks goes to the Research Management Centre (RMC), UTM and the Faculty of Chemical Engineering & Natural Resources Engineering (FKKKSA), UTM for providing all the necessary facilities and support for carrying out this research project.

ABSTRACT

DESIGN AND FABRICATION OF A NOVEL SPINNING FLUIDISED BED

(Keywords: design, fluidised bed, computational fluid dynamics, rice husk)

Existing vertical spinning fluidised bed (SFB) have several drawbacks, such as non-uniform radial and axial bed fluidisation, feeding and ash accumulation problems. The purpose of this research, therefore is to develop a prototype of the horizontal SFB combustor capable of overcoming these drawbacks. The scopes of the research include engineering design of the prototype, computational fluid dynamics (CFD) modelling and set-up/commissioning of the developed prototype. Under this research, a prototype of the horizontal SFB has been successfully developed and is able to overcome the inherent weakness in vertical SFB. The innovative secondary chamber provides more freeboard for more complete combustion and acts as particulate control device. The prototype is suitable for burning low-density materials (rice husk, fibrous materials), which are difficult to be burnt in conventional fluidised bed by imparting a higher centrifugal force. There is also no limit to the amount of air throughput and combustion is only limited by the kinetics in which each different type of waste burns. Results from the CFD modelling narrowed down the parameters to be tested on the SFB in future experimental works, as well as providing design improvements on the current SFB design. Due to its compactness and versatility in burning a wide range of waste, the SFB prototype has the potential to be utilised as small-scale on-site waste incineration facility and high-efficiency gas burner for high-loading waste gas streams in chemical plants or refineries. The whole system is mountable to a truck and can be transported to waste sources such as rice mills, sawmills, wastewater treatment plants to incinerate waste. The full performance on the developed SFB during combustion of various types of wastes is outside the scope of the current research and therefore, is subjected to future experimental works.

Key researchers:
Assoc. Prof. Dr Mohd Rozainee bin Taib
Ms Ngo Saik Peng
Mr Lim Sin Yang
Mr Simon Looi Yat Seong

E-mail: rozainee@fkkksa.utm.my
Tel. No.: 07-5535578
Vot No.: 72225

ABSTRAK

REKABENTUK DAN FABRIKASI LAPISAN TERBENDALIR BERPUTAR NOVEL

(Kata kunci: rekabentuk, lapisan terbendalir, permodelan komputer dinamik bendalir, sekam padi)

Lapisan terbendalir berputar menegak yang sedia ada memilik beberapa kelemahan, misalnya ketidakseragaman perbendaliran secara jejarian dan paksian berserta masalah penyuapan bahan dan pengumpulan abu. Oleh itu, matlamat penyelidikan ini adalah untuk membangunkan suatu prototaip lapisan terbendalir berputar mendatar yang mampu mengatasi kelemahan-kelemahan tersebut. Skop penyelidikan ini melibatkan rekabentuk kejuruteraan prototaip yang dicadangkan, permodelan komputer dinamik bendalir dan pengesahan fungsi prototaip yang telah dibangunkan. Di bawah projek penyelidikan ini, suatu prototaip lapisan terbendalir berputar mendatar yang mampu mengatasi segala kelemahan dalam lapisan terbendalir berputar menegak telah berjaya dibangunkan. Kebuk pembakaran sekunder yang merupakan inovasi kepada teknologi ini membolehkan proses pembakaran yang lebih lengkap di samping bertindak sebagai alat kawalan partikel. Prototaip ini sesuai untuk membakar bahan berketumpatan rendah (sekam padi, bahan berserat) yang amat sukar dibakar dalam lapisan terbendalir konvensional dengan mengenakan daya emparan yang tinggi. Juga, berbanding dengan lapisan terbendalir konvensional, lapisan terbendalir berputar tidak mempunyai had kadar suapan udara dan pembakaran hanya dihadkan oleh kinetik pembakaran bagi setiap jenis bahan yang dibakar. Keputusan daripada permodelan komputer dinamik bendalir berjaya mengurangkan parameter yang perlu dikaji dalam kerja eksperimen ke atas prototaip ini. Memandangkan rekabentuknya yang padat berserta dengan keserbabolehannya dalam membakar pelbagai jenis sisa buangan, prototaip ini mempunyai potensi yang tinggi untuk digunakan sebagai sistem insinerasi setempat berskala kecil dan juga sistem pembakar gas berkecekapan tinggi untuk kilang kimia. Seluruh sistem prototaip ini boleh dimuatkan ke atas trak dan dibawa ke sumber sisa buangan seperti kilang pemprosesan padi, kilang papan dan pusat pemulihan air buangan untuk membakar sisa buangan. Prestasi sepenuh prototaip ini dalam membakar pelbagai jenis sisa buangan adalah di luar skop penyelidikan ini dan oleh yang demikian, adalah di bawah skop penyelidikan pada masa akan datang.

Penyelidik utama:
Prof. Madya Dr Mohd Rozainee bin Taib
Cik Ngo Saik Peng
En. Lim Sin Yang
En. Simon Looi Yat Seong

E-mail: rozainee@fkkksa.utm.my
Tel. No.: 07-5535578
Vot No.: 72225

TABLE OF CONTENTS

LIST OF TABLES

LIST OF FIGURES

LIST OF SYMBOLS

A	-	Empirical constant in Magnussen and Hjertager (1976) model, (= 4.0)
A_k	-	Pre-exponential factor, (1/s)
Ar	-	Archimedes number $\left(= \frac{\rho_f \left(\rho_p - \rho_f\right) g d_m^3}{\mu_f^2} \right)$, (dimensionless)
A_t	-	Cross sectional area of columnar fluidised bed, (m^2)
B	-	Empirical constant in Magnussen and Hjertager (1976) model, (= 0.5)
C	-	Molar concentration of each species, ($kmol/m^3$)
C_D	-	Drag coefficient, (dimensionless)
c_p	-	Mixture heat capacity, (kJ/K)
D	-	Molecular diffusion coefficient in gas phase, (m^2/s)
d_b	-	Bubble diameter, (m)
D_c	-	Column diameter, (m)
D_i	-	Gas orifice inlet diameter, (m)
d_m, d_p	-	Particle diameter, (mm)
d_{pi}	-	Arithmetic mean of screen apertures, (mm)
D_{vs}	-	Volume-surface mean diameter, (mm)
E_k	-	Activation energy for the reaction (J/kmol)
f	-	Mixture fraction, (dimensionless)

$\overline{f}$	-	Time-averaged value of *f*, (dimensionless)
$f^{'2}$	-	Mixture fraction variance, (dimensionless)
F_D	-	Drag force, (N)
F_R	-	Fluidisation ratio in RFB $\left(= \frac{\text{No. of } U_{mfc}}{\text{No. of } U_{mfs}} \right)$, (dimensionless)
g	-	Gravitational acceleration, (= 9.81 m/s^2)
g_c	-	Conversion factor, $\frac{1 kgm/s^2}{N}$
G_κ	-	Generation of turbulent kinetic energy, (m^2/s^2)
h	-	Enthalpy, (kJ/kg)
H	-	Height or depth of bed, (m)
H*	-	Instantaneous enthalpy, (kJ/kg)
k	-	Molecular conductivity, (W/m·K)
k_t	-	Turbulent thermal conductivity, (W/m·K)
L	-	Length, (m)
L_i	-	Length of combustor at bed surface, (m)
L_o	-	Length of air distributor inlet, (m)
M	-	Molecular weight of species, (kg/kmol)
m_i	-	Local mass fraction, (dimensionless)
p	-	Partial fraction, (dimensionless)
P	-	Pressure, (N/m^2)
p_1	-	PDF of f_{fuel}
p_2	-	PDF of p_{sec}
ΔP_b	-	Pressure drop across the bed, (N/m^2)
Q	-	Volumetric flow rate of gas, (m^3/s)
r	-	Radial position of the bed, (m)

R	-	Universal gas constant (J/kmol·K)
r_c	-	Radius of viscous core, (m)
r_E	-	Radius of exit port, (m)
Re	-	Reynolds number $\left(=\frac{\rho_f U d_p}{\mu_f}\right)$, dimensionless
r_i	-	Inner radius of the bed, (m)
R_i	-	Mass rate of creation or depletion by chemical reaction, (kg/m^3·s)
r_o	-	Outer radius of the bed, (m)
r_{pf}	-	Interface of the fluidised and packed bed, (m)
S_{ct}	-	Turbulent Schmidt number, $\frac{\mu_t}{\rho D_t}$
T	-	Temperature, (K)
t	-	Time, (s)
U	-	Fluidising gas velocity, (m/s)
u	-	Velocity component or velocity component in x-direction, (m/s)
U_b	-	Bubble velocity in the bed, (m/s)
u_i	-	Time average velocity component, (m/s)
u_i'	-	Fluctuating component of u_i, (m/s)
$\overline{u_i'}$	-	Instantaneous velocity component, (m/s)
U_{mf}	-	Minimum fluidisation velocity, (m/s)
U_{mfc}	-	Critical minimum fluidisation velocity, (m/s)
U_{mfs}	-	Surface minimum fluidisation velocity, (m/s)
U_o	-	Superficial gas velocity or fluidising gas velocity at the distributor, (m/s)
u_t	-	terminal velocity, (m/s)
v	-	Velocity component in y-direction, (m/s)

w	-	Velocity component in z-direction, (m/s)
W	-	Weight of the bed, (N)
x	-	Coordinate or tapering height, (m)
X	-	Height of tapering, (m)
x_i	-	Mass fraction of the *i-th* size range in the particles screen analysis, (dimensionless)
y	-	Coordinate, (m)
z	-	Coordinate, (m)

Greek Letters

α_ε	-	Inverse effective Prandtl number for turbulent dissipation rate, (dimensionless)
α_κ	-	Inverse effective Prandtl number for turbulent kinetic energy, (dimensionless)
α_s	-	Swirl constant, (dimensionless)
δ	-	Empirical constant, (dimensionless)
ε	-	Turbulent dissipation rate, (m^2/s^3)
ε, ε_{mf}	-	Bed voidage, (dimensionless)
ϕ_i	-	Instantaneous species concentration, density or temperature, ($kmol/m^3$, kg/m^3 or K)
ϕ_s	-	Particle sphericity, (dimensionless)
γ	-	Cone angle, (^{o})
η	-	Rate exponent in Arrhenius equation, (dimensionless)
κ	-	Turbulent kinetic energy, (m^2/s^2)
μ	-	Dynamic fluid viscosity, (kg/m·s)
μ_f	-	Fluid viscosity, (kg/m·s)

μ_t - Turbulent viscosity, (kg/m·s)

μ_{t0} - Turbulent viscosity for high-Reynolds-number limit $\left(= 0.0845\rho\frac{\kappa^2}{\varepsilon}\right)$, (kg/m.s)

θ - Tapering angle, (^{o})

ρ - Density of gas, (kg/m^3)

ρ_b - Bulk density, (kg/m^3)

ρ_f - Fluid density, (kg/m^3)

ρ_p - Particle density, (kg/m^3)

ω - Angular velocity, (rad/s)

Ω - Swirl angular velocity, (rad/s)

Ω_c - Characteristic swirl number, (dimensionless)

Subscripts

i - i-direction or chemical species i

j - j-direction or chemical species j

k - k-direction or chemical species k

t - Turbulent conditions

P - Product

R - Reactant

m - Mixture

fuel - Fuel

sec - Secondary fuel

Abbreviation

CFD	-	Computational Fluid Dynamics
ID	-	Inner Diameter
PDF	-	Probability Density Function
RFB	-	Rotating Fluidised Bed
RPM	-	Revolution per minute

LIST OF APPENDICES

LIST OF ATTACHMENTS

CHAPTER I

INTRODUCTION

1.1 Purpose of Research

The purpose of this research is to design and develop a prototype of the novel horizontal spinning fluidised bed (SFB) combustor.

1.2 Introduction to Spinning Fluidised Bed

High heat and mass transfer rates, temperature homogeneity and high flowability of particles with which fluidised bed is widely known for, are important features for continuous operating, large-scale solid reacting systems. As such, this technology has wide applications in many industrial processes, such as fluidised cracking catalyst (FCC) and fluid coking (Chen, 1987). However, most of these processes are limited to the use of vertical fluidised beds.

As the aeration rate is increased in a vertical fluidised bed to a point where the gravitational force on the particles is balanced off by the fluid drag exerted by the interstitial gas flow, the particles start to fluidise. One significant drawback of this system is that upon the introduction of a large excess amount of aeration, the gas forms large bubbles or slugs that rise through the bed in rapid succession. This extensive bypassing of gas results in poor gas-solid contact. This is where the

relatively new concept of centrifugal or spinning fluidised bed came into play. It has the advantage of higher gas throughput, a significant feature in coal combustion and drying where a high superficial velocity is desirable.

A centrifugal fluidised bed is a cylindrical bucket rotating about its axis of symmetry, as can be seen from Figure 1.1. The centrifugal force causes the fluidisation materials to impact the wall, which serves as the gas distributor. Fluidising gas is introduced in the inward direction of the radius through the porous or perforated wall. The main adjustable parameter in a centrifugal fluidised bed is the body force that is largely determined by the rotation speed and the bucket radius. This is in contrary with the presence of only the fixed gravitational force in a vertical fluidised bed. When the drag force exerted by the fluidising medium is equal to the effective weight of the particles in the centrifugal field, the particles start to fluidise. The rate of gas flowing through the bed can be increased proportionally to the *g*-level produced by the rotation. Thus, the bed particles are able to withstand a large amount of aeration without serious formation of bubbles by using a strong centrifugal force much greater than gravity. Consequently, gas-solid contact at high aeration rate is improved. The intensely turbulent intimate mixing between particles and fluid in a SFB is beneficial to gain a high combustion efficiency (Wong et al., 2000).

1.3 Justification and Objectives of Research

The novel technology of SFB has a good potential in the incineration of waste materials such as sludge with high combustion efficiency, flexible waste throughput and satisfactory flue gas emissions. However, as reported by Rozainee (1998) in his studies on sludge incineration in a vertical SFB, the combustor has several weaknesses which could be overcome by projecting it on a horizontal axis. These weaknesses include non-uniform fluidisation in the axial and radial directions, as well as problems associated with feeding and ash accumulation inside the combustor. Hence, the purpose of this research is to design a prototype of the novel horizontal SFB combustor (Figure 1.2) that is capable of overcoming the inherent

drawbacks in a vertical SFB. The base case design of the proposed horizontal SFB is based on using rice husk as the feed material. Nonetheless, once developed, the application of the prototype could be extended to other types of waste materials.

Rice husk was chosen as the basis for the design of the prototype SFB due to the huge amount generated from rice milling processes. Up to August 2001, the annual paddy output was reported to be 2.14 million tonnes (Department of Statistics, Malaysia) and considering rice husk accounted for 22% of this value, the amount of rice husk generated was approximately 0.47 million tonnes. Left to rot slowly in the field or burnt in the open, these practices clearly pose serious environmental problems. Rice husk, having a calorific value of 13 MJ/kg, is a good renewable energy source. Apart from solving its disposal problems, combustion offers the potential for energy recovery from this waste. In addition, the resulting ash has high commercial value due to its very high silica content (> 95%) (Huang et al., 2001). However, since most rice mills operate as small-scale industries, application of permanent combustion systems for energy recovery and disposal purposes is not cost effective. Therefore, the need arises to develop a small scale waste incineration system to cater for such situations without tolerating in terms of combustion efficiency and pollution emissions. The proposed SFB prototype has the potential to fit into these requirements due to its compact design, relatively shorter start-up time and versatility in handling different types of wastes at different operating conditions.

The objectives of this research are:-

a) To determine the optimum combustor geometry that could overcome the weaknesses associated with a vertical SFB, such non-uniform axial and radial bed fluidisation, ash accumulation and feeding problems,
b) To investigate the behaviour of the proposed combustor with regard to fluid flow profiles, particle trajectories, and gas-phase and solid particles combustion characteristics at various operating conditions through CFD modelling,

c) To determine the suitable operational range for cold and hot commissioning on the proposed system, such as rotating speeds, air feed rates and combustor temperatures, and

d) To investigate the limitations on the proposed system and ways to overcome them.

1.4 Scopes of Research

To achieve the objectives outlined in Section 1.3, the scopes of this research are as follows:-

a) To determine the optimum design parameters, such as sand size for use in design calculations, operating temperature range, rotating speed, bed thickness, fluidising air feed rate and rice husk feed rate to be used in sizing up the horizontal SFB,

b) To determine the optimum combustor dimensions, such as diameter, length and incorporation of any innovative features to eliminate the reported weaknesses in a vertical SFB,

c) To investigate the fluid flow profiles, ash entrainment behaviour, gas-phase combustion and rice husk particle combustion in the developed SFB prototype through CFD modelling with the commercial CFD code of FLUENT,

d) To determine the optimum operating parameters for combustion of rice husk in the SFB prototype, such as operating temperature, rotating speed, air input and feeding rate,

e) Fabrication of the proposed design of the novel horizontal SFB prototype combustor,

f) Trial runs on the developed SFB prototype to determine its operability, and

g) To investigate the weaknesses in the proposed design of the developed SFB prototype and to propose design improvements based on results from CFD modelling and trial runs on the combustor.

1.5 Expected Outputs

The outputs expected from this research are:-

a) A prototype rig of the novel horizontal SFB combustor,
b) The optimum operating parameters for combustion of rice husk in the proposed prototype, and
c) Design improvements on the developed prototype to enhance its performance for future experimental works involving combustion of waste materials.

1.6 Layout of the Report

This report describes the research work to design and develop a novel horizontal SFB for combustion of biomass wastes such as rice husk. This work includes the design procedures for a prototype of the SFB and the investigation of its hydrodynamics features through computational fluid dynamics modelling. The applications of the proposed system in gaseous and solids combustion are also conducted through modelling studies to investigate their combustion characteristics.

Chapter 2 reviews the fundamental theories of fluidisation in a conventional fluidised bed before extending to the more complex fluidisation theories in a SFB. This chapter also discusses the advantages of the proposed horizontal SFB over the vertical SFB and conventional fluidised bed.

Chapter 3 includes the methodology to study the properties of rice husk as feed and sand granules as bed media for use in sizing up the prototype SFB. The results from the determination of rice husk and sand granules properties that will be used in the design and modelling studies are also included.

Results obtained from the research are discussed in three stages (Chapter 4 to Chapter 6) owing to the wide scope of research works involved, which include

engineering design calculations, computational fluid dynamics modelling and commissioning of the developed horizontal SFB prototype.

Chapter 4 presents the procedures to perform design calculations in the course of determining the geometry of the proposed horizontal SFB. Discussions on the reasons for choosing certain dimensions and operating parameters for the proposed combustor are also included.

Chapter 5 deals with computational fluid dynamics studies on the proposed novel horizontal SFB carried out in a three-dimensional frame. Flow behaviours, particle trajectories and combustion characteristics of gaseous mixture and rice husk particles in the proposed system are investigated at different combination of air feed rates, rotating speed and combustor temperatures. Also included in this chapter are the discussions on the recommendable operational ranges and modifications for the current combustor design.

Chapter 6 provides discussions on the trial experimental runs on the prototype SFB combustor carried out at the fabricator's premises. Included in this chapter are visuals (photos and video clips), detailed technical specifications and manuals for operating the developed SFB prototype.

Chapter 7 gives the conclusion derived from this study and proposes some recommendations for future studies on the developed prototype of the horizontal SFB.

CHAPTER II

LITERATURE REVIEW

2.1 Advantages of Rotating Fluidised Bed

Performance of a SFB has been investigated by Takahashi et al. as early as 1984. Lately, this technology is gaining increasing research interests, mainly due to the various advantages it offers in comparison with the conventional fluidised bed technology, such as:-

a) By changing the rotating speed of the bed, the minimum fluidising velocity can be achieved at almost any gas flow rate. Thus, fluidisation of particles at a desired gas flow rate can be controlled by adjustments of the rotational speed of the cylinder. It is termed versatile due to its ability to burn different type of wastes, which may require a different rate of fluidising air. A higher turndown ratio can also be achieved as this feature allows the incinerator to accommodate different rate of waste feeding.

b) The SFB can accommodate a much higher gas flow rate per unit area of the distributor than is possible in a conventional fluidised bed that operates only against the force of gravity by the use of a strong centrifugal field. Serious formation of large bubbles can be suppressed by increasing the rotating speed of the cylinder in conjunction with the fluidising gas flow rate.

c) The absence of gravitational field or the presence of rocking motion will not affect the operation of the SFB. Therefore, it can be utilised in spacecrafts, ships, trains and trucks where the application of conventional fluidised bed is difficult, if not impossible.

d) Due to the cylindrical geometry and small surface area of the distributor, the size of the SFB is much smaller and more compact than the conventional fluidised bed.

e) Relatively shorter start-up time as compared to the conventional fluidised bed.

f) Higher combustion intensity. The throughput and therefore the combustion intensity varies approximately as the square-root of the g-loading and is thus proportional to the RPM. Hence, operating the SFB at about 100-g would give a combustion intensity of the order of 100 MW/m^3, which is almost an order of magnitude higher than a conventional fluidised bed (Swithenbank et al., 1997). Operating at higher rotational speed led to higher combustion intensity as depicted in Figures 2.1 – 2.2 generated using CFD (Rozainee, 1998). Nonetheless, in the combustion of waste such as sewage sludge, the rotating speed is operated at a relatively low *g* level (ranging from 5- to 20-g loading) to give a more modest pressure drop across the bed.

g) Higher combustion efficiency. The intensely turbulent intimate mixing of feed particles and air in the rotating fluidised bed has led to combustion efficiency in the excess of 99% as claimed by Metcalfe and Howard (1977). Conventional solid waste incinerators, in comparison, typically achieve combustion efficiency only in the vicinity of 93 – 95% (Houthon, 1993). High combustion efficiency is crucial for the improvement in ash quality as well as reduction in the amount of pollutants by minimising dioxin/furan emissions.

h) Ability to accommodate larger-sized solid fuel particles. Capital investment and energy consumption required for size reduction during the feed pre-

treatment stage are thus reduced. Efforts for removing fines and ashes from the exhaust gas is minimised as well (Fan, 1978).

i) Good combustion performance achievable with small particles. Broughton (1975) found that stable combustion was impossible to be sustained within a shallow fluidised bed of silica sand of particle sizes less than 246 μm. Radiative heat loss in a shallow fluidised bed is significantly larger than that of a SFB due to its higher geometrical viewfactor. Consequently, as the heat retained in a SFB is higher, the length of the preheat and reaction zones is shortened, thereby reducing the possibility of gas bypassing the bed.

However, there are several limitations to the vertical SFB technology. Non-uniformity in axial bed thickness and radial fluidisation, as well as feeding problems are inherent in the vertical SFB, as shown by Rozainee (1998) in his studies. The horizontal SFB technology offers the potential to solve these problems. It is a variation from the vertical SFB technology whereby the cylindrical bucket is rotating about a horizontal axis of symmetry instead of a vertical one.

2.2 Advantages of Horizontal SFB

The horizontal SFB offers numerous advantages over the vertical SFB, which makes it an important field of study. Important advantageous features of the horizontal SFB are outlined in the following sections.

2.2.1 Uniform Axial Bed Thickness

The inner free surface of the bed in a vertical SFB operating at low rotational speeds will tend to take the shape of a paraboloid of revolution. At high rotational speeds, the bed is almost a cylindrical annulus (Levy et al., 1978; and Demircan,

1979). This is explicable by the fact that at low rotational speeds, the net centrifugal force acting on the bed particles could not overcome the force of gravity, hence causing the particles to accumulate near the bottom of the cylinder. This will lead to a non-uniform axial bed fluidisation as the bed is thin at the top and thick at the bottom. With lower resistance to air flow, the thinner bed fluidises first although the bottom of the bed may still remain packed. Increasing the fluidising air velocities in an attempt to fluidise the whole length of the bed might result in an excessive elutriation of particles from the top end. The horizontal SFB, on the other hand, produces uniform axial bed thickness. The same types and magnitudes of forces act on the particles for the whole length of the bed, resulting in uniform axial bed thickness.

However, the net force of the centrifugal and gravitational acceleration acting on the bed particles at the upper section is higher than at the lower section. The particles from the upper section of the horizontal SFB might fluidise first. Nonetheless, due to the rotating effect, bed particles at both the upper and lower section of the SFB are changed constantly. Consequently, most of the bed particles in the horizontal SFB will fluidise although the circumferential bed fluidisation varies.

2.2.2 Uniform Radial Bed Fluidisation

Non-uniform radial bed fluidisation is typical of the SFB due to the curvature effect. Complete bed fluidisation cannot be achieved at one fluidising velocity in a SFB as opposed to the conventional fluidised bed. The difference in fluidisation velocities for surface fluidisation (U_{mfs}) and complete fluidisation (U_{mfc}) increases as the bed thickness is increased. Therefore, severe elutriation of particles from the bed surface might result as the fluidising velocity is increased to achieve complete fluidisation in a thick bed. These problems could be overcome by tapering the end walls of the horizontal SFB in order to achieve complete fluidisation of the bed materials at one fluidising velocity. With a tapered bed, the fluidising velocities could be made to increase with the bed radius so that they could match the

centrifugal force, which also increased with the bed radius. F_R (the ratio of fluidising velocity near the SFB wall to the fluidising velocity at the bed surface) could be manipulated to reach a value of near unity, depending on the angle of the tapered ends as the cross sectional area at the surface is larger than at the wall. Thus, with a particular air flow rate, the fluidising velocity is decreased as the air flows radially inward.

2.2.3 Feeding Problems in a Vertical SFB

A vertical SFB has an exhaust gas outlet at the top which doubles as the feed inlet. The limited opening area and strong upward velocity of effluent gases rushing out of the combustor posed serious feeding problems especially when the throughput rate is high. The horizontal SFB eliminates these problems as one end of the combustor will accommodate waste feeding while the exhaust gas exits at the other end.

2.2.4 Ash Accumulation

Rice husk waste contains approximately 20% of ash (Mokhtar et al., 1986). Continuous incineration of rice husk therefore will lead to significant ash accumulation. In order to maintain a constant bed thickness, the ash has to be removed. This is possible in a horizontal SFB by use of a weir plate. It is expected that once the bed thickness exceeds the weir plate lip due to ash accumulation, the bed materials from the bed surface will spill out. Ash particles have a lower density than that of sand particles, thus the ash particles tend to accumulate above the bed of sand particles. This is favourable, as most of the spillover particles will comprise mainly of the unwanted ash particles.

2.2.5 Potential to Control Particulate Emissions

The inclusion of a secondary chamber in the horizontal SFB, besides allowing for complete combustion of released volatiles and escaped unburnt particles, also functions as a particulate control device. The particulates in the flue gas are impacted to the wall of the combustor by the centrifugal force due to the rotating action of the combustor. The wall of the secondary chamber will accommodate some drilled holes to allow for the escape of the particulate materials. These particles will eventually be collected in an ash pit.

2.2.6 Possible Enhanced Mixing

The presence of the tapered ends at the horizontal SFB walls might cause the bed materials to exhibit spouting behaviour as observed in a spouted bed. This is justified by the fact that the tapered sections have varying cross sectional areas which is not dissimilar to that in a spouted bed. Khoshnoodi and Weinberg (1978) explained that the ratio of column to gas orifice inlet diameter is usually in the order of 10. At one point, the ratios of the cross sectional area at the bed surface to that at the combustor wall might reach the magnitude of 10. When enough air is introduced into the system, the column of bed materials with a cross sectional area similar to that of the bottom of the tapered end might be lifted up by the entering air. This signifies the onset of bed spouting behaviour which offers better mixing and heat circulation (Mathur and Gishler, 1955) as compared to conventional fluidisation. This phenomenon, coupled with the rapid mixing in the rotating fluidised bed, will significantly enhance the rate of particles mixing in the combustor. The direct beneficial effect of this is the increase in combustion efficiency in the horizontal SFB with tapered ends.

2.3 Unique Advantages of the SFB Freeboard

A very important feature of the SFB is that the gases are imparted a tangential velocity component (Figure 2.3) which accelerates due to the conservation of momentum as the gases converge towards the exit. A swirling flame of volatiles and CO emitted from the bed is therefore formed at the exit of the chamber. Both experimental and modelling studies by Rozainee (1998) showed that the swirling effects in the SFB freeboard resulted in a very efficient secondary combustion process, and higher rotating speeds increased the efficiency of gas phase combustion and the residence time of particles in the SFB freeboard. The intense gas mixing which occurs in the shear layers of such burner resulted in a much higher freeboard combustion intensity than is encountered in the freeboard of a static fluidised bed. Furthermore, the effects of rotation caused the sand particles from the surface of the bed to be returned to the bed. The huge freeboard, which is necessary to separate elutriated particles and complete the gas phase combustion in a conventional fluidised bed, is not necessary with a SFB.

2.4 Fluidisation

2.4.1 Fluidisation in a Conventional Vertical Fluidised Bed

The unit operation fluidisation is typified by the passage of a gas through a packed bed of particles supported by a gas distributor such as a perforated or porous plate. Due to the loss of mechanical energy brought about by the friction of the gas flowing past the particles, a pressure drop over the bed height is observed. This pressure drop rises in proportion with the increasing gas flow rate until it reached a point where its value equals the net weight of the particles per unit cross sectional area of the bed. This signifies the onset of fluidisation and the bed is said to be ‘incipiently’ fluidised. Beyond this point, the bed can in principle be lifted by the gas flow.

The broad sequence of events that occurred in a bed of particles as the gas flow rate is increased progressively from zero is depicted in Figure 2.4. Initially, no changes in the appearance of the bed can be observed while the pressure drop rises with flow rate, until it reached a maximum value at the point of incipient fluidisation. Further increase in gas velocity will 'unlock' the fixed bed. This literally means that there will be a slight decrease in pressure drop as the voidage increases from ε_m ke ε_{mf}. The pressure drop will not increase further upon increasing the velocity beyond the minimum fluidising velocity (U_{mf}). The bed expands to accommodate the extra gas flow at first until at some point, bubbles or particle-free cavities are formed among the particles. These bubbles will then rise through the bed, bursting when they reach the free surface. Particles are scattered into above the bed region, from where they fall back to the bed. As a consequence, the bed exhibits two phases, the bubble and particulate (continuous) phase.

Uniformity of the bed temperature and composition is thereby promoted by the bubbling action, which causes the particles to mix continuously. Nevertheless, this action can also lead to undesirable excessive bypass of unreacted fluidising gas. Some particles will be entrained in the gas leaving the bed at sufficiently high fluidising velocity. Progressive entrainment of particles proceeds with further increase in fluidising velocity and the bed pressure drop is reduced until eventually, all particles are blown out of the vessel.

The Ergun equation (1952) gives the pressure drop over the incipiently fluidised bed.

$$\frac{\Delta P_b}{L} = 150\frac{(1-\varepsilon)^2}{\varepsilon^3}\frac{\mu_f U}{(\phi_s d_m)^2} + 1.75\frac{(1-\varepsilon)}{\varepsilon^3}\frac{\rho_f U^2}{\phi_s d_m} \qquad (2.1)$$

The value of d_m referred to volume-surface mean diameter (Botterill et al., 1982).

From the definition of U_{mf}, the minimum fluidisation occurs when;

(drag force by upward moving gas) = (weight of particles) (2.2)

$$\Delta P_b A_t = W = A_t L_{mf} (1 - \varepsilon_{mf}) (\rho_p - \rho_f) \frac{g}{g_c} \tag{2.3}$$

Re-arranging, we have;

$$\frac{\Delta P_b}{L_{mf}} = (1 - \varepsilon_{mf})(\rho_p - \rho_f) \frac{g}{g_c} \tag{2.4}$$

Combination of Equations (2.1) and (2.4) results in:

$$\frac{\rho_f (\rho_p - \rho_f) g d_m^3}{\mu_f^2} = 150 \frac{(1 - \varepsilon_{mf})}{\phi_s^2 \varepsilon_{mf}^3} \frac{\rho_f U_{mf} d_m}{\mu_f} + 1.75 \frac{(1 - \varepsilon)}{\phi_s \varepsilon_{mf}^3} \frac{\rho_f^2 U_{mf}^2 d_m^2}{\mu_f^2} \tag{2.5}$$

The left hand side of Equation (2.5) is a dimensionless group known as the Archimedes Number, Ar:

$$Ar = \frac{\rho_f (\rho_p - \rho_f) g d_m^3}{\mu_f^2} \tag{2.6}$$

The Reynolds Number at incipient fluidisation is defined as:

$$Re_{mf} = \frac{\rho_f U_{mf} d_m}{\mu_f} \tag{2.7}$$

Thus, at minimum fluidising velocity,

$$Ar = 150 \frac{(1 - \varepsilon_{mf})}{\phi_s^2 \varepsilon_{mf}^3} Re_{mf} + 1.75 \frac{(1 - \varepsilon)}{\phi_s \varepsilon_{mf}^3} Re_{mf}^2 \tag{2.8}$$

Wen and Yu (1966) noted that, for their particular range of materials,

$$\frac{(1-\varepsilon_{mf})}{\phi_s^2 \varepsilon_{mf}^3} \approx 11.0 \qquad \text{and} \qquad \frac{1}{\phi_s \varepsilon_{mf}^3} \approx 14$$

Inserting these values into the Ergun equation and solving for the positive root of Re_{mf},

$$Re_{mf} = (33.7^2 + 0.0408\, Ar)^{1/2} - 33.7 \qquad (2.9)$$

In theory, Equation (2.8) can be used to calculate the minimum fluidising velocity U_{mf} expressed in terms of Ar and Re_{mf}, provided accurate values of ε_{mf} and d_m can be obtained. However, the problems associated with the determination of the properties of particles add to the complexity of the prediction of fluidising velocity. Variation of ε_{mf} for particles in different size ranges with bed temperature can be very unpredictable. Particles in the size ranges of 40 – 500 μm and density range of 1400 – 4000 kg/m^3 (Geldart-B particles) have ε_{mf} values that vary with temperature in a highly complex manner and are not easily predictable, as shown by Botterill et al. (1982). On the contrary, dense and larger particles ($Ar \geq 26\,000$ and $Re_{mf} \geq 12.5$) did not seem to show an increase in ε_{mf} with bed temperature (Botterill et al., 1982).

In determining the minimum fluidising velocity, the best procedure is to make a direct experimental measurement of pressure drop across the bed at gradually decreasing gas velocity (Howard, 1989). This value of U_{mf} can be different from that obtained if the gas velocity is increased instead as the latter will result in hysteresis loops in the pressure drop versus gas velocity plot. U_{mf} is defined as the intersection of the fixed pressure drop line with the (W/A_t) or horizontal line in the plot similar to that of Figure 2.4.

2.4.2 Fluidisation in a SFB

One important criterion of the rotating fluidised bed is that the granules in the cylinder are gradually fluidised layer by layer from the free surface outward at

increasing radius as the gas velocity is increased. The aeration corresponding to the initial fluidisation of the inner surface and the complete fluidisation are termed the surface fluidising velocity, U_{mfs} and the critical fluidising velocity, U_{mfc} respectively. Chen (1987) noted that the gas superficial velocity in a SFB is a function of the position of bed radius, r. Therefore, the fluid drag, centrifugal force and gas inertia are all functions of position r, and the three forces cannot balance one another at all levels at one aeration rate. The fluid drag, in conjunction with the superficial gas velocity, decreases with respect to r $\left(U = \frac{Q}{2\pi r L}\right)$. The centrifugal force, on the other hand, increases monotonously with respect to r. The system configurations at different stages of aeration are shown in Figure 2.5.

Theoretical analysis developed by Chen (1987) showed that the pressure drop in the fixed bed region is given by the following equation:-

$$\frac{dP}{dr} = \Phi_1 \left(\frac{U_o r_o}{r}\right) + \Phi_2 \left(\frac{U_o r_o}{r}\right)^2 + \rho_f r\omega^2 + \frac{\rho_f U_o^2 r_o^2}{\varepsilon^2 r^3} \tag{2.10}$$

where

$$\Phi_1 = \frac{150(1-\varepsilon)^2 \mu}{\varepsilon^3 (\phi_s d_p)^2}, \qquad \Phi_2 = \frac{1.75(1-\varepsilon)\rho_f}{\varepsilon^3 \phi_s d_p}$$

This equation is a derivation from the Ergun equation. Meanwhile, the pressure drop in the fluidised bed region is:-

$$\frac{dP}{dr} = \rho_p (1-\varepsilon) r\omega^2 + \rho_f \varepsilon r\omega^2 + \frac{\rho_f U_o^2 r_o^2}{\varepsilon r^3} + \frac{\rho_f U_o^2 r_o^2}{\varepsilon^2 r^2}\frac{d\varepsilon}{dr} \tag{2.11}$$

It has to be emphasised that the major difference between the present momentum balance and those reported in the literature is that the voidage is treated as a variable. Although this assumption leads to additional numerical complexity of the problem, it is essential in obtaining a good estimation of the overall pressure

drop. A considerable change in pressure drop results with just slight changes in voidage as the first and second drag coefficients, Φ_1 and Φ_2 are both very sensitive functions of voidage.

In a practical point of view, both equations (2.10 and 2.11) can be further simplified. In the fixed bed region (Equation 2.10), the major contribution to the pressure profile is the drag force per unit volume of fluid, which are represented by the first two terms on the right hand side. In the fluidised bed region, however, the major contribution is the total mass of particles (the first term on the right hand side of Equation 2.11). The remaining terms, including the effect of inertia and variable porosity, contribute less than 1% of the total pressure drop (Kao et al., 1987) and thus can be neglected. Hence, in the fixed bed region Equation (2.10) reduces to;

$$\frac{dP}{dr} = \Phi_1 \left(\frac{U_o r_o}{r} \right) + \Phi_2 \left(\frac{U_o r_o}{r} \right)^2 \tag{2.12}$$

while Equation (2.11) in the fluidised bed region reduces to;

$$\frac{dP}{dr} = \left(\rho_p - \rho_f \right)(1-\varepsilon) r \omega^2 \tag{2.13}$$

2.4.2.1 The Surface and Critical Minimum Fluidising Velocities (U_{mfs} and U_{mfc})

The fluidising phenomenon in a SFB varies significantly from that of a conventional vertical fluidised bed, which is completely fluidised at a certain aeration rate. The SFB fluidise layer by layer from the inner surface outward. The inner surface of the bed will first experiences fluidisation and the gas velocity at which this occurs is the surface minimum fluidising velocity, U_{mfs}. Its value can be calculated by equating the local pressure drop across both the fluidised and packed bed using Equations (2.12) and (2.13) evaluated at $r = r_i$. A quadratic equation results;

$$U_o^2\left(\frac{r_o}{r_i}\right)^2\Phi_2 + U_o\left(\frac{r_o}{r_i}\right)\Phi_1 - \left[\left(\rho_p - \rho_f\right)\left(1-\varepsilon\right)\left(r_i\omega^2\right)\right] = 0 \qquad (2.14)$$

Solving for U_o (positive root);

$$U_o = \frac{-\left(\frac{r_o\Phi_1}{r_i}\right) + \sqrt{\left(\frac{r_o\Phi_1}{r_i}\right)^2 + 4\Phi_2\left(\frac{r_o}{r_i}\right)^2\left(\rho_p - \rho_f\right)\left(1-\varepsilon\right)r_i\omega^2}}{2\left(\frac{r_o}{r_i}\right)^2\Phi_2} \qquad (2.15)$$

where $U_o = U_{mfs}$.

The critical fluidising velocity, U_{mfc} (the velocity at which the whole bed is fluidised) can be calculated in a similar manner by use of Equation (2.12) and (2.13) evaluated at $r = r_o$. The positive root obtained for U_o is;

$$U_o = \frac{-\Phi_1 + \sqrt{{\Phi_1}^2 + 4\Phi_2\left(\rho_p - \rho_f\right)\left(1-\varepsilon\right)r_o\omega^2}}{2\,\Phi_2} \qquad (2.16)$$

where $U_o = U_{mfc}$ in this case.

The bed porosity (ε) to be used in both calculations is the bed voidage at the packed condition (ε_o).

The difference between U_{mfs} and U_{mfc} increases with the depth of the particle bed. Thus, in an extremely shallow bed where $r_i \approx r_o$, these two velocities are indistinguishable ($U_{mfs} \approx U_{mfc}$). The indication of this is that the conventional concept of fluidisation at one aeration rate still holds for a SFB with a shallow bed.

2.4.2.2 Pressure Drop

Two types of pressure drop versus superficial gas velocity were reported in the literature. As shown in Figure 2.6, one exhibits a plateau (Metcalfe and Howard, 1977) while the other a maximum (Fan et al., 1985). Based on theoretical studies in which particle loss due to elutriation was unaccounted for, Chen (1987) proposed that the pressure drop should reach a plateau after the critical minimum fluidising velocity. The condition whereby flattening of the pressure drop curve beyond the minimum fluidising velocity occurs, is similar to that of conventional fluidised beds.

The fundamental difference between a SFB and a conventional fluidised bed could be established through the observation of their pressure drop profiles. Regardless of whether the pressure drop exhibits a plateau or a maximum, the fact that fluidisation in a SFB occurs layer by layer resulted in the absence of hysteresis loops. Nevertheless, the definition of the intersection of the extrapolations from the region of fixed bed and fluidised bed as the minimum fluidising velocity, used in conventional fluidised beds, still holds for SFB. A number of studies have adopted this approach, such as Demircan et al. (1978) and Takahashi et al. (1984).

Bed thickness has significant influence on the pressure drop profile in the SFB due to the layered fluidisation phenomenon. This has led to further studies by Kao et al. (1987). It was found that beyond the critical minimum fluidising velocity, the pressure drop reached a plateau for thin beds, but a maximum for thicker beds (Figure 2.7). U_{mfc} is much higher than U_{mfs} for thicker beds. Therefore, at U_{mfc}, the drag force is higher than the centrifugal force at the bed surface. As a consequence, the drag force of the air continuously carries particles at the surface out of the bed, until a point is reached where it is balanced off by the centrifugal force of the remaining particles. As described by Takahashi et al. (1984) and Fan et al. (1985), the pressure drop curve for thick beds exhibits a maximum as opposed to a plateau observed in thin beds. This could be attributed to the loss of particles due to elutriation in thick beds, which reduces the effective weight of the particles, hence the corresponding decrease in pressure drop.

Depending on the superficial velocity, U_o (based on the outside radius, r_o), the pressure drop across the bed could be determined at different stages of fluidisation.

Case I: $\mathbf{U_o < U_{mfs}}$

The whole bed remains packed at this stage since the superficial air velocity, U_o is less than the surface minimum fluidising velocity, U_{mfs}. Using Equation (2.12), the pressure drop is calculated as;

$$\Delta P = \Phi_1 U_o r_o \ln\left(\frac{r_o}{r_i}\right) + \Phi_2 U_o^2 r_o^2 \left(\frac{1}{r_i} - \frac{1}{r_o}\right) \tag{2.17}$$

Equation (2.17) is applicable for the evaluation of ΔP at U_{mfs} by replacing U_o with U_{mfs}.

Case II: $\mathbf{U_{mfs} < U_o < U_{mfc}}$

At this stage, the bed is partially fluidised. Thus, the pressure drop is a combination of pressure drop for the packed bed and the fluidised bed;

$$\Delta P = (1-\varepsilon)(\rho_p - \rho_f)\omega^2(\rho_{pf}^2 - \rho_i^2) + \Phi_1 U_o r_o \ln\left(\frac{r_o}{r_{pf}}\right) + \Phi_2 U_o^2 r_o^2 \left(\frac{1}{r_{pf}} - \frac{1}{r_o}\right) \tag{2.18}$$

where r_{pf} is the interface of the fluidised and packed beds and can be calculated by equating Equations (2.12) and (2.13) at a certain gas velocity, U_o.

Case III: $\mathbf{U_o \geq U_{mfc}}$

This is the stage where the bed is completely fluidised. The bed pressure drop is the effective weight of the bed and is calculated by using Equation (2.13);

$$\Delta P = (1-\varepsilon)(\rho_p - \rho_f)\omega^2\left(\frac{r_o^2 - r_i^2}{2}\right) \tag{2.19}$$

2.5 Physical Properties of Sand Granules

Particle fluidisation depends largely on the properties of the fluidising materials. Generally, good media properties include high resistance to attrition, thermally stable in the operational temperature range, generate acceptable pressure drop and has a combination of particle density, size distribution and shape which gives good fluidising characteristics. Utilisation of sand as the bed media in fluidised bed combustors is commonplace, as it possessed all of the properties as mentioned above.

Physical properties such as particle size, size distribution, density, bed voidage and sphericity have significant influence on the fluidisation of particles.

2.5.1 Particle Size and Size Distribution

One fixed value of diameter does not exist for materials with irregular sizes. Instead, a mean diameter, which could well represent the size distribution of the materials, is more appropriate for such condition. There are different types of mean diameter to characterise the size distribution of irregular materials, and each differs from the other based on different definitions used (McCabe et al., 1993). The weight mean diameter is often used, as given by the equation below:-

$$\text{Weight mean diameter, } D_w = \sum_{i=1}^{n} x_i D_{pi} \qquad (2.20)$$

However, for fluidisation studies, the volume-surface mean diameter (Botterill et al., 1982) is to be used.

$$\text{Volume-surface mean diameter, } D_{vs} = \frac{1}{\sum_{i=1}^{n} (x_i / D_{pi})} \qquad (2.21)$$

where

x_i = mass fraction

D_{pi} = arithmetic mean diameter of screen apertures

2.5.2 Bed Voidage (ε)

The voidage of a bed of particles, ε, is the ratio of the volume of voids in the bed to the total volume (voids plus solids) of the bed. Its value is largely dependable on the shape of particles, particle size distribution (as fine particles tend to fill the voids between larger particles), the ratio of particle size to bed diameter, particle arrangement pattern in the bed and size of the bed (different sections in the bed have different values of voidage). Thus, the practice of voidage prediction from the geometry of single particles is unreliable. Determination of voidage through experiments, such as by comparing the bulk density (ρ_b) of bed particles with the true density of particle (ρ_p) (Howard, 1989), gives more reliable measurements.

$$\varepsilon = \left(1 - \frac{\rho_b}{\rho_p}\right) \tag{2.22}$$

2.5.3 Particle Sphericity (ϕ_s)

Quantification of a non-spherical particle is given by the sphericity, ϕ_s which is defined as:-

$$\phi_s = \frac{\text{surface area of a sphere of the same volume as the particle}}{\text{surface area of the particle}} \tag{2.23}$$

Sand particles, being non-spherical, have sphericities ranging from 0.53 to 0.86 (Kunii and Levenspiel, 1991). Brown (1950) observed an inverse relationship between the bed voidage and particle sphericity (Figure 2.8).

Difficulties in measuring the sphericity of irregular particles has led to recommendations by Kunii and Levenspiel (1991) and Howard (1989) that the sphericity be measured from a minimum fluidising velocity experiment. By measuring the bulk density ρ_b of a loosely packed bed of particles and particle density ρ_p, the voidage at minimum fluidisation (ε_{mf}) can be determined using Equation (2.22). Subsequent calculation of the Archimedes and Reynolds Numbers (Ar and Re_{mf}) are possible, and along with U_{mf}, fluid viscosity μ_f and density ρ_f, and the mean particle diameter d_m, they are then substituted into Equation (2.8). The sphericity ϕ_s can then be solved from Equation (2.8).

2.5.4 The Geldart Classification of Particles

Four categories of particle behaviour have been forwarded by Geldart (1972) based on his observation on bed fluidisation behaviour at ambient conditions. As shown in Figure 2.9, the classification relates the influence of particle mean size and particle density to the bed behaviour. The classification, from the smallest to the largest particles, is described as follows:-

a) Category C

Particles with a mean particle size of less than 30 μm (< 30 μm) or a low density are included in this category. Fluidisation is extremely difficult because the particles exhibit greater inter-particle forces than the forces resulting from the action of fluidising gas. This explains the channelling phenomenon that tends to take place, where a low resistance channel will form in the bed by the upward moving gas. The channel will expand in conjunction with the increase in gas velocity and this leads to non-uniformity in gas distribution in the bed. As a consequence, the bed will not

fluidise. Nevertheless, this situation could be overcome by using a rotating distributor plate. Examples of particles in this category are flour and talcum powder.

b) Category A

The particle sizes in this category ranged from 20 – 100 μm and have a relatively low density (< 1400 kg/m^3). The particles fluidise easily, where fluidisation is smooth at low gas velocities and exhibits controlled bubbling at high gas velocities, with the presence of favourable small bubbles. Bed expansion is stable until the minimum fluidising velocity is reached. However, mixing is limited.

c) Category B

The particle in this size range is characterised by their sandlike properties, with a size range between 40 – 500 μm and density in the range of 1400 – 4000 kg/m^3. In general, fluidising behaviour for these particles is good with vigorous bubbling action and bubble enlargement upon reaching the bed surface. Bed expansion, however, is less stable as compared to Category A particles.

d) Category D

This category includes large (size more than 600 μm) and dense particles. Fluidisation is difficult for deep bed of these particles. Their behaviour is erratical and unpredictive, giving large exploding bubbles or severe channelling, as well as spouting when the gas distribution is uneven. Mixing of particles in this category in the freely bubbling condition is inferior to those of categories A and B.

CHAPTER III

DETERMINATION OF PARTICLE PROPERTIES

3.1 Measurement of Rice Husk Properties

3.1.1 Proximate Analysis

Rice husk samples obtained from the nearby rice mill in Muar were subjected to proximate analysis to determine its gross calorific value (GCV) and contents of moisture, ash, volatile matters and fixed carbon. The American Society of Testing Materials (ASTM) methods were employed in this study:-

a)	Moisture	-	ASTM D 3173
b)	Ash	-	ASTM D 3174
c)	Volatile matters	-	ASTM D 3175
d)	GCV	-	ASTM D 240 – 76 (1980)

3.1.2 Ultimate Analysis

Ultimate analysis includes the determination of elemental components in the rice husk samples, such as C, H, N, S and O. The UOP Method 866 – 86 (determination of carbon, hydrogen and nitrogen by oxidative pyrolysis) was employed. The content of O is found by the differential method, whereby the

subtraction of the sum of C, H, N, S and ash will give the amount of O present in the sample.

3.2 Measurement of the Physical Properties of Sand

Physical properties of sand granules, to be used as the fluidising media, were studied. Properties to be determined included density, voidage, particle size and sphericity, all of which have significant effects on particle fluidisation.

3.2.1 Particle Size, Particle Density and Bed Voidage

The commercial silica sand granules marketed as 20/30 sand under the Tyler Standard Screen Scale has a size range of 600 – 850 μm. Its mean particle diameter, therefore, is 725 μm. The sand granules were first subjected to screen analysis to determine its size distribution. Test sieving were carried out in a sieve shaker manufactured by Pascall Engineering Co. Ltd. Approximately 500 g of sand was sieved for approximately 30 minutes. The sand was sieved into five size ranges: 0.30 – 0.50 mm, 0.50 – 0.71 mm, 0.71 – 1.00 mm, 1.00 – 1.18 mm and 1.18 – 2.00 mm.

A sand sample was loosely filled in a 100 ml graduated cylinder to give its bulk volume. The mass of the sand over its bulk volume gave the bulk density of the sand. The water displacement method was used to determine the particle density of the sand. The mass of sand divided by the volume of water displaced gave the particle density of the sand. The voidage was then determined from Equation (2.22).

3.2.2 Minimum Fluidising Velocity (U_{mf}) and Particle Sphericity (ϕ_s)

Fluidisation studies in a conventional fluidised bed were performed to determine U_{mf}, which is then used to determine the particle sphericity. The latter parameter, together with the physical properties of sand determined earlier, is important for subsequent design calculations.

A small columnar fluidised bed of 80 mm ID made of glass with a flat perforated distributor plate at the bottom was used to determine the minimum fluidising velocity, U_{mf} of the sand granules. Hole area of the distributor plate is 3% of the total plate surface area with each hole having a diameter of 1 mm. Measurement of bed pressure drop was by means of a water manometer. A rotameter was used to measure the volumetric flow rate of air supply from the compressor. The fluidising air was first dried in an air filter to prevent the air humidity from interfering with the fluidisation process.

Approximately 1 kg of sand was charged into the column, which gave a bed depth of approximately 16 cm. The bed was initially fluidised in a vigorous manner in order to break down any packing of the particles. The gas velocity was then decreased in increments of 10 L/min and the corresponding pressure drop recorded. For determination of U_{mf}, the pressure drop of the bed was plotted against the gas velocity. The volumetric flow rates divided by the bed cross sectional area gave the gas velocities required.

3.3 Properties of Rice Husk and Sand Granules

3.3.1 Properties of Rice Husk

Proximate analysis performed on the rice husk samples (Table 3.1) showed that they were mainly constituted by volatile matters. Therefore, combustion of rice husks is predicted to be controlled by volatile-burning, where heat transfer

predominates the drying and subsequent de-volatilisation processes. The understanding of this was crucial in determining the amount of air to be fed into the combustor. As in this case where pyrolysis occurs, air feed at stoichiometric or slightly below stoichiometric is favored. Excess air will only extinguished the flame as pyrolysis is an endothermic reaction.

The elemental components in rice husk, obtained through ultimate analysis were important for the purpose of mass and energy balances. The results obtained were in good agreement with reported literature findings (Mokhtar et al., 1986). These results will later be used in CFD modelling of the combustion of rice husk particles in the proposed RFB design.

Table 3.1: Rice husk analysis

Proximate Analysis	**Weight %**
Moisture	10.1
Volatile matters	64.1
Fixed carbon	11.1
Ash	14.7
Gross Calorific Value (MJ/kg)	13.3
Ultimate Analysis (dry basis)	
C	37.8
H	5.0
O	40.3
N	0.6
Ash	16.3

Ash accumulation from the combustion of rice husk could be significant and this could interfere with the fluidisation process in the primary chamber. However, since the particle density of rice husk ash is 1590 kg/m^3, which is approximately 35% lower than the particle density of sand granules (2430 kg/m^3), the ash is

expected to form a layer above the sand granules. Thus, removal of this ash from the bed is possible with the inclusion of a weir plate at the primary chamber. Once the bed thickness exceeds the weir plate lip due to ash accumulation, the top layer of ash near the bed surface will spill out. Bed thickness in the fluidised bed could therefore be maintained.

Biomass materials such as rice husk offers the potential of renewable energy sources with their relatively high GCV (13 MJ/kg) and considering the abundance of available biomass residues (approximately 20.8 million tonnes) in the country. Utilisation of such renewable energy resources could contribute to some 10 to 12 percent of the national energy consumption as the potential capacity of biomass-based power generation is estimated at 700 MW (NSTP, 13 June 2000). In addition, the growing problems of rice husk disposal in the country (estimated annual production of 470 kilotons corresponding to the annual paddy output of 2,142 kilotons at 2001, as stated by the Department of Statistics Malaysia) could be taken care of.

Results from the ultimate analysis on rice husk samples indicated the absence of chlorine and sulfur. Therefore, combustion of rice husks will not result in the release of acid gases such as hydrogen chloride (HCl) or sulfur dioxide (SO_2). Preventive measures, such as injection of limestone granules into freeboard region of the fluidised bed to absorb such gases, are not necessary.

3.3.2 Physical Properties of Sand

3.3.2.1 Particle Size, Densities and Bed Voidage

The physical properties of sand granules were as shown in Table 3.2. The mean particle diameter was given by the volume-surface mean diameter from screen analysis.

Table 3.2: Physical properties of sand

Physical Properties	Values
Size range (μm)	600 – 850
ρ_b (kg/m^3)	1457.8
ρ_p (kg/m^3)	2429.7
ε	0.40
d_p mean (mm)	0.672
*c_p (J/g • K)	0.8

Note: * Taken from Perry et al. (1997).

These particles fall into Category D according to the Geldart Classification of particles (Geldart, 1972) with their diameter in the excess of 600 μm. They are difficult to fluidise and tend to produce large exploding bubbles that lead to severe channelling and spouting behaviour.

3.3.2.2 Minimum Fluidising Velocity and Particle Sphericity

The value of U_{mf} was found at 0.31 m/s from the pressure drop plot (Figure 3.1). This value is in good agreement with the calculated value of 0.30 m/s from Equation (2.9) using Wen and Yu constants (1966). Thus, the sphericity of the sand particles was 0.89. The mean diameter used in the sphericity calculations was the arithmetic mean diameter as size distribution studies indicated that the sand granules was mainly constituted by particles in the range of 0.5 – 0.71 mm and 0.71 – 1.00 mm (Table 3.3). Therefore, the arithmetic mean diameter of 0.73 mm was found to represent the size of the sand granules better than the volume-surface mean diameter of 0.67 mm. The value of sphericity was found at 0.90 (normal packing) from the plot developed by Brown (1950) as in Figure 2.8, another good agreement with the experimental value.

However, one salient feature worth noticing on the value of sphericity obtained was that it was fairly high compared to the range of sphericities as reported

by Kunii and Levenspiel (1991). The discrepancy arising might be attributed to the source and size distribution of the sand used. The determination of sphericity laid on many uncertainties, mainly the particle size, which in reality differs from time to time even within the same source and type of sand particles used. The sensitivity in sphericity determination in turn affects the fluidisation calculations. It is in this retrospect that the subsequent design calculations were performed with a sphericity value of 0.7, a value more representative of sand particles in the size range of 0.60 – 0.85 μm and size distribution as determined on the sand samples used.

Table 3.3: Size distribution of sand particles with a mesh size of 20/30

Sieve range (mm)	Mass Percentage (%)
1.18 – 2.00	0.15
1.00 – 1.18	0.31
0.71 – 1.00	52.39
0.5 – 0.71	39.80
0.3 – 0.5	6.61
< 0.3	0.74

CHAPTER IV

DESIGN AND DEVELOPMENT OF THE PROTOTYPE HORIZONTAL SFB COMBUSTOR

4.1 Design of the Horizontal SFB Combustor

The proposed design of the horizontal SFB combustor was aimed at overcoming the weaknesses inherent in a vertical SFB. These weaknesses include:-

a) **Non-uniform axial bed thickness.** At low rotational speeds, the bed in a vertical SFB tends to take the shape of a paraboloid of revolution. Increasing the fluidising velocity in order to fluidise the thicker bed at the bottom end results in excessive elutriation of particles from the top of the bed.

b) **Non-uniform radial bed fluidisation.** Due to the curvature effect, complete fluidisation cannot be achieved at one fluidising velocity in a SFB. The ratio of U_{mfc}/U_{mfs} increases with thicker beds and attempts at increasing the fluidising velocity to fluidise particles near the wall lead to severe elutriation from the bed surface.

c) **Feeding problems.** The vertical SFB have only one outlet functioning both as feed inlet and exhaust outlet. The strong upward velocity of effluent gases tends to blow out the feed materials, especially waste with low density such as rice husk.

d) **Ash accumulation.** The resulting ash from continuous combustion of waste materials needs to be removed in order to maintain a constant bed thickness.

Removal of ash from a vertical SFB is complicated due to the presence of only one outlet.

Apart from eliminating the disadvantages discussed earlier, the prototype of the horizontal SFB was engineered to achieve higher combustion efficiency in the gas phase and to control particulate emissions through inclusion of a secondary chamber. The parameters that need to be determined and optimised in the design stage of the combustor are:-

i) Sand size for use in design calculations,
ii) Operating temperature range for sizing of combustor,
iii) Combustor dimensions (diameter and length),
iv) Tapered section geometry (tapering height and degree of tapering),
v) Bed depth,
vi) Rotating speed of combustor,
vii) Fluidising air feed rate, and
viii) Rice husk feed rate.

The inclusion of the tapering ends in the primary chamber of the proposed SFB was aimed at achieving uniform fluidisation in the radial direction. It is important to note that the tapering effect does not alter the ratio of U_{mfc}/U_{mfs} as both values depend on the radius only. Thus, this ratio will remain the same for a certain bed depth in a SFB with or without the tapered ends. The tapering effect only alters the fluidisation number at the wall (no. of U_{mfc}) over the fluidisation number at the bed surface (no. of U_{mfs}). For simplification reasons, this term will be represented by the symbol F_R. As an example, in an untapered SFB, a U_{mfc}/U_{mfs} ratio of 3 indicates that when the fluidising velocity at the bed surface is 3 U_{mfs}, the fluidising velocity near the SFB wall is just 1 U_{mfc}. F_R, in this case, is therefore 1/3, which is also the inverse value of U_{mfc}/U_{mfs}. The tapering effect, on the other hand, could equalise F_R. Manipulation of the cross sectional area for radial airflow could be performed by changing the tapering height and tapering angle to reduce the air velocity in the radial direction inwards until a condition is reached whereby this ratio approaches unity (for a certain bed depth).

All parameters in the design were interrelated. For example, changing the angle of tapering resulted in a change in F_R for a certain bed depth although U_{mfc}/U_{mfs} remains the same. Changing the bed depth while maintaining the same angle of tapering also changed the ratio of U_{mfc}/U_{mfs} and subsequently the value of F_R. The air inputs to achieve a certain fluidising velocity also depend on the rotating speed and size of the combustor. Thus, Excel spreadsheets were constructed to give a clear picture of the effects arising from the modifications of each parameter. The base case design was based on using rice husks as the feed material.

4.2 Calculation of Combustion Air Requirement

Mass balance was conducted to determine the amount of stoichiometric air feed required for the complete combustion of rice husk. Taking 100 g of feed as a basis of calculation, the procedures to calculate the required amount of air were outlined as follows:-

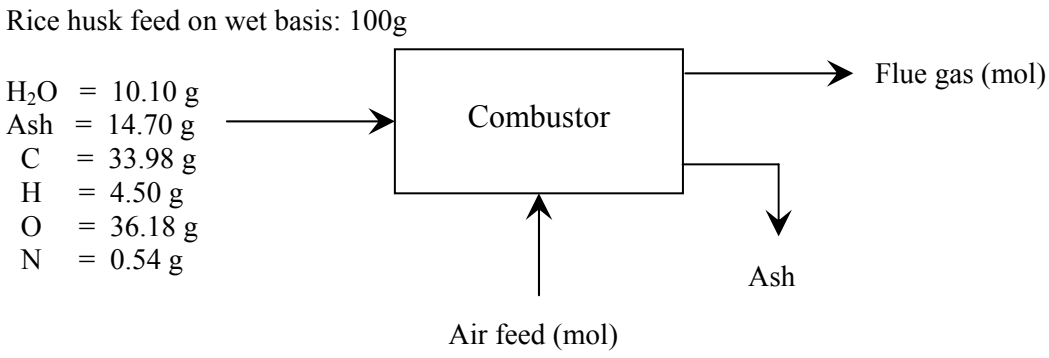

C	=	33.98 g	≡	2.83 mol
H	=	4.50 g	≡	4.50 mol
O	=	36.18 g	≡	2.26 mol

Assuming complete combustion, carbon and oxygen in the feed will be oxidised in the following manner:-

$C + O_2 \rightarrow CO_2$

$4H + O_2 \rightarrow 2\ H_2O$

$\therefore$ 1 mol C $\equiv$ 1 mol O_2

1 mol H $\equiv$ 0.25 mol O_2

Stoichiometric oxygen requirement:-

2.83 mol C $\equiv$ 2.83 mol O_2

4.50 mol H $\equiv$ 1.13 mol O_2

2.26 mol O $\equiv$ (-) 1.13 mol O_2

Amount of oxygen required = 2.83 mol

$$\text{Stoichiometric air requirement} = \frac{1\ \text{mol air}}{0.21\ \text{mol O}_2} \times 2.83\ \text{mol O}_2$$

$$= 13.48\ \text{mol}$$

$$\text{Air feed at ambient (30}^{\text{o}}\text{C)} = 13.48\ \text{mol} \times \frac{22.414\ \text{L}}{\text{mol}} \times \frac{303\ \text{K}}{273\ \text{K}}$$

$$= \frac{335.3\ \text{L}}{100\ \text{g feed}} @ \frac{3.353\ \text{m}^3}{\text{kg feed}}$$

Hence theoretically, 3.35 m^3 of air (at 30^{o}C) is required for the complete combustion of 1 kg of rice husk. However, in actual combustion operation, excess air is required in order to facilitate the complete oxidation of the char fraction. Rice husk particles consist primarily of volatiles (64 wt% on wet basis) with a small amount of char (11 wt% on wet basis). Combustion of high-volatile materials is heat-transferred controlled, whereas combustion of materials with high char content (such as coal) is mass-transferred controlled. In the former case, combustion occurs when the volatiles inside the materials are released into the combustor, where they will then be burnt to completion. The burning of these volatiles releases heat into the combustor necessary to sustain the combustion process. The devolatilisation process is an endothermic process and the presence of a high amount of excess air

will lower the combustor temperature to the point of quenching the flame and suppressing the devolatilisation process. On the contrary, high-char content materials require a high amount of excess air in order to oxidise the chars, thereby releasing the heat into the combustor. Taking these considerations into account, it is suggested that for the combustion of rice husk, a stoichimetric amount of air is fed as primary air while some excess air is fed as secondary air into the freeboard region for the resulting char skeletons to burn to completion. The amount of excess air required is based on the guideline value of achieving a final flue gas composition of higher than 6% oxygen level (Environment Agency, 1996), usually around 8% taking into account the operational safety margin.

4.3 Determination and Optimisation of Design Parameters

4.3.1 Sand Size

Commercial silica sand granules are to be used as the bed media in the proposed SFB combustor. The size of sand needs to be selected for the purpose of design calculations. Larger particles (Geldart Type D) are undesirable in fluidisation studies as they produce large exploding bubbles and severe channelling. Mixing is also limited and this leads to poor combustion of waste. The use of Geldart-B particles is favourable due to its good fluidising behaviour characterised by vigorous bubbling action and bubble enlargement upon reaching the bed surface. Fluidisation of particles in a SFB can be achieved at any fluidising air flow rate by changing the rotating speed of the bed. However, the amount of airflow is limited by the stoichiometric requirements of combustion. Certain conditions may arise whereby the optimum air supply for combustion might not be enough to completely fluidise the bed. Therefore, in order to achieve bed fluidisation at a lower fluidising air flow rate, it is desirable to choose particles of smaller size. On the other hand, the minimum size of bed particles is also limited by the diameter of the distributor holes. Particles that are too small might be centrifuged out of the bed when operating at low fluidising air flow rates. It has been shown by Rozainee (1998) that sand particles as small as 0.5 mm could be used with distributor plate having hole

diameter of 1 mm. Silica sand with a size range of 600 – 850 μm available commercially is suitable for use as the bed media. Screen analysis to determine the particle size distribution of this sand size showed that it consists mostly of particles in the range of 0.5 – 1.00 mm, denoting a mixture of Geldart-B and Geldart-D particles. The arithmetic mean diameter for this range of sand size, which at 0.73 mm, is more representative than the volume surface mean diameter of 0.67 mm. Therefore, this value will be used in the design calculations.

Hence: The chosen sand size is 600 – 850 μm having an arithmetic mean diameter of 0.73 mm.

4.3.2 Operating Temperature Range

Industrial processes for biomass processing are usually designed for temperatures above 600^{o}C (Mansaray and Ghaly, 1998). At higher temperatures, the char could be converted through heterogeneous reactions at appreciable conversion rates to gaseous components (water, carbon dioxide and oxygen). In addition, the oxidation of volatile pyrolysis products in the presence of air at higher temperatures results in flaming combustion. Oxidation of char, therefore, is further enhanced. Moreover, the temperature of a fluidised bed is usually maintained at approximately 850^{o}C in order to sustain the combustion process. On the other hand, in-depth understanding of the hydrodynamic features of a combustor system needs to be carried out at ambient temperature (30^{o}C) before moving on to the more complex combustion studies. Experimental works carried out at ambient is important in determining good mixing behaviour to be used during combustion studies. Therefore, calculations for the design of the horizontal SFB need to be conducted for the both extremes of the temperature range. Cold commissioning of the combustor will be carried out 30^{o}C so this temperature represented the lower extreme. Meanwhile, hot commissioning is targeted at 800^{o}C, and this temperature represented the upper extreme. Due to volume expansion of gas with increasing temperature, these measures were necessary to ensure that the fluidising air to be

supplied to the combustor during cold and hot runs at designated fluidising velocities is within the capacity of the selected blower unit.

4.3.3 Limitations in the Design of the SFB Combustor

Optimising the dimensions and operating parameters for the design of the horizontal SFB combustor was made difficult by the complex manner in which all parameters were interrelated. However, several limitations need to be imposed during the optimisation process in order to address the drawbacks associated with a vertical SFB and to achieve good fluidisation behaviour in the proposed SFB combustor. These limitations also aids in narrowing down the range of values at which each parameter need to be investigated and were discussed in the following sections.

4.3.3.1 Size of the SFB Combustor

One of the original intentions of the research was to come up with a highly compact system with good mobility to cater for small-scale onsite waste incineration. The combustor should be huge enough to be able to maintain the thermal stability of the system and render waste feeding justifiable, yet small enough to occupy a lorry or truck for easy deployment from site to site. Thus, the combustor is expected to occupy a floor area of approximately 4 m^2 (2 m $\times$ 2 m). The length of combustor, therefore, should be in the vicinity of 1 m considering the need for installation of auxiliary equipment such as the feeding and ash collection systems.

The cylindrical combustor is to be partitioned into the primary and secondary chambers. The volume of the primary chamber, after accounting for the volume lost due to tapering and less that occupied by the bed media, should be sufficient to

allow for continuous feeding of waste materials while maintaining sufficient residence time for de-volatilisation process to occur. In addition, there should be some free space at the central core of the cylinder as freeboard region for the evolved gases to proceed to the secondary chamber to complete the combustion process. The diameter of the combustor, therefore, should be as big as possible but is limited by the combustor length. In most rotating combustion systems, in particular rotary kilns, the length to diameter (L/D) ratio usually ranges from 2.5:1 to 4:1 (Niessen, 1995). Having a ratio of L/D less than unity might affect the structural stability of the combustor. The minimum limit of L/D ratio is unity, and thus, the diameter of the combustor should not exceed its length.

The secondary chamber, on the other hand, is a thoroughly hollow chamber and is where most of the unburnt volatiles released earlier burn to completion. It should have a larger volume compared to the primary chamber. A minimum residence time of flue gas of two seconds will be used as a guideline value for design purposes.

Hence: The length of the whole SFB combustor should be designated at approximately 1 m. The combustor diameter should not exceed its length and the secondary chamber should have a larger volume than the primary chamber.

4.3.3.2 Tapering Angle (θ)

The entire circumference of both ends of the primary chamber wall was tapered with the main target of equalising the rate of fluidisation. Tapering angles in this combustor was based on the conical section design of a spouted bed. Too small a cone angle will lead to the formation of dead zones as shown in shallow spouted bed studies (José et al., 1996). Since the symmetrical sections of the tapered primary chamber resembled a shallow spouted bed, optimising the angle to ascertain the maximum threshold value that avoids the creation of dead zones in the primary chamber is not unjustifiable. Spouting stability in a spouted bed depends largely on

particle size and size distribution, gas flow rate, bed height, cone angle, gas inlet diameter (D_i) and column diameter (D_c) (Mathur and Gishler, 1955), in which the latter three are of interest in the present SFB design. Therefore, it is predicted that fluidisation in the primary chamber may exhibit some spout-like behaviour due to the inclusion of the tapered sections. The width of opening at the combustor wall to the free untapered section should be in certain ratios, consistent with those present in a spouted bed.

It is worthy to note that the limit of cone angle for most materials in a spouted bed is in the region of 70^o (Hunt and Brennan, 1965 and Elperin et al., 1967). It was further reported by José et al. (1996) that for cone angle, γ in the range of 60^o to 150^o, the limits of stability in the bed could be maintained as long as $D_i/D_c < 0.4$ and $2 < D_i/d_p < 60$. Superimposing these parameters to the case of the SFB combustor, D_i is the length of the distributor inlet while D_c is the length of the primary chamber at the interface of the bed surface. Meanwhile, the angle of tapering as measured from the horizontal axis should range from 15^o to 60^o. Instability in the bed is characterised by the formation of large bubbles for small particles and the elevation of the whole bed without the spout opening for large particles. On the other hand, the tapering angle is limited by the available tapering height (X) as measured from the wall of the combustor to the edge of either the feed inlet ($X_{in,max}$) or the exhaust outlet ($X_{out,max}$) (Figure 4.1) while ensuring sufficient opening at the distributor plate for the fluidising gas to enter. Since the conical section in a spouted bed is symmetrical in design, the width of both the feed inlet and exhaust outlet of the SFB should therefore be equal in order for the tapering height, X to be maximised.

Hence: The range of tapering angle, θ to be investigated was limited to 15^o – 60^o while ensuring that $D_i/D_c < 0.4$ and $2 < D_i/d_p < 60$, where D_i is the length of the distributor inlet and D_c is the length of the primary chamber at the interface of the bed surface. The angle of tapering, θ is maximum when the whole length of the available height of tapering, X is utilised while simultaneously maintaining a sufficient distributor width as fluidising air inlet. For symmetry in tapering, the width of both the feed inlet and exhaust outlet should be similar.

4.3.3.3 Bed Depth (H)

The ratio of U_{mfc}/U_{mfs} is higher for thicker beds. Although shallower beds give more uniform fluidisation in the radial direction, a sufficient bed thickness should be used in order for combustion process to occur in the bed. This is crucial as the heat evolved from combustion process in the bed is required for maintaining its thermal stability. The bed should not be too deep so as to allow for bed expansion during fluidisation. Moreover, too deep a bed will reduce the free volume available to accommodate the feed materials, evolved volatiles as well as the resulting chars and ash. Rice husk contains approximately 15% of ash, which might lead to severe ash accumulation the bed. A bed thickness ranging of one-tenth (1/10) to two-third (2/3) of the combustor radius should be sufficient to satisfy these criteria.

Hence: The bed thickness to be investigated ranged from one-tenth (1/10) to two-third (2/3) of the combustor radius.

4.3.3.4 Air Feed Rate

To ensure stable fluidisation, fluidising velocities should be at least 3 U_{mfs} at the bed surface, and 2 U_{mfc} near the combustor wall (Rozainee, 1998). Thus, the surface fluidising velocities investigated during the design of the SFB combustor were set at 3 – 3.5 U_{mfs} while the corresponding U_{mfc} observed so much so that F_R is maintained at near unity for all rotating speeds.

Hence: The fluidising air should be at least 2 U_{mfc} at the combustor wall and 3 U_{mfs} at the bed surface.

4.3.3.5 Rotating Speed

Contrary to conventional fluidised bed, the operation of the SFB is no longer limited by the amount of air throughput. Fluidisation can be achieved at higher gas flow rates by increasing the *g*-level in the bed through increase in bed rotating speeds. The amount of fluidising air to be used depends on the amount of waste feed, and a point is reached whereby the kinetics in waste combustion limits the amount of feed that the combustor could accommodate. This has direct relation with the free volume of the primary chamber. Increasing the feed beyond this limit results in incomplete combustion and accumulation of unburnt materials in the bed. These conditions are detrimental to the operation of combustor in that the temperature of the bed might drop too low to the point of quenching the combustion process. Therefore, for a certain size of free volume in the primary chamber, there exists a maximum value of waste feed in order for the waste to burn to completion. Taking into the account that the fluidising velocities should be maintained in the excess of 2 U_{mfc} to establish sufficient turbulence inside the bed crucial in attaining good mixing behaviour, there is also a limit of to the amount of fluidising air. This in turn sets the maximum speed at which the bed could be rotated. The maximum rotating speed can be determined by first investigating the maximum amount of waste that could be accommodated by the free volume of a certain size of primary chamber. This allows for the subsequent determination of the maximum flow rate of fluidising air at stoichiometric conditions, and finally the maximum rotating speed could be back-tracked while maintaining fluidisation at approximately 2 U_{mfc}.

Hence: The kinetics of combustion limits the amount of waste feed to a certain size of the SFB primary chamber. This sets a limit to the amount of fluidising air input, which in turn limit the rotating speed of the bed.

4.3.3.6 Rice Husk Feed

Results from proximate and ultimate analyses of rice husk samples were used to carry out mass balance calculations in order to determine the rate of rice husk

feeding. Materials with high volatile matters such as rice husk favour air feed at stoichiometric or substoichiometric condition since combustion of such materials are dominated by the drying and de-volatilisation processes. These processes are heat-transfer controlled and therefore feeding of more air will only lead to the undesirable condition of lower rate of heat transfer. Materials with high content of char, on the other hand, favour higher feeding rate of air as the mass transfer phenomenon predominates. Air should be supplied to the burning materials in sufficient rate in order for combustion to be sustained while maintaining the minimum requirements of fluidisation (2 U_{mfc} at wall, 3 U_{mfs} at bed surface). The phenomenon of volume expansion of gas with temperature should be taken into account. As the fluidising air at ambient (30^{o}C) enters the hot combustor, the gas expands accordingly with the temperature of the bed. The amount of rice husk feed, therefore, should be determined in such a manner that the fluidising air is sufficient to allow for its stoichiometric combustion and for maintaining the minimum fluidisation requirements at a temperature of 800^{o}C, the highest limit of temperature intended for operation of the SFB combustor.

Hence: By maintaining the SFB at 800^{o}C, the air input for maintaining the minimum requirements for good fluidisation behaviour (2 U_{mfc} and 3 U_{mfs}) is determined and this value of air input is in turn used to calculate the amount of rice husk feed for its stoichiometric combustion.

4.3.4 Combustor Dimensions for Uniform Fluidisation

4.3.4.1 Determination of Combustor Size and Optimum Bed Depth (H)

Observing the limitations that the whole length, L of the SFB combustor should be approximately 1 m with a minimum L/D ratio of 1, the cylinder of the SFB combustor was first designated at a length of 800 mm with an ID of 800 mm. The whole combustor was partitioned equally to form a primary chamber and a secondary chamber. Fluidisation occurs in the primary chamber and thus, investigations on the ways to achieve good fluidisation behaviour was focused in the

primary chamber. These comprise the determination of the optimum angle of tapering (θ), tapering height (X) and bed depth (H). Design of the secondary chamber will be dwelled in later sections. In addition, to study the maximum bed depth attainable while achieving good fluidisation behaviour in the bed (2 U_{mfc} at the wall, 3 U_{mfs} at the bed surface), both the tapering angle, θ and tapering height, X were maximised in this stage. Optimisation of the tapering height and tapering angle will be investigated in Section 5.3.4.2 and Section 5.3.4.5, respectively. For the current combustor size having a feed inlet with an ID of 200 mm, X is 300 mm and θ is 60^o. Further, the relevant design calculations were conducted at ambient conditions (30^oC). Design calculations at combustion temperature of 800^oC will also be investigated further in later sections. The proposed dimensions of the SFB were depicted in Figure 4.2.

The bed depths were varied from 50 mm (approximately one-tenth of the combustor radius) to 300 mm and the rotating speeds ranging from 5- to 25-g loadings (which gave RPMs of 106 – 236). The important parameters to be observed due to the variations in bed depths were F_R, fluidising air feed requirements and the ratio of L_o/L_i, where L_o is the length of the air distributor inlet and L_i is the length of the combustor at the bed surface. The ratio of L_o/L_i is consistent with the ratio of D_i/D_c in a spouted bed and is important in the SFB design as it reflects the stability of the bed fluidisation to a certain extent. This is because the tapered section geometry resembled that of the conical section of a spouted bed.

The fluidising conditions and air feed requirements at ambient for different bed depths and rotating speeds in the primary chamber (length 400 mm, ID 800 mm) were as shown in Table 4.1. For comparison purposes, the ratio of U_{mfc}/U_{mfs}, which gave indication on F_R in an untapered SFB, was also included. For a shallow bed (50 mm), the ratio of U_{mfc}/U_{mfs} approached unity (ranging from 1.24 – 1.26) for all rotating speeds. For deeper beds, this ratio got larger and larger, indicating highly non-uniform radial bed fluidisation. For example, the ratio of U_{mfc}/U_{mfs} is approximately 3 for a bed depth of 200 mm at all rotating speeds ranging from 5- to 25-g loadings. F_R, in this case, is therefore approximately 0.30. This means that

when the sand near the wall reached sufficient turbulence conditions of 2 U_{mfc}, the fluidising velocity at the bed surface had reached 6 U_{mfs}, leading to high potential of particle elutriation from the bed surface. Tapering the walls at 60^o, on the other hand, significantly increased F_R so that their values approach unity. Judging the significance of maintaining the fluidising velocities at 2 U_{mfc} near the wall and 3 U_{mfs} at the bed surface, the minimum acceptable value of F_R is 2/3 or 0.67. It was obvious from Table 4.1 that increasing the bed depth beyond 200 mm resulted in the values of F_R dropping too low to less than the minimum limit of 0.67.

The air feed requirements to maintain 3 U_{mfs} at the bed surface were observed to be lowered as the bed depths were increased. Tapering the end walls of the primary chamber resulted in the increase in cross sectional area as the air moved radially inward. Consequently, the air velocity is lowered in the radial direction inwards so much so that sufficient fluidising velocity (2 U_{mfc}) is reached at the SFB wall while simultaneously keeping the surface fluidising velocity in the vicinity of 3 U_{mfs}. Since the centrifugal force increases with radius, the deeper the bed (which means smaller bed radius), the lower the value of U_{mfs}. At a rotational speed of 5-g loading, for instance, U_{mfs} is 0.24 m/s for a bed depth of 200 mm, decreasing to 0.14 m/s when the bed depth is increased to 250 mm. Therefore, to maintain a condition of 3 U_{mfs} at the bed surface required less air input for a deeper bed. At 5-g loadings, an air input of 494.5 m^3/hr was required for a 250 mm bed (to maintain 3 U_{mfs} at the bed surface) compared to 925.5 m^3/hr for a 200 mm bed. Thus, deeper beds were favourable. Reaching a compromise in terms of fluidising air inputs and fluidising condition (F_R), a bed depth of 200 mm was chosen. Beds deeper than 200 mm, such as 250 mm and 300 mm had too low a value of F_R in the sense that when the fluidising velocity reached 3 U_{mfs} at the bed surface, the values of U_{mfc} were only 1.2 – 1.5 U_{mfc} and approximately 0.5 U_{mfc} respectively, at all the rotating speeds investigated. These low values of U_{mfc} were evidently were not high enough to achieve sufficient turbulence in the bed. The ratio of L_o/L_i, which gave indication of the bed stability, was also within the desired limit of less than 0.4 (at 0.19) for the chosen bed depth of 200 mm.

Hence: The chosen bed depth for the SFB combustor (length 800 mm, ID 800 mm) having a primary chamber of length 400 mm is 200 mm.

Table 4.1: Fluidisation conditions and air feed requirements at ambient (30°C) for different bed depths and rotating speeds in the primary chamber (length 400 mm, ID 800 mm, tapered height 300 mm, tapered angle 60°)

g-loading	L_o (m)	L_i (m)	U_{mfc}/U_{mfs}	F_R (untapered)	F_R (tapered)	Air flow rate, Q @ 3 U_{mfs}, 30°C (m^3/hr)	L_o/L_i
Bed height = 50 mm							
5	0.0534	0.1112	1.26	0.79	1.44	1,715.18	0.48
10			1.25	0.80	1.45	2,830.74	
15			1.25	0.80	1.46	3,724.51	
20			1.24	0.80	1.46	4,492.10	
25			1.24	0.81	1.47	5,175.44	
Bed height = 100 mm							
5	0.0534	0.1690	1.66	0.60	1.43	1,702.62	0.32
10			1.63	0.61	1.46	2,837.22	
15			1.61	0.62	1.47	3,751.53	
20			1.60	0.62	1.48	4,538.88	
25			1.60	0.63	1.48	5,240.91	
Bed height = 200 mm							
5	0.0534	0.2845	3.42	0.29	0.78	925.50	0.19
10			3.27	0.31	0.81	1,583.38	
15			3.20	0.31	0.83	2,123.18	
20			3.15	0.32	0.84	2,592.11	
25			3.12	0.32	0.85	3,012.38	
Bed height = 250 mm							
5	0.0534	0.3422	5.78	0.17	0.42	494.47	0.16
10			5.43	0.18	0.44	862.22	
15			5.25	0.19	0.46	1,168.58	
20			5.13	0.19	0.47	1,436.78	
25			5.05	0.20	0.48	1,678.30	
Bed height = 300 mm							
5	0.0534	0.4000	12.25	0.08	0.15	181.74	0.13
10			11.20	0.09	0.17	325.33	
15			10.66	0.09	0.18	447.89	
20			10.32	0.10	0.18	556.59	
25			10.08	0.10	0.19	655.30	

4.3.4.2 Determination of Optimum Tapering Height (X)

Having determined the optimum bed depth at 200 mm, the effect of varying the tapering height, X on the fluidising conditions and air feed requirements in the SFB (length 800 mm, ID 800 mm, primary chamber length 400 mm) was further investigated. Realising that X is maximum at 300 mm, the tapering height was varied from 100 mm to 300 mm while maintaining the tapering angle at 60^{o}. Similar to earlier procedures in determining the optimum bed depth, calculations were performed at an ambient temperature of 30^{o}C and at rotating speeds ranging from 5- to 25-g loadings. The results were tabulated in Table 4.2.

Table 4.2: Fluidisation conditions and air feed requirements at ambient (30^{o}C) for different bed depths and rotating speeds in the SFB primary chamber (length 400 mm, ID 800 mm, tapered angle 60^{o}, bed depth 200 mm)

g-loading	L_o (m)	L_i (m)	U_{mfc}/U_{mfs}	F_R (untapered)	F_R (tapered)	Air flow rate, Q @ 3 U_{mfs}, 30^{o}C (m^3/hr)	L_o/L_i
Tapering height = 100 mm							
5	0.2845	0.5155	3.42	0.29	0.26	1,715.18	0.55
10			3.27	0.31	0.28	2,830.74	
15			3.20	0.31	0.28	3,724.51	
20			3.15	0.32	0.29	4,492.10	
25			3.12	0.32	0.29	5,175.44	
Tapering height = 200 mm							
5	0.1690	0.4000	3.42	0.29	0.35	1,702.62	0.42
10			3.27	0.31	0.36	2,837.22	
15			3.20	0.31	0.37	3,751.53	
20			3.15	0.32	0.38	4,538.88	
25			3.12	0.32	0.38	5,240.91	
Tapering height = 300 mm							
5	0.0534	0.2845	3.42	0.29	0.78	925.50	0.19
10			3.27	0.31	0.81	1,583.38	
15			3.20	0.31	0.83	2,123.18	
20			3.15	0.32	0.84	2,592.11	
25			3.12	0.32	0.85	3,012.38	

From Table 4.2, it could be observed that, for a tapering height of 100 mm, F_R was way too low (in the vicinity of 0.30) in order to achieve good fluidisation in the bed. For the bed depth of 200 mm, when the surface of the bed was fluidising at 3 U_{mfs}, the bed particles near the wall were barely fluidised (at less than 1 U_{mfc}) at all rotating speeds. Increasing the tapering height to 200 mm resulted in the slight increase in this ratio for the same bed depth. However, this increase was still not sufficient, as can be demonstrated by taking the example of a bed rotating at 5-g loading, whereby a condition of 3 U_{mfs} at the bed surface resulted in the bed near the wall fluidising at only 1 U_{mfc}, which was clearly not sufficient for good mixing behaviour in the bed. Increasing the tapering height to 300 mm, which is also the maximum tapering height allowable by the combustor geometry, on the other hand, gave the desired value of F_R of more than the minimum limit of 0.67. Operating the SFB again at the same bed depth and rotating speed as the previous case with X at 300 mm resulted in a wall fluidising velocity of 2.34 U_{mfc} when the surface fluidising velocity was designated at 3 U_{mfs}. Changes in rotating speeds only resulted in slight difference in F_R. This value of wall fluidising velocity in the excess of 2 U_{mfc} attainable in the 200 mm bed due to a tapering height of 300 mm clearly showed good mixing in the bed could be achieved while maintaining a fairly uniform radial bed fluidisation. Another advantage of maximising the tapering height was the reduction in the air feed requirements. This was because as the tapering height was increased (while keeping the angle at 60^o), the length for radial airflow at the bed surface (L_i) was decreased accordingly. For example, with a tapering height of 200 mm, L_i is 400 mm but decreases to 284.5 mm when the tapering height is increased to 300 mm. This in turn resulted in a smaller surface area for airflow at the bed interface. Therefore, lesser amount of air was required to fluidise these particles to the same fluidising conditions (for example 3 U_{mfs}). For instance, 1702.1 m^3/hr of air was required to fluidise the bed to 3 U_{mfs} (bed depth 200 mm) at 5-g loading with a tapering height of 200 mm. The amount of fluidising air required to achieve the same fluidising condition at the same operating speed was reduced by 45.6% to 925.5 m^3/hr when the tapering height was increased to 300 mm. It should also be noted that the higher amount of air in the former case only fluidise the bed near the distributor wall to approximately 1 U_{mfc}, while the latter to a fluidising velocity in the excess of 2 U_{mfc}.

Hence: The chosen tapering height, X for the SFB combustor (length 800 mm, ID 800 mm) having a primary chamber of length 400 mm is 300 mm.

4.3.4.3 Rotating Speed, Fluidising Air Feed Rate and Rice Husk Feed Rate

Determination of the range of feasible operating conditions for the proposed design of the SFB such as rotating speed, fluidising air feed rate and rice husk feed rate had to be investigated collectively since all three parameters have significant influence on each other. To determine the maximum rotating speed at which the combustor can be operated at required the knowledge of the chemical kinetics of rice husk combustion, that is, the minimum time for the combustion process to reach completion. This is because the fluidising air input into a SFB can be manipulated through adjustment in the rotating speed while being able to maintain the desired fluidising conditions. The fluidising conditions being held constant, the higher the rotating speed, the higher the air input required. Preliminary investigations into the combustion of rice husk conducted in a laboratory scale conventional fluidised bed maintained at a temperature of approximately 600^{o}C and operating at 2.5 – 3 U_{mf} showed rice husk were burnt to completion in a rapid manner, taking less than 1 minute in order for the ash to be observed. Increasing the combustor temperature to 750^{o}C further reduced the burnout time to less than 0.5 minute. Mathematical modelling using the FLUENT program code (Section 6.6.4.3) for the combustion of rice husk particles in a SFB showed that when rotating at 5-g loading, complete combustion of the particles could be achieved at approximately 1.3 minutes at 600^{o}C and less than 0.5 minute at 700^{o}C. Therefore, taking into account the margin of safety due to fluctuations in bed temperature, the residence time of rice husk in the primary chamber of the proposed SFB should not be less than 1.5 minutes. Imposing this restriction set the maximum value of rice husk feed that the SFB combustor could accommodate, which in turn set a limit to the maximum amount of fluidising air that can be fed as combustion air. Subsequently, the combustor can only be rotated up to a certain level of g-loading since the maximum air input have to balance not only the conditions of being in stoichiometric amount for the

combustion of the maximum rice husk feed rate but also satisfying the conditions of good mixing behaviour in the bed (2 U_{mfc} near wall, 3 U_{mfs} at bed surface).

From earlier findings, the initial SFB design (total length 800 mm, ID 800 mm, primary chamber length 400 mm, feed inlet ID 100 mm, tapering height 300 mm, tapering angle 60^{o}) should be operated at a bed depth of 200 mm in order to achieve uniform radial bed fluidisation. However, the previous investigations were limited to operation at ambient conditions (30^{o}C). Therefore, in this section, calculations were performed for operations of the combustor for both cold commissioning (at 30^{o}C) and hot commissioning (at 800^{o}C). Calculations for hot commissioning enabled the determination of the rate of rice husk feed and also the estimated residence time of rice husk in the combustor at each rotating speed as well as the amount of air to be fed at ambient. Calculation results for cold commissioning and hot commissioning were shown in Table 4.3 and Table 4.4 respectively.

From Table 4.3, it was found that for rotating speeds up to 15-g loading at ambient operation, air feed rates as high as 2000 m^3/hr need to be supplied to the primary chamber at very high pressure drops (as high as 3.3 m H_2O) in order to maintain a minimum turbulence conditions of 3 U_{mfs} at the bed surface and at least 2 U_{mfc} near the combustor wall. Such high air inputs coupled with high pressure drops could only be supplied by blowers that could overcome huge drops in pressure. Capital investments for such blowers are huge, and the higher the capacity, the higher its cost. Apart from that, the produce a huge discharge volume (approximately 35 m^3/min) with a pressure drop up to 4 m H_2O, blowers such as those available commercially need to be operated up to a rotating speed of 2000 RPM. Operating the blower unit at very high RPMs incurred higher operating costs as well as resulting in the rapid wear and tear of the fan blades. Therefore, in order to reduce the capacity of the blower unit required, the current dimension of the combustor need to be scaled down.

When operating at 800^{o}C and 3.5 U_{mfs}, the fluidisation behaviour (F_R) remained more or less the same in the current design of the SFB as when it was operated at 30^{o}C. Values of these ratio remained above the minimum limit of 0.67

(Table 4.3 and Table 4.4) for all rotating speeds. Due to the nature of volume expansion of gas with temperature, the fluidising air input to the bed operating at 800^{o}C was reduced by a factor of 3.54 (= 1073K / 303K) when the air is fed at ambient (30^{o}C). Thus, the air feed requirements for rotating speeds up to 25-g loading was only 750 m^3/hr (at 30^{o}C). The corresponding rice husk feed rates for stoichiometric combustion ranged from 48.0 to 224.5 kg/hr (Table 4.4) for rotating speeds ranging from 5- to 25-g loadings. The volume of the primary chamber is 0.103 m^3 and after taking into account the volume occupied by the sand bed of depth 200 mm, the free volume (please refer to Appendix A for calculation steps) available for waste is 0.044 m^3. The residence time of rice husk in the primary chamber could be estimated through the following formula:-

$$\text{Estimated } \tau = \frac{\text{Combustor volume}}{\text{Feed rate}} \times \rho_b \qquad (4.1)$$

where in this case, the combustor volume referred to the free volume in the primary chamber, feed rate is the rate of rice husk feeding to maintain fluidising velocity of 3.5 U_{mfs} at the bed surface at 800^{o}C and ρ_b is the bulk density of rice husk. It was found from Table 4.4 that the estimated residence times of rice husk in the primary chamber were all in the excess of 1 minute and therefore should be sufficient in order for the waste to burn to completion. Operating at lower rotating speed (such as 5-g loading giving a RPM of 106) required lesser amount of rice husk feed, leading to higher residence time of solid (5.9 minutes).

The air feed requirements were within operational boundaries (less than 1000 m^3/hr even a rotating speed as high as 25-g loading) for the current design of the SFB operating at 800^{o}C. Burning time, in the excess of 1.5 minutes, was also sufficient when operating up to 20-g loadings. However, as discussed earlier, the air feed requirements when operating the bed at ambient even up to 15-g loading was way too high. The high capacity and pressure drop requirement for the air blower unit rendered this geometry infeasible in terms of blower capital and operating costs. Therefore, the combustor was then scaled down to an inner diameter of 600 mm. The total length was still maintained, but the primary chamber length was scaled down proportionately with the combustor inner diameter to 300 mm. Similarly, the

bed depth was proportionately scaled down to 150 mm. The optimum bed depth for this combustor size will be determined in Section 5.3.4.4. The feed inlet diameter was also scaled down proportionately to 150 mm, resulting in a maximum tapering height of 225 mm. The difference in dimensions between the initial SFB combustor and its scaled down version was shown in Table 4.5 while the schematic diagram of the scaled down SFB was shown in Figure 4.3.

The angular velocity (ω) varies with the bed radius (r) according to the relationship $\omega \propto (r)^{-0.5}$. Since the ratio of ($r_o/r_i$) for both the initial combustor and scaled down combustor remained unchanged due to the proportional scaling and also the fact that ω for a certain g-loading for both combustors follows the relationship as mentioned above, the value of U_{mfs} for both combustors remained unchanged as well. On the other hand, the surface area at the bed surface was reduced as much as 44% (from 0.134 m^2 to 0.076 m^2) due to the scaling down. Therefore, the air feed rate was reduced significantly, whereby at 15-g loading and 3 U_{mfs}, the air feed requirement was just 1194.3 m^3/hr at ambient (Table 4.6). The significant reduction in air feed requirements, coupled with lower pressure drops, made the choice of the scaled down combustor geometry feasible. A blower with a smaller capacity is thus required, and this translates to significant reduction in terms of capital and operating costs. Also, due to limitations in terms of capital investment, a blower unit having a capacity of up to 1200 m^3/hr while being able to overcome a pressure drop of up to 4 m H_2O, which cost approximately RM 50,000, was chosen. During cold commissioning at 30^oC, the scaled down SFB combustor could be operated up to a rotating speed of 15-g loading using air supplied from this blower. Hot commissioning, on the other hand, could be carried out at higher rotating speeds due to the nature of gas volume expansion with increasing temperature ($V \propto T$). Nevertheless, chemical kinetics in rice husk combustion determined the maximum allowable feed rate of rice husk to the combustor. Subsequently, there existed a limit to the rate of air inputs to maintain certain fluidisation behaviour in the bed. This in turn set the highest limit of rotating speeds allowable that ensured complete combustion of all the rice husk feed. From Table 4.7 and realising that the cut-off residence time (for the rice husk to stay in the primary chamber) of 1.5 minutes is required, it was found that rotating the SFB up to 15-g loadings. Estimated

residence time of rice husk in the primary chamber when operating at 15-g loading is 1.52 minutes. As a margin of safety, the bed should be operated only up to 15-g loadings.

As a result of tapering at 60^{o}, the length of the primary chamber wall meant as airflow inlet was reduced to 40.1 mm. Consequently, the entering air velocity is reduced as the air moves radially inward. This condition was best illustrated in Figure 4.4 whereby the velocity profile of airflow entering at 1 U_{mfc} and $30^{o}C$ (ambient) and at different g-loadings was evaluated. All five curves were fairly flat in the region with the radius ranging from 0.125 m to 0.225 m. However, the velocity gradients beyond 0.25 m till the end wall of the primary chamber were very steep. This phenomenon is due to the length of the airflow interface being reduced progressively as the radius is increasing as a result of the inclusion of the tapered ends. Hence, the curve for the area of the airflow interface versus the chamber radius exhibited a maximum parabolic curve as in Figure 4.5, as the decreasing values of interface length and increasing values of radius balance each other. Nevertheless, the overall distinctive effect is that the cross sectional area is increased (to a certain extent, where it began decreasing slightly) as the air flows radially inward. This desirable condition leads to uniform radial fluidisation in the rotating fluidised bed. In addition, the higher the rotating speed, the greater the decrease in air flow as demonstrated by the steeper velocity gradients with increasing g-loadings in Figure 4.4. The fluidising number at the bed surface (no. of U_{mfs}) at this entering air flow rate were approximately 1.2 for all rotating speeds, another means of proving that the inclusion of the tapered ends equalised the fluidisation at the wall and at the bed surface.

Hence: The ID of the SFB combustor was scaled down from 800 mm to 600 mm while the length of the primary chamber was proportionately scaled to 300 mm. The entire length of the combustor remained at 800 mm. The feasible rotating speeds for combustion of rice husk in the SFB at $800^{o}C$ was up to 15-g loading.

Table 4.3: Fluidisation conditions and air feed requirements at different rotating speeds for a SFB operated at 30°C (primary chamber length 400 mm, ID 800 mm, tapered angle 60°, bed depth 200 mm)

g-loading	Rotational speed (RPM)	U_{mfs} (m/s)	U_{mfc} (m/s)	F_R (untapered)	Operating U_{mfs}	No. of U_{mfc} near wall at operating U_{mfs}	F_R (tapered)	Air flow rate, Q @ operating U_{mfs}, 30°C (m^3/hr)	ΔP_{max} (m H_2O)
5	105.70	0.24	0.82	0.29	3.00	2.33	0.78	925.50	1.09
10	149.49	0.41	1.34	0.31		2.44	0.81	1,583.38	2.19
15	183.08	0.55	1.76	0.31		2.50	0.83	2,123.18	3.28
20	211.41	0.67	2.12	0.32		2.53	0.84	2,592.11	4.37
25	236.36	0.78	2.43	0.32		2.56	0.85	3,012.38	5.47

Table 4.4: Fluidisation conditions, air feed requirements and stoichiometric rice husk feed rates at different rotating speeds for a SFB operated at 800°C (primary chamber length 400 mm, ID 800 mm, tapered angle 60°, bed depth 200 mm)

g-loading	U_{mfs} (m/s)	U_{mfc} (m/s)	F_R (untapered)	Operating U_{mfs}	No. of U_{mfc} near wall at operating U_{mfs}	F_R (tapered)	Air flow rate, Q @ operating U_{mfs}, 800°C (m^3/hr)	Air flow rate, Q @ operating U_{mfs}, 30°C (m^3/hr)	Rice husk feed rate @ 3.5 U_{mfs}, 800°C (kg/hr)	Burnout time of rice husk (min)
5	0.13	0.50	0.25	3.50	2.37	0.68	568.91	160.65	47.97	5.86
10	0.25	0.96	0.26		2.41	0.69	1,117.73	315.63	94.24	2.98
15	0.37	1.40	0.26		2.44	0.70	1,648.45	465.50	138.99	2.02
20	0.48	1.81	0.26		2.47	0.71	2,162.75	610.73	182.36	1.54
25	0.59	2.21	0.27		2.49	0.71	2,662.06	751.73	224.46	1.25

Table 4.5: Dimensions and operating conditions of the initial SFB combustor and the scaled down SFB combustor

Dimension / Operating Condition	Initial SFB	Scaled down SFB
Total combustor length, L (mm)	800	800
Inner diameter, ID (mm)	800	600
Primary chamber length (mm)	400	300
Secondary chamber length (mm)	400	500
Feed inlet diameter (mm)	200	150
Exhaust outlet diameter (mm)	200	150
Tapering height, X (mm)	300	225
Tapering angle, θ (^{o})	60	60
Distributor inlet width, L_o (mm)	53.4	40.1
Bed depth, H (mm)	200	150

Table 4.6: Fluidisation conditions and air feed requirements at different rotating speeds for a SFB operated at 30°C (primary chamber length 300 mm, ID 600 mm, tapered angle 60°, bed depth 150 mm)

g-loading	Rotational speed (RPM)	U_{mfs} (m/s)	U_{mfc} (m/s)	F_R (untapered)	Operating U_{mfs}	No. of U_{mfc} near wall at operating U_{mfs}	F_R (tapered)	Air flow rate, Q @ operating U_{mfs}, 30°C (m^3/hr)	ΔP_{max} (m H_2O)
5	122.05	0.24	0.82	0.29	3.00	2.33	0.78	520.60	0.82
10	172.61	0.41	1.34	0.31		2.44	0.81	890.65	1.64
15	211.41	0.55	1.76	0.31		2.50	0.83	1,194.29	2.46
20	244.11	0.67	2.12	0.32		2.53	0.84	1,458.06	3.28
25	272.92	0.78	2.43	0.32		2.56	0.85	1,694.46	4.10

Table 4.7: Fluidisation conditions, air feed requirements and stoichiometric rice husk feed rates at different rotating speeds for a SFB operated at 800°C (primary chamber length 300 mm, ID 600 mm, tapered angle 60°, bed depth 150 mm)

g-loading	U_{mfs} (m/s)	U_{mfc} (m/s)	F_R (untapered)	Operating U_{mfs}	No. of U_{mfc} near wall at operating U_{mfs}	F_R (tapered)	Air flow rate, Q @ operating U_{mfs}, 800°C (m^3/hr)	Air flow rate, Q @ operating U_{mfs}, 30°C (m^3/hr)	Rice husk feed rate @ 3.5 U_{mfs}, 800°C (kg/hr)	Burnout time of rice husk (min)
5	0.13	0.50	0.25	3.50	2.37	0.68	320.01	90.37	26.98	4.40
10	0.25	0.96	0.26		2.41	0.69	628.73	177.54	53.01	2.24
15	0.37	1.40	0.26		2.44	0.70	927.25	261.84	78.18	1.52
20	0.48	1.81	0.26		2.47	0.71	1,216.55	343.54	102.58	1.16
25	0.59	2.21	0.27		2.49	0.71	1,497.41	422.85	126.26	0.94

4.3.4.4 Optimum Bed Depth for the Scaled Down SFB Combustor

With the SFB combustor scaled down to an ID of 600 mm and primary chamber length of 300 mm, the optimum bed depth of 200 mm determined for the initial combustor dimensions (ID 800 mm, primary chamber length 400 mm) was no longer valid. Determination of the optimum bed depth applicable for the scaled down SFB was thus carried out.

The bed depths in the primary chamber with an ID of 600 mm were varied from 50 mm to 200 mm. The effect of varying the bed depths on the fluidising conditions and air feed requirements were shown in Table 4.8. Similar to the initial SFB combustor, shallow bed (50 mm) in the scaled down SFB had a U_{mfc}/U_{mfs} ratio that approached unity (ranging from 1.34 – 1.38 for rotating speeds of 5- to 25-g loadings) even without the tapering effect. The value of F_R in this shallow bed, is approximately 0.74. The value of U_{mfc} is thus always lower than the value of U_{mfs} in an untapered SFB. Inclusion of the tapering end walls increased this ratio to approximately 1.50, indicating that the fluidising velocity near the wall (U_{mfc}) is higher than the fluidising velocity at the bed surface (U_{mfs}). However, beyond a bed depth of 150 mm, F_R decreased to a value of less than one in the tapered SFB.

The range of fluidising velocities for good mixing behaviour in a SFB is in the excess of 2 (either U_{mfc} or U_{mfs}). Using a shallow bed such as 50 mm, resulted in a fairly uniform fluidising velocity at the combustor wall (U_{mfc}) and at the bed surface (U_{mfs}). For instance, operating at a bed depth of 50 mm at 10-g loading in the scaled down tapered SFB gave a wall fluidising velocity of 4.5 U_{mfc} when the surface fluidising velocity is 3 U_{mfs}. Therefore, the required turbulence conditions for good mixing behaviour could be fulfilled using such a shallow bed. However, during combustion of solid particles such as rice husk, it is desirable for the waste to burn in the bed so that the heat released is stored in the bed. Since shallower beds have limited depths for these particles to penetrate and burn inside the bed, deeper beds are necessary. In addition, the higher turbulence conditions near the wall (with the wall fluidising velocity in the excess of 2 U_{mfc}) might make it difficult for these particles to penetrate deeper into the bed.

Increasing the bed depth to 100 mm resulted in a value of F_R of approximately 1.3 for all rotating speeds (ranging from 5- to 25-g loadings). This value is still within the acceptable limits to achieve good mixing behaviour in the bed. Operating at this bed depth at 10-g loading, for instance, resulted in a wall fluidising velocity 3.9 U_{mfc} when the surface fluidising velocity is 3 U_{mfs}. However, operating at this bed depth required high air inputs, up to 1900 m^3/hr (at 30°C) when rotating up to a speed of 15-g loading (211 RPM) in order to maintain the surface fluidising velocity at the minimum requirement of 3 U_{mfs}. It should be noted that, while keeping the fluidising velocity at the bed surface constant at 3 U_{mfs}, the deeper the bed, the less air input is required. This is due to the decrease in U_{mfs} when the bed depth increases, as had been discussed in Section 5.3.4.1. However, there is a limit to operating deeper beds without sacrificing in terms of uniformity in radial fluidisation while simultaneously gaining advantage of the lower air feed requirements. Increasing the bed depth to 200 mm (two-third of the radius of the scaled down SFB) resulted in the ratio of U_{mfc}/U_{mfs} dropping too low a point whereby variation in the fluidisation in the radial direction is very high. For example, at a bed depth of 200 mm, rotating the bed at 5-g loading gave a value of F_R of 0.31. Operating this bed at the minimum requirement of 2 U_{mfc} resulted in the fluidising velocity at the bed surface, U_{mfs} being too high (at 6.45 U_{mfs}), which poses a significant potential for severe particle elutriation. Therefore, reaching a balance between uniform fluidisation in the radial direction as well as lesser air feed requirements, the bed depth of 150 mm was chosen for the scaled down combustor. Moreover, the ratio of L_i/L_o and L_o/D_p (consistent with D_i/D_c and Di/D_p in a spouted bed) are 0.19 and 55 respectively, and are still within the stability limits of the bed provided the tapering effect resulted in the bed behaving like a spouted bed. Nevertheless, further experimental investigations need to be carried out in order to proved whether the bed in the SFB behaved as like a spouted bed.

Hence: Chosen bed depth for the scaled down SFB combustor (primary chamber length 300 mm, ID of 600 mm, tapered height 225 mm and tapered angle 60°) was 150 mm.

Table 4.8: Fluidisation conditions and air feed requirements at ambient (30°C) for different bed depths and rotating speeds in the SFB primary chamber (length 300 mm, ID 600 mm, tapered height 225 mm, tapered angle 60°)

g-loading	L_o (m)	L_i (m)	U_{mfc}/U_{mfs}	F_R (untapered)	F_R (tapered)	Air flow rate, Q @ 3 U_{mfs}, 30°C (m^3/hr)	L_o/L_i
Bed height = 50 mm							
5	0.0401	0.0978	1.38	0.73	1.48	989.41	0.41
10			1.36	0.73	1.50	1,637.87	
15			1.35	0.74	1.50	2,158.32	
20			1.35	0.74	1.51	2,605.67	
25			1.34	0.74	1.51	3,004.10	
Bed height = 100 mm							
5	0.0401	0.1556	2.04	0.49	1.27	848.17	0.26
10			1.99	0.50	1.30	1,424.04	
15			1.97	0.51	1.32	1,890.36	
20			1.95	0.51	1.33	2,292.84	
25			1.94	0.52	1.34	2,652.19	
4.3.4.4.1 Bed height = 150 mm							
5	0.0401	0.2134	3.42	0.29	0.78	520.60	0.19
10			3.27	0.31	0.81	890.65	
15			3.20	0.31	0.83	1,194.29	
20			3.15	0.32	0.84	1,458.06	
25			3.12	0.32	0.85	1,694.46	
Bed height = 200 mm							
5	0.0401	0.2711	7.18	0.14	0.31	210.25	0.15
10			6.69	0.15	0.34	369.47	
15			6.44	0.16	0.35	503.01	
20			6.28	0.16	0.36	620.33	
25			6.17	0.16	0.37	726.21	

4.3.4.5 Determination of the Optimum Angle of Tapering

From earlier discussions, it was noted that the tapering angle in the primary chamber of the SFB should range from a minimum of 15° to a maximum of 60°. Previous calculations to determine the optimum bed depth and tapering height, as well as the range of feasible air inputs and rotating speeds for the SFB design, were based on a SFB that was tapered at the maximum angle of 60°. Having proved that

the scaled down SFB dimensions gave feasible combinations of air inputs, rotating speeds and rice husk feed rates both during hot and cold commissioning, it will be used during the process of optimising the tapering angle. Also, it have been proven that using a bed depth of 150 mm (Section 5.4.4.4) was beneficial in attaining uniform radial bed fluidisation while keeping the air feed requirements within feasible range. Thus, optimisation of the tapering angle will be carried out by using a bed depth of 150 mm. It should further be noted that, for the maximum length of the SFB primary chamber of 300 mm, there is a minimum value at which the tapering angle should be designated. For example, using a maximum tapering height of 225 mm, the tapering angle should be more than 56.3^{o}. The minimum value of 56.3^{o} is based on using all of the available primary chamber length (at 150 mm since the tapered section should be symmetrical in geometry), leaving no space as air feed inlet. Therefore, taking into account that a sufficient length of the primary chamber is to be designated as the air inlet, the minimum tapering angle available for a tapering height of 225 mm should be more than 56.3^{o}. In addition, the process of optimising the tapering angle was focused on achieving a uniform radial bed fluidisation and a feasible range of air inputs at different rotating speeds with calculations carried out at ambient conditions (30^{o}C). Results on value of F_R at ambient temperature is sufficient to give insight on the uniformity in radial bed fluidisation at higher temperatures such as 800^{o}C since this ratio remained more or less the same at both temperatures. For example, for the scaled down SFB (primary chamber length 300 mm, ID 600 mm, tapering height 225 m and tapering angle 60^{o}) operating at 5-g loading and 30^{o}C with a bed depth of 150 mm resulted in a value of F_R of 0.78. Operating the same SFB at the same operating conditions but at a temperature of 800^{o}C gave a value of F_R of 0.68.

Choosing a tapering angle of 60^{o} when X is 225 mm gave an air inlet length of 40.1 mm (Case I). Results from the previous section showed that these combinations of tapering height and angle resulted in not only a fairly uniform radial bed fluidisation but also a combination of feasible range of air inputs, rotating speeds and rice husk feed rates for good combustion behaviour. To prove that the tapering angle should not be increased beyond 60^{o}, the tapering angle in the current SFB was increased to 70^{o} (Case II). The fluidisation behaviour and air feed requirements in order to maintain 3 U_{mfs} at the bed surface was shown in Table 4.9.

Table 4.9: Fluidisation conditions and air feed requirements at ambient (30°C) for tapering angles and rotating speeds in the SFB primary chamber (length 300 mm, ID 600 mm, tapered height 225 mm, bed depth 150 mm)

g-loading	L_o (m)	L_i (m)	U_{mfc}/U_{mfs}	F_R (untapered)	F_R (tapered)	Air flow rate, Q @ 3 U_{mfs}, 30°C (m^3/hr)	L_o/L_i
CASE I : Tapering angle = 60°							
5	0.0401	0.2134	3.42	0.29	0.78	520.60	0.19
10			3.27	0.31	0.81	890.65	
15			3.20	0.31	0.83	1,194.29	
20			3.15	0.32	0.84	1,458.06	
25			3.12	0.32	0.85	1,694.46	
CASE II : Tapering angle = 70°							
5	0.1362	0.2454	3.42	0.29	0.26	598.78	0.56
10			3.27	0.31	0.28	1,024.41	
15			3.20	0.31	0.28	1,373.65	
20			3.15	0.32	0.29	1,677.03	
25			3.12	0.32	0.29	1,948.93	

It was evident from Table 4.9 that increasing the tapering angle to 70° while keeping the tapering height constant at 225 mm in the scaled down SFB resulted in a highly non-uniform radial bed fluidisation. Tapering the SFB at 60° resulted in the wall fluidising velocity being approximately 2.5 U_{mfc} for all rotating speeds when the surface fluidising velocity was designated at 3 U_{mfs}. Increasing the tapering angle to 70° resulted in a drastic decrease in F_R to a value of less than 0.3. This is undesirable in the sense that when the bed surface is already fluidising at a velocity of 3 U_{mfs}, the bed particles near the wall barely fluidise since the wall fluidising velocity is less than 1 U_{mfc}. Increasing the tapering angle also resulted in higher air feed requirements in order to maintain 3 U_{mfs} at the bed surface for the same bed depth of 150 mm. This can be attributed to the bigger cross sectional area for airflow at the bed surface when tapering at 70° (0.231 m^2) compared to tapering the SFB at 60° (0.201 m^2) with the same tapering height of 225 mm. This 15% reduction in surface area was also reflected in the air feed requirements, whereby operating the SFB tapered at 60° at 5-g loading, for example, required 520.6 m^3/hr (at 30°C) of air input while 598.8 m^3/hr (at 30°C) of air was required when the tapering angle was increased to 70° for the same operating conditions. In addition, the ratio of L_o/L_i for a SFB tapered at 70° was 0.56, which had exceeded the limit of

0.4. Therefore, increasing the tapering angle from 60^o to 70^o not only resulted in a highly non-uniform radial fluidisation but also higher air feed requirements.

To investigate the effect of tapering the SFB at different angles, the tapering height had to be varied as well for the reason discussed previously regarding the limit of tapering angle at a certain tapering height. Reducing the tapering height from 225 mm to 200 mm shifted the minimum limit of tapering angle to 53.1^o. To allow for sufficient length for air inlet, the feasible tapering angle for this tapering height is in the excess 60^o. Since the effects of tapering at an angle of 60^o had been studied extensively in the previous section and that increasing the angle beyond 70^o is detrimental to fluidisation in the radial direction, investigations on the optimum tapering angle at a tapering height of 200 mm were abandoned. To study the effect of tapering at angles of 50^o and 40^o, the tapering height should be reduced to 150 mm and 100 mm respectively. Maintaining the bed depth at 150 mm, the effects of changing the tapering angle (and corresponding tapering height) were presented in Table 4.10.

Tapering the SFB at a height of 150 mm and angle of 50^o (Case III) resulted in F_R being approximately one. Decreasing the tapering height to 100 mm while maintaining the same angle of 50^o (Case IV) resulted in very low values of this ratio (in the vicinity of 0.5). These values were clearly lower than the acceptable limit of 0.67. However, decreasing the tapering angle to 40^o while maintaining the tapering height at 100 mm (Case V) also resulted in equal fluidisation at the bed surface and near the combustor wall ($F_R \approx 1$). However, decreasing the tapering height from 150 mm to 100 mm and the tapering angle from 50^o to 40^o resulted in the increase in L_i (the length of the combustor at the bed surface) at a constant bed depth of 150 mm from 300 mm to 419.2 mm. Thus, the cross sectional area for airflow at the bed surface was increased by approximately 40% to 0.395 m^2. This increase in surface area led to an increase in air feed requirements (at a similar percentage) in order to reach a condition of 3 U_{mfs}. Since, all three cases of I, III and V gave desirable values of F_R and range of air feed requirements when operated at ambient conditions (30^oC), the optimisation of the tapering angle was further extended to include

operation at combustion temperature (800^{o}C). The results obtained were tabulated in Table 4.11.

Table 4.10: Fluidisation conditions and air feed requirements at ambient (30^{o}C) for different tapering angles, tapering heights and rotating speeds in the SFB primary chamber (length 300 mm, ID 600 mm, bed depth 150 mm)

g-loading	Tapering height, X (m)	L_o (m)	L_i (m)	F_R (tapered)	Air flow rate, Q @ 3 U_{mfs}, 30^{o}C (m^3/hr)	L_o/L_i
CASE III : Tapering angle = 50^{o}						
5	0.15	0.0483	0.3000	0.91	732.00	0.16
10				0.95	1,252.33	
15				0.97	1,679.28	
20				0.99	2,050.16	
25				1.00	2,382.57	
CASE IV : Tapering angle = 50^{o}						
5	0.1	0.1322	0.3839	0.42	936.74	0.34
10				0.44	1,602.61	
15				0.45	2,148.97	
20				0.46	2,623.59	
25				0.47	3,048.97	
CASE V : Tapering angle = 40^{o}						
5	0.1	0.0616	0.4192	0.99	1,022.79	0.15
10				1.04	1,749.83	
15				1.06	2,346.38	
20				1.08	2,864.59	
25				1.09	3,329.05	

Table 4.11: Fluidisation conditions, air feed requirements and stoichiometric rice husk feed rates for a SFB tapered at different heights and angles while operating at 800°C (primary chamber length 300 mm, ID 600 mm, bed depth 150 mm)

g-loading	Tapering height, X (m)	Operating U_{mfs}	No. of U_{mfc} near wall at operating U_{mfs}	F_R (tapered)	Air flow rate, Q @ operating U_{mfs}, 800°C (m^3/hr)	Air flow rate, Q @ operating U_{mfs}, 30°C (m^3/hr)	Rice husk feed rate @ 3.5 U_{mfs}, 800°C (kg/hr)	Primary chamber volume, V_c (m^3)	V_{free} ($V_c - V_{sand}$) (m^3)	Rice husk burnout time (min)
CASE I : Tapering angle, θ = 60°										
5	0.225	3.5	2.37	0.68	320.01	90.37	26.98	0.04356	0.01866	4.40
10			2.41	0.69	628.73	177.54	53.01			2.24
15			2.44	0.70	927.25	261.84	78.18			1.52
20			2.47	0.71	1,216.55	343.54	102.58			1.16
25			2.49	0.71	1,497.41	422.85	126.26			0.94
CASE III : Tapering angle, θ = 50°										
5	0.150	3.5	2.77	0.79	449.97	127.06	37.94	0.05521	0.02121	3.56
10			2.81	0.80	884.04	249.64	74.54			1.81
15			2.85	0.81	1,303.80	368.17	109.93			1.23
20			2.88	0.82	1,710.57	483.04	144.23			0.94
25			2.91	0.83	2,105.49	594.56	177.53			0.76
CASE V : Tapering angle, θ = 40°										
5	0.100	3.5	3.03	0.87	628.72	177.54	53.01	0.06489	0.02964	3.56
10			3.07	0.88	1,235.23	348.81	104.15			1.81
15			3.12	0.89	1,821.74	514.43	153.60			1.23
20			3.15	0.90	2,390.10	674.93	201.53			0.94
25			3.19	0.91	2,941.90	830.75	248.05			0.76

From Table 4.11, decreasing the tapering angle from 60^o to 40^o resulted in more uniform radial bed fluidisation, as can be seen from the value of F_R, which was approaching unity (Case V). However, the smaller the angle of tapering, the wider the length of the primary chamber as the air moves radially inward. And since the bed depth was maintained at 150 mm at all three cases investigated, the cross sectional area for airflow at the bed surface is the biggest for the smallest tapering angle. For instance, tapering at 40^o gave a cross sectional area for airflow at the bed surface of 0.395 m^2. This value was reduced to 0.283 m^2 and 0.201 m^2 when the tapering angles were increased to 50^o and 60^o, respectively. Therefore, to maintain fluidisation at 3 U_{mfs} at the bed surface, higher air feed rates were required when tapering the bed smaller angles. Increase in air feed requirements led to a direct increase in waste inputs. Although the free volume in the primary chamber is bigger when tapering at smaller angles, the higher rice husk feed rates when tapering at smaller angles resulted in lower residence times of feed particles in the primary chamber. Operating at 15-g loading, for example, gave an estimated rice husk residence time of less than 1.5 minutes (at 1.2 minutes) for both SFB tapered at 50^o and 40^o. Taking into account the lower air feed requirements and higher residence times of feed in the primary chamber when tapering at bigger angles, it was concluded that 60^o is the optimum angle of tapering for the SFB.

Hence: The optimum angle of tapering in the SFB is 60^o.

4.3.5 Terminal Velocity of Rice Husk

Operating the fluidised bed at fluidising velocities exceeding the terminal velocities of particles will result in the elutriation of particles from the bed. Thus, the terminal velocity, u_t is the highest velocity at which a fluidised bed could be operated at to prevent particles from being blown out of the bed. The terminal velocity of a particle could be estimated from the following expression (McCabe et al., 1993):-

$$u_t = \sqrt{\frac{4d_p(\rho_p - \rho_f)g}{3\rho_f C_D}} \tag{4.2}$$

in which the drag coefficient, C_D has to be determined experimentally. The terminal velocity of non-spherical particles could be determined from the following dimensionless expressions from Haider and Levenspiel (1989) and as cited by Kunii and Levenspiel (1991):-

$$d_p^* = d_p\left[\frac{\rho_g(\rho_p - \rho_g)g}{\mu^2}\right]^{\frac{1}{3}} \tag{4.3}$$

$$u^* = u\left[\frac{\rho_g^2}{\mu(\rho_p - \rho_g)g}\right]^{\frac{1}{3}} \tag{4.4}$$

Determination of u_t using these expressions required the reference of Figure 4.6, which is the graphical representation of the expression for C_D developed by Haider and Levenspiel (1989).

Low-density materials, such as rice husk, have very low values of terminal velocity. Rice husk has a boat-like shape and its sphericity (as determined from the method suggested in Section 2.5.3) was 0.19. Hence, the curve representing particles with disk-like shape of sphericity 0.230 could be used to estimate its terminal velocity. The terminal velocity for rice husk particles under the influence of gravity was determined to be less than 1.5 m/s (Figure 4.7) for temperature ranging from 30^{o}C to 800^{o}C. Therefore, operating a conventional fluidised bed at a minimum requirement of 3 $U_{mf,}$ for example, might result in sufficient air velocity to blow these particles out of the bed before combustion could take place. For example, for the chosen sand size (600 – 850 μm), operating at 3 U_{mf} in a conventional fluidised gives a fluidising velocity of 0.93 m/s. At combustion temperatures ranging from 600 – 800^{o}C, the terminal velocity of rice husk is approximately 1.3 m/s. Hence, the operating range of fluidising velocities in a conventional fluidised bed is very narrow. The terminal velocity of particles in a SFB, on the other hand, is higher due to the higher *g*-level, which could be manipulated by adjustment of the rotating speed. The gravitational

term (g) in both Equations (5.3) and (5.4) is replaced by radial acceleration (a_r) for application in a SFB. The radial acceleration in the irrotational flow region of the freeboard (Chevray et al., 1980) and evaluated at the inner radius of the bed is given by:-

$$a_r = r\,\omega^2 \tag{4.5}$$

For the proposed SFB (primary chamber length 300 mm, ID 600 mm, tapering height 225 mm and tapering angle 60^o) operated at a bed depth of 150 mm, the terminal velocities of rice husk evaluated at the bed surface and at different g-loadings were also shown in Figure 4.7. It was evident from Figure 4.7 that increasing the g-loadings at which the SFB is rotated at elevated the terminal velocities to higher values. During operation of the SFB, the surface fluidising velocity is maintained at 3 U_{mfs}. These fluidising velocities, at different rotating speeds at temperatures of cold and hot commissioning (30^{o}C and 800^{o}C, respectively), were tabulated in Table 4.12.

Table 4.12: Fluidising velocities at the bed surface of the SFB operating at 3 U_{mfs} (primary chamber length 300 mm, ID 600 mm, tapering height 225 mm, tapering angle 60^o, bed depth 150 mm, sand size 600 – 850 μm)

Rotating speed (g-loading)	Fluidising velocity (at 3 U_{mfs}) at different temperature	
	30 (^{o}C)	800 (^{o}C)
5	0.72	0.38
10	1.23	0.74
15	1.65	1.10

These fluidising velocities were much lower than the terminal velocities of rice husk for both operating temperatures at all rotating speeds. It should also be noted that the air velocity is further reduced progressively as the air moves radially inward due to the tapering effect in the proposed SFB. Thus, rice husk particles will remain in the primary chamber to be burnt instead of being blown out by the fluidising air. These findings, apart from reiterating the advantages of a SFB over a conventional fluidised bed, also proved that:-

a) Elutriation of low-density materials from the SFB could be prevented by increasing its rotating speed, which will increase their terminal velocities, and

b) Inclusion of the tapering section in the primary chamber of the proposed SFB, which decreases the fluidising velocity in the radial direction inwards, aids in preventing waste particles from being blown out of the freeboard region before completing the combustion process.

4.3.6 Secondary Chamber Design

The proposed SFB combustor has a secondary combustion chamber, which is projected at the same axis of rotation as the primary chamber. It has a much bigger volume than the primary chamber (ID 600 mm and length 500 mm). The aim of incorporating the secondary chamber are:-

i) To complete combustion in the gas phase at higher combustion efficiency due to the higher turbulence induced by the swirling flows, and

ii) To act as a particulate control device by removing ash through holes drilled at the circumference of the chamber wall.

During the combustion process, especially of materials with high-volatile content, the hot fluidised bed in the primary chamber acts as a heat source to pyrolyse the waste materials. Thereafter, depending on the density of the resulting chars and the mixing pattern inside the fluidised bed, the chars will either be burnt inside the bed or at the freeboard region (central core of the primary chamber). It is desirable that these chars burn inside the bed in order for the bed temperature to be maintained. However, in the event that these chars be ejected to the freeboard region by bubble eruption at the bed surface and be blown out of the primary chamber even before complete conversion has occurred, the presence of the secondary chamber will ensure that they burnt to completion and not be blown out of the combustor together with the flue gas. Thus, the presence of products of

incomplete combustion (PICs) in the flue gas could be minimised. In addition, given the small volume of freeboard region in the primary chamber, the evolved volatiles has sufficient residence time to be burnt to completion as they proceed to the secondary chamber.

Accumulation of ash in the fluidised bed during the combustion of rice husk could be significant due to its high content of ash (14.7%). This will consequently lead to the increase in bed depth that will interfere with the fluidisation process. The rear end of the tapered section in the primary chamber, apart from separating the secondary chamber from the primary chamber, also acts as a weir plate for the spillover of ash from the sand bed once its thickness exceeded the height of the plate. The spillover ash will then proceed to the secondary chamber, where the high-degree of swirling flows will drive these particles to the wall region. Thereon, holes incorporated at the wall of the secondary chamber allow for the escape of these ash particles that will subsequently be collected in an ash pit. It is expected that the secondary chamber will work as a cyclone in removing these ash particles, resulting in minimised emissions of particulate matters in the exhaust gas. Hence, a cyclone might not be needed to collect the resulting fly-ash and to control particulate emissions from the flue gas in order to comply with existing regulations.

4.4 The Proposed SFB Combustor System

The SFB combustor will be fabricated using suitable materials (such as stainless steel) that are able to withstand temperatures of up to 1200^{o}C. The system is equipped with a variable speed motor assembly capable of rotation of up to 1000 RPM, which give g-loadings of up to 335. Both the primary and secondary combustion chambers should be jacketed and insulated. Appropriate insulation materials should be used to minimise heat loss to the surroundings. A customised insulation clamper should also be included for rotary motion and should be able to seal the air, so that pressurised air of up to 4 m H_2O could be supplied into the rotating combustor.

Waste materials are fed via a feed hopper into the primary chamber using screw conveyor with a diameter of 100 mm at an adjustable speed of up to 150 RPM. The screw conveyor is equipped such that it is jacketed for secondary air inlet.

Fluidising gas enters through a perforated distributor plate (3% hole area distributed equally) from an airtight seal jacketed around the cylindrical primary combustion chamber. The fluidising gas is supplied by a blower that is able to withstand very high-pressure drop (up to 4m H_2O) with a maximum capacity of 1200 m^3/hr (at ambient temperature). The secondary air blower has a capacity of 250 m^3/hr and able to withstand pressure drop up to 1 m H_2O. The secondary chamber acts as a freeboard where complete combustion of the volatile matters in the flue gas takes place. It was designed to allow for a minimum residence time of flue gas of two seconds, consistent with existing regulations for incineration of waste. Secondary combustion air is fed through the pipe jacketing the screw conveyor, penetrating through the freeboard area of the primary chamber to the secondary chamber.

The combustor will be operated with excess air level in the range of 60% to 100% depending on the types of waste in order to comply with the regulations of 6% oxygen level in the flue gas. Spillover ash particles from the weir plate lip will be collected in an ash pit located downstream of the combustor. A long reach torch will ignite the materials in the primary chamber. Chromel/alumel (Type-K) thermocouples (with jacketed sleevings) to record temperatures in the primary combustion chamber (located 50 mm, 100 mm and 200 mm from the combustor wall) as well as the flue gas temperature at the secondary combustion chamber are connected via a rotating slip rings assembly to the display instruments. The primary burner should be able to withstand high-pressure drop in the primary combustion chamber while the secondary burner should be able to maintain temperatures in the secondary combustion chamber of up to 1200^{o}C. The blueprint of the prototype tapered horizontal SFB combustor was shown in Figure 4.8.

Further development will involve energy recovery through a heat exchanger to preheat the primary air prior to entering the primary combustion chamber to

minimise the consumption of auxiliary fuel. The proposed experimental set-up for the entire system was shown in Figure 4.9.

CHAPTER V

THREE-DIMENSIONAL COMPUTATIONAL FLUID DYNAMICS MODELLING OF THE SFB COMBUSTOR

5.1 Introduction

Computational fluid dynamics modelling was carried out to verify the design of the proposed horizontal SFB combustor with tapered ends and to determine the suitable range of operating parameters for optimum operation of the combustor. The application of CFD to combustor design is widespread in all the new research and development techniques in combustion technology (Nasserzadeh et al., 1993). In particular, the use of the commercial code FLUENT is extensive due to its ability in replicating actual trends observed experimentally. FLUENT is a powerful general-purpose computer program for modelling fluid flow, heat transfer and chemical reaction. The basic approach utilised is that of solving the conservation equations for mass, momentum, energy and chemical species using a control volume based finite difference method. Researchers such as Nasserzadeh et al. (1993) and Rozainee (1998) had proven the validity of the results obtained through modelling in FLUENT. In their study of the flows and combustion profiles in a municipal solid waste (MSW) incinerator, Nasserzadeh et al. (1993) found that the program was capable in predicting all the major features of the incinerator flow and temperature fields. On the other hand, Rozainee (1998) showed that modelling results had correctly indicated the trends in gaseous combustion and particle trajectories in a vertical SFB. Hence, the results obtained in this modelling works could be utilised with a very high level of confidence.

The scopes of modelling of the horizontal SFB combustor are:-

a) determination of the flow profiles in the combustor to investigate the flow patterns and to provide a basis for design improvements,
b) investigation into the trajectories of particles of different sizes at different combination of operating conditions (air inputs, rotating speeds) to provide insight into the ash accumulation and entrainment behaviour,
c) simulation of gaseous combustion to determine the optimum operating parameters for bed starting-up and for efficient gas-phase combustion, and
d) simulation of rice husk combustion to determine the allowable range of operating parameters for optimum and efficient combustion.

5.2 Model Set-Up

The modelling domains were created using the GAMBIT software package (pre-processor for CFD packages). GAMBIT is a versatile software package designed to help analyst and designer build and mesh models for CFD and other scientific applications. Although the basic steps of building and meshing a model are made simple and intuitive, it is capable to accommodate a wide range of modelling applications.

5.2.1 Factors Influencing the Choice of Grid

Although FLUENT can use grid comprising of triangular or quadrilateral cells (or a combination of the two) in 2D, and tetrahedral, hexahedral, pyramid or wedge cells (or a combination of these) in 3D, the choice of mesh type depended largely on specific application. The choice of mesh type, in turn, is largely controlled by the following issues:-

i) Set-up time
ii) Computational Expense
iii) Numerical diffusion

Although not impossible, the creation of structured grids (consisting of quadrilateral or hexahedral elements) for complex geometries can be extremely time-consuming. The major motivation for using unstructured grids employing triangular or tetrahedral cells, therefore, lies in the significant savings in set-up time. Savings in time apart, the geometry involved in the present modelling cases was relatively complex, rendering the implementation of the unstructured grid practical.

A triangular/tetrahedral mesh can often be created with far fewer cells than the equivalent mesh consisting of quadrilateral/hexahedral elements. This has direct effect on the expense of computation as a triangular/tetrahedral mesh allows cells to be clustered in selected regions of the flow domain, whereas structured quadrilateral/hexahedral meshes will generally force cells to be placed in regions where they are not needed. However, quadrilateral/hexahedral elements permit a much larger aspect ratio than triangular/tetrahedral cells. Aspect ratio is the measure of the stretching of the cell. A large aspect ratio in triangular/tetrahedral cell will invariably affect the skewness of the cell, an undesirable trait as it impedes accuracy and convergence. Thus, the practice of using high-aspect-ratio quadrilateral/hexahedral cells is recommendable for simple geometry as the mesh is likely to have far fewer cells than if triangular/tetrahedral cells were used.

Numerical diffusion is a dominant source of error in multidimensional modelling. The amount of numerical diffusion is inversely related to the resolution of the mesh and is minimised when the flow is aligned with the mesh. The flow in a domain using quadrilateral/hexahedral cells can be aligned with the mesh in simple flows, but not if triangular/tetrahedral cells are used instead.

Another factor to be considered is the inclusion of swirling motion, which generates steep gradients in the flow domain. Typically, rotating boundary layers may be very thin, and the FLUENT model will require a very fine grid near a rotating wall. In addition, swirling flows will often involve steep gradients in the circumferential

velocity (eg, near the centreline of a free-vortex type flow), and thus require a fine grid for accurate resolution.

5.2.2 Grid Optimisation

Numerical errors in computation during the modelling works are largely determined by the quality of the grid generated. This necessitates the use of a more refined grid. Nonetheless, the computing time involved in order to reach converged solutions should also be taken into account as it highly depends on the size of the grid cells. Finer grid cells are able to capture thinner layer in the gradients of the flow variables, thereby able to give a more accurate solution to the problem. For a fixed size of a modelling domain, the smaller the size of the grid cells, the bigger the amount of the cells at which the governing equations should be solved for. As the choice of grid determined in early stages of the cold-flow modelling will be applied in subsequent non-isothermal reacting flows, it is imperative to optimise the size of the grid to be used. The purpose of the optimisation process is to determine an acceptable grid size that is able to reach a balance between the amount of computing time and the accuracy in the solution of the flow variables.

The geometry of the proposed horizontal SFB with tapered ends is complex due to the presence of the tapered section in the primary chamber. In the modelling domain, both end walls of the primary chamber are oblique to the chamber axis whereas the secondary chamber is a cylinder. With the foresight that future improvements, if any, on the design of the proposed SFB might be necessary, it is therefore crucial to select a consistent meshing scheme so that any changes observed in the flow variables of the solved cases is due only to the changes applied to the design. The TGrid meshing scheme satisfied this criterion in terms of its ability to mesh any complex geometry especially those with the presence of internal structure such as baffle. It is an unstructured form of meshing scheme that creates a mesh consisting primarily of tetrahedral mesh elements but which may also contain hexahedral, pyramidal and wedge mesh elements. Therefore, this meshing scheme was chosen.

In the optimisation process, the spacing between the nodes in the mesh was varied. Nodes are points at which flow variables are to be calculated from the governing equations. The dimensions of the grid generated are similar to the actual dimensions of the proposed SFB prototype. The modelling domain created was a 90^o slice of the entire SFB due to its axisymmetrical nature. By setting the boundary condition at the axisymmetric plane as periodic to represent rotational movement, the solution for the flows in the SFB could be obtained at fraction of the time required if the entire rig were to be modelled. It was found that decreasing the interval size of the nodes by half from 20 to 10 resulted in a slight increase in the amount of grid cells (from 32 509 to 32 578). The slight increase was not in proportion to the reduction in interval size due the random order in which cells were placed in the TGrid meshing scheme. The velocity vectors captured in the axisymmetric plane for both grids were in good agreements with each other, as shown in Figure 5.1 and Figure 5.2 (for node size interval of 10 and 20 respectively). Reducing the interval size further to 1 resulted in the same amount of grid cells as that of an interval size of 10 (at 32 578). However, solving for the flow variables in this grid was highly unstable, with residuals that did not show the decreasing trend. With the choice of grid with interval sizes of 20 and 10, the former was chosen based on the lesser computing time involved.

5.3 Governing Equations and Numerical Solution

5.3.1 Mathematical Model of the Gas Phase

Prediction of the isothermal flow field in the computational grid is through solution of the equations for the conservation of mass and momentum in their time averaged form.

Conservation of mass (incompressible flow):-

$$\frac{\partial}{\partial x_i}\left(\rho\, u_i\right) = 0 \tag{5.1}$$

The velocity at any one point in turbulent flows is taken as the sum of the mean (ensemble-averaged) and fluctuating components:-

$$u_i = \overline{u_i} + u_i' \tag{5.2}$$

Substituting expression of this form into the instantaneous momentum equations yields the ensemble-averaged momentum equation:-

$$\frac{\partial}{\partial x_j}\left(\rho u_i u_j\right) = \frac{\partial}{\partial x_j}\left\{\mu\left[\left(\frac{\partial u_i}{\partial x_j} + \frac{\partial u_j}{\partial x_i}\right) - \frac{2}{3}\frac{\partial u_l}{\partial x_l}\delta_{ij}\right]\right\} - \frac{\partial P}{\partial x_i} + \frac{\partial}{\partial x_j}\left(-\rho\overline{u_i' u_j'}\right) \tag{5.3}$$

A turbulence model is required since the process of Reynolds decomposition and time averaging results in unknown correlations of the fluctuating velocity components. Using the $\kappa - \varepsilon$ model, the second order tensor of "Reynold stresses" or $\left(-\rho\overline{u_i' u_j'}\right)$ (incorporating the effect of turbulence) is modelled using the Boussinesq hypothesis. The Reynold stresses is related to the mean velocity gradients via:-

$$\left(\rho\overline{u_i' u_j'}\right) = \frac{2}{3}\left(\rho\kappa + \mu_t\frac{\partial u_i}{\partial x_i}\right)\delta_{ij} - \mu_t\left(\frac{\partial u_i}{\partial x_j} + \frac{\partial u_j}{\partial x_i}\right) \tag{5.4}$$

For swirling flows in a SFB, the RNG (renormalization group) $\kappa - \varepsilon$ model was used. Belonging to the $\kappa - \varepsilon$ family of models, the model equations in their RNG form are similar to those for the standard $\kappa - \varepsilon$ model. The standard $\kappa - \varepsilon$ model is widely applied in engineering practice (Tobiś, 2000). However, several researchers (Sloan et al., 1986; Sturgess and Syed, 1985; Srinivasan and Moagia, 1980) noted through Xia et al. (1998) that its performance is less satisfactory for swirling flows as it poorly predicts the size and strength of recirculating zones. It tends to produce an excessive solid-body component type of rotation for swirling flows. This was proved in the initial investigations into the airflow profile in the SFB operated at 15-g loading and 3 U_{mfc} (at room temperature) as shown in Figure 5.3. The steep velocity gradients in the swirling flows in the SFB (especially in the secondary chamber) were not fully captured using the standard $\kappa - \varepsilon$ model. As a

result, the flows in secondary chamber tend to approach that of a solid body rotation type of movement, with velocity vectors of the airflow (Figure 5.4) near the vortex regions moving primarily in the circumferential direction due to the rotational movement. According to Lilley and Chigier (1971), this phenomenon might be attributed to the isotropic eddy viscosity assumption in the standard $\kappa - \varepsilon$ model. The RNG $\kappa - \varepsilon$ model, on the other hand, takes better account of the effect of extra strain rates, as indicated by Hanjalic (1994) through Xia et al. (1998). This can be observed from Figure 5.5, which showed improvements in the stepping of velocity gradients especially in the vortex regions for the SFB operated at the same operating conditions but using the RNG $\kappa - \varepsilon$ model instead of the standard $\kappa - \varepsilon$ model. The swirling flows in these free vortex regions were no longer moving as a solid body rotation, but found to moving as recirculating flows (Figure 5.6). This is because the RNG $\kappa - \varepsilon$ model takes into account the effect of swirl on turbulence, thus enhancing the accuracy for swirling flows. In general, turbulence in swirling flows is affected by rotation or swirl in the mean flow. The RNG model in FLUENT provides an option to account for the effects of swirl or rotation by modifying the turbulent viscosity appropriately. A differential form of the relation for effective viscosity was employed, yielding an accurate description on how the effective turbulent transport varies with the effective Reynolds number.
The turbulent viscosity, μ_t was computed from the functional form:-

$$\mu_t = \mu_{t0} f\left(\alpha_s, \Omega_c, \frac{\kappa}{\varepsilon}\right) \tag{5.5}$$

where

μ_{t0} = $0.0845\rho\frac{\kappa^2}{\varepsilon}$

Ω_c = characteristic swirl number (evaluated within FLUENT)

α_s = swirl constant
(0.05 for mildly swirling flow; 0.07 for swirl-dominated flow)

The values of turbulent kinetic energy, κ and its rate of dissipation, ε were determined by numerical integration of the system of differential equations (5.6) and (5.7):-

$$\frac{\partial}{\partial x_i}\left(\rho u_i \kappa\right) = \frac{\partial}{\partial x_i}\left(\alpha_\kappa \mu_t \frac{\partial \kappa}{\partial x_i}\right) + G_\kappa - \rho\varepsilon \tag{5.6}$$

$$\frac{\partial}{\partial x_i}\left(\rho u_i \varepsilon\right) = \frac{\partial}{\partial x_i}\left(\alpha_\varepsilon \mu_t \frac{\partial \varepsilon}{\partial x_i}\right) + C_{1\varepsilon} G_\kappa \frac{\varepsilon}{\kappa} - C_{2\varepsilon}\rho\frac{\varepsilon^2}{\kappa} - R \tag{5.7}$$

The term G_κ represents the generation of turbulent kinetic energy due to the mean velocity gradients, given by:-

$$G_\kappa = -\rho\overline{u_i' u_j'}\frac{\partial u_j}{\partial x_i} \tag{5.8}$$

or, consistent with the Boussinesq hypothesis,

$$G_\kappa = \mu_t\left(\frac{\partial u_i}{\partial x_j} + \frac{\partial u_j}{\partial x_i}\right)\frac{\partial u_j}{\partial x_i} \tag{5.9}$$

The effects of rapid strain and streamline curvature is given by the last term in equation (5.7), where

$$R = \frac{0.0845\rho\eta^3\left(1 - \dfrac{\eta}{4.38}\right)}{1 + 0.012\eta^3}\frac{\varepsilon^2}{\kappa} \tag{5.10}$$

and

η = $S\dfrac{\kappa}{\varepsilon}$

S = modulus of the mean rate-of-strain tensor

S_{ij} = mean strain rate, $\left[\frac{1}{2}\left(\frac{\partial u_i}{\partial x_j}+\frac{\partial u_j}{\partial x_i}\right)\right]$

For high Reynolds number, the values of the inverse Prandtl numbers for κ and ε $(\alpha_\kappa \text{ and } \alpha_\varepsilon)$ are approximately 1.393. The coefficients $C_{1\varepsilon}$ and $C_{2\varepsilon}$ are empirical constants having the following values:-

$C_{1\varepsilon} = 1.42$ and $C_{2\varepsilon} = 1.68$

5.3.2 Equation of Motion for A Particle

FLUENT predicted the trajectory of a discrete phase particle by integrating the force balance on the particle, which is written in a Langrarian reference frame. This force balance equates the particle inertia with the forces acting on the particle, and can be written (for the *x* direction in Cartesian coordinates) as

$$\frac{du_p}{dt} = F_D\left(u - u_p\right) + \frac{g_x\left(\rho_p - \rho\right)}{\rho_p} + F_x \tag{5.11}$$

where $F_D(u - u_p)$ is the drag force per unit particle mass and

$$F_D = \frac{18\mu}{\rho_p D_p^2}\frac{C_D \,\mathrm{Re}}{24} \tag{5.12}$$

Here, u is the fluid phase velocity, u_p is the particle velocity, μ is the molecular viscosity of the fluid, ρ is the fluid density, ρ_p is the density of the particle, and D_p is the particle diameter. *Re* is the relative Reynolds number, which is defined as

$$\mathrm{Re} = \frac{\rho D_p \left|u_p - u\right|}{\mu} \tag{5.13}$$

The drag coefficient, C_D can be taken from either

$$C_D = a_1 + \frac{a_2}{\mathrm{Re}} + \frac{a_3}{\mathrm{Re}^2} \tag{5.14}$$

where a's are constants that apply for smooth spherical particles over several ranges of *Re* given by Morsi and Alexander (1972) or

$$C_D = \frac{24}{\mathrm{Re}}\left(1 + b_1\,\mathrm{Re}^{b_2}\right)\frac{b_3\,\mathrm{Re}}{b_4 + \mathrm{Re}} \tag{5.15}$$

where

$$b_1 = 2.3288 - 6.4581\phi + 2.4486\phi^2$$
$$b_2 = 0.0964 + 0.5565\phi$$
$$b_3 = 4.905 - 13.8944\phi + 18.4222\phi^2 - 10.2599\phi^3$$
$$b_4 = 1.4681 + 12.2584\phi - 20.7322\phi^2 + 15.8855\phi^3$$

which is taken from Haider and Levenspiel (1989) for nonspherical particles. The shape factor, ϕ, is defined as

$$\phi = \frac{s}{S} \tag{5.16}$$

where s is the surface area of a sphere having the same volume as the particle, and S is the actual surface area of the particle.

The additional force term, F_x in Equation (5.11) includes the Coriolis and centrifugal forces acting on the particle arising from the rotational movement of the SFB. For rotation defined about the *x* axis, the forces on the particles in the Cartesian *x* and *y* direction can be written as

$$\left(1-\frac{\rho}{\rho_p}\right)\Omega^2 y + 2\Omega\left(u_{z,p}-\frac{\rho}{\rho_p}u_z\right) \tag{5.17}$$

where $u_{z,p}$ and u_z are the particle and fluid velocities in the Cartesian z direction, and

$$\left(1-\frac{\rho}{\rho_p}\right)\Omega^2 z - 2\Omega\left(u_{y,p}-\frac{\rho}{\rho_p}u_y\right) \tag{5.18}$$

where $u_{y,p}$ and u_y are the particle and fluid velocities in the Cartesian y direction.

The trajectory equations were solved by stepwise integration over discrete time steps. Integration in time of Equation (5.11) yielded the velocity of the particle at each point along the trajectory, with the trajectory itself predicted by

$$\frac{dx}{dt} = u_p \tag{5.19}$$

$$\frac{dy}{dt} = v_p \tag{5.20}$$

$$\frac{dz}{dt} = w_p \tag{5.21}$$

The particle phase was assumed to be sufficiently dilute, thus rendering negligible effects on the continuous phase.

5.3.3 Mathematical Model for Reactive Chemistry

5.3.3.1 Single Phase Reacting Flows

Governing equations for modelling of single phase reacting flows were presented as follows:-

Conservation equation for enthalpy:-

$$\frac{\partial}{\partial x_i}(\rho u_i h) = \frac{\partial}{\partial x_i}\left[\left(\frac{k+k_t}{c_p}\right)\left(\frac{\partial h}{\partial x_i} - \sum_j h_j \frac{\partial m_j}{\partial x_i}\right)\right] + S_h \qquad (5.22)$$

where

k = molecular conductivity

k_t = turbulent thermal conductivity

c_p = mixture heat capacity, $\left[= \sum_j m_j C_{pj}\right]$

S_h = enthalpy source term due to chemical reaction

= $\left[= \sum_j \left(\frac{h_j^o}{M_j} + \int_{T_{ref_j}}^{T_{ref}} c_{p,j} dT\right) R_j\right]$ with h_j^o being the enthalpy of formation of species j and R_j being the volumetric rate of creation of species j

Conservation of chemical species in turbulent flows:-

$$\frac{\partial}{\partial x_i}(\rho u_i m_i) = \frac{\partial}{\partial x_i}\left(\rho D_{i,m} + \frac{\mu_t}{S_{ct}}\right)\frac{\partial m_i}{\partial x_i} + R_i \qquad (5.23)$$

where

m_i = local mass fraction of chemical species i

R_i = mass rate of creation or depletion by chemical reaction

$D_{i,m}$ = diffusion coefficient of i in the mixture

S_{ct} = turbulent Schmidt number, $\frac{\mu_t}{\rho D_t}$ (with a default setting of 0.7)

The source of chemical species i due to reaction, R_i is computed as the sum of the reaction sources over the N_R reactions that the species may participate in:-

$$R_i = M_i \sum_{k=1}^{N_R} \hat{R}_{i,k} \tag{5.24}$$

where

M_i = molecular weight of species i

$\hat{R}_{i,k}$ = molar rate of creation/destruction of species i in reaction k

The reaction rate, $\hat{R}_{i,k}$ is controlled either by an Arrhenius kinetic rate expression or by the mixing of the turbulent eddies containing fluctuating species concentration.

Arrhenius reaction rate:-

$$R_{i,k} = -\upsilon_{i,k} M_i T^{\beta,k} A_k \exp\left(-\frac{E_k}{RT}\right) \prod_{j\ reac\tan ts}^{N} C_j^{\eta_{j,k}} \tag{5.25}$$

where

$\upsilon_{i,k}$ = molar stoichiometric coefficient of species i in reaction k (positive value or reactants, negative value for products)

M_i = molecular weight for species i (kg/kmol)

β_k = temperature exponent (dimensionless)

A_k = pre-exponential factor (consistent units)

E_k = activation energy for the reaction (J/kmol)

R = universal gas constant (J/kmol-K)

C_j = molar concentration of each reactant j (kmol/m^3)

$\eta_{j,k}$ = rate exponent for reactant j in reaction k

Input values for $\upsilon_{i,k}$, $\eta_{j,k}$, β_k, A_k and E_k are user-specified or retrieved from the database during problem definition in FLUENT.

The influence of turbulence on the reaction rate is taken into account by employing the Magnussen and Hjertager (1976) model. In this model, the rate of reaction, $R_{i,k}$ is given by the smaller (limiting value) of the following two expressions:-

$$R_{i,k} = \upsilon_{i,k} M_i A \rho \frac{\varepsilon}{\kappa} \frac{m_R}{\upsilon_{R,k} M_R} \tag{5.26}$$

$$R_{i,k} = \upsilon_{i,k} M_i AB \rho \frac{\varepsilon}{\kappa} \frac{\sum m_P}{\sum_j^N \upsilon_{j,k} M_j} \tag{5.27}$$

where

m_P	=	mass fraction of any product species P
m_R	=	mass fraction of a particular reactant R
R	=	reactant species giving the smallest value of $R_{i,k}$
A	=	empirical constant (= 4.0)
B	=	empirical constant (= 0.5)

The eddy dissipation model relates the rate of reaction to the rate of dissipation of the reactant- and product-containing eddies. The time scale of the turbulent eddies is represented by $\frac{\varepsilon}{\kappa}$, following the eddy dissipation model of Spalding (1970). In turbulent reacting flows, reaction rates from the Arrhenius expression and eddy dissipation model are calculated within FLUENT. The slowest (limiting) rate is then used as the controlling reaction rate, whereupon the contributions to the source terms in the species and energy conservation equations are calculated from.

In modelling of reacting gas flow, the fluid density is calculated based on the ideal gas law for an incompressible flow:-

$$\rho = \frac{P}{RT\sum \frac{m_i}{M_i}} \tag{5.28}$$

where R is the universal gas constant, $\frac{m_i}{M_i}$ provides the molecular weight of the local mixture and P is the input value of the operating pressure.

5.3.3.2 Mixture Fraction / PDF Modelling Approach for Particle Combustion

The mixture fraction / PDF modelling approach involves the solution of transport equations for one or two conserved scalars (the mixture fractions). Through this approach, instead of solving the transport equations for individual species, the individual component concentrations for a certain species of interest are derived from the predicted mixture fraction. Therefore, the usually unknown reaction mechanisms need not be explicitly user-defined but is treated using certain system chemistry calculations (eg the flame sheet approximation, equilibrium assumption and non-equilibrium chemistry). Physical properties of chemical species and equilibrium data are retrieved from the chemical database while the interaction of turbulence and chemistry is accounted for with a probability density function or PDF.

The PDF modelling approach is specifically developed for reaction processes in which turbulence mixing is the limiting rate for reaction progress. By allowing intermediate species formation, dissociation effects and the coupling between turbulence and chemistry to be accounted for in a rigorous way, this method is computationally efficient by making the solution of a large number of species transport equations unnecessary. The basis of the mixture fraction approach is that under a certain set of simplifying assumptions, the instantaneous thermochemical state of the fluid is related to a conserved scalar quantity known as the mixture fraction, *f*. Being a conserved scalar quantity, the value of *f* at each point in the flow

domain is computed in FLUENT through the solution of the conservation equation for mean (time-averaged) value of *f* in the turbulent flow field, $\overline{f}$:-

$$\frac{\partial}{\partial x_i}\left(\rho u_i \overline{f}\right) = \frac{\partial}{\partial x_i}\left(\frac{\mu_t}{\sigma_t}\frac{\partial \overline{f}}{\partial x_i}\right) + S_m \tag{5.29}$$

where S_m represents the transfer of mass from reacting particles into the gas phase.

In addition to solving the conservation equation for the mean mixture fraction, a conservation equation for the mixture fraction variance, $\overline{f'^2}$ is also solved:-

$$\frac{\partial}{\partial x_i}\left(\rho u_i \overline{f'^2}\right) = \frac{\partial}{\partial x_i}\left(\frac{\mu_t}{\sigma_t}\frac{\partial \overline{f'^2}}{\partial x_i}\right) + C_g \mu_t \left(\frac{\partial \overline{f}}{\partial x_i}\right)^2 - C_d \rho \frac{\varepsilon}{\kappa}\overline{f'^2} \tag{5.30}$$

where the constants σ_t , C_g and C_d take the values of 0.7, 2.86 and 2.0, respectively. The mixture fraction variance is used in the closure model describing the turbulence-chemistry interactions.

Calculation of a single conserved scalar field, *f* enables the derivation of other important scalars (individual species mole fractions, density and temperature) without the need to solve their respective transport equations. Provided the description of the reacting system chemistry, the mixture fraction value at each point in the flow field can be used to compute the instantaneous values of these scalars. If a secondary stream is included in a non-adiabatic system, the instantaneous values will depend on the instantaneous fuel mixture fraction, f_{fuel}, the secondary partial fraction, p_{sec} and the enthalpy, H^*:-

$$\phi_i = \phi_i\left(f_{fuel}, p_{\sec}, H^*\right) \tag{5.31}$$

where ϕ_i represents the instantaneous species concentration, density or temperature, while H^* is given by:-

$$H^* = \sum_i m_{i'} H_{i'} = \sum_i m_{i'} \left[\int_{T_{ref_{i'}}}^{T} c_{p,i'} dT + h_{i'}^o \left(T_{ref_{i'}} \right) \right] \tag{5.32}$$

The non-adiabatic model is required in particle-laden flows (particle combustion systems) since such flows include heat transfer to the dispersed phase.

The functional relationship between ϕ_i (species, density and temperature) and mixture fraction depend on the description of the system chemistry. For modelling of rice husk particle combustion in which the formation of intermediate species takes place, the equilibrium assumption chemistry model is appropriate. With this model, no specific reaction mechanism and specific reaction rates are required. Only important chemical species that will be present in the system need to be defined. Prediction of the mole fraction of each species will then be carried out by FLUENT based on chemical equilibrium.

However, FLUENT prediction of the turbulent reacting flow is concerned with the prediction of the time-averaged values of the scalars in Equation (5.31). The next step, hence, is to relate these instantaneous values to their respective time-averaged values based on the turbulence-chemistry interaction model, which in this case applies the PDF approach as its closure model since the mixture fraction / PDF modelling approach is used.

The probability density function, written as $p(f)$, describes the fraction of time that the fluctuating variable f takes on a value between f and $f + \Delta f$. Expressed mathematically, it takes on the following form:-

$$p(f)\,\Delta f = \lim_{T \to \infty} \frac{1}{T} \sum_i \tau_i \tag{5.33}$$

where τ_i is the fraction of time that f spends in the Δf band.

The probability density function, $p(f)$ which describes the temporal fluctuations of f in the turbulent flow is used to compute time-averaged values of variables that depend on f. Time-averaged values of species mole fractions and temperature can be computed, in a non-adiabatic system with a secondary stream, as:-

$$\overline{\phi_i} = \int_0^1 \int_0^1 \phi_i \left(f_{fuel}, p_{\sec}, \overline{H^*} \right) p_1 \left(f_{fuel} \right) p_2 \left(p_{\sec} \right) df_{fuel}\, dp_{\sec} \tag{5.34}$$

where p_1 is the PDF of f_{fuel}, p_2 is the PDF of p_{sec}, and $\overline{H^*}$ is the time-averaged enthalpy solved from:-

$$\frac{\partial}{\partial x_i}\left(\rho u_i \overline{H^*}\right) = \frac{\partial}{\partial x_i}\left(\frac{k_t}{c_p}\frac{\partial \overline{H^*}}{\partial x_i}\right) + \tau_{ik}\frac{\partial u_i}{\partial x_k} + S_h \tag{5.35}$$

where S_h accounts for source terms due to radiation, heat transfer to wall boundaries, and heat exchange with the second phase.

In a similar form, the true time-averaged fluid density is computed as:-

$$\frac{1}{\rho} = \int_0^1 \int_0^1 \frac{p_1\left(f_{fuel}\right) p_2\left(p_{\sec}\right)}{\rho\left(f_{fuel}, p_{\sec}, \overline{H^*}\right)} df_{fuel} dp_{\sec} \tag{5.36}$$

In Equation (5.36), $\rho\left(f_{fuel,} p_{\sec}, \overline{H^*}\right)$ is the instantaneous density obtained using the instantaneous species mole fractions and temperature in the gas law equation. Using equations (5.34) and 5.36), the shape of the function $p_1(f_{fuel})$ and $p_2(p_{sec})$ need to be specified in order to determine the local time-averaged state of the fluid at all points in the flow field. In FLUENT, the shape of the PDF, $p(f)$, is described by either the double delta function or the β-function. Since the β-function is thought to represent most closely experimentally observed PDF's than the easily computed but less accurate double delta function, it is used in the present modelling study. The β-function PDF shape is given by the following function of $\overline{f}$ and $\overline{f'^2}$:-

$$p(f) = \frac{f^{\alpha-1}(1-f)^{\beta-1}}{\int f^{\alpha-1}(1-f)^{\beta-1}df} \tag{5.37}$$

where

$$\alpha = \overline{f}\left[\frac{\overline{f}(1-\overline{f})}{\overline{f'^2}} - 1\right] \qquad \text{and} \qquad \beta = (1-\overline{f})\left[\frac{\overline{f}(1-\overline{f})}{\overline{f'^2}} - 1\right]$$

5.3.4 Modelling and Solution Procedures

For the two-mixture-fraction (secondary stream) case, the preprocessor prePDF calculates the instantaneous values for the temperature, density and species mole fractions (Equation 5.31) and stores them in the look-up tables. For the non-adiabatic case with two mixture fractions, the 3D look-up table contains the physical properties as functions of the fuel mixture fraction, the secondary partial fraction and the instantaneous enthalpy. The PDF functions p_1 and p_2 of the fuel mixture fraction and the secondary partial fraction, respectively, are calculated inside FLUENT from the values of the fractions and their variances. The PDF integrations for calculating the mean values for the properties are also performed inside FLUENT (using Equation 5.34 together with Equation 5.36). The instantaneous values required in the integrations are obtained from the look-up tables. The algorithm for solving a non-adiabatic two-mixture-fraction case was depicted in Figure 5.7.

For two-mixture-fraction problems, the 3D look-up table allows FLUENT to determine the instantaneous values for the scalar properties from instantaneous values of f_{fuel}, p_{sec} and H^*. The three-dimensional table is the visual representation of Equation (5.31). These instantaneous values are used to perform the integration of Equation (5.34).

5.4 Numerical Approach

The FLUENT computer code (version 5.3 and version 5.5) together with calculation data from the equations of fluidisation in a SFB to provide boundary conditions, were used to model the fluid flows and trajectories of particles in a SFB at various operating conditions. Judging from the symmetry in geometry of the SFB and computational efforts, only a quarter of the entire SFB combustor was modelled. The boundary condition at the axisymmetrical cross sectional area was set as periodic to represent rotational movement (Figure 5.8). The model consisted of an unstructured grid of 32 509 cells employing the TGrid meshing scheme, consisting primarily of tetrahedral cells, with hybrid (hexahedral, pyramidal and wedge) cells being placed at appropriate locations. The axis of rotation was set at the *x* direction in the Cartesian coordinates. The flow profiles in the model were first established in an isothermal condition after which ash particles of various sizes were injected and their respective trajectories charted. Air at ambient temperature and certain flow rates consistent with the desired operating conditions entered radially through the distributor plate. However, velocity vectors of the airflow were imparted a tangential component upon entering the porous or perforated distributor plate due to frictional force. The default convergence criteria were that iterations were performed until the scaled residuals decrease to a value of 10^{-3} for all equations except for energy, whereby the value of 10^{-6} applies.

5.5 Fluid Dynamics Feature of the SFB Freeboard

Flow field in the freeboard of the SFB is divided into three distinct regions (Figure 5.9) and is affected, in general, by cylinder geometry, bed rotating speed and fluid flow rate. In Region 1, the tangential velocity component varies inversely with radius to maintain a constant angular momentum in gas. The flow in this region is irrotational, very similar to the free vortex flow. Region 2 consists of regions whereby the fluid is in contact with the top and bottom end walls and moving as a rigid body. The tangential velocity component is proportional to the radius

($u_t \propto r$). The radial variation in pressure in the end wall boundary layers (Region 2) is determined by radial variations in u_t in Region 1. Axial differences in tangential velocity between Region 1 and Region 2 results in positive radial pressure gradients. Hence, there are net radial flows inward along the end walls towards axis of rotation. Near the axis of rotation, viscous effect limits the $\frac{1}{r}$ increase in u_t (as in Region 1). A region of solid body rotation is thus established (Region 3). With decreasing radial position, the tangential velocity component started to decrease, until it becomes zero at the axis of rotation. The variation in the tangential velocity component in the SFB was given by Figure 5.10.

The extent of Region 1 and Region 3 is determined by ratio of tangential to radial initial component of momentum (Equation 5.38). The higher the ratio, the greater the extent of rotational core (Region 3). On the other hand, the lower the ratio, the higher the extent of free vortex region (Region 1).

$$\frac{r_m}{r_i} = 0.05\frac{u_t(r_i)}{u_r(r_i)} \;;\; u_r = -\frac{Q}{2\pi r_i H} \text{ and } u_t = \omega r_i \tag{5.38}$$

where Q = volumetric flow rate of gas

r_i = inner radius of bed

H = height of bed

Radius of the viscous core, r_c corresponds to the location of maximum u_t. For SFB with small values of bed length-to-diameter $\left(\frac{H}{D}\right)$ ratios, the locations of the exit port and maximum tangential velocity are nearly coincident $(r_E \approx r_m \approx r_c)$.

The velocity distribution of the tangential, axial and radial components in the SFB were given by the following equations:-

Tangential component

Viscous core : $u_t(r) = \frac{100Q^2}{\omega \pi^2 r_i^4 H^2} r$; $0 \le r \le r_m$ (5.39)

Irrotational region : $u_t(r) = \frac{\omega r_i^2}{r}$; $r_m \le r \le r_i$ (5.40)

Axial component

Viscous core : $u_z(z) = \frac{Q}{\pi r_m^2 H} z$; $0 \le r \le r_m$ (5.41)

Irrotational region : $u_z(z) = 0$; $r_m \le r \le r_i$ (5.42)

Radial component

Viscous core : $u_r(r) = -\frac{Q}{2\pi r_m^2 H} r$; $0 \le r \le r_m$ (5.43)

Irrotational region : $u_r(r) = -\frac{Q}{2\pi r H}$; $r_m \le r \le r_i$ (5.44)

5.6 Analysis of Modelling Results

Results from the computer modelling were held in storage arrays of very large size representing complicated three-dimensional distribution. Hence, presentation of the data in an intelligible form demanded almost as much efforts as the computations themselves. To facilitate interpretation of results, vector plots, isometric projections and contour lines had been employed. In the discussion of the modelling results, the SFB combustor referred to the proposed design of the tapered horizontal SFB as determined in Chapter V, unless otherwise stated.

5.6.1 Modelling of Airflow Profiles in the SFB

Fluid flow profiles inside a combustor affect the distribution of unburnt gaseous components as well as the trajectories of particles. Such flow profiles, which could be captured and studied through CFD package such as FLUENT, are useful in providing information on how the flow behave inside the combustor. Moreover, the formation of undesirable dead zones inside the combustor could be determined so that design modifications could be made to the combustor to rectify the design drawbacks. The distribution of unburnt gases inside the combustor, on the other hand, could in turn provide insight into the efficiency of combustion in the gas phase. Meanwhile, the trajectories of particles inside the combustor serve to provide information on the entrainment of particles from the combustor. Thus, a cold flow model of the proposed SFB combustor was established to simulate the airflow behaviour inside the combustor. The fluidising velocity at the distributor inlet of the SFB was designated at 3 U_{mfc} to satisfy the requirement to establish sufficient turbulence inside the bed. The rotating speed of the SFB was set at 15-g loading, which gave a rotational speed of 211 RPM.

Modelling of flow field profiles in the horizontal tapered SFB showed that regions of recirculating flows were dominant in the secondary chamber, especially near the entrance of the secondary chamber (Figure 5.11). This was due to the rapid convergence of fluid to the primary chamber exit (effect of the tapered end walls) followed by sudden expansion in flow as the fluid entered the secondary chamber, resulting in the formation of eddies behind the expansion region. This phenomenon was also observed by Xia et al. (1998) in their numerical and experimental study of swirling flow in a model combustion chamber with an inlet that is oblique to the chamber axis. They observed that a corner recirculation zone appeared just behind the expansion region adjacent to the air inlet, as had been observed in the present SFB model. Contours of static pressure inside the tapered horizontal SFB (Figure 5.12) showed that regions of low static pressure were mainly concentrated at the exit of the primary chamber only. This was in contrast to the pressure profiles in the untapered horizontal SFB, whereby regions of low static pressure stretched from the primary chamber exit till the secondary chamber exit and concentrated along the central core of the secondary chamber (Figure 5.13). According to Bernoulli

equation for flow along a streamline, simplified for inviscid, incompressible, steady flow without heat addition and with negligible change in height, the sum of static pressure and dynamic pressure gives the total pressure of a system, in which the total pressure is a constant. Therefore, due to the conservation of mechanical energies within the fluid, the region of low static pressure coincided with the region of high velocity as the momentum of the ordered motion of the gas in the flow direction resulted the increase in dynamic pressure (density times the square of velocity divided by two) and the decrease in static pressure. In a tapered SFB, regions of low static pressure at the secondary chamber entrance expanded radially outward nearly halfway through the secondary chamber radius (Figure 5.12). This resulted in the airflow being directed to the free vortex region of the secondary chamber upon exit from the primary chamber. On the other hand, the low-static-pressure region in the untapered SFB, which did not expand at the entrance of the secondary chamber, resulted in the air rushing along the central core of the secondary chamber without any flow expansion (Figure 5.14). The expansion of airflow to the wall regions of the secondary chamber as observed in the tapered SFB showed that in actual combustion operations, the unburnt gaseous components could be distributed rather uniformly to the entire secondary chamber. Thus, the residence time of these gaseous components is higher compared to the case whereby the gases were rushing along the central core of the secondary chamber straight to the exit of the secondary chamber. Higher residence time of gases, which allows for more complete combustion to take place, will result in higher combustion efficiency. In addition, modelling results obtained on the airflow profiles in the tapered SFB indicated that no internal device such as a cowling is required to diverge the airflow to the wall regions of the secondary chamber upon its exit from the primary chamber.

Deeper understanding of the flow structure inside the SFB could be obtained through injection of tracer particles into the established flow field to enable visual observation of the directions of flow. Therefore, tracer particles (rice husk ash; D_p = 10 μm and ρ_p = 1590 kg/m^3) were injected into the established flow field of the tapered SFB. Results showed that the existence of recirculating regions might be detrimental to the operation of the combustor as particles could be trapped in the eddies and remained there infinitely (Figure 5.15). This, apart from restricting

mixing in the entire chamber, will ultimately cause the flow to be heavily-laden with particles. The need for improvement to this situation prompted the study on the effect of inclusion of internal baffles or cowling in the secondary chamber to breakthrough the current limitation of the SFB with a hollow secondary chamber.

5.6.1.1 Effect of Internal Baffles and Cowling

With the aim of minimising the formation of eddies and increasing the swirling flows in the secondary chamber, investigations had been made to determine the effect of the inclusion of baffles or cowling on the flow field profiles. In the case of baffles inclusion, four internal baffles (500 mm long, 5 mm thick) were placed co-centrally and 90^o apart from each other on the secondary chamber wall. The width of the baffles was varied from 50 mm to 75 mm and 100 mm. As for the case of the inclusion of a cowling (60^o-cone with a height of 200 mm located co-axially with the horizontal SFB), the cowling was either placed 50 mm or 100 mm from the primary chamber exit. In all cases, tracer particles (rice husk ash; D_p = 10 μm and ρ_p = 1590 kg/m^3) were injected to give information on particle trajectories, serving to provide a supplement to the overall understanding of the flow field structure of the combustor. The operating conditions were kept constant at 15-g loading (giving a rotational speed of 211 RPM) and 3 U_{mfc} (at room temperature of 300 K).

Modelling results showed that the inclusion of baffles of all three widths (50 mm, 75 mm and 100 mm) were successful in breaking eddies near the primary chamber exit (Figures 5.16, 5.18 and 5.20). The tracer particles were no longer trapped in the recirculating regions (Figures 5.17, 5.19 and 5.21). In the case of baffles with width of 50 mm and 75 mm, the tracer particles were blown out of the combustor in less than 0.3 s. Although the recirculating zones were minimised in both cases (Figure 5.16 and Figure 5.18), flow field profiles in the SFB with baffles of width 50 mm showed two desirable traits. The tracer particles in this case exhibited a significantly higher degree of swirl in the secondary chamber (Figure

5.17), especially near the exit of the combustor, compared to the case of the 75 mm-wide baffles (Figure 5.19). In addition, this phenomenon was enhanced by another desirable trait, its higher residence time (0.278 s) compared to the latter case (0.253 s), representing an increment of approximately 10%.

When the baffles width was increased to 100 mm, the recirculating zones were less profound (Figure 5.20). It was initially speculated that with less eddy formation and wider baffles, the degree of swirling flows in the secondary chamber would be higher. However, it turned out that the contrary was true as the trajectory of the tracer particles showed that they were heading straight to the exit without any degree of swirling. Also, their residence time were the lowest, at 0.201 s (Figure 5.21).

Inclusion of a cowling into the secondary chamber of the SFB also successfully minimised the formation of eddies, to the level sufficient as to eliminate tracer particles from being trapped inside the recirculating zones. Figure 5.22 and Figure 5.23 showed respectively, the airflow profile and trajectories of tracer particles in the tapered SFB with a cowling placement of 50 mm from the primary chamber exit. For the case of cowling placement at 100 mm from the primary chamber exit, the results on the airflow profile and particle trajectories were shown in Figure 5.24 and Figure 5.25, respectively. Cowling placed farther down the exit of the primary chamber (100 mm distance) shifted the recirculating regions farther downstream (Figure 5.24) in comparison with the case whereby the cowling was placed at a distance of 50 mm from the primary chamber exit (Figure 5.22). The former situation resulted in the tracer particles being directed by the cowling to the free vortex region of the flow having high axial velocity. Thus, they were blown out rapidly from the combustor after 0.22 s (Figure 5.25). This phenomenon was also observed when the cowling was placed farther upstream (50 mm distance), but in this case the residence time of the tracer particles were higher (0.28 s, Figure 5.23) due to the longer distance they had to travel to the exit of the combustor.

Without tolerating in terms of particle residence time, the case whereby 50 mm-wide baffles were included in the secondary chamber provided a basis for design improvements for the tapered horizontal SFB. The significantly high degree

of swirling exhibited by the tracer particles (Figure 5.17) compared to other cases served to promote better mixing of unburnt matters such as char with the combustion air in the secondary chamber. The "t" paramount in combustion – turbulence, was hence provided. Sacrifices in term of residence time were not made as the tracer particles in the present case had among the highest residence time compared to other case studies.

Hence: Incorporation of four internal baffles (500 mm × 50 mm × 5 mm) onto the secondary chamber wall of the SFB was successful in reducing the recirculating zones near the entrance of the secondary chamber.

5.6.2 Modelling of Particle Trajectory in the SFB Freeboard

The trajectories of particles inside the SFB combustor may vary according to the type and size of particles as well as the operating conditions (fluidising air velocity and rotating speed). Of particular interest is the trajectory of ash particles, as knowledge of their trajectories at different particle sizes and operating conditions could provide insight into the accumulation of ash in the bed and also their elutriation behaviour.

Ejection of particles from the bubbling fluidised bed into the freeboard region is the result of bubble eruption on the bed surface. It was reported by Rozainee (1998) that the initial velocity of ejected particles is independent of the size and density of the particles, being largely dependant on the size and rise velocity of the bubble (Caram et al., 1984). It was further reported that if the ejected particles were from bubble wakes, the particle ejection velocity could be as high as 2.5 times the bubble rise velocity ($V_m = 2.5\ U_b$) (Pemberton and Davidson, 1986).

In a SFB, the velocity of bubble swarms can be estimated by the following equation by Subzwari (1983):-

$$U_b = U - U_{mf} + 0.71\,\omega\sqrt{rd_b} \tag{5.45}$$

where

U_b = bubble velocity

U = fluidising velocity

U_{mf} = minimum fluidising velocity

d_b = bubble diameter

r = radial position

All parameters for Equation (5.45) were evaluated at the radial position of the bed surface ($r = r_i$) since the values of fluidising velocity and minimum fluidising velocity in a SFB are dependent upon the radial position. With a bed thickness of 150 mm made up of 0.725 mm sand in the horizontal SFB combustor (ID = 300 mm) operating at room temperature, the corresponding parameters were evaluated and presented in Table 5.1.

Table 5.1: Particle ejection velocities at different operating conditions

g-loading	ω (rad/s)	No. of U_{mfc}	U_{mf} (U_{mfs} @ $r = r_i$)	U (m/s)	U_b (m/s)	2.5 x U_b (m/s)	u_p (m/s)	v_p (m/s)	w_p (m/s)
5	12.79	1	0.24	0.31	0.57	1.41	0	-1.41	1.92
		2		0.62	0.87	2.18	0	-2.18	
		3		0.92	1.18	2.95	0	-2.95	
10	18.08	1	0.41	0.50	0.80	1.99	0	-1.99	2.71
		2		1.01	1.30	3.25	0	-3.25	
		3		1.51	1.81	4.51	0	-4.51	
15	22.15	1	0.55	0.66	0.97	2.43	0	-2.43	3.32
		2		1.32	1.63	4.08	0	-4.08	
		3		1.98	2.29	5.73	0	-5.73	

In estimating the bubble velocity, the bubble diameter was assumed to be 20 mm, a value obtained by Rozainee (1998) from his visual observation of the bubbling bed in a Perspex SFB. Consistent with the prediction of particle ejection

velocity by Pemberton and Davidson (1986), the maximum ejected particles velocities at each operating condition was evaluated. The eruption of bubbles was assumed to have ejected the particles in the radial direction only. Therefore, the axial velocity of the ejected particles was assumed to be zero. Also, the ejected particles have a tangential velocity component due to the solid body rotation effect of the rotating beds.

For the sake of tracking their trajectories, the particles were assumed to be ejected singly into the freeboard region. Thereon, the particles were acted upon by the centrifugal force, which tended to return them to the bed. At the same time, the drag force acting in the direction of the gas velocity relative to the particle, tended to bring them towards the centre. In addition, in a frame of reference rotating with the bed, the Coriolis force acted on the particles in such a way as to tend to displace them in a direction normal to their velocity and in the direction of rotation (Chevray et al., 1980).

5.6.2.1 Effect of Particle Diameter

Accumulation of ash inside the fluidised bed in the primary chamber of the SFB could be significant due to the high content of ash in rice husk (14.7%). Therefore, the purpose of investigating the effect of particle diameter on the trajectories of rice husk ash particles in the SFB was to gain information on the sizes of particles that will be retained or blown out from the fluidised bed in the primary chamber. With the knowledge of the rate of feeding and the size distribution of rice husk ash, the rate of ash accumulation in the bed could be determined. Subsequently, the time for spillover of ash through the weir plate in order to maintain the bed depth could be estimated.

To determine the size distribution of rice husk ash, approximately 100 g of fly-ash obtained from the combustion of rice husk in a conventional fluidised bed was subjected to screen analysis. Rice husk ash has a fluffy texture with a bulk density of 141.4 kg/m^3. Screen test results showed that rice husk ash consisted

mostly of particles in the size range of 125 – 300 μm (Figure 5.26). Rice husk burns according to the shrinking core model, whereby a char skeleton remains after the evolution of volatiles. After the char ignites and burns, the resulting ash still takes the shape of the skeleton. These skeletons are brittle and break easily. Therefore, during the operation of the fluidised bed, more fine ash particles are to be expected as the turbulent mixing inside the bed further breaks down these ash skeletons. Nonetheless, current results on the size distribution of these ash particles were acceptable and more or less representative of the actual size distribution as the shaking motion during the screening test further broke down the ash particles, similar to the motion induced by the fluidising bed materials.

To study the effect of particle diameters on the trajectories of particles ejected into the freeboard region due to bubble eruption at the bed surface, the horizontal SFB was operated at 15-g loading (211 RPM) and 3 U_{mfc} (5.28 m/s @ room temperature). The particles used were rice husk ash particles having a particle density of 1590 kg/m^3. The particles were assumed to be ejected from the bed surface of the 150 mm thick bed, mid-length of the primary chamber (x = 150 mm). It was found that, at these operating conditions, the particle trajectories were distinguishable with five particle diameters (5 μm, 10 μm, 25 μm, 50 μm and 1 mm).

As shown in Figure 5.27, particles with a diameter of 5 μm moved radially inward inside the primary chamber due to high initial radial velocity. High axial velocity at the exit of the primary chamber (as high as 3.76 m/s, Figure 5.28) then caused the particles to be blown into the secondary chamber, after which they were blown out from the combustor at less than 0.02 s. Particles with a diameter of 10 μm were recirculating infinitely at regions just after the exit from the primary chamber (Figure 5.29). Particles of this size were trapped in the recirculating zones near the front wall of the secondary chamber of the horizontal SFB (Figure 5.28). Particles with a diameter of more than 25 μm remained in the primary chamber without entering the secondary chamber. Ash particles with diameters of 25 μm and 50 μm were moving with the swirling flows in the primary chamber in helical trajectories, with the latter having a helical trajectory of larger radius due to higher

particle mass (Figure 5.30 and Figure 5.31). Particles having a diameter of 1 mm were returned to the bed rapidly due to higher momentum. This phenomenon indicated that at the designated operating conditions, the drag force of the fluid was not sufficient to entrain the particles from the bed surface into the freeboard region.

For optimum operation of the SFB, an air feed rate of 3 U_{mfc} was usually required in order to establish sufficient turbulence inside the bed. Particles with sizes of more than 25 μm (> 25 μm) were found to be retained inside the primary chamber of the SFB up to air feed rates of 3 U_{mfc}. Screen analysis showed that approximately 0.1% of rice husk ash consisted of particles with a size of less than 20 μm. Hence, based on the modelling results, it could be said that nearly all of the ash will be retained in the bed. According to the proposed design of the SFB, the primary chamber volume available after accounting for the volume of sand bed (of depth 150 mm) is 0.01866 m^3. Once the bed depth exceeded 225 mm (height of the weir plate lip or height of the tapered section at the rear end of the primary chamber), the ash will spill over to the secondary chamber. However, for a bed of depth 150 mm, the accumulation of materials inside the bed will be too much before the bed reaches a depth of 225 mm. This condition, apart from interfering with the fluidisation process (a deeper bed will alter the value of F_R), will also reduce the volume to accommodate the rice husk feed. There is also a possibility whereby the ash will spill over from the front end of the tapered section where the screw feeder is located and enters the piping for secondary air. To prevent these undesirable conditions from occurring, the height of the tapered section near the primary chamber exit should be reduced to less than 225 mm while maintaining the angle of tapering at 60^o, for instance to 200 mm. With this modification (as shown in Figure 5.32), once the bed depth exceeded 200 mm, the ash will spill over from the bed to the secondary chamber. Based on the calculations of the free volume in the primary chamber as presented in Appendix A, it was found that the free volume with the suggested design modification (bed depth remained the same at 150 mm) increased a little to 0.019 m^3. Applying the same calculation procedures as in Appendix A, the volume that could be occupied by ash before the spillover occurs is 0.010 m^3. The time before the ash spill over to the secondary chamber and the accumulation rate of

rice husk in the bed at different rotating operating conditions were shown in Table 5.2.

Table 5.2: Accumulation of ash particles in the fluidised bed of depth 150 mm in the modified SFB combustor (primary chamber length 300 mm, ID 600 mm, tapered angle 60^o, front tapering height 225 mm, rear tapering height 200 mm) operating at 800^{o}C

g-loading	Rice husk feed at stoichiometric at 3.5 U_{mfs} (kg/hr)	Time for ash spillover (min)	Rate of ash accumulation (mm/min)
5	26.98	21.49	1.16
10	53.01	10.94	2.29
15	78.18	7.42	3.37

The time for ash spillover and rate of ash accumulation in the modified SFB was estimated without accounting for the volume occupied by the rice husk feed. Thus, in actual operations, the time for ash spillover will be lower than those shown in Table 5.2. It could be observed from Table 5.2 that the higher the rotating speed, the higher the rate of ash accumulation in the bed due to the higher rice husk feed rate. For instance, the rate of ash accumulation in the bed is 3.37 mm/min for the SFB operated at 15-g loading, which was three times the rate when it was operated at 5-g loading (at 1.16 mm/min). The higher rice husk feed corresponded to the higher air feed rate required at higher rotating speed to establish a condition of 3.5 U_{mfs}.

Once the ash spill over from the weir plate lip into the secondary chamber, their trajectories at the wall regions will depend on their saltation velocities. Saltation velocity is the minimum superficial air velocity required for the transport of particles without the formation of a particle layer at the bottom of the transporting domain in flows under gravitational force. The empirical Rizk saltation correlation, valid for relatively dilute transport, and as cited by Hong et al. (1995) is as follows:-

$$m^* = \frac{1}{10^{1.44d_p+1.96}}\left[\frac{u_{sa}}{(gD)^{0.5}}\right]^{1.1d_p+2.5} \tag{5.46}$$

where d_p refers to particle diameter in mm, u_{sa} the saltation velocity and m* the solids loadings ratio (q_s/q_g), with q_s being the mass flow rate of solid and q_g the mass flow rate of gas. Superimposing the saltation effect to flows under centrifugal force, such as swirling flows in the SFB, the saltation velocity refers to the superficial gas velocity at which a particle begins to separate from the gas phase and form a layer along the entire circumference of the transporting domain. The Rizk correlation, therefore, could be modified for application in swirling flows by replacing the gravitational term with that of the radial acceleration (Equation 5.5). The resulting correlation, modified for swirling flows, is as follows:-

$$m^* = \frac{1}{10^{1.44d_p+1.96}}\left[\frac{u_{sa}}{(r\omega^2 D)^{0.5}}\right]^{1.1d_p+2.5} \tag{5.47}$$

Thus, it is expected that the spillover ash will form a layer along the entire circumference of the secondary chamber wall. Holes incorporated at certain intervals around the wall, will therefore allow for the escape of these ash particles. To determine if the ash particles will lose their momentum upon impacting the wall and be deposited to form the ash layer, their saltation velocities, which depend on particle diameter, gas and solids loadings, combustor diameter and centrifugal force, will be calculated based on modelling results on the airflow profiles and trajectories of spillover ash particles.

To capture the velocity contours and particle trajectories of spillover ash near the wall of the secondary chamber, CFD modelling was carried out by injecting ash particles of various sizes near the weir plate lip into the modified SFB flow field established at 800^{o}C at various g-loadings with air inlet consistent to give a fluidising condition of 3.5 U_{mfs} at the bed surface of depth 150 mm (or approximately 2.5 U_{mfc}). The particles were assumed to have zero velocity components in the axial and radial directions, except in the tangential direction owing to solid body rotation effect of the rotating beds. Further, the mass flow rate

of ash (q_s) in the secondary chamber was assumed to be equal to the generation rate of ash at certain g-loadings. The average mass flow rate of air (q_g) in the secondary chamber could be estimated from the modelling study, which could then be inserted into the modified Rizk correlation (Equation 5.47) to calculate the saltation velocities for ash particles of various sizes at various g-loadings. Consequently, the determination whether the ash will be deposited at the wall regions and the location where each differently-sized particle will deposit could be estimated. The latter could be used for designing the diameter and placing of holes on the secondary chamber wall for the escape of ash particles.

The saltation velocities of rice husk ash particles of various sizes at various g-loadings were as shown in Table 5.3.

Table 5.3: Estimated saltation velocities of rice husk ash of different sizes in the modified SFB (with rear tapering height of 200 mm) at various g-loadings (air inlet to establish 3.5 U_{mfs} at bed surface, bed depth 150 mm, operating temperature 800^{o}C)

D_{pi} (mm)	Estimated saltation velocity (m/s) at different g-loading		
	5-g loading	10-g loading	15-g loading
0.010	15.57	22.06	27.03
0.037	15.92	22.56	27.64
0.058	16.21	22.97	28.14
0.067	16.33	23.14	28.35
0.081	16.51	23.39	28.66
0.098	16.74	23.72	29.06
0.116	16.98	24.05	29.47
0.213	18.26	25.87	31.70
0.400	20.72	29.35	35.96
0.605	23.35	33.07	40.51
0.855	26.44	37.44	45.87
1.090	29.22	41.37	50.69
1.590	34.71	49.14	60.20

Note: $m^* \sim 0.15$ at all g-loadings

Modelling results showed that the velocity contours in the secondary chamber were lower than the saltation velocities (Figures 5.33 – 5.35) and thus, the ash particles will be deposited at the wall regions. It was also observed that larger-sized ash particles were deposited more rapidly due to their higher momentum (Figure 5.36). Smaller-sized ash particles were transported further downstream before being deposited. Furthermore, the expansion in airflow in the vicinity of the primary chamber exit aided in directing these particles to the wall regions. Ash particles of sizes less than 400 μm were deposited on the wall regions in the secondary chamber with trajectories similar to that shown in Figure 5.37 at all rotating speeds investigated (5- to 15-g loadings). Except for the modified SFB operating at 5-g loading, ash particles of with a size of 10 μm were blown further downstream of the secondary chamber before hitting the wall near the SFB outlet and be deposited there (Figure 5.36). According to the cumulative plot (Figure 5.38), approximately 95% of the rice husk ash sample consisted of particles with sizes of less than 400 μm. Thus, it was speculated that most of the spillover ash were deposited at positions less than mid-length of the secondary chamber wall. Therefore, holes intended for the escape of these ash particles should be concentrated at this region. Particles with sizes in the excess of 400 μm (about 5% of the ash) collided with the wall regions near the weir plate lip as soon as they spilled over. However, due to the motion of particles spilling over the weir plate lip, these particles will be pushed out further into the secondary chamber and be deposited at the wall regions.

Sand particles have a particle density of 2430 kg/m^3. Modelling results on the trajectories of ash particles with different sizes could still be used to provide information on the bed entrainment behaviour in the SFB as bubble eruption on the bed surface also throw the sand particles into the freeboard region. It is expected that due to the higher density, with the same particle size, sand particles will have a higher momentum compared to the ash particles. It was determined from the previous modelling study that particles of sizes more than 25 μm will be retained in the primary chamber of the SFB. This finding is important, as the entrainment of bed media from the primary chamber could be minimised. Entrainment of bed

particles is highly undesirable as it leads to a drop in bed pressure due to the loss of mass. Also, higher mass loss necessitates the frequent topping-up of bed media. Subsequently, the temperature of the bed will drop during combustion operations due to the addition of fresh bed materials, with the extent in temperature drop being dependant on the amount of bed materials to be compensated due to entrainment. Thus, the combustion process will be interrupted due to the lag in combustion process, resulting in increase of combustion reaction time. Particles with sizes of more than 1 mm (> 1 mm), on the other hand, were rapidly returned to the bed due to higher momentum. This is also crucial to the operation of a centrifugal fluidised bed by ensuring that the heat evolved from the combustion process into the freeboard region is transferred back to the bed through these particles. Thermal stability of the bed could therefore be maintained.

Hence: To prevent the bed from being too thick due to ash accumulation and also the spillover of ash from the front end of the tapered section, the tapering height at the rear end of the tapered section in the primary chamber should be reduced from 225 mm to 200 mm.

5.6.2.2 Effect of Rotating Speed

The entrainment behaviour of the SFB combustor, apart from being influenced by the particle size, also varies according to the combustor rotating speed. The purpose of investigating the effect of rotating speed on the trajectory of particles in the SFB is to determine the applicable range of rotating speeds that could maximise the residence time of particles such as char in the primary chamber. Higher residence time of char particles in the primary chamber allows for more complete combustion to take place, thus minimising the emissions of products of incomplete combustion (PICs) in the flue gas.

The effect of rotating speed on the trajectories of ash particles entrained into the freeboard region by bubble eruption at the bed surface was investigated by

operating the horizontal SFB at 5-g, 10-g and 15-g loadings with air feed rates of 3 U_{mfc}. At these g-loadings, the air feed rates to establish operating conditions of 3 U_{mfc} were 2.46 m/s, 4.02 m/s and 5.28 m/s (at room temperature) respectively. The size of particle chosen was 25 micron as particles of this size were the biggest particle (as determined in Section 6.6.2.1) that will be retained in the primary chamber due to the swirling flows. As such, it provided insight as to the effect of changing the rotating speed on the particle residence time in the primary chamber. Besides, another intention was to determine the return of these particles to the bed. Smaller sized particles (5 – 10 μm) were rapidly blown out from the primary chamber into the secondary chamber. Larger sized particles (> 50 μm), on the other hand, tended to move towards the distributor plate, similar to that observed for particles of 1 mm as in Figure 5.31.

The particle residence time was found to be decreasing as the bed rotating speeds were increased. This may sound ironic but it should be noted that the air feed rate was increased accordingly with the increase in rotating speed with the aim of maintaining a fluidising condition of 3 U_{mfc}. If the air feed rates were to be kept constant while increasing the rotating speeds, the residence time of particles will found to be higher with the increase in rotating speed. With a higher degree of rotational movement, the higher centrifugal force imparted onto the particles could counterbalance the constant drag force from the fluidising air. Thus, the net force to elutriate the particles out of the combustor will be lower at higher rotating speed, resulting in higher residence time of particles in the combustor.

As discussed earlier, the increase in bed rotating speeds resulted in higher air feed rates in order to maintain operating conditions of 3 U_{mfc}. Hence, in the present cases, the gas residence time in the primary chamber varies inversely with the bed rotating speed (Figure 5.39). Although the particle trajectories were quite similar in all three cases (Figures 5.40 – 5.42), the residence time in the primary chamber decreased from 0.412 s to 0.292 s and 0.235 s as the rotating speeds were increased from 5-g, 10-g and 15-g loadings respectively. The air feed rate to the primary chamber has to be maintained at about 3 U_{mfc} to establish turbulence conditions crucial in attaining good mixing behaviour inside the bed. Therefore, it was

recommendable that the bed be operated at low rotating speeds in order to increase the particle residence time. Also apparent was the observation that particles in all three cases were hovering near the surface of the sand bed at a radial position of r = 0.15 m.

Operating at higher rotating speeds led to a reduction in particle residence time in the primary chamber due to the increase in air feed rates (at 3 U_{mfc}). To obtain a higher residence time of particles, the SFB should be rotated at lower speeds (i.e. 5- to 10-g loadings). It is desirable to operate the SFB at lower rotating speeds because when the combustor was rotated at a higher speed, the corresponding air feed rates to maintain a condition of 3 U_{mfc} also increased. With the higher drag force from the higher air feed rates, the residence time of particles in the primary chamber was lowered. This undesirable trait will reduce the duration for particles such as chars to complete their oxidation.

Hence: Due to the corresponding increase in air input with rotating speed (to maintain fluidising condition of 3 U_{mfc}) which will lower the residence time of particles in the primary chamber, it is recommended that the SFB be operated at low rotating speeds (5- to 10-g loadings).

5.6.2.3 Effect of Air Feed Rates

The presence of a lot of fine particles (Geldart-C particles with sizes less than 30 μm) in the fluidised bed could interfere with the stability of fluidisation due to the high interparticle forces. Therefore, it is desirable to remove these fine particles from the bed. A SFB could be operated at a fluidising velocity of 2 – 3 U_{mfc} while being able to provide sufficient turbulence conditions in the bed. As determined from earlier studies, particles with sizes of less than 25 μm will be retained in the primary chamber. In this section, the trajectories of particles smaller than this size will be investigated at different fluidising air inputs to determine the air feed rate that is sufficient to entrain these fine particles from the primary

chamber. This finding is important, as the minimum air input to elutriate these fine particles from the bed could be determined.

The effect of air feed rates on the trajectories of rice husk ash particles was investigated by operating the horizontal SFB at 1 – 3 U_{mfc} while keeping the rotating speed constant at 15-g loading (211 RPM). Particles having a size of 10 μm were chosen since particles of this size are classified as Geldart-C and exhibited significantly different trajectories due to the change in air feed rates. Similar to earlier cases, smaller sized particles (5 μm) were rapidly blown out from the primary chamber while larger sized particles (> 25 μm) were either moving with the swirling flows in the primary chamber or were impacted towards the distributor.

Figure 5.43 and Figure 5.44 clearly showed that particles of size 10 μm were captured and remained in circular orbits in the primary chamber. However, the circular orbit of the case whereby the air input was 2 U_{mfc} had a fairly constant diameter (Figure 5.44). This, in part, was due to the increase in drag force with the increase in air feed rate, resulting in the net balancing between the centrifugal force (from the rotational effect) and drag force (from the fluidising air) on the particles. Lower drag force in the case of an air feed rate of 1 U_{mfc} resulted in a helical particle trajectory with a diverging trend (Figure 5.43). Air feed rate of 3 U_{mfc} was sufficient to blow out the 10-μm particles from the primary chamber (Figure 5.29). In addition, consistent with earlier explanation, the particle helical trajectory had a converging trend due to the much higher drag force from the air feed rate of 3 U_{mfc}. The residence times of the 10 μm-particles in the primary chamber were also observed to be decreasing from 0.325 s to 0.168 s and 0.0647 s as the air feed rates were increased from 1- to 2- and 3 U_{mfc} respectively.

For particles with sizes in the range of 10 – 25 μm, air feed rates exceeding 3 U_{mfc} were required to generate sufficient drag force to blow them out of the primary chamber. Particle in this size range consisted primarily of fines in the fluidised bed (sand, char and ash), produced through perpetual attrition between the bed particles during fluidisation. The presence of a large amount of fines in the bed is detrimental to the operation of fluidised bed. The interparticle forces present among these fine

particles will cause the fluidised bed to behave erratically consistent with particles classified as Geldart-C. The entrainment of these particles from the primary chamber to the secondary chamber of the SFB proved beneficial, as they can then be collected through holes incorporated at the end walls of the secondary chamber as part of the particulate emission control measure.

Hence: To remove fine particles (< 25 μm) from the bed, the SFB should be operated at a fluidising velocity exceeding 3 U_{mfc}.

5.6.3 Gaseous Combustion

Modelling of methane combustion was performed to illustrate the effect of tapering and bed rotating speed on the gas-phase combustion in the tapered horizontal SFB. The combustion of methane was modelled using a two-step reaction mechanism:-

$$2\ CH_4 + 3\ O_2 \rightarrow 2\ CO + 4\ H_2O$$

$$2\ CO + O_2 \rightarrow 2\ CO_2$$

Since both methane and air will enter the SFB combustor through the same inlet jacketed around the combustor, both gases were pre-mixed before being fed into the SFB. The pre-mixed methane/air mixture entering the combustors at 300 K was at a stoichiometric composition of 9.5% methane. At this concentration, the normal flame velocity, defined as the velocity at which the flame front moves in the direction of the unburned gases, was approximately 0.36 m/s (Figure 5.45). With the wall boundary condition of the combustor set at zero heat flux, the temperature predicted was the adiabatic flame temperature of the system. The adiabatic flame temperature of a stoichiometric mixture of methane/air is approximately 2200 K. The higher temperature (beyond the 2200 K) captured in the contours of the modelling results was due to the utilisation of a constant default value of mixture heat capacity. In actual, the heat capacities (especially for gases) are strict functions

of temperature and are often expressed in the polynomial form. However, it should be stressed here that the aim of the current investigations were to determine the sustainability and extent of gaseous combustion at different designs and rotating speeds of the SFB, and not the intimate details of the combustion characteristics of methane/air mixture. Hence, extra efforts to search for the appropriate heat capacity to be applied in the modelling study are unwarranted.

5.6.3.1 Effect of Tapering in the Primary Chamber of SFB

To study the effect of tapering in the primary chamber of the horizontal SFB, methane combustion was first simulated in an untapered SFB and then in a SFB with tapered end walls. Apart from the tapered section, both combustors have the same dimensions.

Pre-mixed methane/air mixture entered both stationary SFB combustors at 0.5 m/s. The choice of this value of inlet velocity lay in the fact that it was higher than the normal flame velocity of 9.5% methane mixture in air. Since both combustors were not rotating (0 RPM), flow recirculation in the freeboard regions was virtually non-existent. Also, since the rate of turbulence was very low, it was speculated that the value of flame velocity at the designated operating conditions was close to the normal flame velocity. As such, if the velocity profiles in any of the combustors exceed 0.36 m/s, the flame could not propagate and will ultimately be quenched. To illustrate this phenomenon, methane combustion was modelled in a fluidised bed. Results showed that combustion was barely sustainable in the fluidised bed (Figure 5.46) due to flame-quenching as the mixture velocity inside the chamber was higher than 0.36 m/s. Combustion was concentrated at very small regions adjacent to the top wall of the chamber.

Modelling results showed that without the tapering effect, combustion could not be sustained in the SFB (Figure 5.47). To maintain flame stability, the velocity of the gas mixture had to be lower than the flame velocity of the mixture. Velocity contours inside the untapered SFB (Figure 5.48) showed that the velocities in nearly

the entire combustor were more than 0.36 m/s. Since the unburned gas mixture moved faster than the flame front or flame velocity, the mixture could not be ignited. Consequently, flame propagation was terminated and combustion process did not take place.

Methane combustion, on the other hand, was sustainable in the tapered SFB. Although the inlet velocity of 0.5 m/s was higher than the normal flame velocity, this value was progressively reduced as the mixture moved radially inward. The tapering effect resulted in increasing cross sectional area of the fluid interface with the decrease in radius. This in turn, caused the velocity of the mixture to decrease as it moved from the distributor inlet towards the central core region. According to Figure 5.49 and Figure 5.50, the region of intense combustion coincided with regions of low velocity. This was the region spanning from the front wall to approximately mid-length of the primary chamber. In the secondary chamber, this was the free vortex region adjacent to the exit from the primary chamber. Velocities at these regions were no more than 0.16 m/s, which was less than half the normal flame velocity of the 9.5% methane mixture in air. Thus, the mixture was ignitable and these low velocity regions enabled the propagation of flame to the unburned mixture.

At the regions of higher velocities (0.3 – 0.6 m/s) near the right tapered section of the primary chamber, the flame could no longer travel as fast as the rate at which the unburned mixture was travelling. Flame propagation in these regions was terminated, resulting in 'dead' regions (blue-coloured region in Figure 5.49) in which flame extinction took place.

Hence: Inclusion of the tapered end walls in the primary chamber of the SFB allowed combustion of premixed methane/air mixture to take place even for a stationary SFB and mixture inlet velocity that exceeded the normal flame velocity of the mixture (0.36 m/s).

5.6.3.2 Effect of Combustor Rotating Speed

Methane combustion was simulated in the tapered horizontal SFB at different rotating speeds to investigate its effect on the gas-phase combustion (combustion intensity and carbon burnout rate). The primary purpose of this study is to determine applicable rotating speed during bed starting-up that could result in uniform heating of the 150 mm thick bed. In all cases, pre-mixed methane/air mixture entered the combustor at 300 K with an inlet velocity of 2 m/s. The bed rotating speed was increased from 0 RPM to 122-, 173- and 211 RPM, to give g-loadings of 0, 5, 10 and 15 respectively.

a) Effect on Combustion Intensity

Figure 5.51 showed that combustion took place in the non-rotating SFB although the inlet velocity was as high as 2 m/s. Since the overall turbulence in the stationary SFB was expected to be low, the flame velocity was assumed to be close to that of the normal flame velocity (0.36 m/s). The unique tapering feature of the SFB rendered combustion sustainable due to the progressive reduction of mixture velocity as it moved radially inward. At the present operating conditions, there existed regions of low velocities (0 – 0.36 m/s, Figure 5.52) sufficient to enable the flame front to move faster than the unburned gas mixture. The gas mixture in this region was ignited and ultimately led to the propagation of flame to the rest of the combustor. Nonetheless, turbulence rate at the central core region of the primary chamber might be quite high as the gases converged towards the exit. Thus, the flame velocity at this region was expected to be higher, explaining the sustenance of combustion in this high-velocity region. However, combustion was not intense, largely due to flame quenching at regions with high velocities particularly at the tapered section near the primary chamber exit.

It was reported by Ishizuka (1990) that a flame propagates rapidly in a rotating flow. Rotation in the mean flow affects the turbulence in swirling flows, with its rate varying proportionately with the degree of rotation. It is known that large-scale turbulence exerts a dual influence on pre-mixed combustion (Kagan and Sivashinsky, 2000). Moderately strong turbulence results in the extension of the

flame interface, leading to burning rate enhancement. As the flame propagates, turbulence in the flow field causes a flame to "fold" and "stretch", resulting in an increase in the flame surface area. An overall higher burning rate, in turn, produces a higher flow velocity in the unburned gas and consequently results in a continuous acceleration of the propagating flame (Chan et al., 1996). Although it was widely reported that swirl can substantially decrease the burning duration of a combustible mixture (Zhang and Hill, 1996), leading to higher combustion efficiency, there existed a limit at which excessive swirl can be detrimental. When that limit is reached, flame quenching takes place due to high turbulent strain rate.

Modelling results showed that methane combustion was increasingly more intense in the primary chamber of the SFB as the bed rotating speed was increased from 5-g to 10- and 15-g loadings (Figures 5.53 – 5.55). This phenomenon was expected as the rate of flow recirculation and turbulence increased with the increase in bed rotating speed. The recirculating flow recirculated the combustion products and the heat evolved to continually re-ignite the oncoming gas. In addition, flame "stretching" and "folding" due to the increasing rate of turbulence in the combustor led to an increase in flame velocity. Hence, the region of intense combustion extended farther and farther towards the distributor plate at higher rotating speeds. The extent of intensity in the combustion of premixed methane/air mixture at different rotating speeds is important in the selection of appropriate rotating speed during bed starting-up in order to achieve uniform pre-heat of the bed materials. The bed materials will occupy the entire circumference of the distributor plate of the SFB during fluidisation. The regions occupied by the bed are also the regions of low combustion intensity due to the flow of unburnt gaseous mixture entering at room temperature (300 K). At a rotational speed of 5-g loading, nearly half of the entire bed thickness, at approximately 75 mm thick (Figure 5.53), will not be pre-heated as the entering unburnt mixture was not ignited. As a result, the temperature in these regions was still at room temperature and the whole bed of thickness 150 mm could not be pre-heated uniformly. Only the upper half of the bed will be heated up.

When the rotating speed was increased to 10-g loading, the regions occupied by the unburnt mixture reduced to approximately one-third of the entire bed

thickness, at 50 mm (Figure 5.54). The upper two third of the bed could be heated up due to the higher combustion intensity with the increase in rotating speed compared to the SFB rotated at 5-g loading. At 15-g loading, further increase in combustion intensity reduced these low temperature regions to approximately one-quarter of the entire bed thickness (Figure 5.55). Nearly the whole of the bed could then be heated up. Although operating at higher rotating speeds led to more uniform bed pre-heating, it should be noted that the higher the rotating speed, the higher the extent of low temperature regions (1500 – 2500 K) in the central core of the secondary chamber. The formation of these low temperature regions will be discussed further in the following sections. Therefore, a compromise should be reached in order to achieve uniform bed pre-heating while simultaneously suppressing these low temperature regions to the minimum level.

It was long observed that for each gaseous pre-mixture, there is a certain level of turbulence at which the flame velocity reaches a maximum (Kagan and Sivashinsky, 2000). A further increase in the flow intensity leads to a drop in the flame velocity, followed by flame disintegration and extinction. The overall burning rate is lowered due to excessive flame stretching and rapid mixing of the burned products and cold unburned mixture. As the velocity of the unburned gas increases, the quenching by turbulence becomes more significant (Chan et al., 1996). Nevertheless, results from modelling showed that combustion was still sustainable even when the SFB was operated at a rotating speed of as high as 1000 RPM or 335 g-loadings.

Hence: To achieve more uniform pre-heating of the 150 mm thick bed, the SFB should be operated at higher rotating speeds (10- to 15-g loadings).

b) Effect on CO Burnout

Apart from providing information on the extent of bed pre-heating in the primary chamber, results from modelling of methane combustion in the SFB could provide insight into the effect of rotating speed on the burnout of CO. Higher turbulence in the combustor induced by the higher degree of rotational movement increase the rate

of mixing between the unburnt mixture with the products of combustion as well as the heat source so that the unburnt mixture could be ignited.

In a stationary SFB, turbulence was low and mixing was limited. The intermediate product of combustion, CO was largely concentrated in the central core region of the combustor (Figure 5.56). With rotation, this product was dispersed to the entire combustor by turbulence generated by the swirling flows. From observation of the modelling results, regions of high CO-content were significantly reduced in a SFB rotating at 122 RPM (Figure 5.57), being confined only to the primary chamber compared to a stationary SFB. With increasing rotating speed (Figure 5.58 and Figure 5.59), these regions were less profound and were confined to regions adjacent to the distributor plate. Comparisons between Figures 5.57 – 5.59 showed that CO burnout was more rapid as the rotating speed was increased, resulting in smaller regions occupied by CO in the primary chamber.

To further illustrate the more efficient gas-phase combustion due to the increase in combustor rotating speed, contours of CO/CO_2 product ratio in the SFB were plotted. As expected, regions of high CO/CO_2 product ratios were observed near the distributor inlet in the primary chamber (Figure 5.60), but were found to be less and less prominent as the rotating speed of the SFB was increased (Figure 5.61 and Figure 5.62). The enhanced mixing promoted by the increasing swirling flows aided in the more rapid transfer of oxidants to the intermediate product (CO) to form CO_2. The levels of CO emissions in the exhaust gases were reduced drastically from 0.051% in a stationary SFB to less than 1 part per trillion when the same combustor was rotated at 122 RPM. Further increase in bed rotating speeds resulted in a two order magnitude drop in CO emission levels (Figure 5.63).

In FLUENT, the level of CO emissions from the exhaust outlet were determined by custom definition of the following formula:-

$$CO\,(part\ per\ trillion) = \frac{\mathrm{CO}\ mole\ fraction \times 10^{12}}{1 - H_2O\ mole\ fraction} \tag{5.48}$$

where

$$CO\ mole\ fraction\ =\ \frac{CO\ mass\ fraction\ \times\ mixture\ molecular\ weight}{28}$$ and

$$Mixture\ MW\ =\ \frac{1}{\sum_i \frac{mass\ fraction}{molecular\ weight}}$$

Although rotating at higher rotating speeds resulted in smaller regions with high CO/CO_2 ratio near the distributor inlet, in actual combustion operations, these regions will be occupied by the sand bed. Most of the unburnt gaseous components are expected to be burnt in the freeboard region of the primary chamber and also in the secondary chamber, and since CO was undetectable from the freeboard of the primary chamber onwards, operating the SFB at higher rotational speed to achieve higher CO burnout rate might not be necessary. The emission level of CO at 5-g loading, in fact, was more than sufficient to comply with the existing regulations applicable for burning wastes in incinerators (at 125 mg/Nm^3 or 100 ppm).

Hence: Operating at a rotating speed as low as 5-g loading is sufficient to achieve high rate of CO burnout in the SFB and emission level of CO that complied with existing regulations.

c) Gas Phase Combustion in the Primary and Secondary Chambers

It was observed that regions of turbulence were concentrated at the primary chamber of the SFB due to the tangential flow inlet. With the increase in bed rotating speed, the increasingly high centrifugal force forced the swirling flow regions to move radially outward (Figure 5.64). These, in turn, promoted good mixing and recirculation of combustion products to the incoming unburned mixture. As a result, the combustion intensity in the primary chamber increased with bed rotating speed.

In the secondary chamber, mixing was not good when the bed rotating speed was increased. Low-temperature regions at the central core of this chamber expanded farther upstream from the combustor outlet when the rotating speed was

increased from 5- to 10- and 15-g loading. These phenomena were due to the shift in recirculating flows generated by eddy formation farther upstream to the region adjacent to the primary chamber exit (Figure 5.64). The flows tended to move to near-wall regions with higher rotating speeds. The higher the rotating speed, the higher the degree of swirl in the primary chamber, resulting in the tendency of the gas to diverge and be flung to the wall regions in the secondary chamber upon discharge from the primary chamber. From thereon, the high axial velocity pushed the gas out of the combustor. Hence, combustion products did not reach the central core region, and without the heat source, combustion in this region could not be sustained. Temperature in this region eventually dropped. As a consequence, operating at higher rotating speeds will result in the formation of colder-flow regions at the centre core of the secondary chamber. Nevertheless, the volume of these colder-flow regions in the secondary chamber was considered to be quite small compared to the overall volume of the secondary chamber. This condition is still acceptable and thus does not warrant extra efforts in design improvement to suppress these colder-flow regions.

In determining the optimum rotating speed as bed starting-up procedure for the SFB and also to achieve high rate of CO burnout, the important findings obtained in the modelling of methane combustion were reiterated as follows:-

i) The SFB should be rotated at rotating speeds of more than 10-g loadings to achieve uniform pre-heating of bed materials,
ii) Operating the SFB at rotating speed as low as 5-g loading could result in high rate of CO burnout and emissions level of CO that complied with existing regulations, and
iii) The expansion of the colder flow regions in the secondary chamber when operating at higher rotating speeds might not be detrimental to the overall operation of the SFB due to the relatively smaller volume of these regions compared to the volume of the secondary chamber.

Hence: Therefore, during bed starting-up, the rotating speed recommended for the SFB is in the range of 10- to 15-g loading. For combustion operations, the

SFB could be rotated at as low as 5-g loading and still be able to achieve good CO burnout rate and CO emission level that complied with existing regulations.

5.6.4 Particle Combustion

The combustion of rice husk in the tapered SFB combustor was modelled using the mixture fraction / PDF approach in FLUENT (version 5.5). The mixture fraction / PDF approach enabled the modelling of non-premixed turbulent combustion by solving transport equations for one or two conserved scalars – the mixture fractions. Use of this approach required the preparation of a PDF file with the preprocessor, prePDF (version 3.3). The PDF file contained information that relates species concentrations and temperatures to the mixture fraction values, and was used by FLUENT to obtain these scalars during the solution procedure. Chemical properties of rice husk for preparation of the PDF file were enclosed in Appendix B. The temperature at the onset of rice husk de-volatilisation was set at 275^{o}C, a value obtained from TGA analysis.

5.6.4.1 Thermogravimetric Analysis of Rice Husk

In-depth understanding on the basic mechanisms in rice husk combustion is crucial in attaining high efficiency for its use as an energy source. More importantly, these understandings affect the development of a more precise model at a later stage (Ismail, 1996a; Ismail, 1996b), which appropriately describes the intermediate processes occurring during combustion (Ismail et al., 1997). Accurate characterisation of fuel is significant in the development of optimum design for thermochemical conversion systems that can achieve high conversion, besides ensuring compliance with strict environmental regulations (Mansaray and Ghaly, 1998b). Thermogravimetric analysis (TGA) is used to profile the mass loss due to chemical and physical phenomena when a sample is subjected to high temperature.

a) TGA in a Reducing (Nitrogen) Environment

In general, the combustion profile of rice husk is divided into three stages (Ismail et al., 1997):-

a) Evaporation of moisture content (50 – 150^{o}C),

b) Rapid mass loss (300 – 380^{o}C), and

c) Slow combustion but with ignition (> 400^{o}C).

TGA has been performed on the rice husk samples in this study with a heating rate of 10^{o}C/min from ambient temperature to 800^{o}C, in a reducing environment. The use of an inert gas such as nitrogen serves the purpose of creating an oxygen-free environment required for the pyrolysis process. According to Mansaray and Ghaly (1998a), the rate of thermal degradation and the mass of residue increase as the heating rate is increased.

Referring to the thermogram obtained (Figure 5.65), an initial slight weight loss was observed between ambient temperature and about 100^{o}C. The weight loss could be probably contributed by the elimination of physically absorbed water in the rice husk and superficial or external water bounded by surface tension, and also probably due to the loss of light volatiles. The curve began to flatten out from 100^{o}C to approximately 275^{o}C, incurring very slight weight loss. Majority of the mass loss was in the range of 275 – 375^{o}C, referred to as the active pyrolysis zone. This stage was indicated as the curve of mass loss in the thermogram. Studies (Shafizadeh, 1968; Ramiah, 1970; Koufopanos et al., 1989; Bining dan Jenkins, 1992; Williams dan Besler, 1994; Vargheyi et al., 1994) have strongly proved that this zone could be attributed to the evolution of volatiles that was generated during primary decomposition of hemicellulose and cellulose. A major change in the slope of the TGA could be observed at a temperature of 375^{o}C, indicating the onset of the second reaction zone. This zone ended at a temperature around 500^{o}C, also called the passive zone. Mass loss in this zone was contributed by the conversion of lignin (Shafizadeh, 1968; Ramiah, 1970; Koufopanos et al., 1989; Bining and Jenkins, 1992; Williams dan Besler, 1994; Vargheyi et al., 1994).

At the end of the analysis (800^{o}C), the final mass of the sample (supposedly the ash content) was approximately 30% of the initial mass, which highly disagreed with the ash content of 14.7% obtained from proximate analysis. The discrepancy can be attributed to the presence of materials other than ash, such as char, a carbon skeleton that results after evaporation of hemicellulose, cellulose and lignin (volatiles). The heating environment has an influence on the composition of the final mass. A reducing environment does not allow for complete conversion of chars to take place due to the absence of oxygen required for oxidation. Hence, the final mass in this study consisted of ash and unburnt chars.

Thermal degradation is influenced by the chemical composition of rice husk (cellulose, hemicellulose and lignin) as different lignocellulose components have different thermal characteristics. Studies have shown that decomposition begins with hemicellulose (150 – 350^{o}C), followed by cellulose (275 – 350^{o}C) and lastly lignin (250 – 500^{o}C) (Ramiah, 1970; Shafizadeh dan DeGroot, 1976). Also, it was suggested that the higher the content of cellulose, the higher the rate of organics evaporation (devolatilisation).

According to Mansaray and Ghaly (1998b), thermal degradation of biomass in the active zone occurs in two steps. The first thermal degradation step may be attributed to the decomposition of hemicellulose and initial decomposition of cellulose, while the second step comprises the final decomposition cellulose and initial decomposition of lignin. They further concluded that the components of hemicellulose and cellulose in rice husk played an important role in the evaporation of volatiles, while lignin is responsible in the formation of char.

b) Comparisons of TGA in Reducing (Nitrogen) and Oxidising (Air) Environments

TGA in a reducing environment proved useful in giving important insights into the types of materials (cellulose, hemicellulose or lignin) lost at certain temperature ranges. This was because the evolved volatiles were not immediately oxidised and thus, did not interfere with actual mass loss contributed by each type of materials. However, in actual operations, combustion is usually carried out in an oxidising environment.

In an oxidising environment, a shift in temperature ranges corresponding to each combustion stage was observed. Major weight loss due to the evolution of volatiles and their subsequent oxidation was observed at approximately 230 – 330^{o}C. The char oxidation stage took place at a temperature range of 300 – 500^{o}C (Mansaray and Ghaly, 1998a). Comparing the corresponding temperature for each combustion stage, the onset temperature for devolatilisation in an oxidising environment was found to be lower (~230^{o}C) than that in a reducing environment (~300^{o}C). Similarly, the onset temperature for char combustion was found to be lower (~300^{o}C) compared to more than 400^{o}C for a reducing environment. This can be attributed to the presence of oxygen in the former case, which aided in the faster ignition of char particles. Oxidation in a reducing environment was only supported by atomic oxygen present as part of the chemical built of rice husk.

Beyond 700^{o}C, no further weight loss was observed in a TGA carried out in an oxidising environment (Mansaray and Ghaly, 1998a). The final mass obtained consisted only of ash and not a combination of ash and unburnt chars, due to the complete oxidation of chars in the presence of sufficient oxidising agent.

5.6.4.2 Biomass Particle Combustion

a) Mechanism of Biomass Combustion

The three stages involved in the combustion of biomass are (i) devolatilisation to char and volatiles, (ii) combustion of volatiles and (iii) combustion of char. During the devolatilisation stage, oxygen- and carbon-rich gases, mainly carbon monoxide (CO) are released and the process is rapid due to the low calorific nature of these biomass volatiles. In fluidised bed combustion, the combustion process was widely believed to be limited by the char oxidation stage (Kulasekaran et al., 1998) as the conversion of carbon to CO_2 generates three times the heat released in comparison to its conversion to CO. Due to their porous and highly disordered carbon structure, chars from biomass are the most reactive of technical carbon materials (Henrich et

al., 1999). Apart from the highly microporous structure, their relatively high ash and oxygen contents also results in a quicker burnout than analogous coal char. Ignition temperatures of biomass chars are also shorter compared to coal chars as biomass volatiles contain mainly CO, while coal volatiles contain a large amount of tar. Complete combustion of biomass chars can be achieved in temperatures of more than 377^{o}C (650 K) given sufficiently long residence time of solid. According to Di Blasi et al. (1999) in his study on the reactivities of biomass chars in air, the temperature for complete conversion of wheat straw chars was 517^{o}C while the ignition temperature was as low as 146^{o}C. However, a temperature of 385^{o}C was necessary to achieve the maximum combustion rate. Rice husk has similar properties as wheat straw, as can be seen in Table 5.4. The relatively low conversion temperature for biomass chars are also observed by Henrich et al. (1999). In their char incineration tests in a small rotary kiln facility, complete char burnout could be attained at temperatures down to approximately 600^{o}C.

Table 5.4: Chemical properties of wheat straw and rice husk

Parameter	Wheat Straw*	Rice Husk[#]
Proximate Analysis (%)		
Moisture	8.0	10.1
Volatile Matter	71.7	64.1
Fixed Carbon	15.1	11.1
Ash	5.2	14.7
Ultimate Analysis (% dry-ash-free)		
Carbon (C)	47.7	45.2
Hydrogen (H)	6.0	6.0
Oxygen (O)	44.0	48.1
Nitrogen (N)	0.5	0.7
Calorific Value (MJ/kg)	19.25	17.7

Note: * - Jones et al. (2000)

[#] - from analysis

b) Controlling Factor in Particle Combustion

Depending on the combustor operating conditions, particle combustion may be controlled by chemical reaction or transport phenomena. At low temperatures, chemical reaction is a dominating factor but not at high temperatures, where chemical kinetics are fast. At high temperatures, intra- and extra-particle mass transfer resistance of the oxidising agent plays a major role in determining the combustion rate. Combustion at these high temperatures regime, therefore, is diffusion limited. It has been noted by Dutta and Wen (1977) through Di Blasi et al. (1999) that for coal chars, combustion is diffusion limited for temperature above 650^{o}C. It is expected that the temperature regime for diffusion-limited combustion of biomass chars is lower as they are more reactive due to their more porous structure.

c) Char Combustion Mechanisms

The resulting chars from the devolatilisation stage still contain some residue volatile matters. Considering the close similarity in chemical properties between rice husk samples in the study and wheat straw from literature (Jones et al, 2000), it can be assumed that rice husk chars also possessed the same chemical properties as wheat straw chars. In their study using the Functional-Group, Depolymerisation, Vaporization, Cross-Linking (FG-DVC) pyrolysis model, it was predicted that wheat straw chars consisted of 68.17% C, 15.12% H, 2.9% N and 13.91% O (dry-ash-free basis). Hence, as the combustion of char progressed, some weight loss can be attributed to the devolatilisation of these residual volatile matters (H and O). According to Wornat et al. (1995), the char combustion stage can be split into three further steps:-

i) devolatilisation of residue volatiles
ii) slight release of H and O accompanied by several inorganic transformations
iii) loss of other organic elements (C and N)

The first char combustion step corresponded to the loss of large amounts of H and O. This can be attributed to the release of volatiles (eg CO, CO_2, H_2O and

other gases) resulting from the breakdown of weaker bonds within the char structure. In addition, the volatiles released were found to consist primarily of CO, CO_2 and H_2O, and not hydrocarbons due to the absence of visible volatile flame.

At the second char conversion step, steady but less dramatic release of H and O continued. Several inorganic transformations took place, such as the vaporisation of metals (particularly Na and K) as well as surface migration and coalescence of these metals. Beyond a char conversion step of 50%, more drastic mass change was observed due to the steady losses of C and N. The carbon-oxygen reaction during this step was proposed by Hurt and Calo (2001) to proceed according to a three-step semi-global mechanism:-

Adsorption	:	$C + O_2 \rightarrow 2\ C(O)$
Surface reaction	:	$C(O) + O_2 \rightarrow CO_2 + C(O)$
Desorption	:	$C(O) \rightarrow CO$

5.6.4.3 Modelling of Rice Husk Particle Combustion in the SFB Combustor

The objective of the modelling study was to investigate the effects of combustor temperature and rotating speed on the combustion characteristics of rice husk particles. In actual, the heat of combustion evolved during the burning of rice husk particles in the SFB is stored in the sand bed, which functioned to sustain combustion by continuously igniting the incoming fresh feed. However, simulation of a fully bubbling fluidised bed required the use of the multiphase Eulerian (continuum) models, which are not available in the current version (5.3 and 5.5) of the FLUENT program code. Different from the Langrarian (discrete particle) models used in tracking individual particle trajectory in a modelling domain (Section 6.6.2), the Eulerian models consider all phases to be continuous and interpenetrating. Hence, to investigate the rice husk combustion characteristics in the SFB, several simplifications and assumptions made in the modelling study were:-

i) The temperature inside the SFB was assumed to be more or less uniform at a certain value of interest after accounting for heat loss to the surrounding (at approximately 20%, according to the first approximation factor of 0.80 for heat loss to the surrounding suggested by Gaydon and Wolfhard, 1979) by manipulating the air factors. Since a fluidised bed could not be simulated in FLUENT to retain the heat of combustion, the air feed temperature was designated at that value of interest to approximate the uniform temperature inside the combustor,

ii) The composition of gases in the air feed corresponded to that of the air factors used in order to approximate the actual gaseous components that are present in the combustor during the combustion process, and

iii) Only the combustion profile of a discrete particle was tracked.

Having a U_{mf} value of 0.5 m/s (Hao Liu et al., 1995), the sphericity, ϕ_s of the rice husk particles was found to be 0.19. Also the volume-surface mean diameter was calculated to be 1.6 mm (Mansaray and Ghaly, 1997). The air factors to reach a certain operating temperature inside the SFB and the corresponding gaseous components to be used in FLUENT were pre-determined using the FLAME program code.

a) Effect of Temperature on the Quality of Rice Husk Ash

Operating temperatures in the SFB for combustion of rice husk were restricted to the range of 500 – 700^{o}C. A temperature of at least 500^{o}C was required for the complete oxidation of chars (Di Blasi et al., 1999). The range of temperature investigated was also limited to less than 700^{o}C to prevent structural changes to the resulting ash. As cited by Lin et al. (1998), Kaupp (1984) and Schiefelbein (1989) had indicated in their previous studies that physical structural transformation of silica from its original amorphous state to a crystalline state occurs should the oxidation of rice husks be carried out at a temperature beyond 700^{o}C (973 K). Residual carbons will be encapsulated inside the crystallised silica, making the combined carbon unavailable for further oxidation reactions even at higher temperatures. Furthermore, the combustion of rice husk should be complete at

700^{o}C as TGA results (in an oxidising environment) (Mansaray and Ghaly, 1998a) showed that no further mass changes took place beyond this temperature.

Hence: Temperature range selected for the investigation of rice combustion characteristics in the SFB was 500 – 700^{o}C.

b) Effect of Combustor Temperature

To study the effect of combustor temperature on the combustion characteristics of rice husk particles, the rotating speed of the SFB was held constant at 122 RPM (5-g loading). The combustor temperature was maintained at 500^{o}C, 600^{o}C and 700^{o}C after accounting for heat loss to the surrounding (~20%) while the air inputs in all cases were that sufficient to yield a fluidising velocity of 2.5 U_{mfc} at the distributor plate or 3.5 U_{mfs} at the bed surface (bed height = 0.15 m). The rice husk particles were assumed to be ejected to the freeboard region in the SFB combustor by bubble eruption at the bed surface.

From Figures 5.66 – 5.68, it could be observed that the duration for the complete combustion of rice husk particles were significantly reduced as the temperature in the combustor was increased from 500^{o}C to 600^{o}C and 700^{o}C. Conversion in the figures was defined as the change in particle mass at time *t* divided by the initial mass of the particle. It only took less than 0.50 min (27 s) (Figure 5.68) for the particles to complete the devolatilisation and char combustion stages when the combustor temperature was maintained at 700^{o}C. This was in contrast with the duration of 1.35 min (81 s) at 600^{o}C (Figure 5.67) and 5.88 min (353 s) at 500^{o}C (Figure 5.66), a significant reduction of 3 times and 13 times respectively. Rapid and complete combustion of particles in the SFB is paramount to its operation by ensuring that the heat evolved maintains the bed temperature, besides preventing the bed temperature from dropping too low, which will subsequently quench the combustion process. Moreover, accumulation of feed that will subsequently reduce the freeboard volume can be prevented.

It was also observed from Figure 5.66 that at 500^{o}C, the duration for the release of volatiles (241 s) was approximately two times higher than the duration for

the burnout of char (110 s). This can be attributed to the fact that the combustion of high-volatile content materials such as rice husk is heat transferred-controlled. Hence, it is vital that the temperature inside the combustor is sufficiently high to allow for the devolatilisation process to occur. From the TGA analysis, the release of volatiles from rice husk took place at a temperature between 275^{o}C and 375^{o}C, while char burning took place beyond 375^{o}C (Figure 5.65). The combustor temperature at 500^{o}C therefore, was sufficient to allow for the complete combustion of rice husk to occur, albeit very slowly in which the rate of devolatilisation was controlling. When the temperature inside the combustor was increased (600^{o}C and 700^{o}C), the rate of char burnout, in turn become the dominating factor. Similar to high carbon-content materials such as coal, the burnout of the resulting char particles is controlled by the mass transfer of oxygen into and around the char particles (diffusion limited). At 600^{o}C and 700^{o}C, the temperatures were high enough as to allow for fast chemical kinetics to occur. The rate of char burnout, hence was limited by the rate at which the oxidant was brought into contact with the surface of the char particles. In other words, the combustion process was diffusion limited, whereby heterogeneous mixing of the gaseous oxidant and solid char particles was crucial. This explained the longer duration of char burnout compared to devolatilisation experienced in the SFB combustor operating at temperatures above 600^{o}C. Another feature observed from the combustor operating at more than 600^{o}C was that temperature no longer exerted a strong influence on the rate of char-burnout. The reduction in char burnout time from 600 – 700^{o}C was not as high as that from 500 – 600^{o}C (Figure 5.69) primarily because the mixing process inside the combustor limited the rate of char burning. Thus, it was expected that the drop in char burnout time will be insignificant even if the combustor temperature was increased beyond 700^{o}C unless other operating conditions were changed. To prove this point, the combustor temperature was increased to 800^{o}C for the same operating conditions. As can be seen from Figure 5.69, the reduction in combustion reaction time was very little from 700^{o}C to 800^{o}C. The combustion reaction time tend to reach a plateau beyond the temperature of 700^{o}C.

Hence: At the same operating conditions (rotating speed = 5-g loading @ 122 RPM, air feed rate = 3 U_{mfc}), the reduction in combustion reaction time was very huge with the increase in combustor temperature from 500^{o}C to 600^{o}C. Beyond

600^{o}C, the decrease in combustion reaction time was insignificant due to diffusion-controlled reactions.

c) Effect of Combustor Rotating Speed

In the study of the effect of rotating speed, the combustor temperature was held constant at 700^{o}C while the rotating speed was varied from 122 to 211 RPM (to give g-loadings of 5- to 15-g). The value of 700^{o}C was chosen as at this temperature, chemical kinetics are fast, thus rendering the combustion rate to be diffusion-controlled.

The temperature and conversion profiles of rice husk particles were presented in Figures 5.70 – 5.72. Meanwhile, from Figure 5.73, there appeared to be an optimum rotating speed for reduction in combustion reaction time for the rice husk particles. The duration for devolatilisation remained more or less the same (~10 s) for all rotating speeds. The rate of turbulence inside the combustor due to the increase in swirl projected no influence at all to the rate of devolatilisation. This can be attributed to the nature of the devolatilisation process, which is strongly affected by temperature only. However, the duration for char combustion increased beyond a rotating speed of approximately 170 RPM, and this contributed to the overall increase in combustion reaction time. The duration of char combustion was expected to be dominating over the duration of devolatilisation when operating at a temperature of 700^{o}C, in which the reaction was diffusion-limited with respect to char burning. The existence of the optimum point was expected as in all swirling-flow combustions, there appeared to be an optimum swirl intensity at which the combustion reaction time was minimal. In their studies of swirling combustion of pre-mixed natural gas in air, Zhang and Hill (1996) also proved that low to moderate swirl was beneficial to combustion reaction time while excessive swirl led to increment in combustion reaction time.

Also apparent from Figure 5.73 was the observation that the increase in combustion reaction time became more pronounced at high swirl conditions.

Referring to Figure 5.72, one possible explanation was that at high swirl, there might be augmented heat transfer between the particle and the hot gases in the combustor. This effect might subsequently lead to the drop in temperature of the char particle to the vicinity of 650^{o}C for a period of approximately 6 s. Taking the conventional assumption that rice husk chars have a cut-off temperature between kinetic-controlled and diffusion-controlled combustion of 650^{o}C (similar to coal chars), it was speculated that the combustion of rice husk chars (in the SFB combustor rotating at 211 RPM) entered the regime whereby chemical kinetics were slow. The rate of char combustion, then, was kinetically-controlled until the temperature of the char particles increased back to 700^{o}C as combustion progressed and heat was released within the char particles. Although the period of kinetic-controlled combustion signified only about one-third of the total char burning duration at this high swirl conditions, it should be noted that the same period represented a significant one-half of the total char burning duration (~13 s) at lower swirls. Also, in between the low-temperature band, some combustion time was somehow lost in order for the temperature of the char particles to drop and then to increase again. Excessive swirl in the SFB combustor, therefore, was detrimental to the combustion of rice husk particles by significantly increasing the combustion reaction time.

Hence: Operating the SFB beyond 10-g loading (173 RPM) @ 700^{o}C resulted in the increase of combustion reaction time of rice husk.

Investigations on both the effects of combustor temperature and rotating speed on the combustion characteristics of rice husk particles showed that the combustion reaction time was reduced from 5.88 minutes at 500^{o}C to 1.33 minutes at 600^{o}C, representing a significant reduction of approximately 4.4 times. Further increase in temperature to 700^{o}C led to a lower reduction in combustion reaction time (to 0.44 minutes) due to diffusion-controlled reactions. Also, operating the combustor beyond a rotating speed of 173 RPM (10-g loading) at 700^{o}C resulted in the increase in combustion reaction time from a minimum of 24.5 s at 173 RPM to 31.3 s at 211 RPM (15-g loading). Hence, in actual operation for burning of rice husk particles, the SFB combustor should be operated at a temperature range of 600 – 700^{o}C and a rotating speed of less than 10-g loading.

CHAPTER VI

COMMISSIONING AND DELIVERY OF THE DEVELOPED SFB COMBUSTOR

6.1 Commissioning of the SFB Combustor System Components

Preliminary test-runs on the developed SFB combustor system was performed at the fabricator's premises on 24th to 25th July 2002 in order to assess the functionality of the system as specified in the tender document (Appendix A). Due to space and power limitations at the laboratory where the system is supposed to be delivered (Block N12 of Faculty of Chemical Engineering & Natural Resources Engineering, UTM Skudai, Johor), the test-runs were conducted at the fabricator's premises, as shown in the footages included in Attachment I. In general, operations of the major components of the SFB prototype, such as:-

a) Spinning bed
b) Screw conveyor unit
c) Main blower unit with air heating
d) Secondary blower unit
e) Temperature monitoring in the primary chamber
f) Liquefied Petroleum Gas (LPG) Flame Pilot Burner

complied with the requirements specified in the tender document. The full operational functions of the system, however, can only be assessed once proper experimental works on the system commences. Since the scope of the current

research is for the design and development of the prototype SFB combustor, the performance of the system during actual cold and hot commissioning, therefore, is subjected to future research works. The major components of the SFB prototype were shown in Plates 6.1 to Plate 6.9.

6.2 Delivery of the SFB Combustor System

The prototype of the SFB combustor system was delivered to the Faculty of Chemical Engineering & Natural Resources Engineering, UTM Skudai, Johor on 27th August 2002. As mentioned earlier, due to space limitations at Block N12, the SFB combustor was placed at Makmal Kerja Berat (Block N10) pending the construction of a new laboratory building to accommodate the rig for future experimental works. Footages of the SFB delivery to UTM premises were included in Attachment II.

CHAPTER VI

CONCLUSIONS AND RECOMMENDATIONS

7.1 Conclusions

7.1.1 The Developed SFB Combustor Design

The prototype of the tapered horizontal SFB combustor was designed to consist of a cylinder (ID 600 mm × 800 mm) partitioned into two sections - the primary chamber and the secondary chamber. The primary chamber (300 mm in length) will house the fluidised bed while the secondary chamber (500 mm in length) was meant to ensure complete combustion in the gas phase and as a particulate control device. The whole combustor is to be rotated co-axially on the horizontal axis. The end walls of the primary chamber were tapered at 60^o (measured horizontally) to equalise the non-uniform radial bed fluidisation inherent in centrifugal beds. A centrifugal bed fluidised layer by layer from the inner surface outward. Tapering these end walls significantly increase the value of F_R (ratio of the number of U_{mfc} near the SFB wall to the number of U_{mfs} at the bed surface) from approximately 0.3 in an untapered bed to nearly one (1) for a bed depth of 150 mm. A minimum fluidising velocity of 2 U_{mfc} or 3 U_{mfs} are required in order to establish sufficient turbulence inside the bed. For the proposed SFB dimensions, the tapering angle and bed depth were found to be optimum at 60^o and 150 mm, respectively while simultaneously maintaining the desired fluidising conditions and ensuring that the air feed requirements were within operational capability of the blower unit. The

maximum operating speed applicable to the SFB is limited by the fluidising air feed that could be supplied by the blower and the temperature inside the combustor. The choice of the present combustor geometry was based on optimisation on the complex combinations of the operating conditions (air feed, rotating speed) and the rig dimensions during ambient and combustion studies. The SFB could be rotated up to 15-g loadings (211 RPM) during cold runs but during hot runs, the rotating speed could be increased further (depending on the combustor temperature) with the same amount of air due to volume expansion of gas. The bed height, chosen at 150 mm, occupies approximately 40% of free volume in the primary chamber (of 0.044 m^3). This bed height accounted for one half of the chamber radius, thus ensuring the sufficient freeboard region for bed expansion during fluidisation and combustion of evolved volatiles.

7.1.2 Computational Fluids Dynamics Modelling on the Developed SFB Combustor

7.1.2.1 Hydrodynamics in the SFB Combustor

Results from CFD modelling showed that there existed zones of recirculating flows at the entrance of the secondary chamber. These dead zones could lead to the formation of products of incomplete combustion that results in emission of volatile organic compounds. Observation to the particle trajectories indicated that particles with sizes of more than 25 μm were retained inside the primary chamber of the RFB up to air feed rates of 3 U_{mfc}. Since most of the rice husk ash consists of particles more than 20 μm, it is expected that all the ash will be retained in the bed. These ash, which spills over to the secondary chamber once the bed thickness exceeds the height of the rear tapered section (also called the weir plate lip), will impact the wall and be deposited. This phenomenon is due to the saltation velocities of the ash particles being higher than the velocities of airflow inside the secondary chamber. Therefore, holes incorporated that the circumference of the secondary chamber wall allows for the escape and subsequent collection of these ash. Particles of sizes more

than 1 mm were rapidly returned to the bed due to higher momentum and hence, aided in the transfer of heat from the freeboard region back to the bed as they were ejected from the bed surface. Finer particles (< 25 μm) were observed to be blown out of the primary chamber with air inputs exceeding 3 U_{mfc}. This helped in separating fines (sand, ash or char) that were generated during the constant attrition among these particles during fluidisation. The bed will behave erratically with the presence of large amounts of fines due to the interparticle forces between them. Tapering the primary chamber of the RFB was also beneficial to combustion of premixed gas mixtures. Flame could be sustained inside the combustor even for inlet mixture velocities far exceeding the normal flame velocity due to the progressive reduction in velocity as the mixture moved radially inwards. Rotating the tapered RFB at higher speeds increased the combustion intensity and the rate of CO burnout. The rate of flow recirculation and turbulence increased when operating at higher rotating speeds. The higher degree of recirculating flows recirculated the combustion products and the heat evolved more rapidly to continually re-ignite the oncoming unburnt mixture, resulting in more intense combustion. More rapid mixing between reactants and oxidants at higher rotating speeds also led to a higher rate of CO burnout and subsequently a reduction in CO emission level in the RFB outlet.

7.1.2.2 Optimum Operational Range for Combustion of Rice Husk

The optimum operating temperature for combustion of rice husk was in the range of 500 – 700^{o}C. In fluidised bed applications, the combustion was widely believed to be limited by the char combustion stage. The minimum temperature of 500^{o}C was required for the complete combustion of chars while 700^{o}C was the highest temperature for the combustion of rice husk if the undesirable physical transformation of the resulting ash from an amorphous to crystalline state is to be prevented. For combustion of rice husk in the RFB, the combustion reaction time was observed to be significantly reduced as the temperature in the combustor was increased from 500^{o}C to 600^{o}C (from 5.88 minutes to 1.33 minutes). Beyond

600^{o}C, chemical kinetics were fast and the reduction in combustion reaction time was not as significant (combustion reaction time reduced to only 0.44 minute at 700^{o}C). Combustion of rice husk at these temperatures was diffusion-controlled. The combustion reaction time was also found to be increasing when the RFB were operated at g-loadings in the excess of 10-g (173 RPM). At higher swirls (> 10-g loadings), some degree of quenching was observed on the particle due to augmented heat transfer between the particles and the hot gases. This might cause the char-burning reactions to be kinetically-controlled for a certain period of time until the heat evolved increased the temperature of the particle and shifted the reactions to the diffusion-controlled regime.

7.1.2.3 Recommendations for Design Improvement

During modelling studies on the prototype of the RFB combustor, a number of design and operational problems had been identified. The modelling results provided a guide for specific modifications to the current design of the prototype. Several recommendations to improve the design of the RFB combustor are as follows:-

a) Inclusion of baffles

Near the primary chamber exit, zones of recirculating flows were formed due to the sudden expansion of swirling gases from the tapered outlet of the primary chamber. In actual combustion operations, particles such as ash could be trapped in these zones and therefore could not be removed. Modelling results showed that the inclusion of four internal baffles (500 mm long, 5 mm thick) placed co-centrally and 90^{o} apart from each other on the secondary chamber wall could reduced the degree of recirculating flows in these zones to the extent whereby particles were no longer trapped. The presence of baffles with width ranging from 50 to 100 mm was successful in breaking eddies formed near the primary exit. However, baffles with width of 50 mm were found to increase the degree of swirling and residence time of

gases in the secondary chamber. Hence, the efficiency of gas-phase combustion in this chamber could be increased.

b) Reducing the rear tapering height at the primary chamber

The initial designation of the tapering height at both ends of the primary chamber at 225 mm resulted in two operational problems. Firstly, the bed might be too thick due to the ash accumulation during the combustion process before the ash layer at the top of the bed spills over to the secondary chamber. Secondly, there is a possibility of the ash layer spilling over into the piping for secondary air at the front end of the primary chamber and resulted the obstruction of secondary airflow. Therefore, it is recommended that the tapering height at the rear tapered section be reduced to 200 mm so that the ash could spill over once the bed thickness increased from 150 mm to 200 mm. Moreover, the spillover of ash from the front end of the tapered section could be prevented.

c) Rotating the RFB at two different speeds

The limitation of operating the current design of the RFB is the amount of air input to the primary chamber that could be supplied by the blower unit to fluidise the bed media, which in turn, is determined by the rotating speed. Operating the RFB at higher rotating speeds no doubt improved gas-phase combustion in the secondary chamber, but that necessitates higher air feed to fluidise the bed which is beyond the capacity of the blower. Modifications could be made by rotating the RFB at different speeds (co-axially). The secondary chamber could be rotated at very high speeds (up to 1000 RPM) without any influence to the fluidising state in the primary chamber that is rotated at a lower speed. Computer simulations showed CO emission levels in the exhaust gases were lowered by several times for a RFB operating at two different speeds (15-g loading primary chamber, 30-g loading secondary chamber) compared to a RFB operating at only one speed (15-g loadings for primary and secondary chambers).

7.1.3 Commissioning and Delivery of the SFB Combustor

The prototype of the SFB combustor system was successfully delivered to the premises of Universiti Teknologi Malaysia, Skudai after being commissioned at the fabricator's premises. Due to limitations of space and power requirements at the laboratory, preliminary cold and hot experimental works could not be performed on the prototype. Nonetheless, the functionality of the system had been proven and the performance of the system will be subjected to future experimental works, which are not included in the current research scopes.

7.2 Recommendations for Future Research Works

Several recommendations for future study on the developed tapered horizontal RFB rig are as follows:-

a) Cold commissioning

Cold commissioning on the developed RFB rig should be carried out to investigate its operational capability as designed, such as the applicable rotating speeds and fluidising air inputs. Determination of the basic hydrodynamics of the rig (minimum fluidising velocities, pressure drops, bed thicknesses, fluidisation phenomena) should also be carried out and the results compared with theoretical values. The information obtained from this study will provide a better understanding on the behaviours and the optimum operating parameters of the RFB rig before the more complicated combustion study is carried out.

b) Hot commissioning

Hot commissioning on the RFB rig include the determination of bed starting-up procedures and combustion characteristics of rice husk. Apart from investigating the suitable procedure for bed starting-up and the optimum operating parameters applicable for rice husk combustion in the rig, the study should also covered

performance study (the determination of combustion efficiency, analysis of resulting ash which will indicate the degree of char burning in the RFB, flue gas emissions). Results from CFD modelling obtained from the current research such as the range of rotating speeds and combustor temperatures applicable for good combustion characteristics of rice husk in the RFB rig should be used as a basis for the proposed combustion study.

c) Combustion of different types of waste materials

Apart from the combustion of rice husk, combustion of other types of waste such as palm waste, municipal solid waste (MSW) and sludge could be carried out in the RFB rig to study its versatility in burning different types of waste. In-depth combustion study (determination of optimum operating parameters and combustor performance) such as those proposed for the combustion of rice husk could be extended to these types of waste. The suitable operating mode (starved or excess air conditions) in burning different types of wastes should first be determined based on mass and energy balances.

d) CFD modelling on the formation of pollutants such as NO_x and soot

Computational fluids dynamics modelling could also be carried out to determine the levels of pollution emissions from the developed RFB when operating at various operating conditions (rotating speeds, fluidising air inputs, temperatures) and while burning different types of waste. Results from the proposed modelling study could provide insights into the conditions inside the rig leading to the formation of pollutants such as NO_x (thermal NO_x, fuel NO_x, prompt NO_x) and soot. These conditions include the formation of hot-spots, incomplete combustion of particles and low particle residence time due to high air inputs.

e) Development of air pollution control (APC) systems

Results from combustion studies and CFD modelling on the levels of pollutant emissions during combustion of different types of waste in the RFB rig could be utilised in the selection of appropriate APC device to mitigate the pollution

problems. This work includes the design of the APC device and perhaps the determination of the effectiveness of the proposed device in mitigating the levels of pollutants through CFD modelling.

f) Energy recovery

Heat evolved from the combustion of different types of waste in the RFB rig could be targeted for energy recovery. Experiments and simulation studies should be carried out to determine the optimum design of the heat recovery system and the optimum operating parameters for efficient energy recovery.

g) Techno-economic evaluation

The determination of the economics of the developed RFB technology and its feasibility for commercialisation should also be conducted.

REFERENCES

Bining, A. S. and Jenkins, B. M. (1992). "Thermochemical reaction kinetics from rice straw from an approximate integral technique." *ASAE Paper*. **No. 92-6029**. St. Joseph, MI.

Botterill, J. S. M.; Teoman, Y. and Yuriger, K. R. (1982). "The effect of operating temperature on the velocity of minimum fluidisation bed voidage and general behaviour." *Powder Technology*. **31**. pp 101 – 110.

Boubel, R. W. and Junge, D. G. (1971). "A study of fluidised bed filter subjected to high radial acceleration." *AIChE Symp. Series*. **69**. No. 128. pp 138 – 141.

Broughton, J. (1975). "Gas combustion in shallow fluidised beds." *Applied Energy*. **1**. pp. 61 – 79.

Broughton, J. and Elliott, D. E. (1975). "Heat transfer and combustion in centrifugal fluidised beds." *Inst. Chem. Eng. Symposium Series*. **No. 43**. pp 11-1 to 11-5.

Brown, G. E.; Farkas, D. F. and De Marchena, E. S. (1972). "Centrifugal fluidised bed." *Food Technology*. **Dec**. 1972. pp 23 – 30.

Brown, G. G. (1950). "Unit Operations." New York: Wiley.

Caram, H. S.; Efes, Z. and Levy, E. K. (1984). "Gas and particle motion induced by a bubble eruption at the surface of a gas fluidized bed." *AIChE Symposium Series*. **80** (234). pp 103 – 106.

Chalchal, S.; Sheehan, T. V. and Steinberg, M. (1974). "Coal combustion and desulphurisation in a RFB reactor." *BNL Report*. **No. 19308**.

Chan, C. K.; Loesel Sitar, J. L.; Beauvais, R. and Mayinger, F. (1996). "Modelling maximum flame speeds." *Nuclear Engineering and Design*. **166**. pp 463 – 469.

Chen, Y.M. (1987). "Fundamentals of a Centrifugal Fluidized Bed." *AIChE Journal*. **Vol. 33**. No. 5. pp 722 – 728.

Chevray, R.; Chan, Y. N. I.; and Hill, F. B. (1980). "Dynamics of bubbles and entrained particles in the rotating fluidized." *AIChE Journal*. **26**. No. 3. pp 390 – 398.

Chevray, R.; Chan, Y. N.I. and Hill, F. B. (1980). "Dynamics of bubbles and entrained particles in the rotating fluidized bed." *AIChE Journal*. **Vol. 26**. No. 3. pp 390 – 398.

Cohen, J. S. and Yang, T. C. S. (1995). "Progress in food dehydration." *Trends in Food Science & Technology*. **Vol. 6**. pp. 20 – 25.

Demircan, N. (1979). "Rotating Fluidized Bed Combustion." University of Sheffield: PhD Thesis.

Di Blasi, C.; Buonanno, F. and Branca, C. (1999). "Reactivities of some biomass chars in air." *Carbon*. **Vol. 37**. Issue 8. pp 1227 – 1238.

Dutta, S. and Wen, C. Y. (1977). "Reactivity of Coal and Char Em Dash 2. In Oxygen-Nitrogen Atmosphere." *Ind Eng Chem Process Des Dev*. **Vol. 16**. Issue 1. pp 31 – 37.

Edisham Mohd Sukor (1999). "Pemisahan Partikel Abu Sekam Padi Dengan Menggunakan Siklon." Universiti Teknologi Malaysia, Skudai: Final Year Dissertation.

Elperin, I. T.; Zabrodsky, S. S.; Yefremtsev, V. S. and Mikhailik, V. D. (1967). Collected papers on "Intensification of transfer of heat and mass in drying and thermal processes." *Nauka i Tekhnika*. **232**. Minsk: BSSR.

Environment Agency (1996). "Integrated Pollution Control (IPC) Guidance Note, Series 2 (S2): Waste Disposal and Recycling Sector, S2 5.01: Waste Incineration." London: IPC S2 5.01

Ergun, S. (1952). "Fluid flow through packed bed column." *Chem. Eng. Progress*. **48.** pp 89 – 94.

Fan, L. T. (1978). "Fluidization Bed Combustion in Centrifugal Field." *Energy Communications*. **4** (6). pp. 509 – 512.

Fan, L. T.; Chang, C. C.; and Yu, Y. S. (1985). "Incipient fluidization condition for a centrifugal fluidized bed." *AIChE Journal*. **31**. No. 6. pp 999 –1009.

Farkas, D. F.; Lazar, M. E. and Butterworth, T. A. (1969). "The centrifugal fluidised bed." *Food Technology*. **23**. pp 125 – 156.

Felder, R. M. and Rosseau, R. W. (1978). " Elementary Principles of Chemical Processes." USA: John Wiley & Sons, Inc.

FLUENT 5 User's Guide. (1998). Fluent Incorporated, Centerra Resource Park, 10 Cavendish Court, Lebanon NH 03766.

Gaydon, A. G. and Wolfhard, H. G. (1979). "Flames: Their Structure, Radiation and Temperature." **4th Ed**. London: Chapman and Hall.

Geldart, D. (1972). "The effect of particle size and size distribution on the behaviour of gas-fluidized beds." *Powder Technology*. **6**. pp 201 – 215.

Geldart, D. (1973). "Type of gas fluidization." *Powder Technology*. **7**. pp 285 – 292.

Haider, A. and Levenspiel, O. (1989). "Drag Coefficient and Terminal Velocity of Spherical and Nonspherical Particles." *Powder Technology*. **58**. pp 63 – 70.

Hanjalic, K. (19947). “Advanced turbulence closure models, a view of current status and future prospects.” *International Journal of Heat and Fluid Flow*. **15** (3). No 3. pp 178.

Hao Liu, Zhijie Lin, Dechang Liu and Weiheng Wu. (1995). “Combustion Characteristics of Rice Husk in Fluidised Beds.” *Fluidised Bed Combustion*. **Vol. 1**. pp 615 – 618.

Hatch, L. P.; Regan, W. H. and Powell, J. R. (1960). “Fluidised bed for rocket propulsion.” *Nucleonics*. **18**. No. 12. pp102.

Henrich, E.; Bürkle, S.; Meza-Renken, Z. I. And Rumpel, S. (1999). “Combustion and gasification kinetics of pyrolysis chars from waste and biomass.” *Journal of Analytical and Applied Pyrolysis*. **49**. pp 221 – 241.

Hong, J.; Shen, Y. and Tomita, Y. (1995). “Phase diagrams in dense phase pneumatic transport”. *Powder Technology*. **84**. pp 213 – 219.

Houthon, J. (1993). “Royal commission on environmental pollution, seventeenth report: incineration of waste.” London: Her Majesty Stationery Office.

Howard, J. R. (1989). “Fluidized Bed Technology.” New York: Adam Hilger.

Huang, S.; Jing, S.; Wang, J. F.; Wang, Z. W and Jin, Y. (2001). “Silica white obtained from rice husk in a fluidized bed.” *Powder Technology*. **117**. pp 232 – 238.

Hunt, C. H. and Brennan, D. (1965). *Aust. Chem. Eng*. March 9.

Hurt, R. H. and Calo, J. M. (2001). “Semi-global intrinsic kinetics for char combustion modeling.” *Combustion and Flame*. **125**. pp 1138 – 1149.

Ishizuka, S. (1990). *Combust. Flame*. **82**:176.

Ismail, A. F. (1996a). "Modelling of char structure influence on the self-ignition temperature during coal gasification." *In Proceedings of First Trabzon International Energy and Environmental Symposium*. pp 721 – 726. Trabzon, Turkey.

Ismail, A. F. (1996b). "2-D and 3-D Cellular models using erosion and dilation: Development and applications." *Malaysian Journal of Computer Science*. **9**. pp 18 – 24.

Ismail, A. F.; Yusaf, T. F.; Mahdi, F. M. A. dan Shamsuddin, A. H. (1997). "Combustion Processes of Rice Husk For Energy." *RERIC International Energy Journal*. **Vol. 19**. No. 2.

Jones, J. M.; Pourkashanian, M.; Williams, A. and Hainsworth, D. (2000). "A comprehensive biomass combustion model." *Renewable Energy*. **19**. pp 229 – 234.

José, M. J. S.; Olazar, M.; Aguado, R.; and Bilbao, J. (1996). "Influence of the conical section geometry on the hydrodynamics of shallow spouted beds." *Chemical Engineering Journal*. **62**. pp. 113 – 120.

Kagan, L. and Sivashinsky, G. (2000). "Flame propagation and extinction in large-scale vortical flows." *Combustion and Flame*. **120**. pp 222 – 232.

Kao, J.; Pfeffer, R. and Tardos, G. I. (1987). "On partial fluidisation in rotating fluidizing beds." *Powder Technology*. **33**, No. 5. pp 858 – 861.

Kaupp, A. (1984). "Gasification of Rice Hulls: Theory and Practices." Eschborn: Deutsches Zentrum Fuer Entwicklungs Technologien (GATE).

Khoshnoodi, M. and Weinberg, F. J. (1978). "Combustion in Spouted Beds." *Combustion and Flame*. **33**. pp 11 – 21.

Koufopanos, C. A.; Maschio, G. and Lucchesi, A. (1989). "Kinetic modelling of the pyrolysis of biomass and biomass components." *Canadian Journal of Chemical Engineering*. **67** (1). pp 75 – 84.

Kroger, D. G.; Levy, E. K. and Chen, J. C. (1979). "Flow characteristics in a packed and fluidized rotating beds." *Powder Technology*. **24**. pp 9 – 18.

Kulasekaran, S.; Linjewile T. M.; Agarwal, P. K. and Biggs, M. J. (1998). "Combustion of a porous char particle in an incipiently fluidized bed." *Fuel*. **Vol. 77**. No. 14. pp 1549 – 1560.

Kunii, D. and Levenspiel, O. (1991). "Fluidization Engineering." **2nd Ed**. Boston: Butterworth-Heinemann.

La Nauze, R. D. (1986). "A review of the fluidised bed combustion of biomass." *Journal of the Institute of Energy*.

Lazar, M. E. and Farkas, D. F. (1971). "The centrifugal fluidised bed drying studies on piece form foods." *J. Food Science*. **36**. pp 315 – 319.

Levy, E. K., Martin, N. and Chen, J. (1978). "Minimum fluidization and start-up of a centrifugal fluidized bed." *Fluidization – Proceedings of the Second Engineering Foundation Conference (J.F. Davidson and D.L. Kearns, Eds)*. Cambridge University Press. pp 71-80.

Levy, E. K.; Dodge, C. and Chen, J. C. (1976). "Parametric analysis of a centrifugal fluidized bed coal combustor." *ASME paper*. **76HT68**. Presented at National Heat Transfer Conference, Boulder Colorado.

Levy, E. K.; Martin, N. and Chen, J. C. (1977). "Centrifugal fluidised bed combustion." *Proc. 5th Int. Fluidized Bed Combustion*. **Vol. 3**. pp 288 – 296.

Levy, E. K.; Shakespeare, W. J.; Tabatabaie-Raissi, A. and Chen, C. J. (1981). "Particle elutriation from centrifugal fluidized beds." *AIChE Symposium Series*. **77**. No. 205. pp 86 – 95.

Lilley, D. G. and Chigier, N. A. (1971). "Non-isotropic turbulent stress distribution." *International Journal of Heat and Mass Transfer*. **14**. pp 573.

Lin, K. S.; Paul Wang, H.; Lin, C. J. and Ching I-Juch. (1998). "A process development for gasification of rice husk." *Fuel Processing Technology*. **55**. pp 185 – 192.

Magnussen, B. F. and Hjertager, B. H. (1976). "On mathematical models of turbulent combustion with special emphasis on soot formation and combustion." *In 16th Symp. (Int'l) on Combustion*. The Combustion Institute.

Mansaray, K. G. and Ghaly, A. E. (1997). "Physical and Thermochemical Properties of Rice Husk". *Energy Sources*. **19**. pp 989 – 1004.

Mansaray, K. G. and Ghaly, A. E. (1998a). "Thermogravimetric Analysis of Rice Husk in an Air Atmosphere." *Energy Sources*. **20**. pp 653 – 663.

Mansaray, K.G. and Ghaly, A. E. (1998b). "Thermal Degradation of Rice Husks In Nitrogen Atmosphere." *Bioresource Technology*. **65**. pp 13 – 20.

Mathur, K. B. and Gishler, P. E. (1955). "Spouted Beds." *A. I. Ch. J.* **1**. pp 157.

McCabe, W. L.; Smith, J. C. and Harriot, P. (1993). "Unit Operations of Chemical Engineering." **5th Ed**. New York: McGraw Hill.

Metcalfe, C. I. And Howard, J. (1977). "Fluidisation and combustion in a rotating fluidised bed." *Applied Energy*. **3**. pp. 65 – 74.

Metcalfe, C. I. and Howard, J. R. (1978). "Towards higher intensity combustion:- Rotating fluidised beds." *In Fluidization – Proceedings of the Second*

Engineering Foundation Conference (J. F. Davidson and D. L. Keairns, Eds.). Cambridge University Press.

Mokhtar, H.; Ab. Rashid, A. H.; Salleh, M. S. dan Ujang, Z. (1986). "Malaysian Experience on Fluidised Bed Combustor for Agricultural Wastes." *Proc. ASEAN Conf. on Energy from Biomass*. pp 62 – 75.

Monthly Statistical Bulletin, Department of Statistics Malaysia. Mac 1999.

Morsi, S. A. and Alexander, A. J. (1972). "An Investigation of Particle Trajectories in Two-Phase Flow Systems." *J. Fluid Mech*. **55(2)**. pp 193 –208.

Nasserzadeh, V.; Swithenbank, J.; Schofield, C.; Scott, D. W.; Loader, A.; Leonard, A.; Russell, R. and Winn, D. (1993). "Three-dimensional Modelling of the Conventry MSW Incinerator Using Computational Fluid Dynamics and Experimental Data." *Trans IChemE*. **Vol 71**. Part B. pp 269 – 279.

Niessen, W. R. (1995). "Combustion and Incineration Processes: Applications in Environmental Engineering." **2nd Ed**. New York: Marcel Dekker, Inc.

Pemberton, S. T. and Davidson, J. F. (1986). "Elutriation from fluidized beds – 1.Particle ejection from the dense phase into the freeboard." *Chemical Engineering Science*. **41**. pp 243 – 251.

Perry, R. H.; Green, D. W. and Maloney, J. O. (Eds.) (1997). "Perry's Chemical Engineer's Handbook." **7th Edition**. New York: McGraw-Hill.

Pfeffer, R. and Hill, F. B. (1978). "A feasibility study on the use of a RFB as a dust filter." *BNL Report*. **No. 50990**. Sept. 1978.

Ramiah, M. V. (1970). "Thermogravimetric and differential thermal analysis of cellulose, hemicellulose and lignin." *Journal of Applied Polymer Science*. **14**. pp 1323 – 1337.

Rozainee (1998). “Incineration of Sludge Waste in a Novel Rotating Fluidized Bed.” University of Sheffield: PhD Thesis.

Salib, P. F. (1984). “Rotating Fluidised Bed Coal Combustion.” University of Sheffield: PhD Thesis.

Schiefelbein, G. F. (1989). “Biomass thermal gasification research. Recent results from the United States DOE’s research program.” *Biomass*. **Vol. 19**. Issue 1 – 2. pp 145 – 159.

Shafizadeh, F. (1968). “Pyrolysis and combustion of cellulosic materials.” *Advanced Carbohyrate Chemistry*. **23**. pp 419 – 474.

Shafizadeh, F. dan DeGroot, W. F. (1976). pp 1 – 18, in F. Shafizadeh, K. V. Sarkanen and D. A. Tillman, eds. New York: Academic.

Shakespeare, W. J. (1977). “Analysis of power cycles with centrifugal fluidised bed coal combustion.” *Proc. Intersoc. Energy Conversion Conference*. Washington DC.

Shi, M. H.; Wang, H. and Hao, Y. L. (2000). “Experimental investigation of the heat and mass transfer in a centrifugal fluidised bed dryer.” *Chemical Engineering Journal*. **Vol. 78**. Iss. 2 – 3. pp 107 – 113.

Sloan, D. G.; Smith, P. J. and Smoot, L. D. (1986). “Modelling of swirl in turbulent flow systems.” *Prog. Energy Combust. Sci*. **12**. pp 163.

Spalding, D. B. (1970). “Mixing and chemical reaction in steady confined turbulent flames.” *In 13th Symp. (Int’l) on Combustion*. The Combustion Institute.

Srinivasan, R. and Moagia, H. C. (1980). “Numerical computation of swirling recirculating flow.” *NASA CR*. **No. 165197**.

Sturgess, G. J. and Syed, S. A. (1985). “Calculation of confined swirling flows.” *AIAA Paper*. **No. 85-0060**.

Subzwari, M. P. (1983). “Atmospheric and Pressurized Rotating Fluidized bed Combustion.” University of Sheffield: PhD Thesis.

Swithenbank, J.; Nasserzadeh, V.; Taib, R.; Stagg, D.; Moore, D.; Ward, M. and Bone, J. (1997). “Incineration of Wastes in Novel High-Efficiency Tumbling and Rotating Fluidized Bed Incinerator.” *Journal of Environmental Engineering*. October 1997. pp 1047 – 1052.

Taib, M. R.; Nasserzadeh, V.; Swithenbank, J.; and Basire, S. (1997). “Process intensification of sewage sludge disposal.” *Proceedings in the 1st International Symposium on Incineration and Flue Gas Treatment Technologies*. Sheffield: The University of Sheffield. July 1997.

Takahashi, T.; Tanaka, Z.; Itoshima, A.; and Fan, L. T. (1984). “Performance of a rotating fluidized bed.” *Journal of Chemical Engineering of Japan*. **17**. pp 333 – 336.

Tobiś, J. (2000). “Influence of bed geometry on its frictional resistance under turbulent flow conditions.” *Chemical Engineering Science*. **55**. pp 5359 – 5366.

Vargheyi, G., Szabo, P. and Antal, M. J. (1994). “Reaction kinetics of the thermal decomposition of hemicellulose and cellulose in biomass materials.” *In Advances in Thermochemical Biomass Conversion, A. V. Bridgwater (ed.)*. London: Blackie. pp. 760 – 770.

Wen, C. Y. and Yu, Y. H. (1966). “A generalized method for predicting the minimum fluidising velocity.” *AIChE Journal*. **Vol. 12**. pp. 610 – 612.

Williams, P. T. and Besler, S. (1994). “Thermogravimetric analysis of the components of biomass.” *In Advances in Thermochemical Biomass Conversion, A. V. Bridgwater (ed).* London: Blackie. pp. 771 – 783.

Wong, W. Y.; Lu, Y.; Nasserzadeh, V. S.; Swithenbank, J.; Shaw, T. and Madden, M. (2000). "Experimental investigation into the incineration of wool scouring sludges in a novel rotating fluidised bed." *Journal of Hazardous Materials*. **Vol. 73**. No. 2. pp 143 – 160.

Xia, J. L.; Yadigaroglu, G.; Liu, Y. S.; Schmidli, J. and Smith, B. L. (1998). "Numerical and experimental study of swirling flow in a model combustor." *Int. J. Heat Mass Transfer*. **Vol. 41**. No. 11. pp 1485 – 1497.

Yeoh , A. K. and Ong, K. H. (1988). "Rice husk ash utilisation in Malaysia – SIRIM Experience." Presented at workshop on appropriate technologies on farm and village level postharvest grain handling.

Zenz, F. A. and Othmer, D. F. (1960). "Fluidization and Fluid Particle Systems." New York: Van Nostrand Reinhold.

Zhang, DeHong and Hill, P. G. (1996). "Effect of swirl on combustion in a short cylindrical chamber." *Combustion and Flame*. **106**. pp 318 – 332.

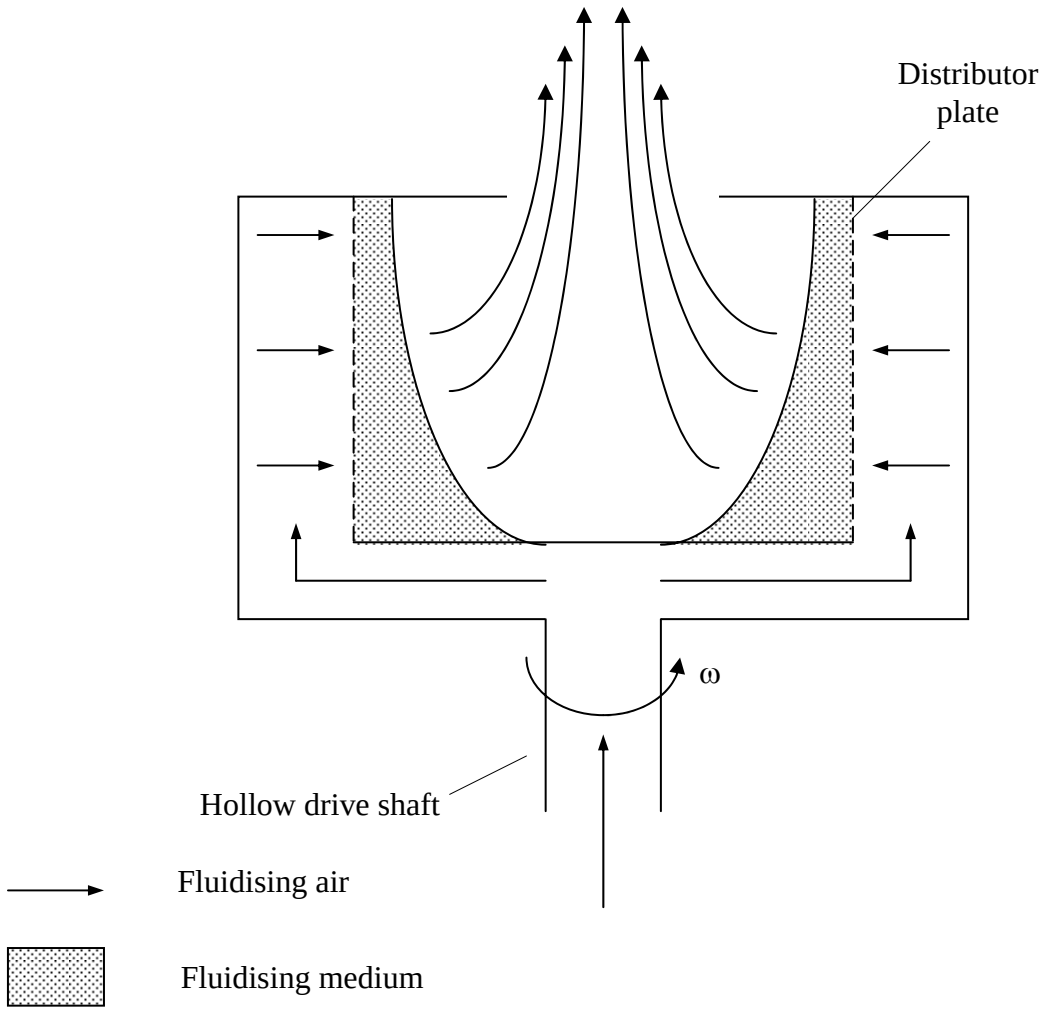

Figure 1.1: A rotating fluidised bed

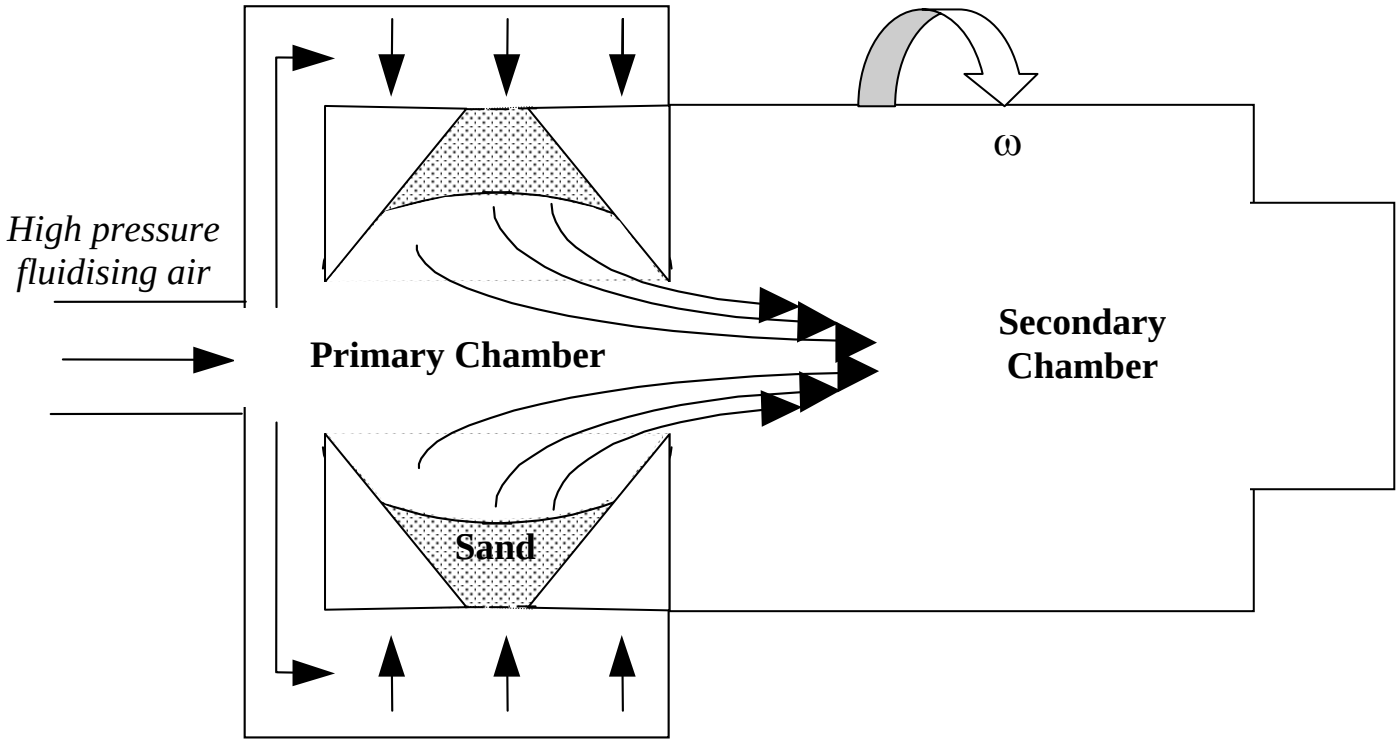

Figure 1.2: Concept of a horizontal SFB combustor

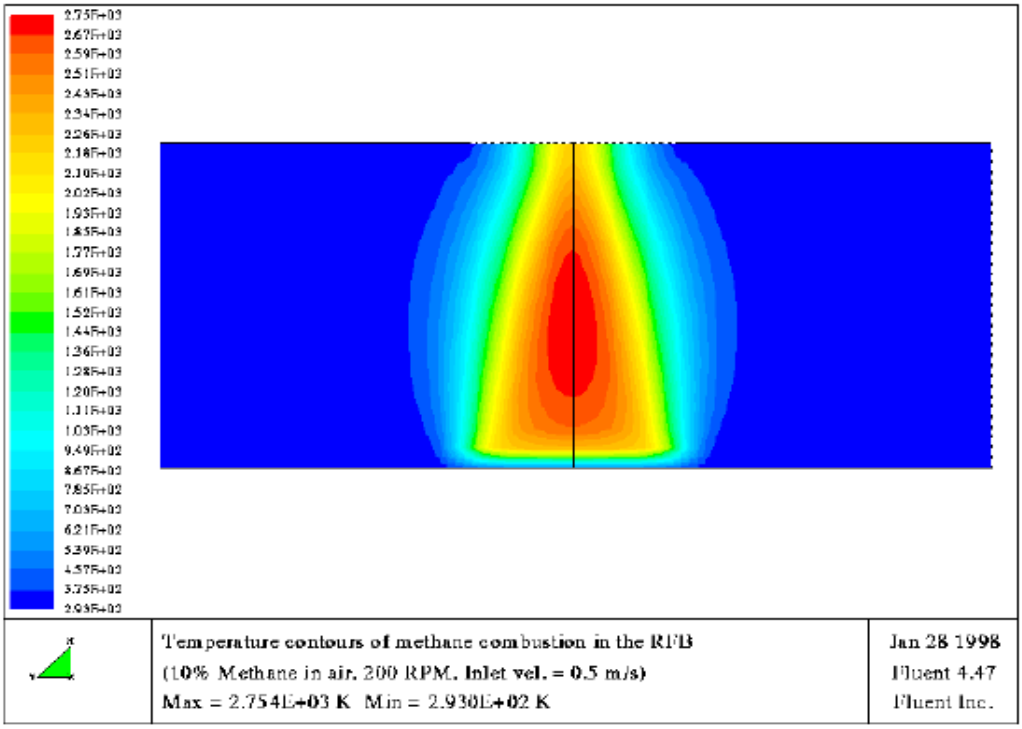

Figure 2.1: Combustion intensity in the bed burning methane at 200 RPM (Rozainee, 1998)

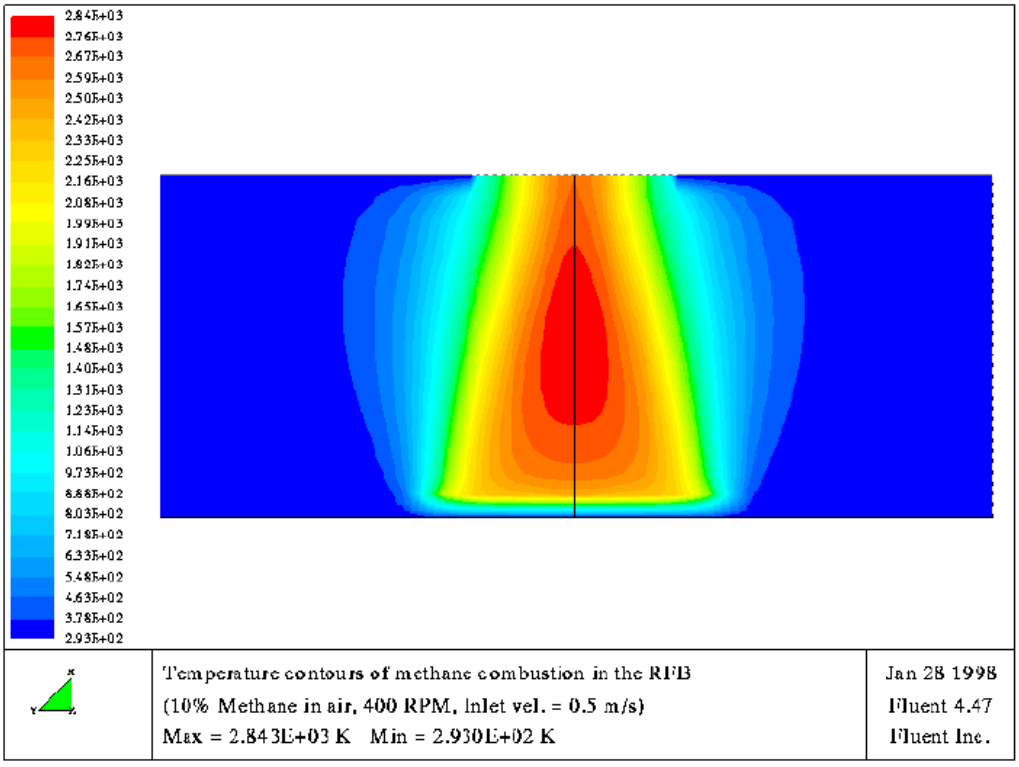

Figure 2.2: Combustion intensity in the bed burning methane at 400 RPM (Rozainee, 1998)

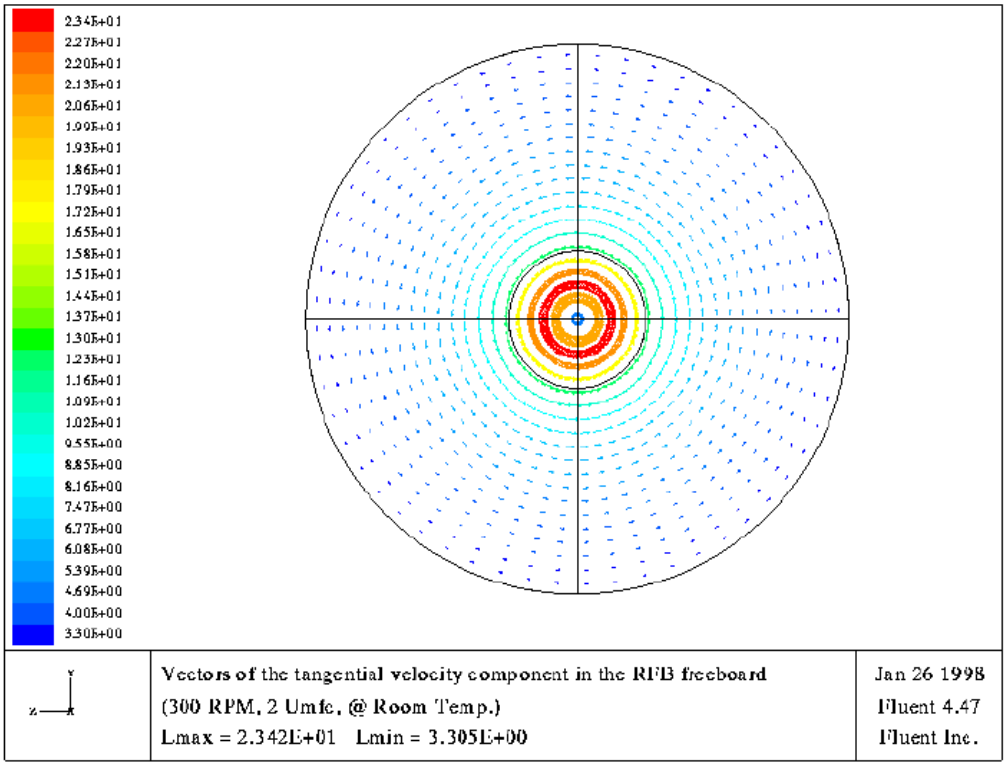

Figure 2.3: Vectors of the tangential velocity component in the RFB freeboard (Rozainee, 1998)

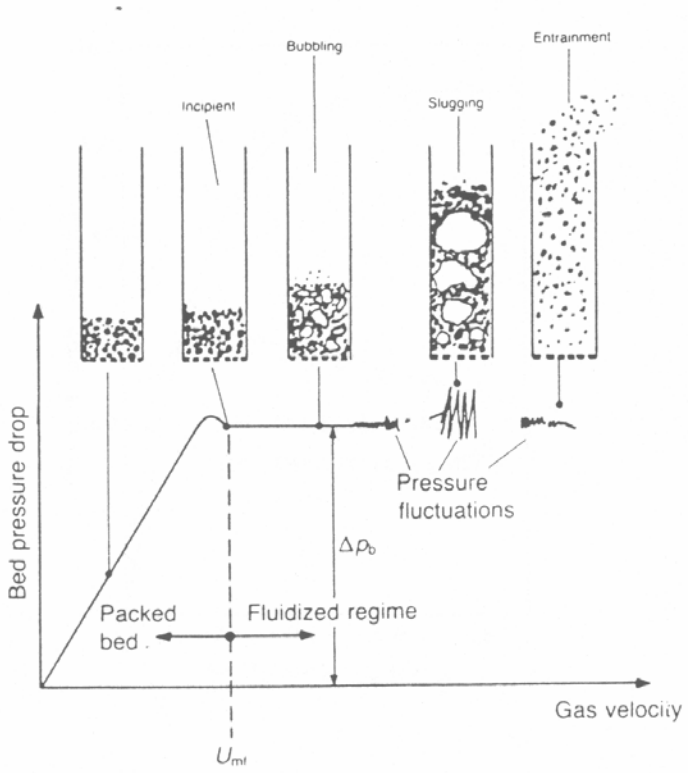

Figure 2.4: Behavioural changes of bed with gas velocity in a conventional fluidised bed (Howard, 1989)

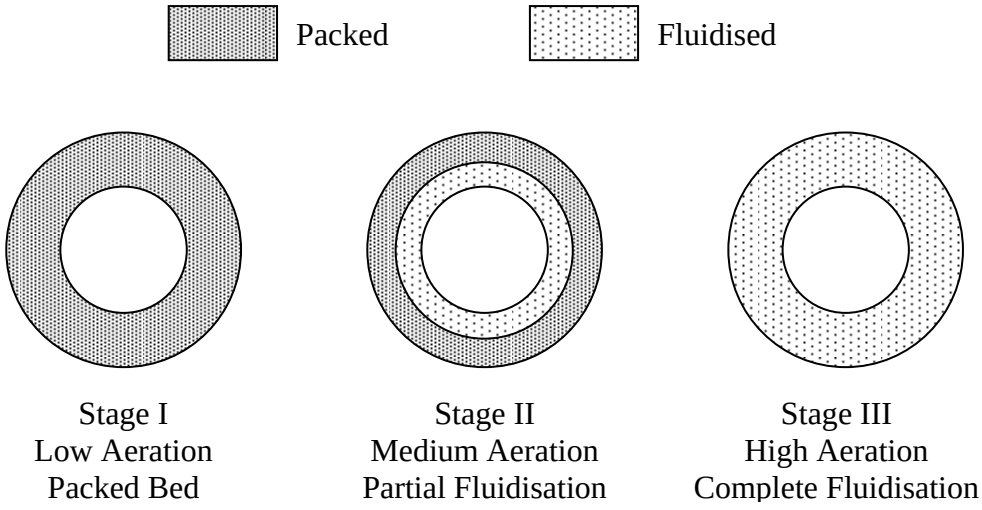

Figure 2.5: System configurations at different stages of aeration rate

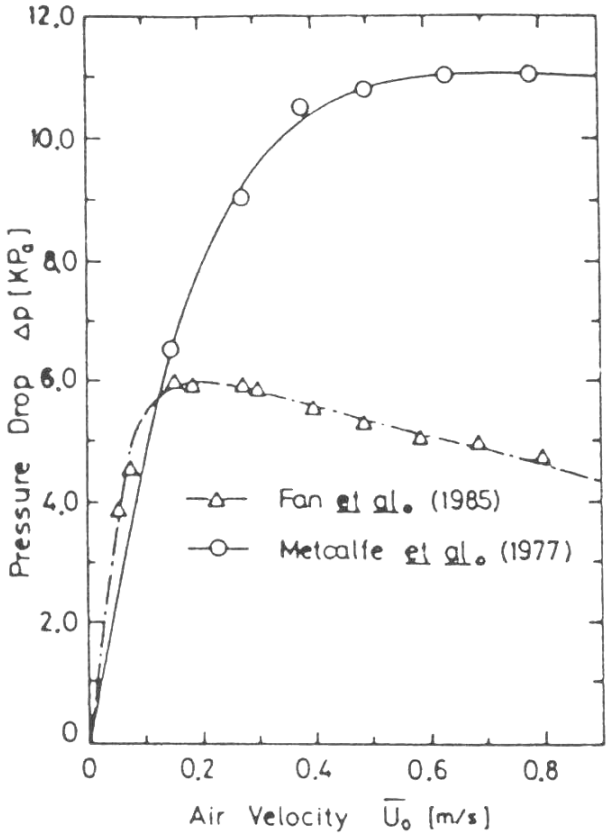

Figure 2.6: Two types of pressure drop vs. gas velocity curves in a RFB, a plateau or a maximum (Chen, 1987)

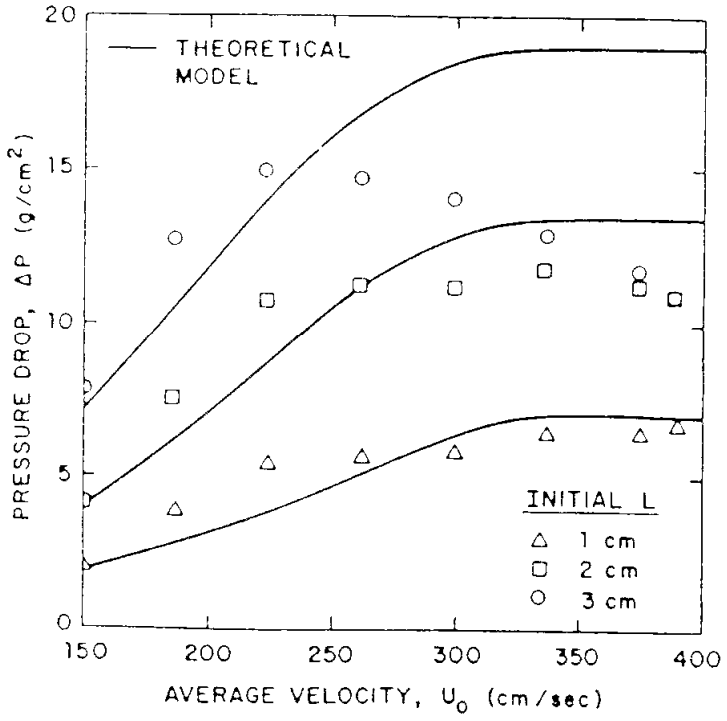

Figure 2.7: Pressure drop in a RFB as a function of air velocity for various initial bed thickness (Kao et al., 1987)

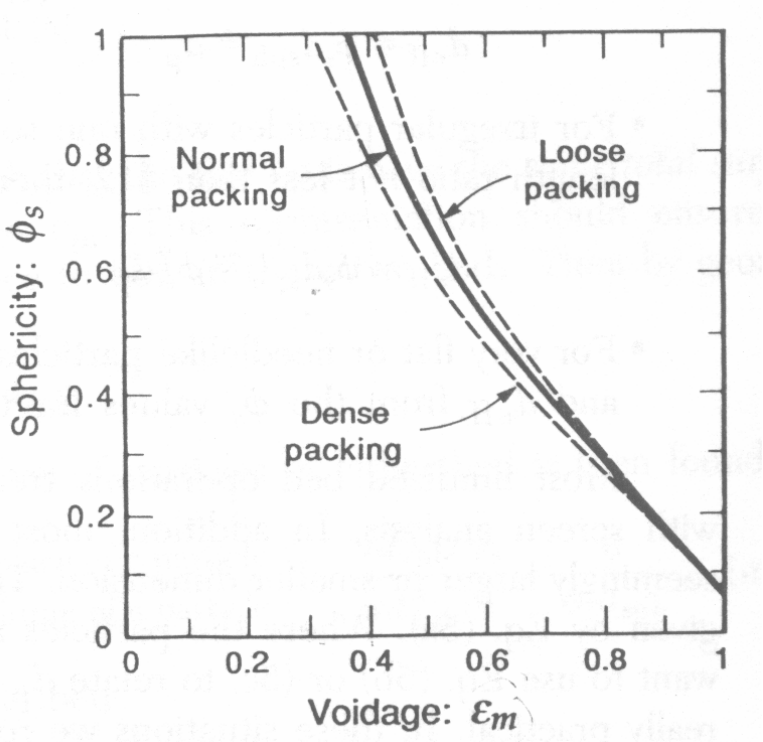

Figure 2.8: Voidage of a randomly packed bed of uniformly sized particles increases as particles become less spherical (Brown, 1950)

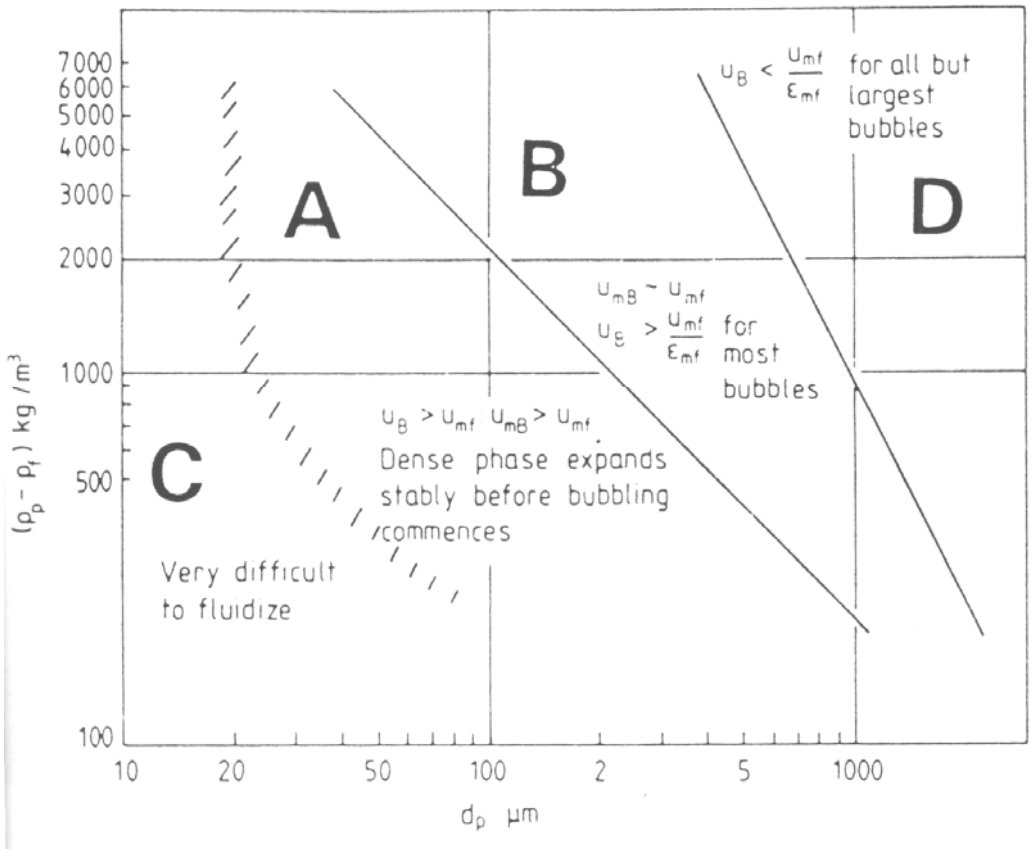

Figure 2.9: A powder classification diagram (Geldart, 1972)

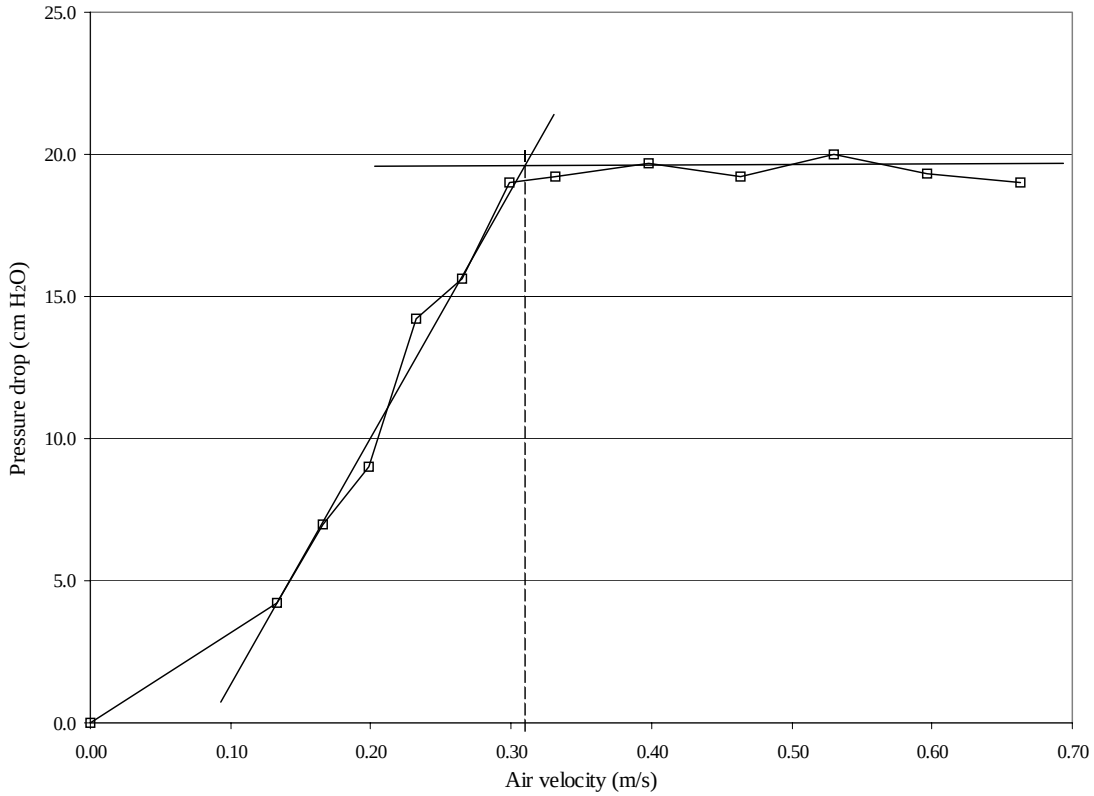

Figure 3.1: Minimum fluidisation velocity (U_{mf}) of 0.60 – 0.85 mm sand in a conventional fluidised bed at room temperature

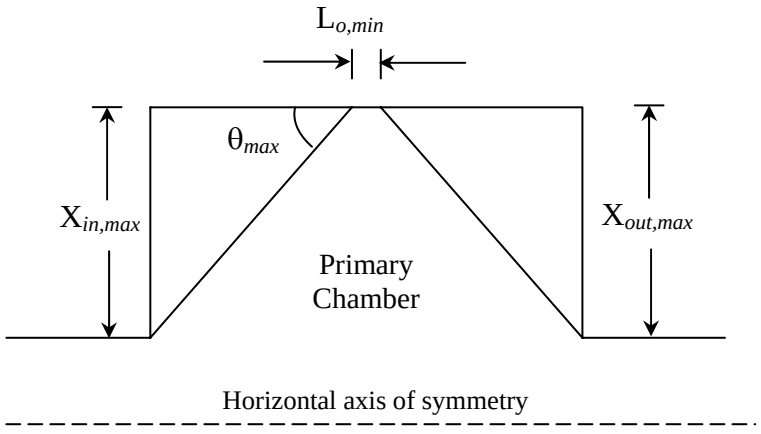

Figure 4.1: Tapered section geometry in the primary chamber of the horizontal RFB

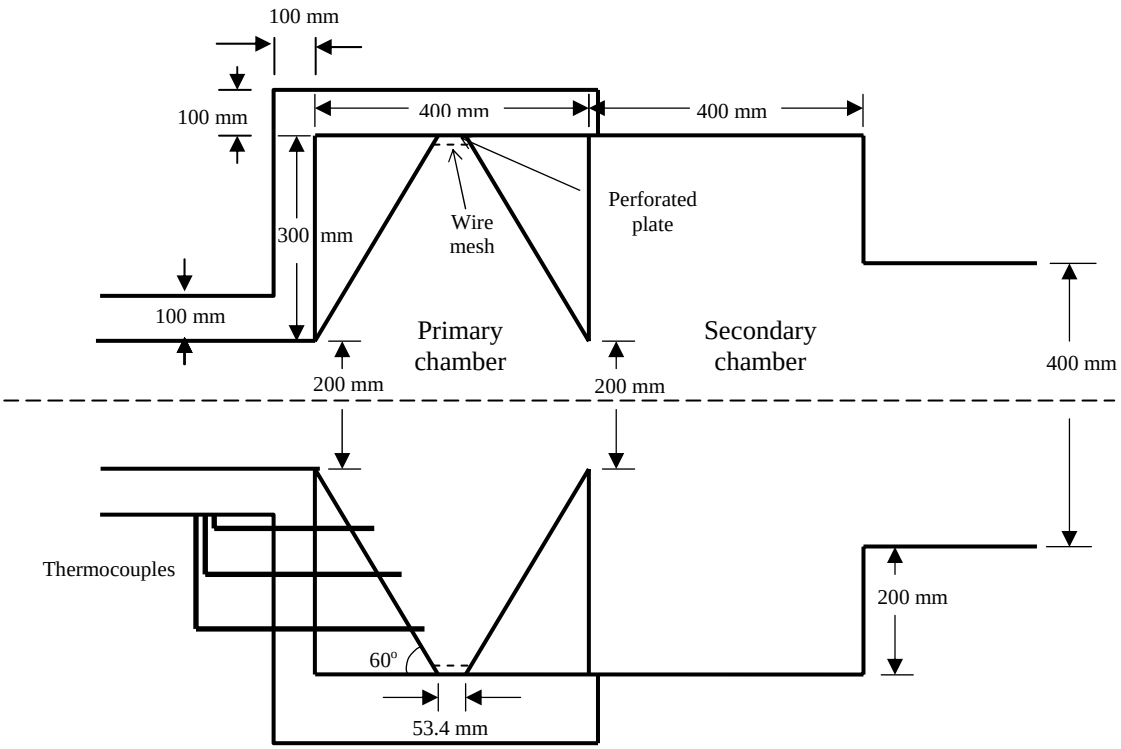

Figure 4.2: Schematic diagram of the proposed dimensions of the novel horizontal rotating fluidised bed combustor

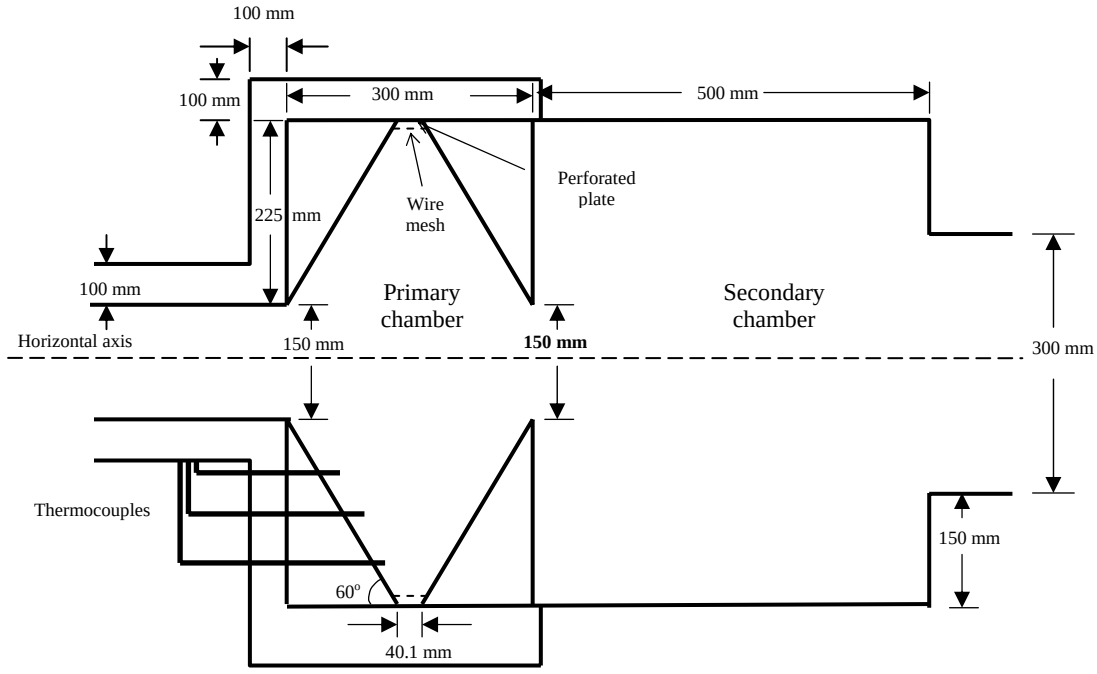

Figure 4.3: Schematic diagram of the scaled down novel horizontal rotating fluidised bed combustor

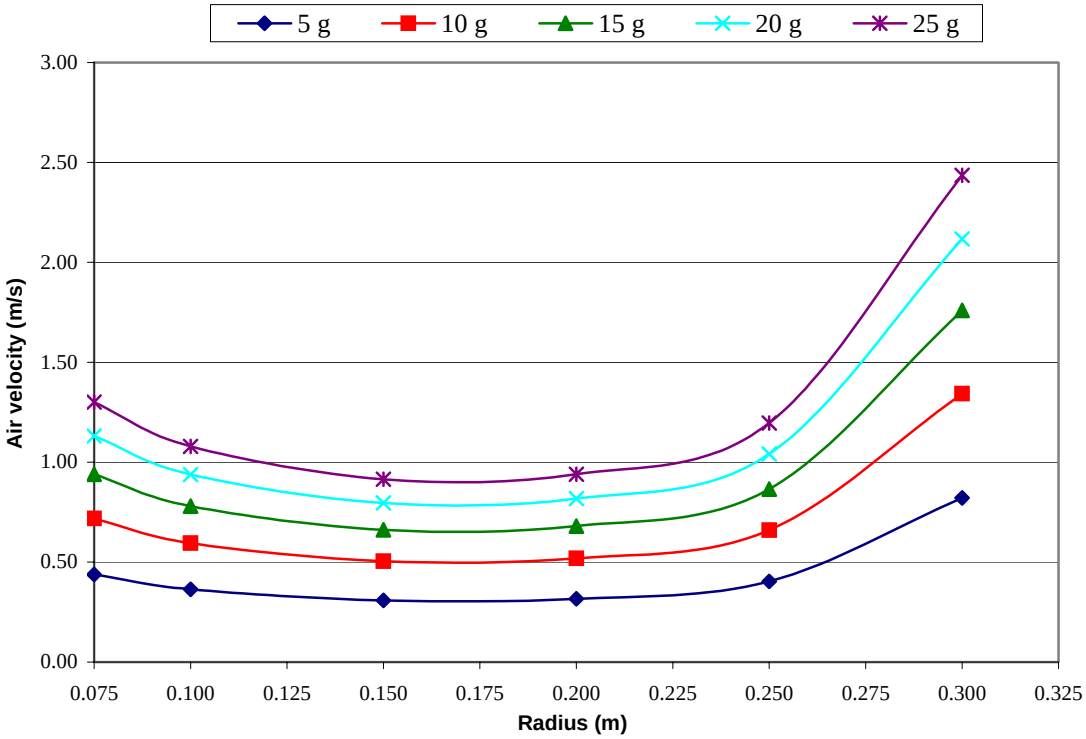

Figure 4.4: Radial velocity profile of air flow in the primary chamber of the scaled down RFB at different g-loadings (entering air flow at 1 U_{mfc}, 30^{o}C)

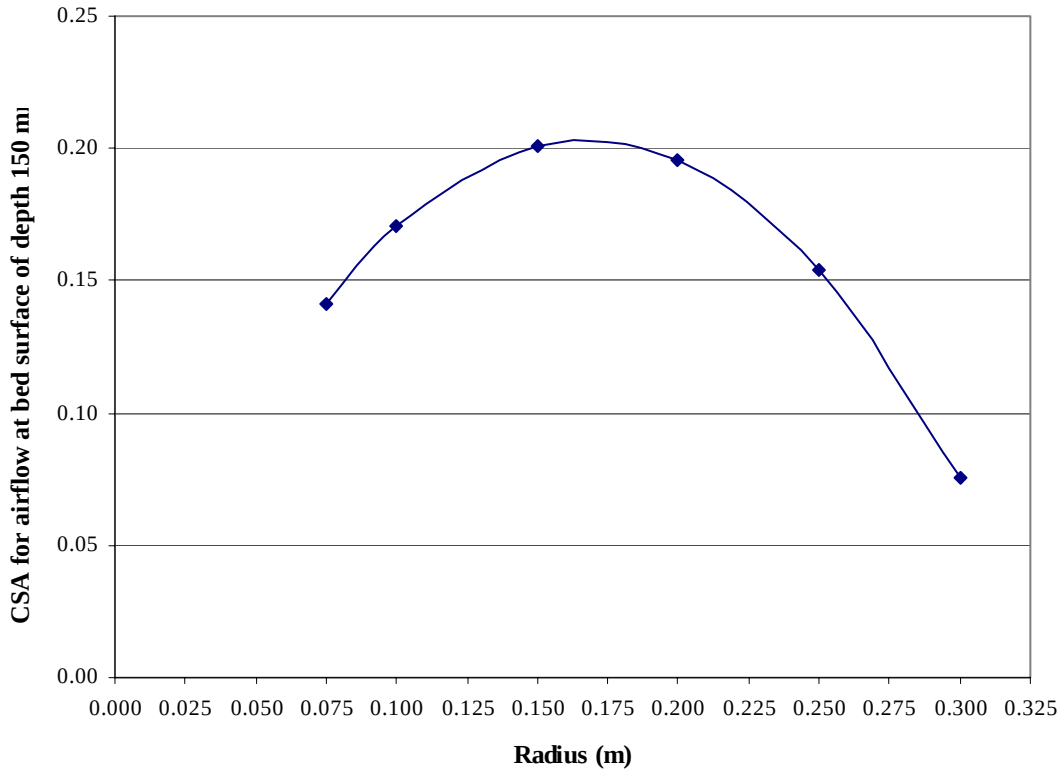

Figure 4.5: Profiles of cross sectional area for airflow at bed surface (of depth 150 mm) with changes in the radius of the primary chamber of the scaled down RFB

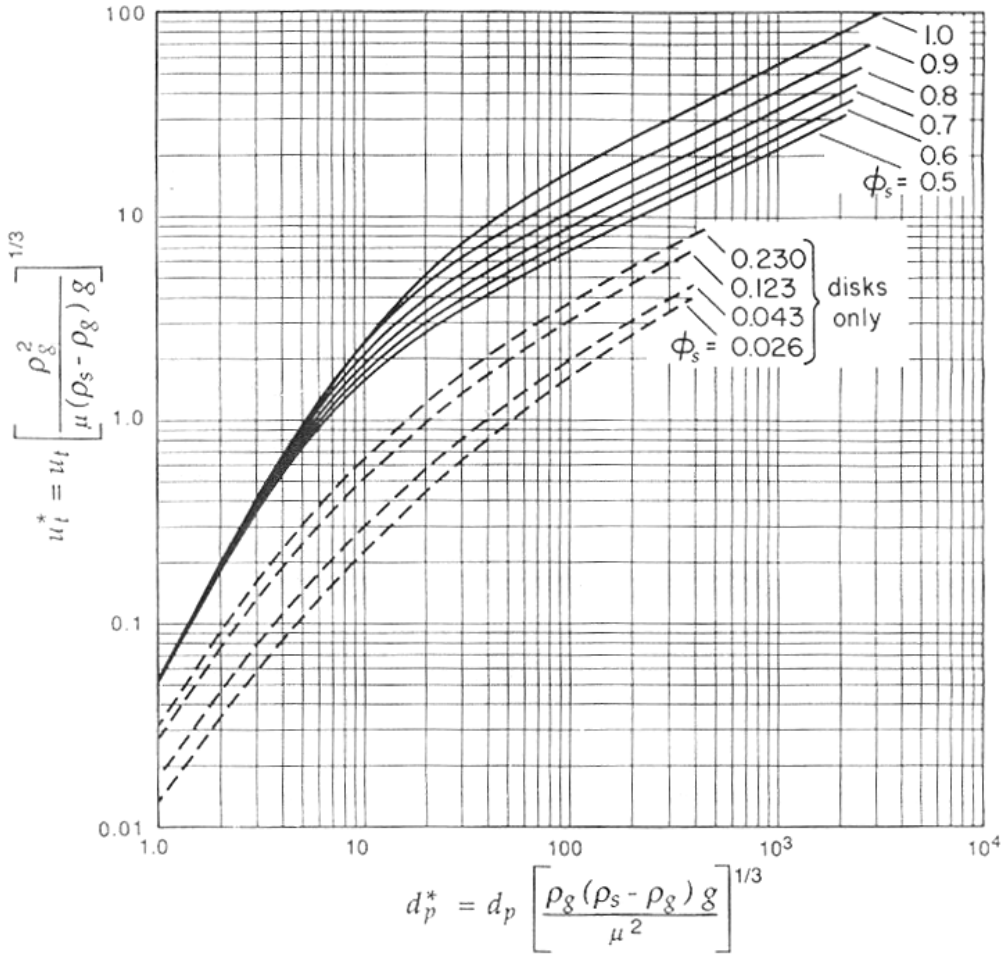

Figure 4.6: Chart for determining the terminal velocity of particles falling through fluids (Haider and Levenspiel, 1989)

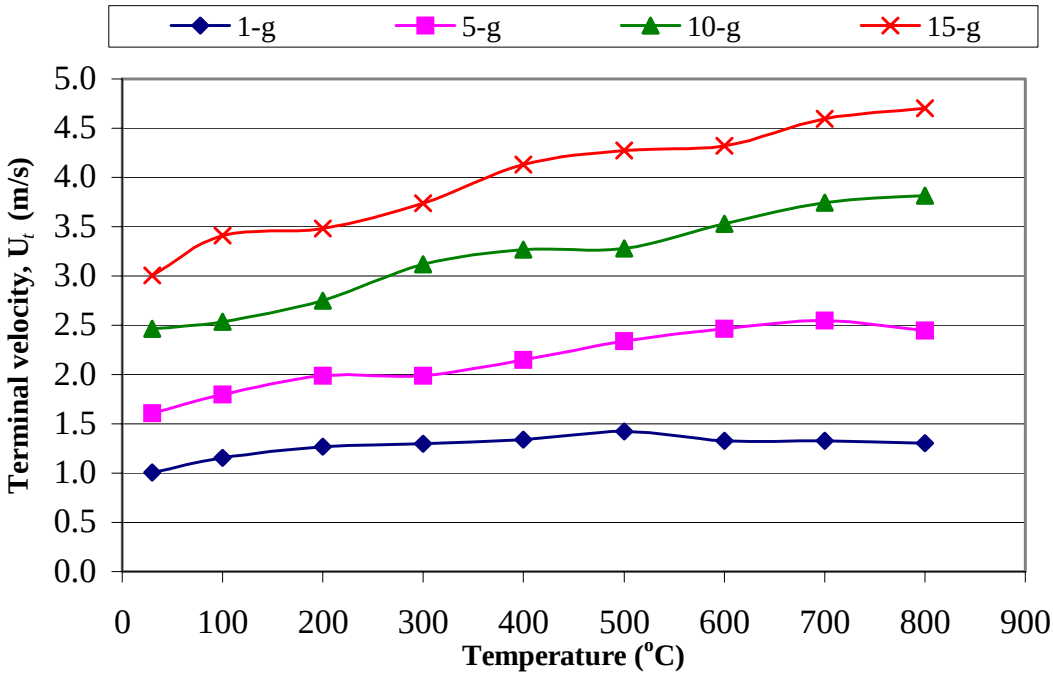

Figure 4.7: Terminal velocity of rice husk at different temperatures and g-loadings (for g-loadings of 5 – 15, the terminal velocities were evaluated at the bed surface of the RFB with bed depth of 150 mm, ID 600 mm and tapered at 60°)

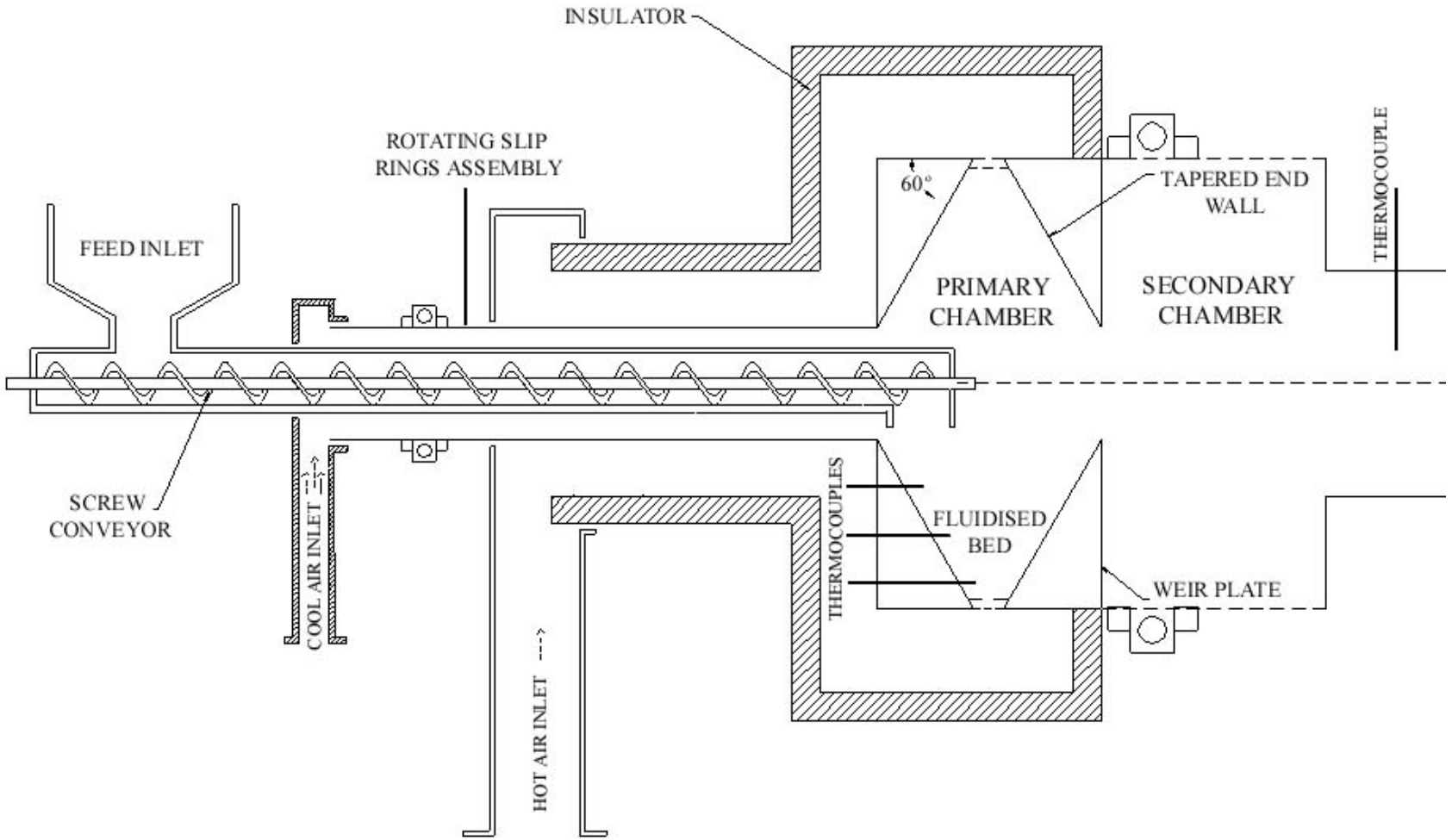

Figure 4.8: Blueprint of the prototype novel horizontal tapered rotating fluidised bed combustor

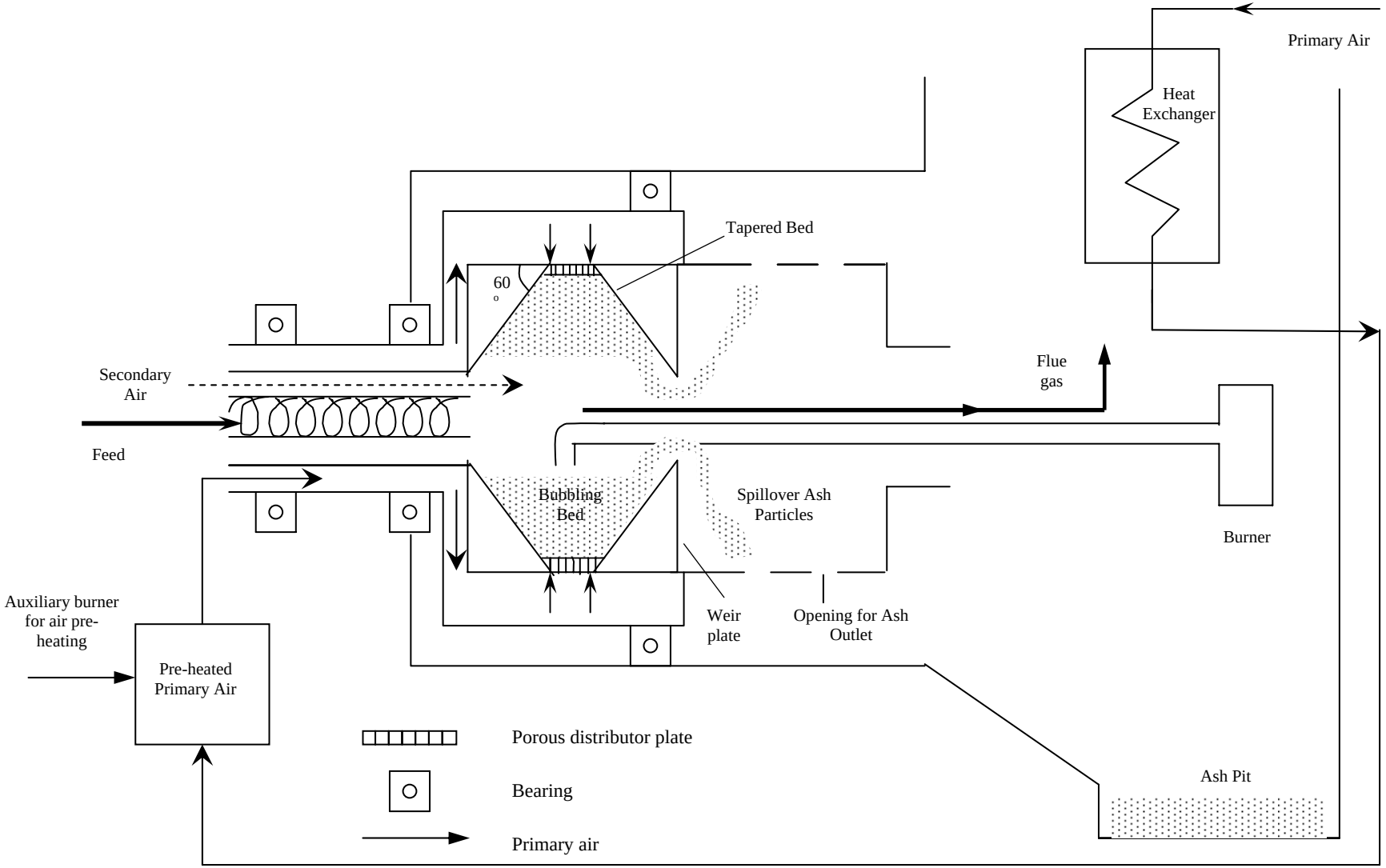

Figure 4.9: Experimental set-up of the novel horizontal rotating fluidised bed system

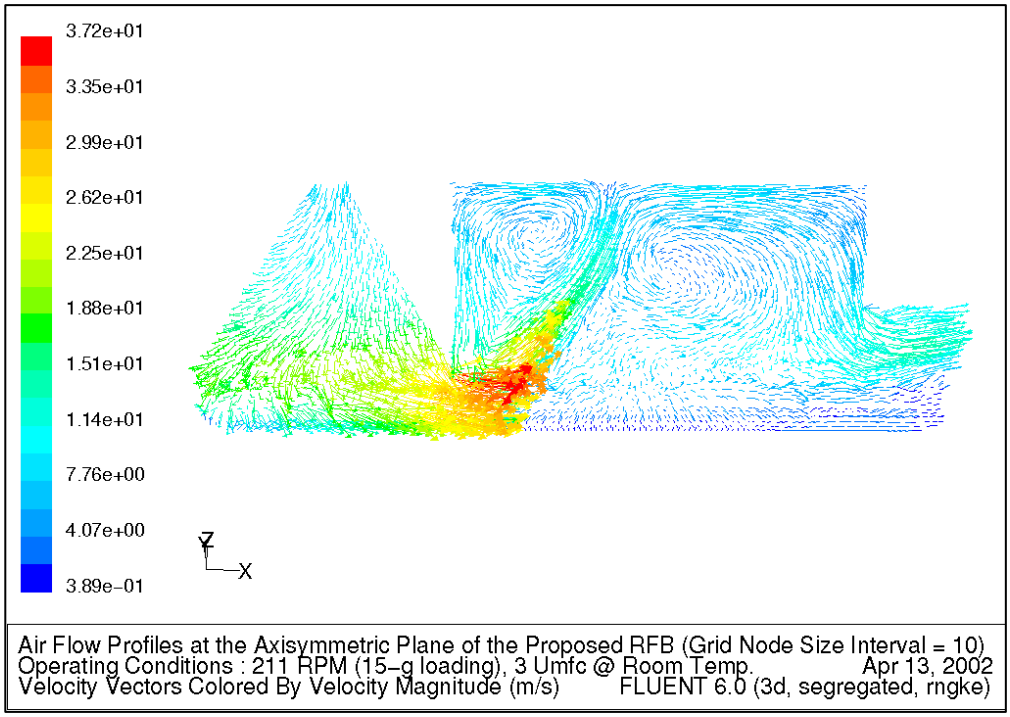

Figure 5.1

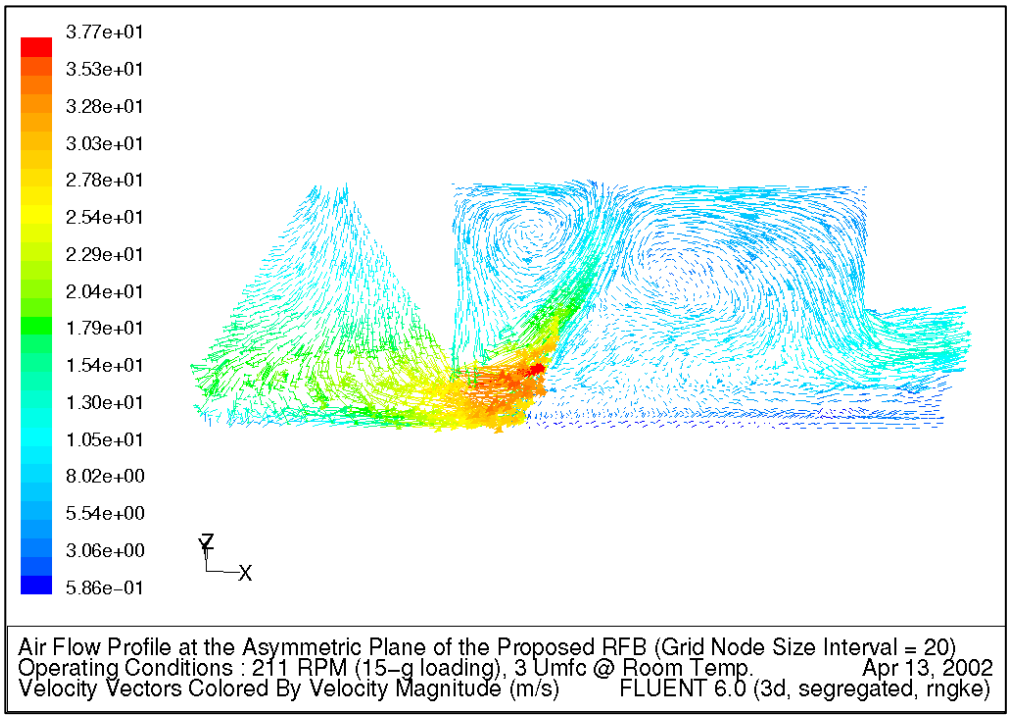

Figure 5.2

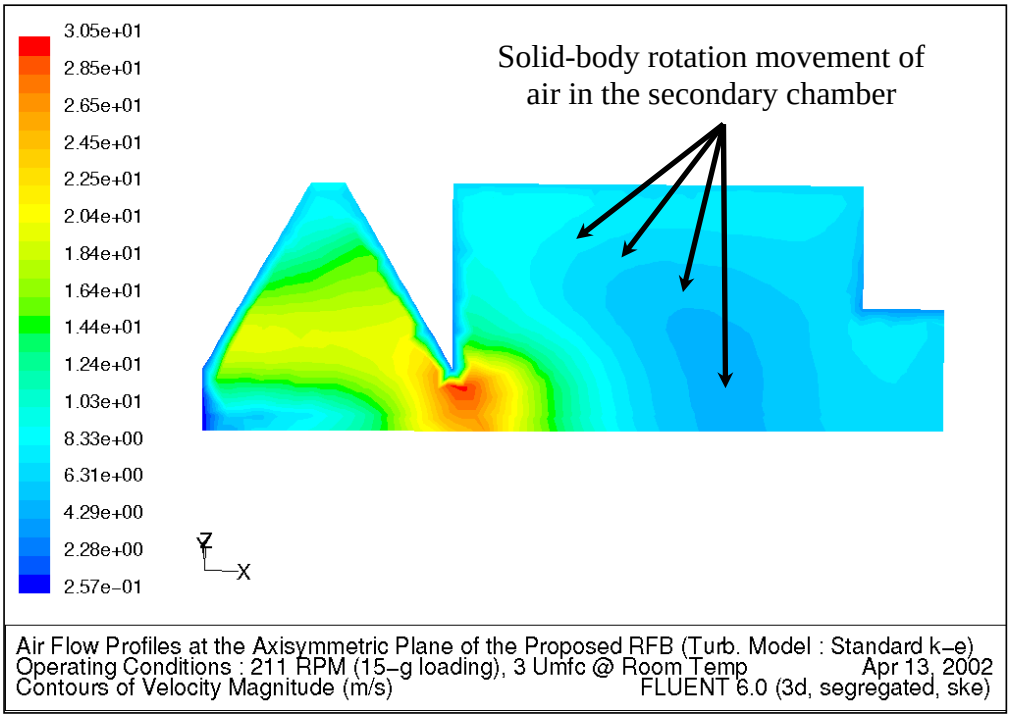

Figure 5.3

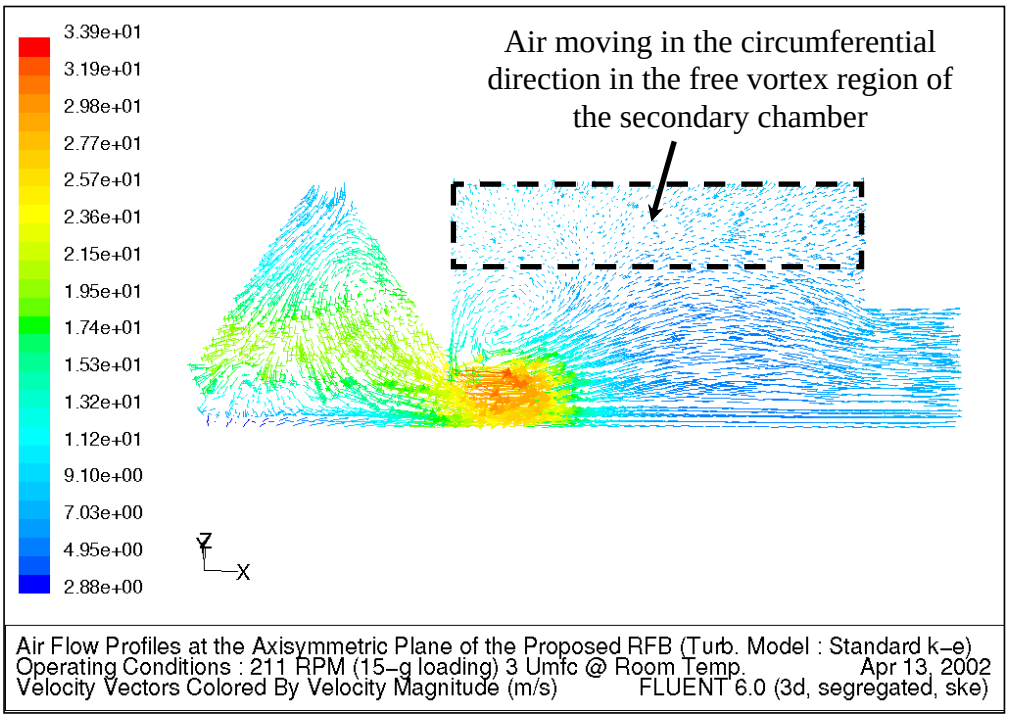

Figure 5.4

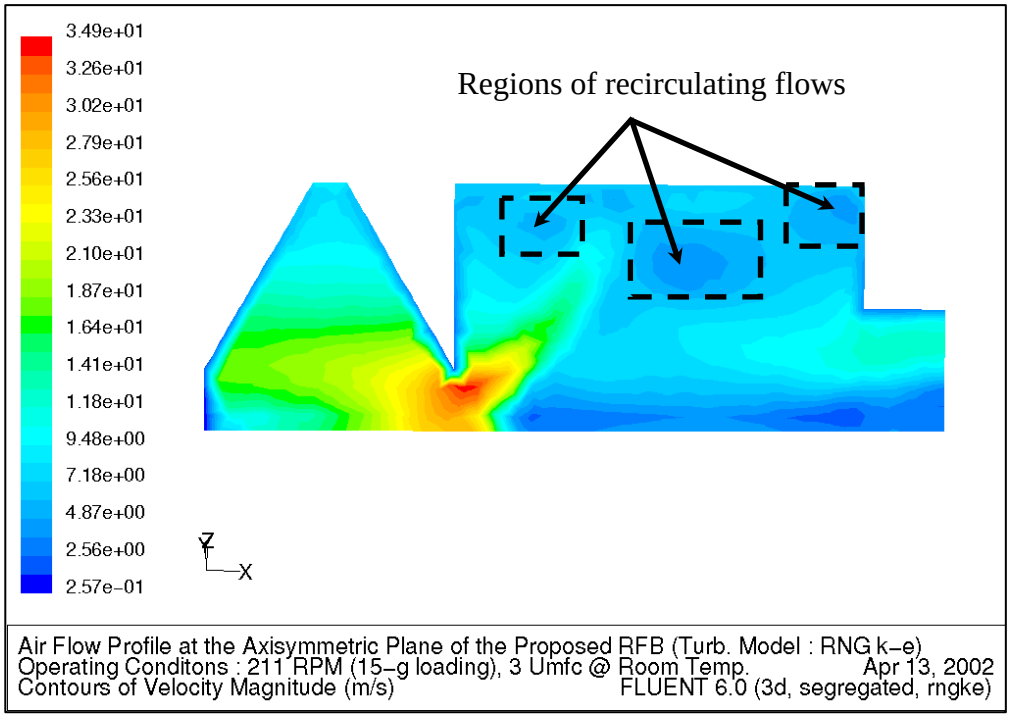

Figure 5.5

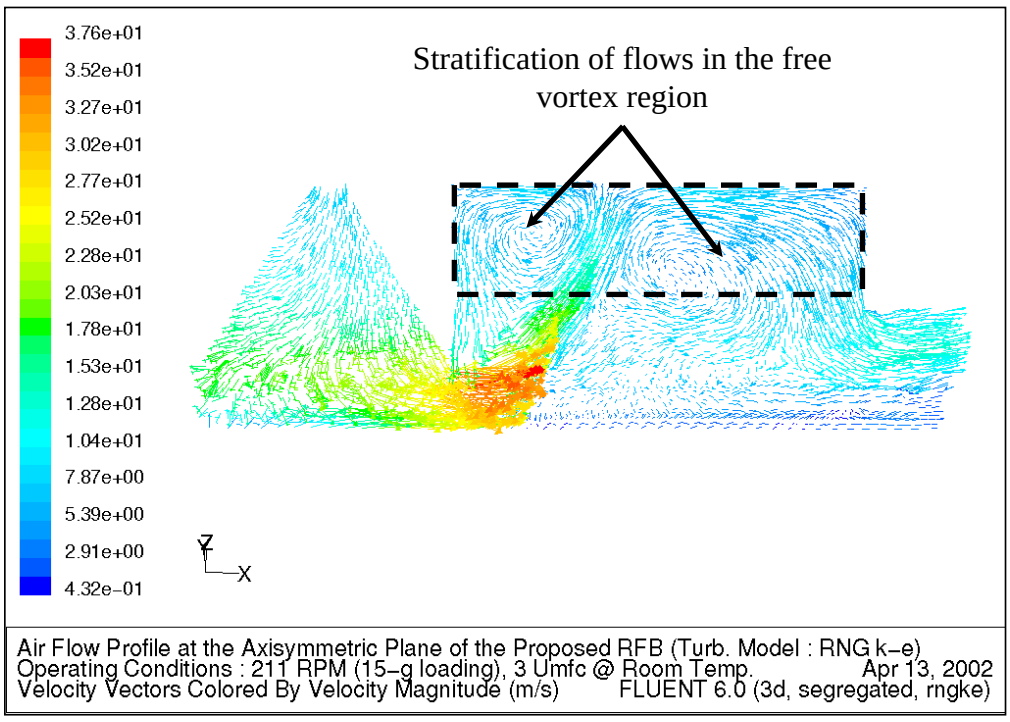

Figure 5.6

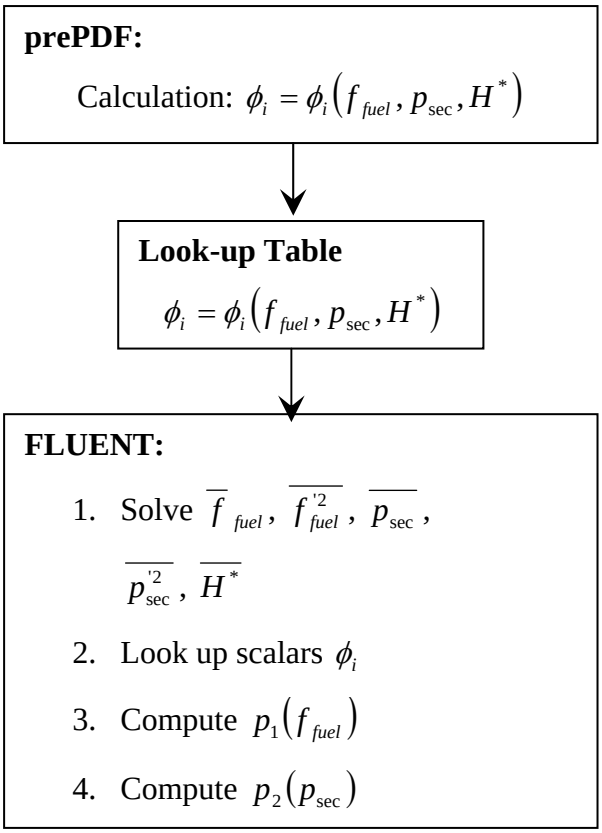

Figure 5.7: Algorithm for the solution of a non-adiabatic two-mixture-fraction case in pre-PDF and FLUENT

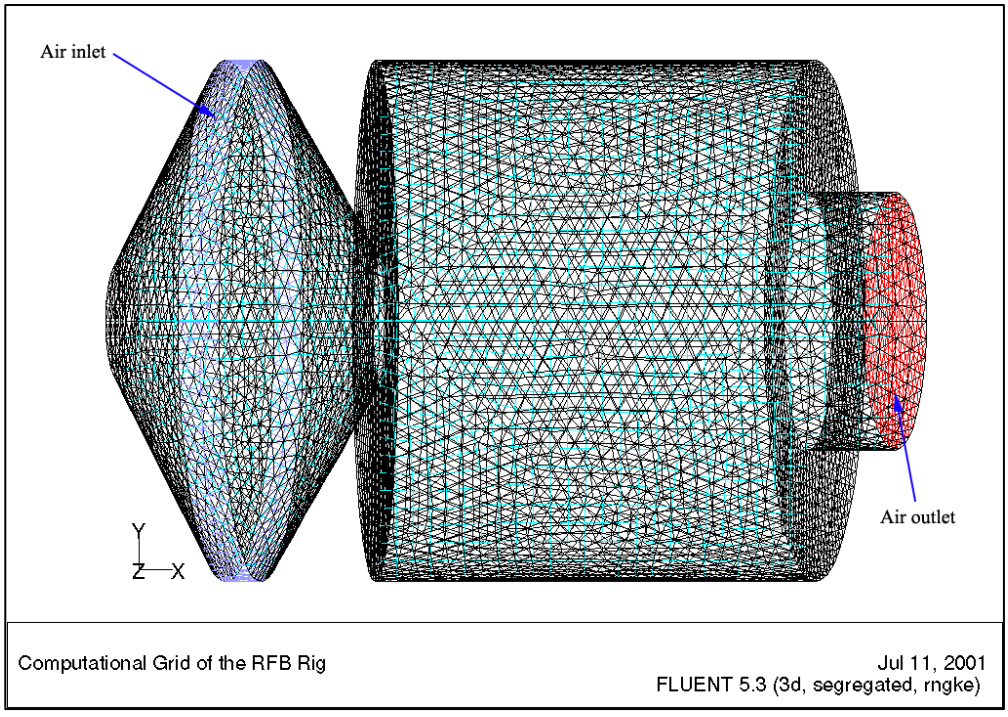

Figure 5.8: Three-dimensional computation grid of the tapered horizontal RFB combustor

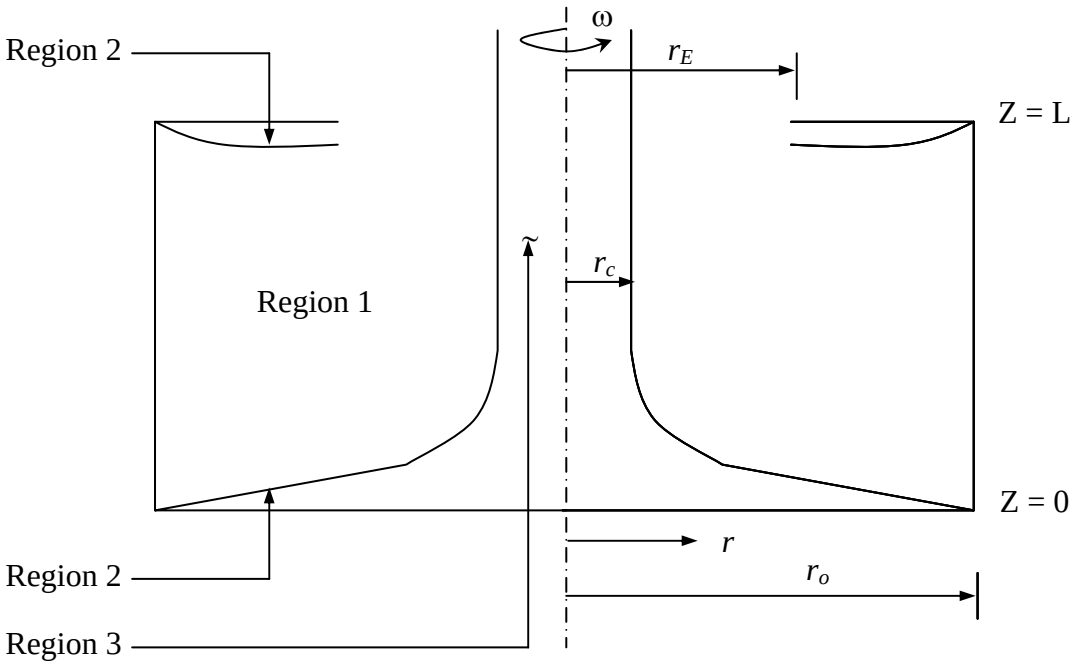

Figure 5.9: Flow regions in a RFB (Levy et al., 1981)

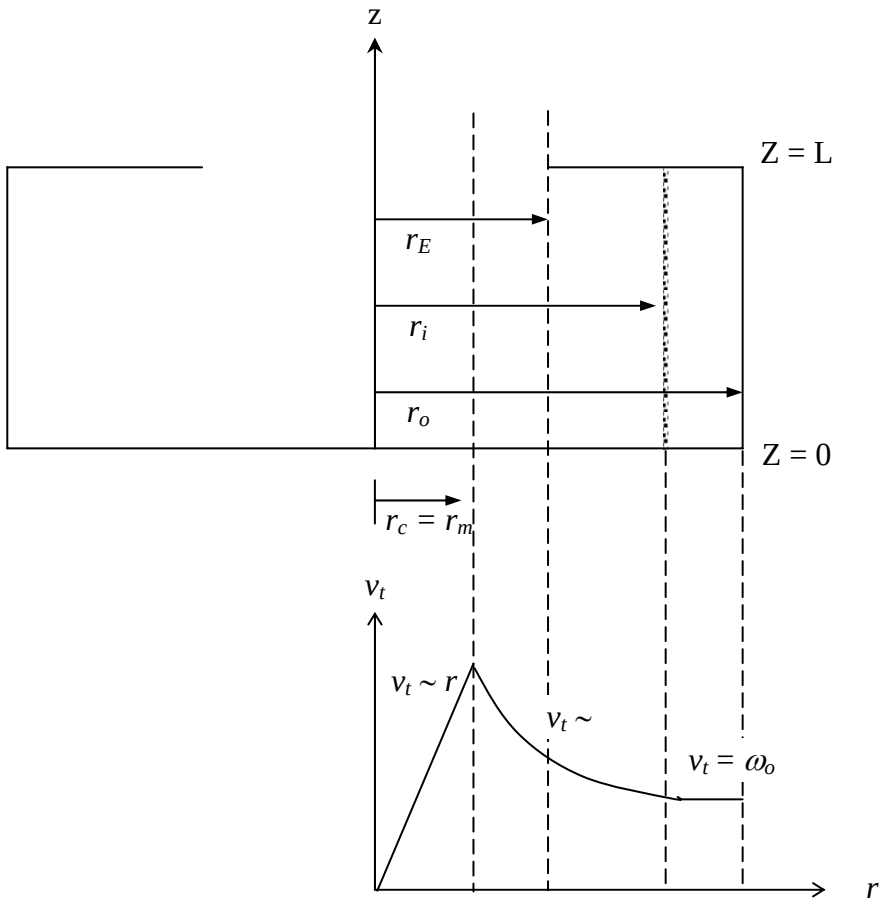

Figure 5.10: Variation in tangential velocity component in the RFB

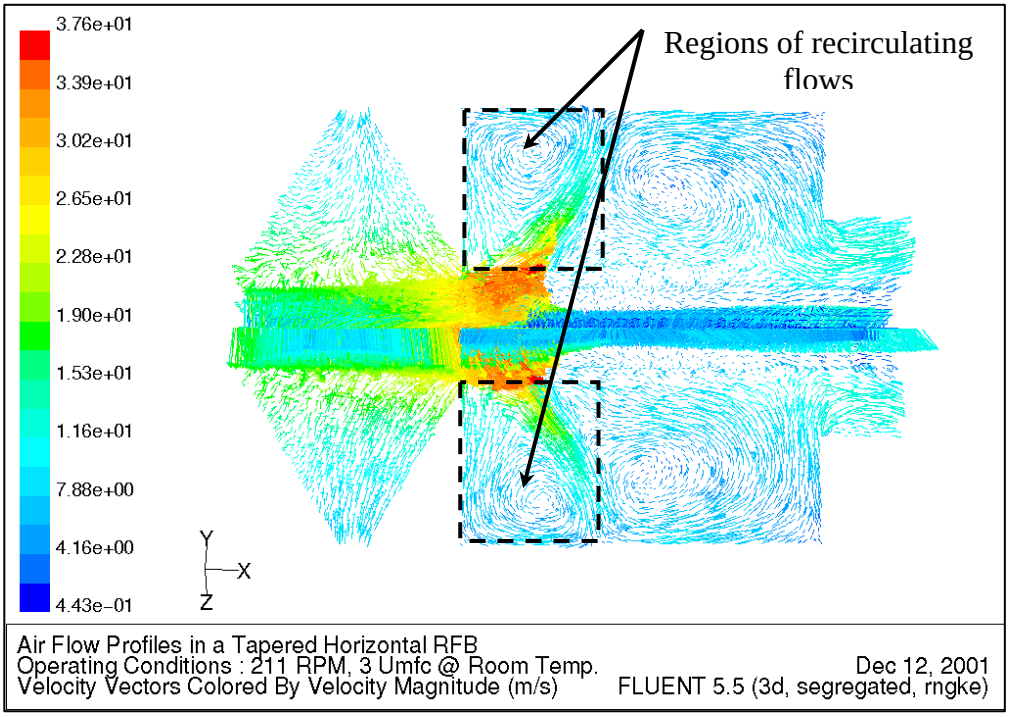

Figure 5.11

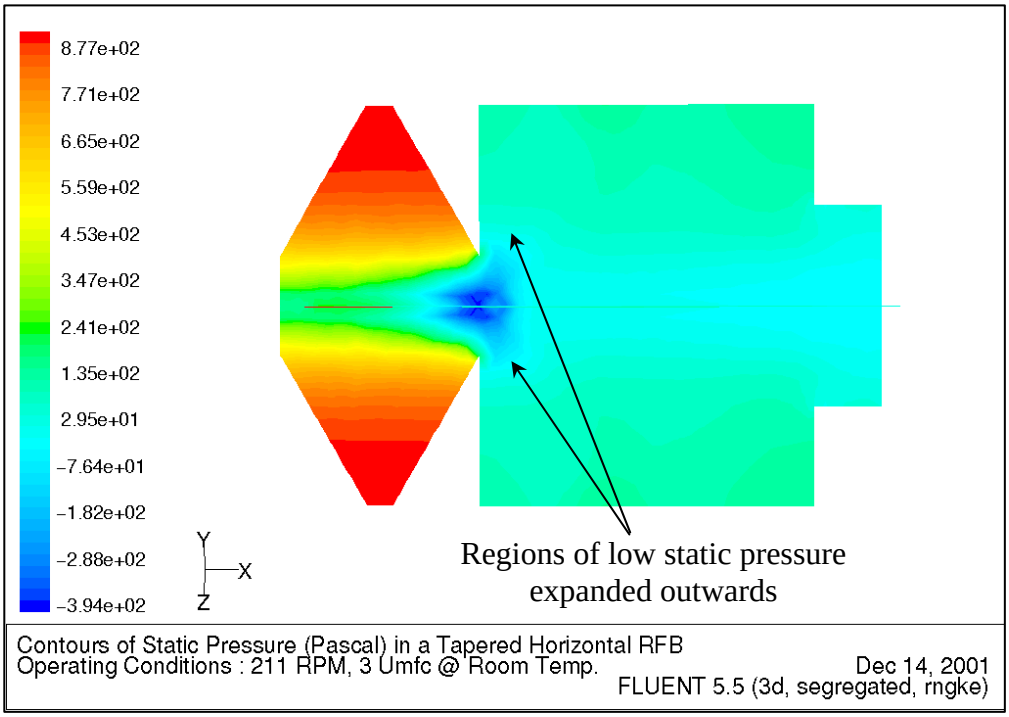

Figure 5.12

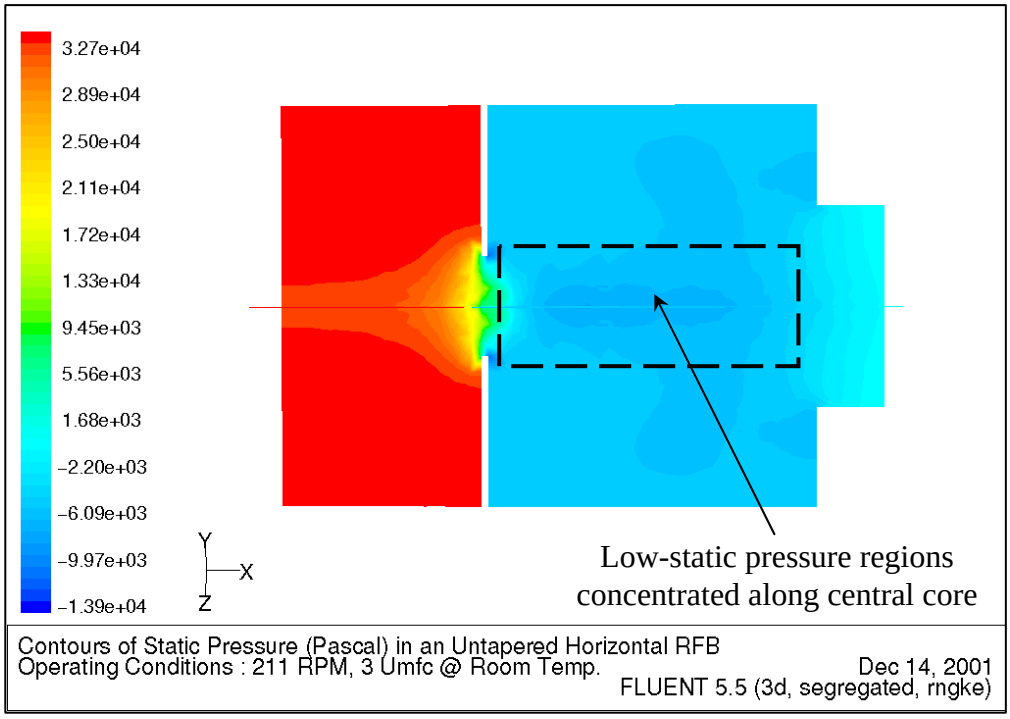

Figure 5.13

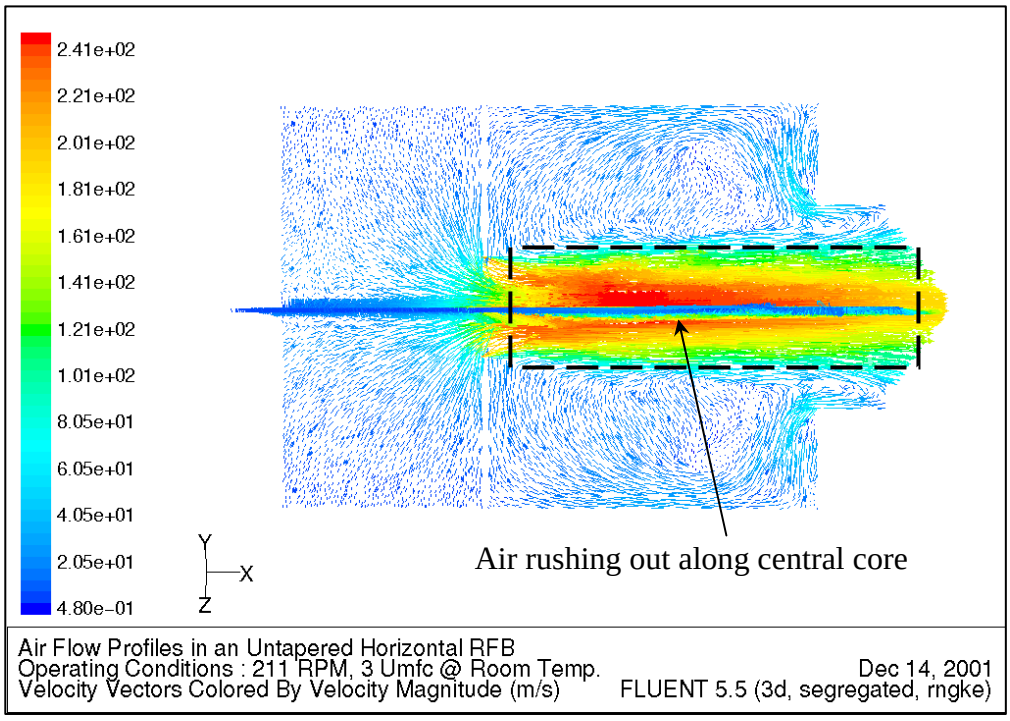

Figure 5.14

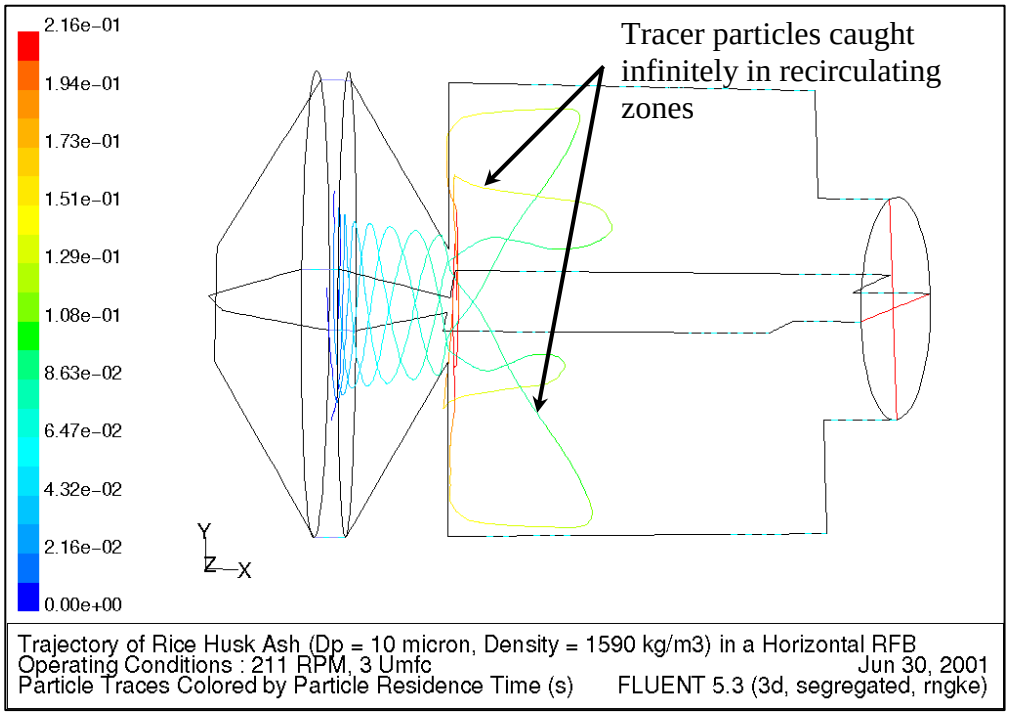

Figure 5.15

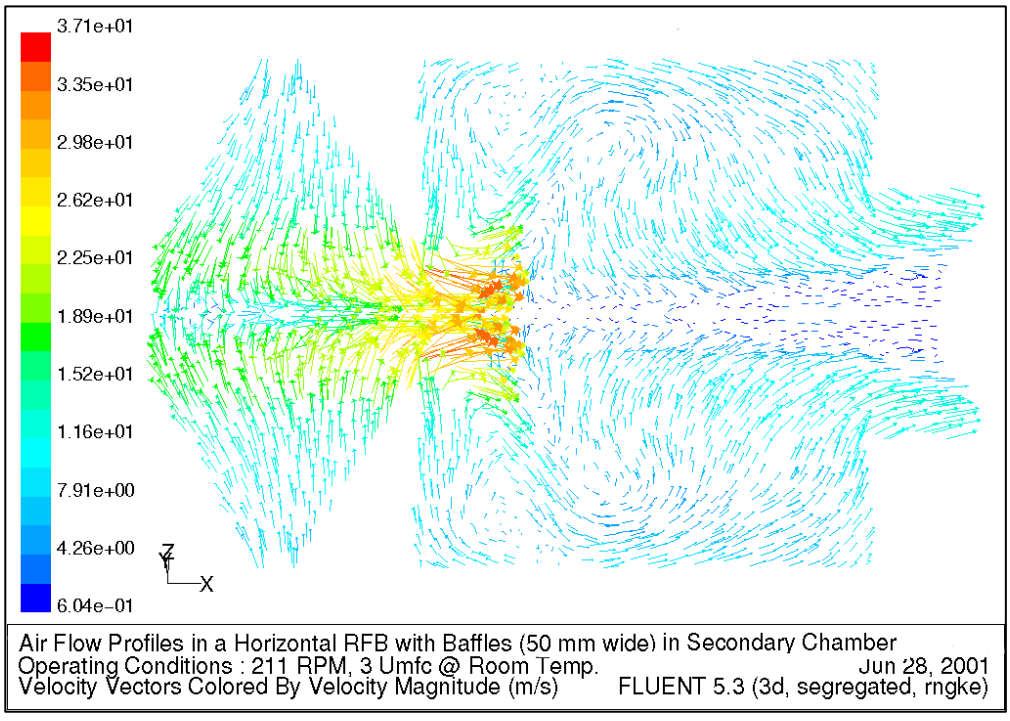

Figure 5.16

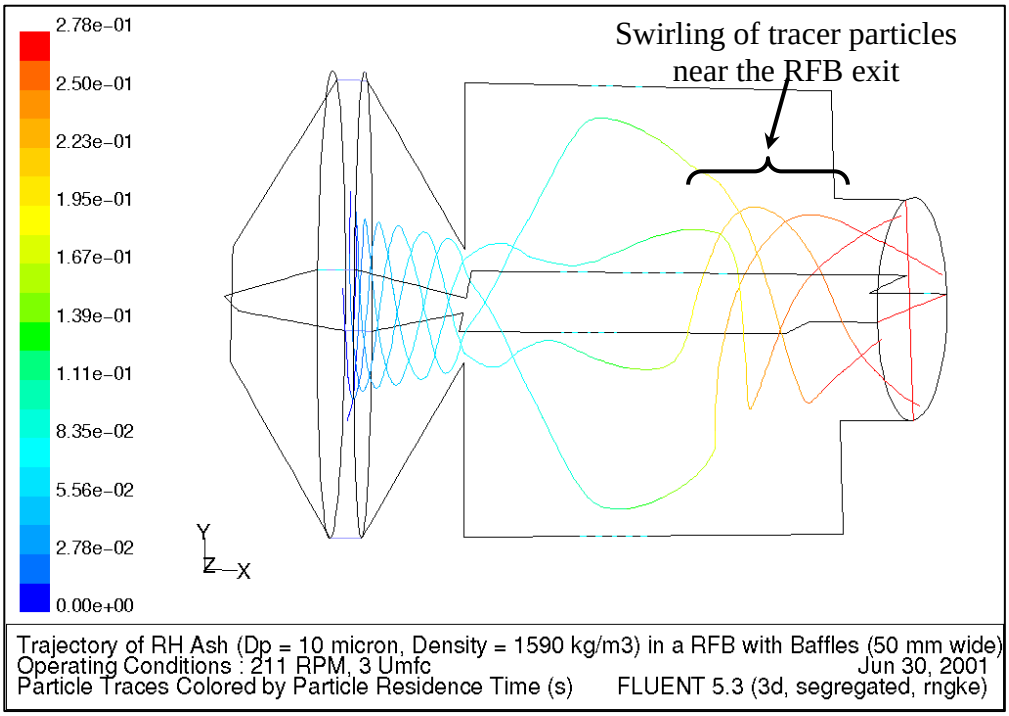

Figure 5.17

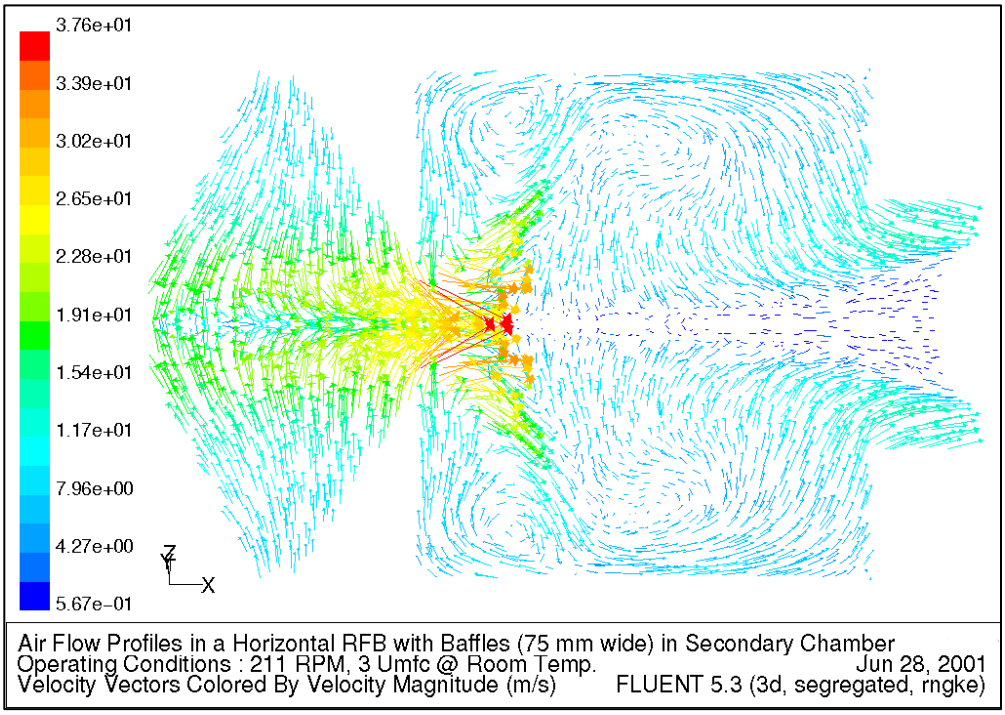

Figure 5.18

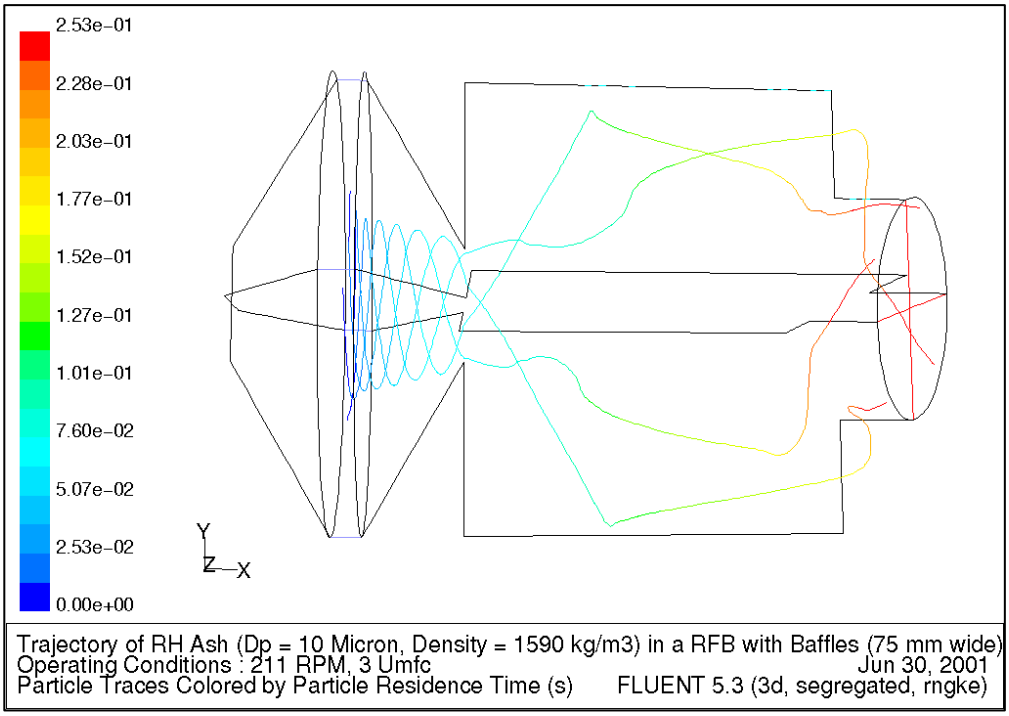

Figure 5.19

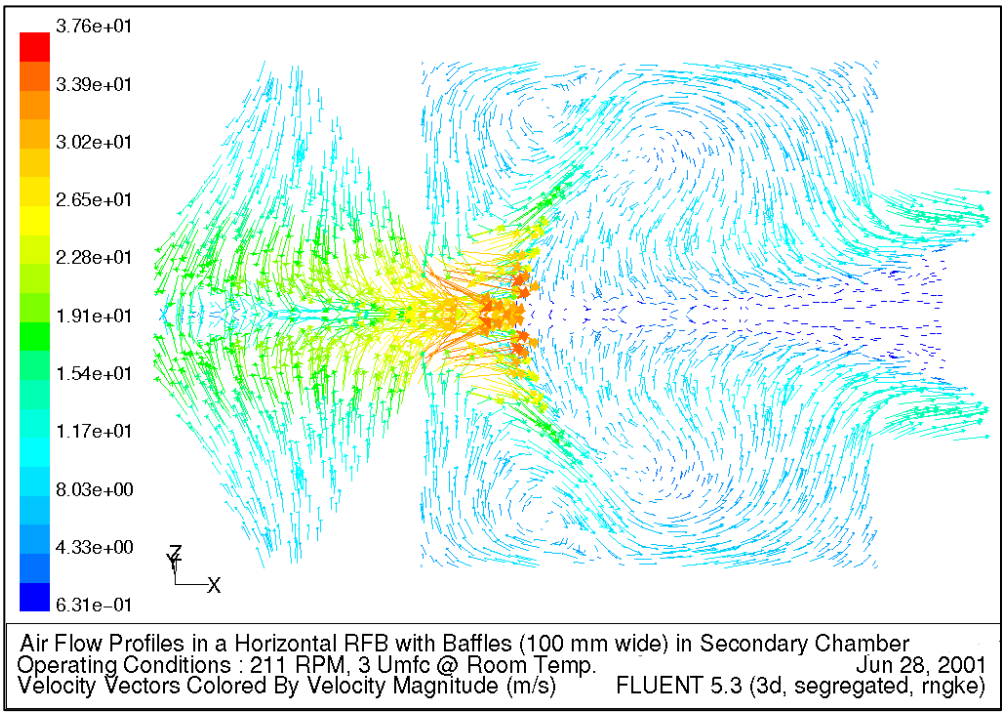

Figure 5.20

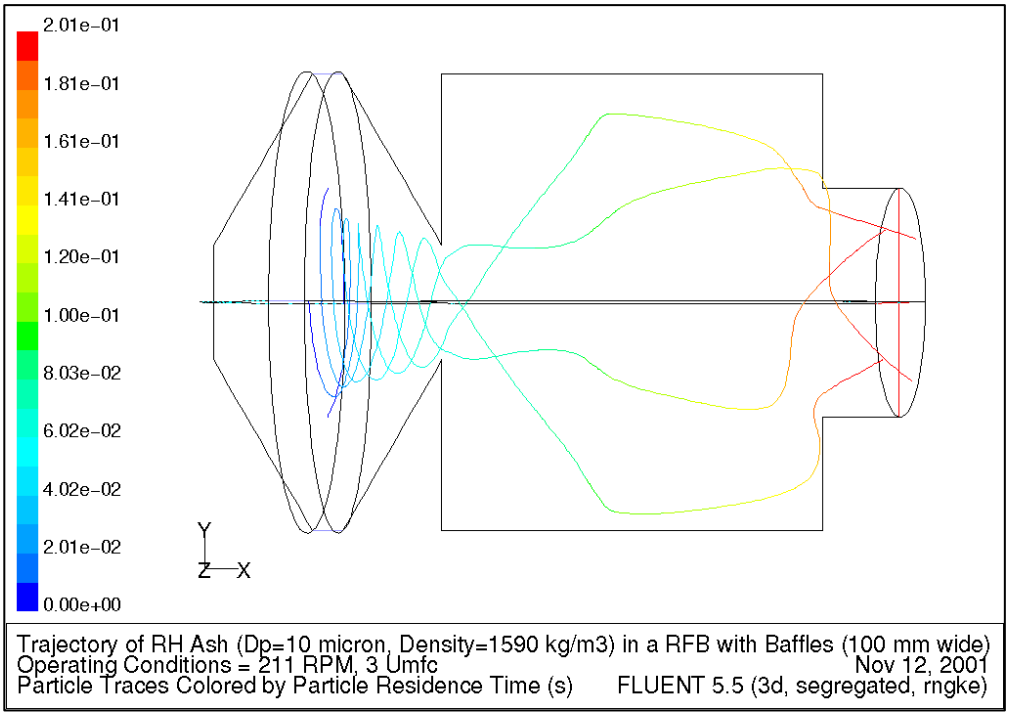

Figure 5.21

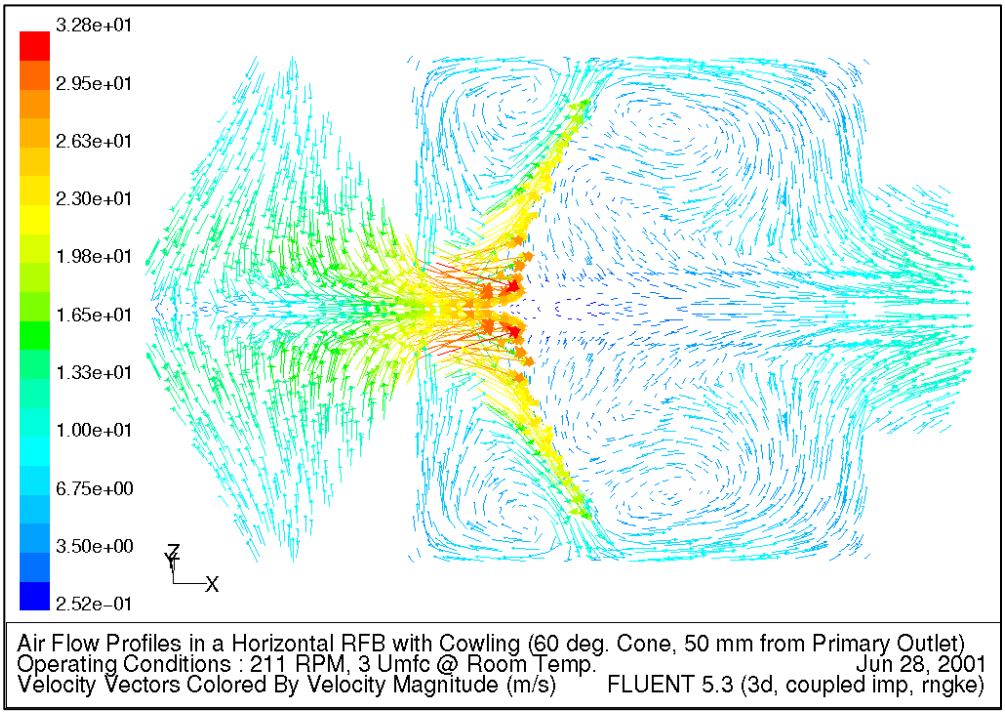

Figure 5.22

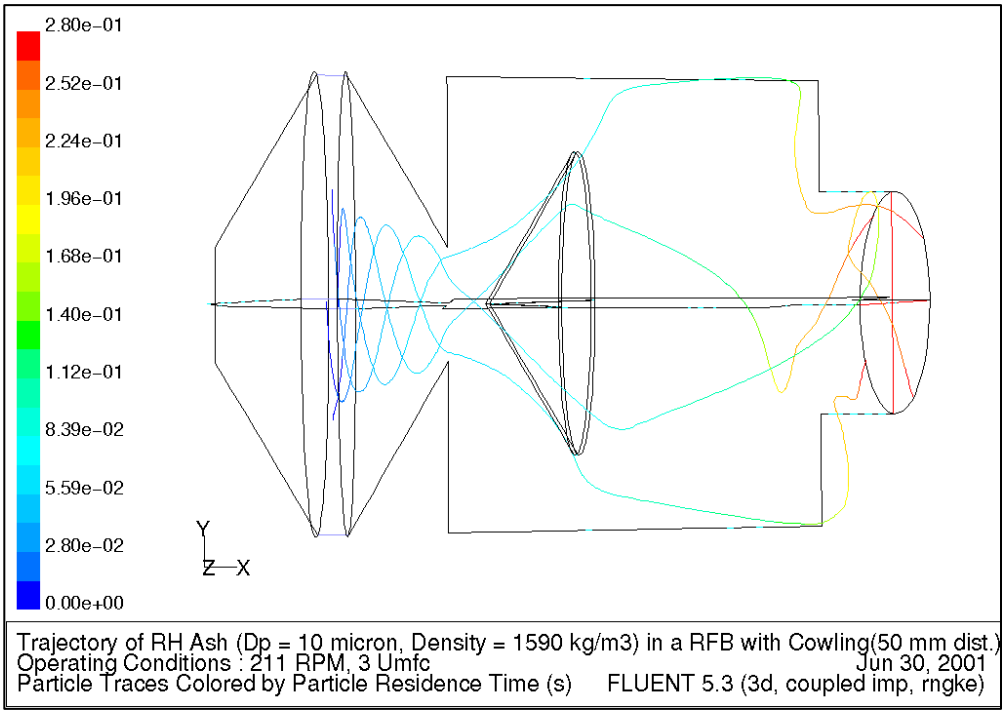

Figure 5.23

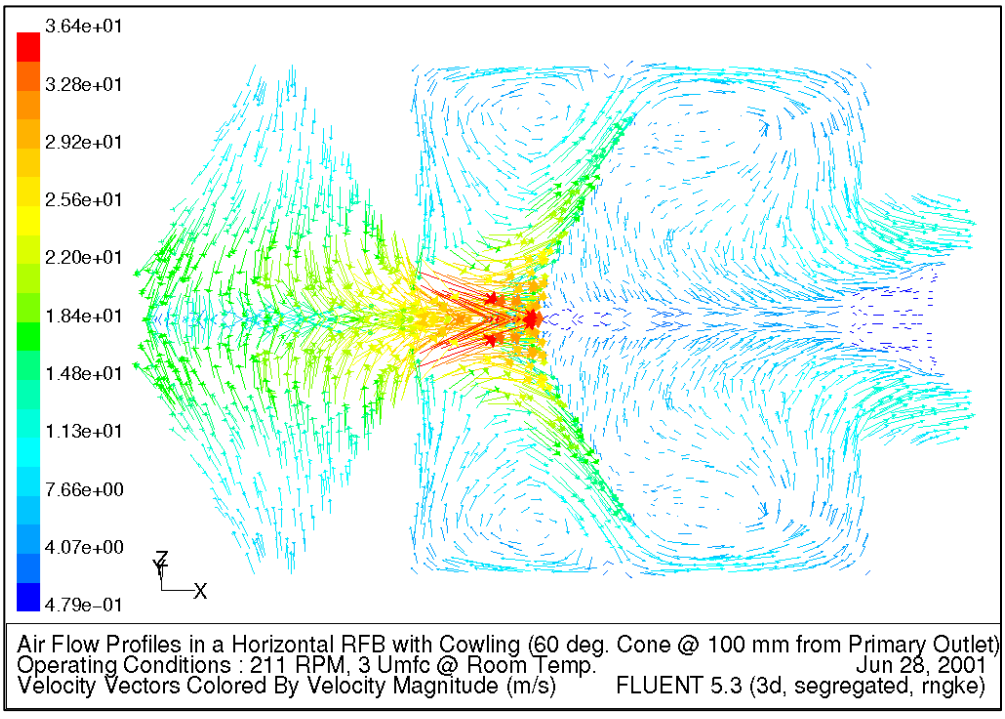

Figure 5.24

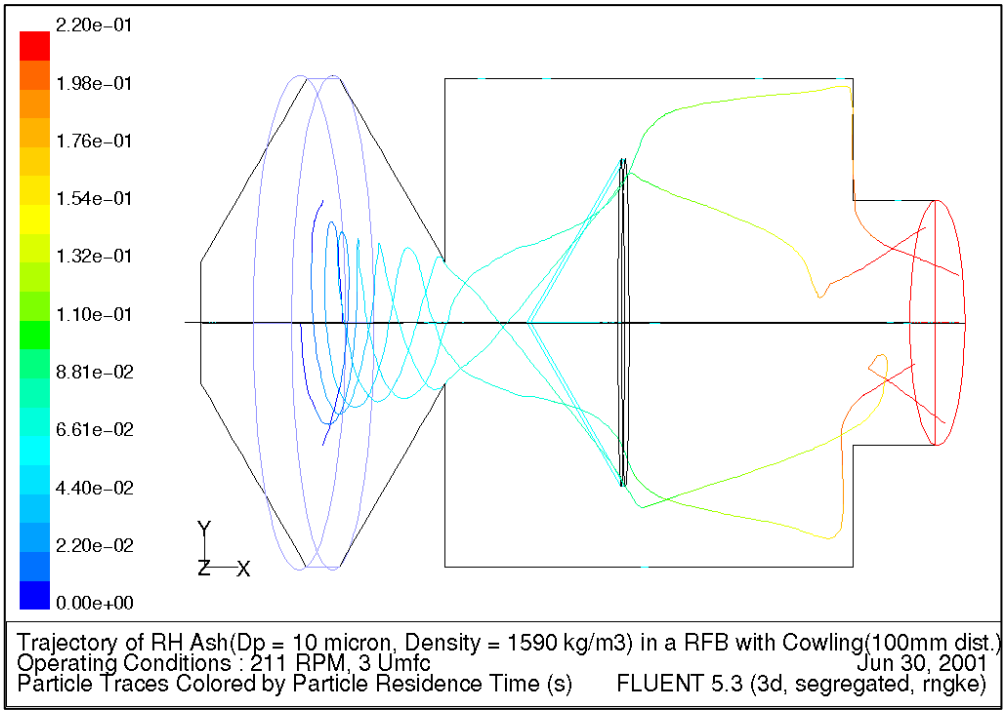

Figure 5.25

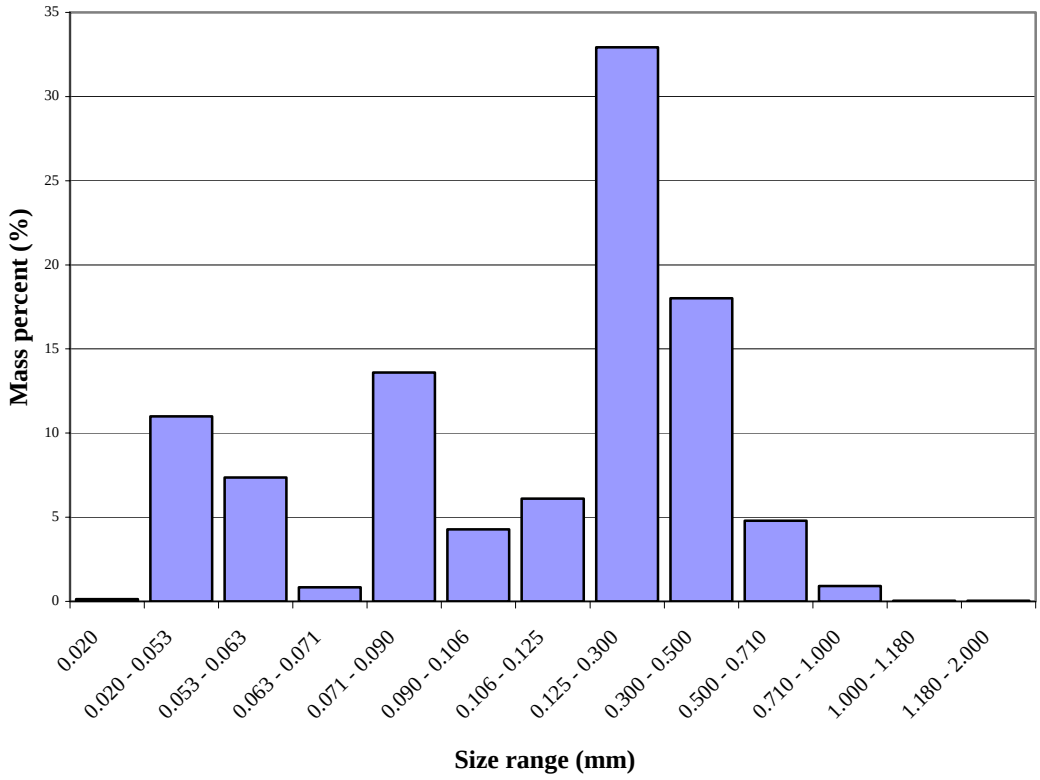

Figure 5.26: Particle size distribution of rice husk ash obtained from combustion of rice husk in a conventional fluidised bed

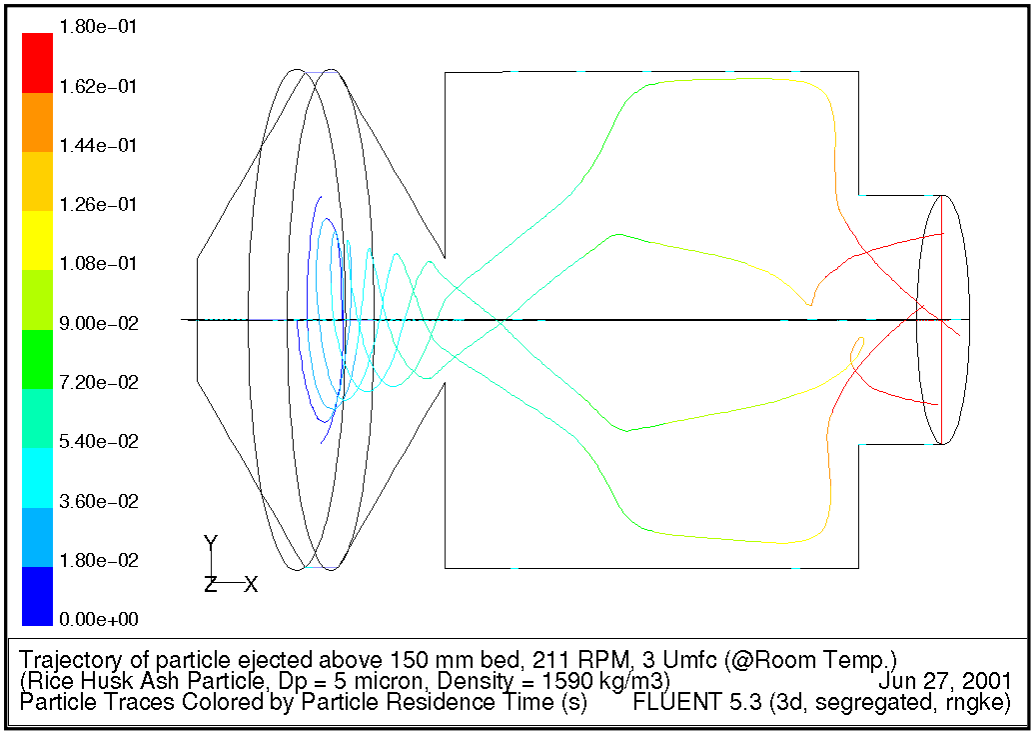

Figure 5.27

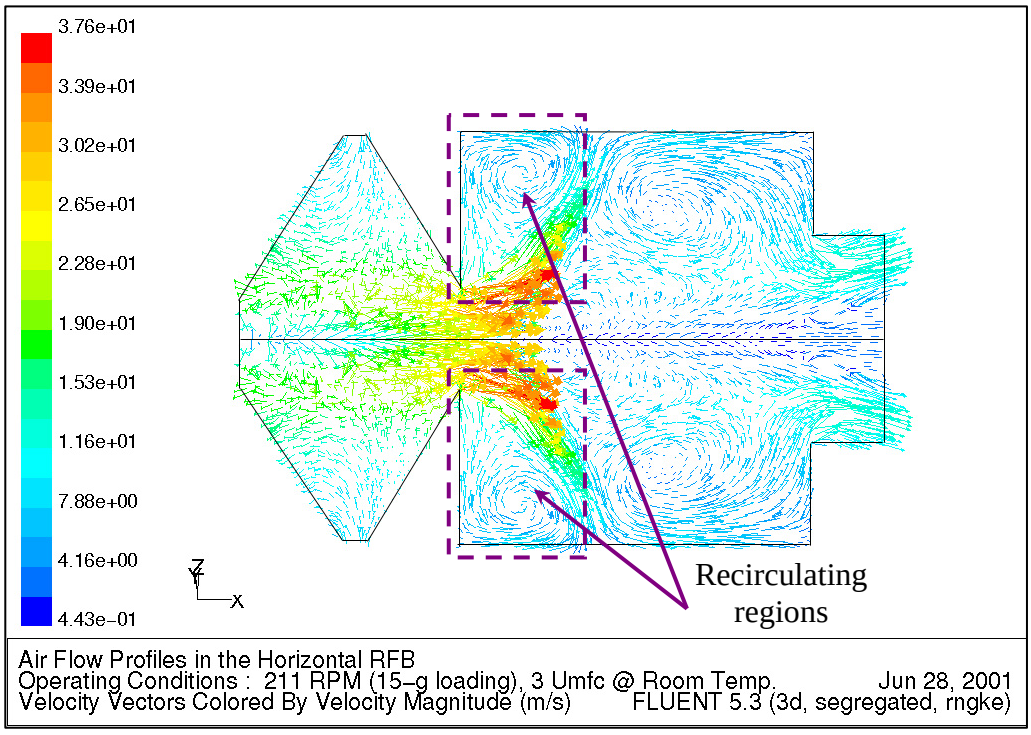

Figure 5.28

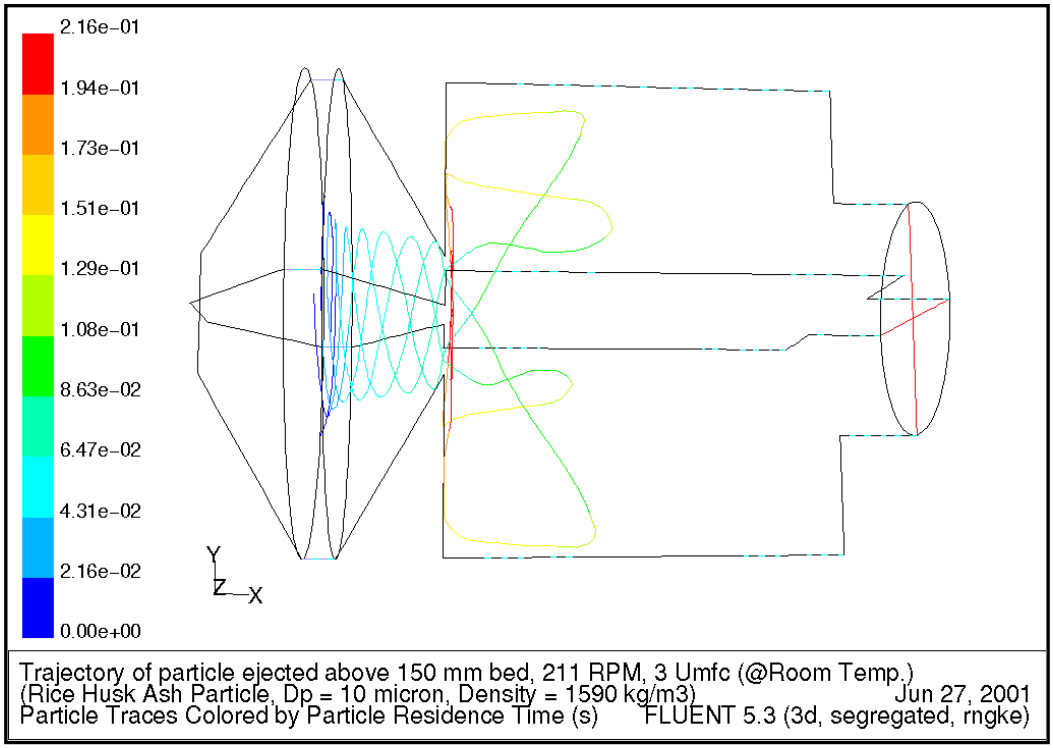

Figure 5.29

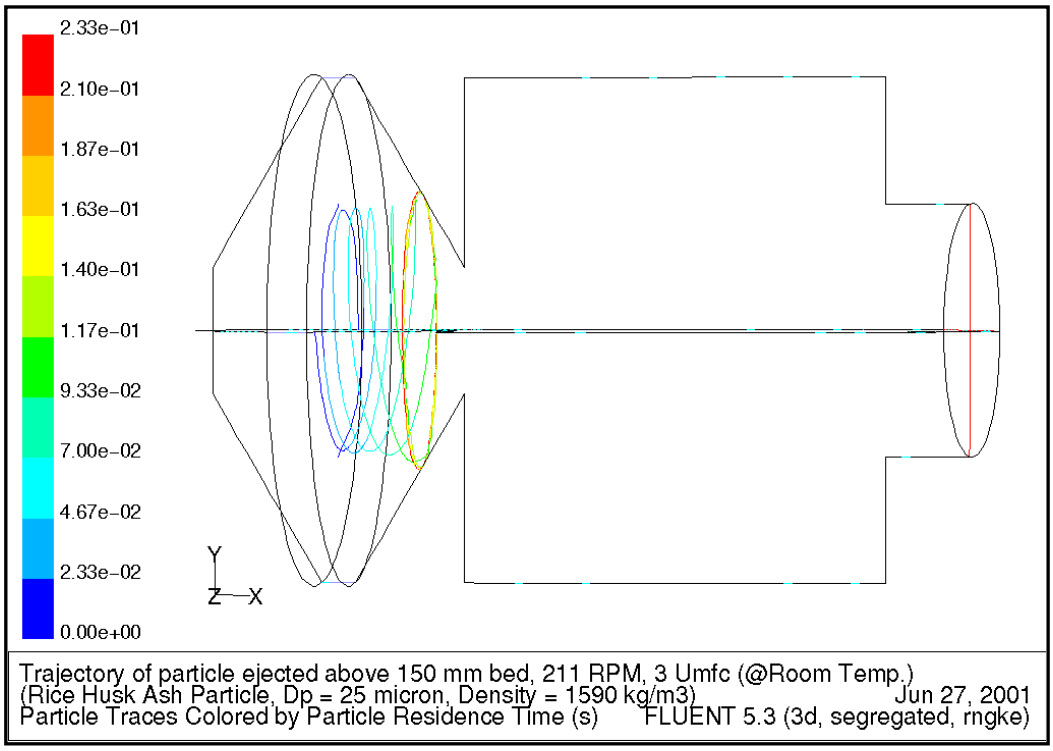

Figure 5.30

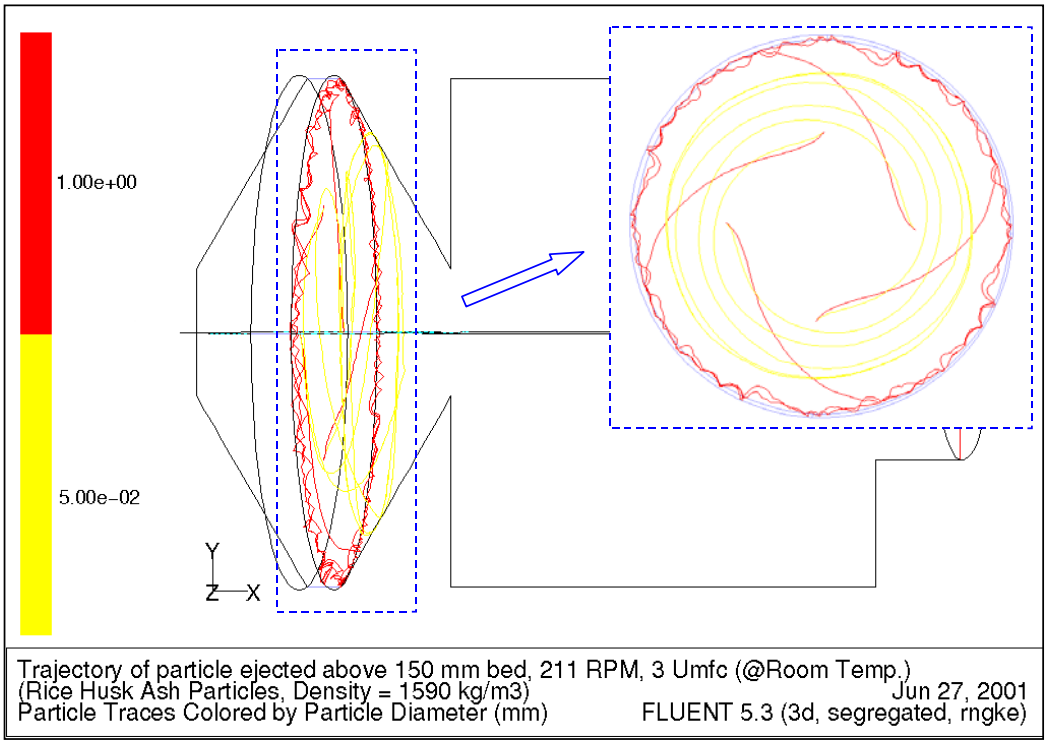

Figure 5.31

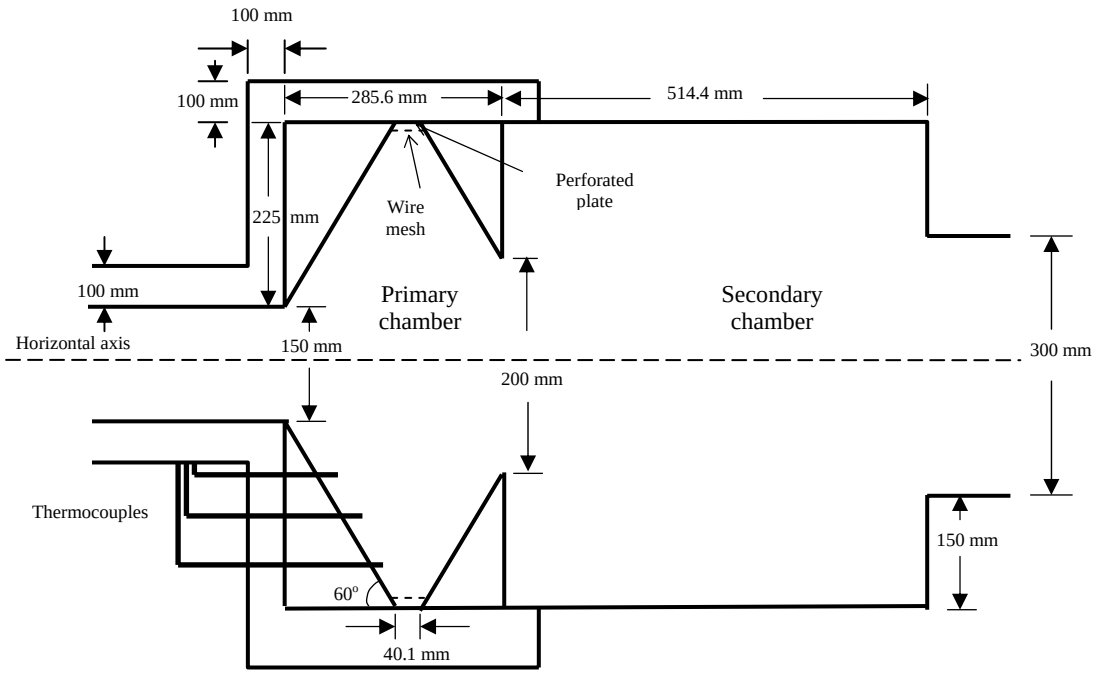

Figure 5.32: Proposed modification to the RFB combustor to allow for spillover of ash particles from the bed

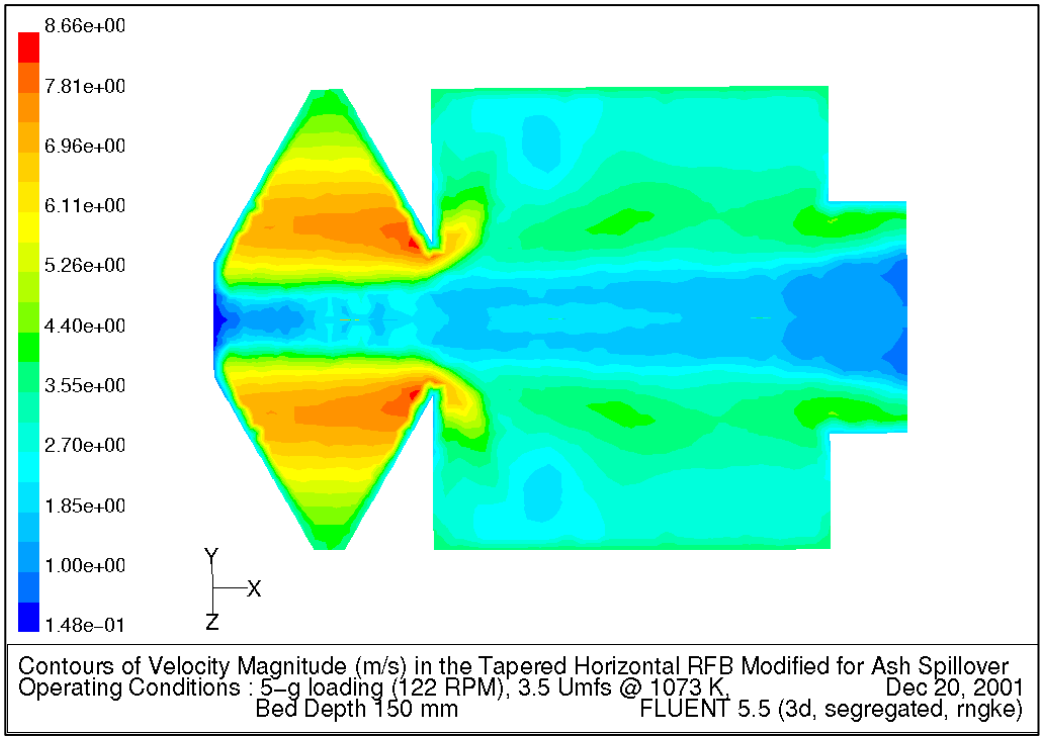

Figure 5.33

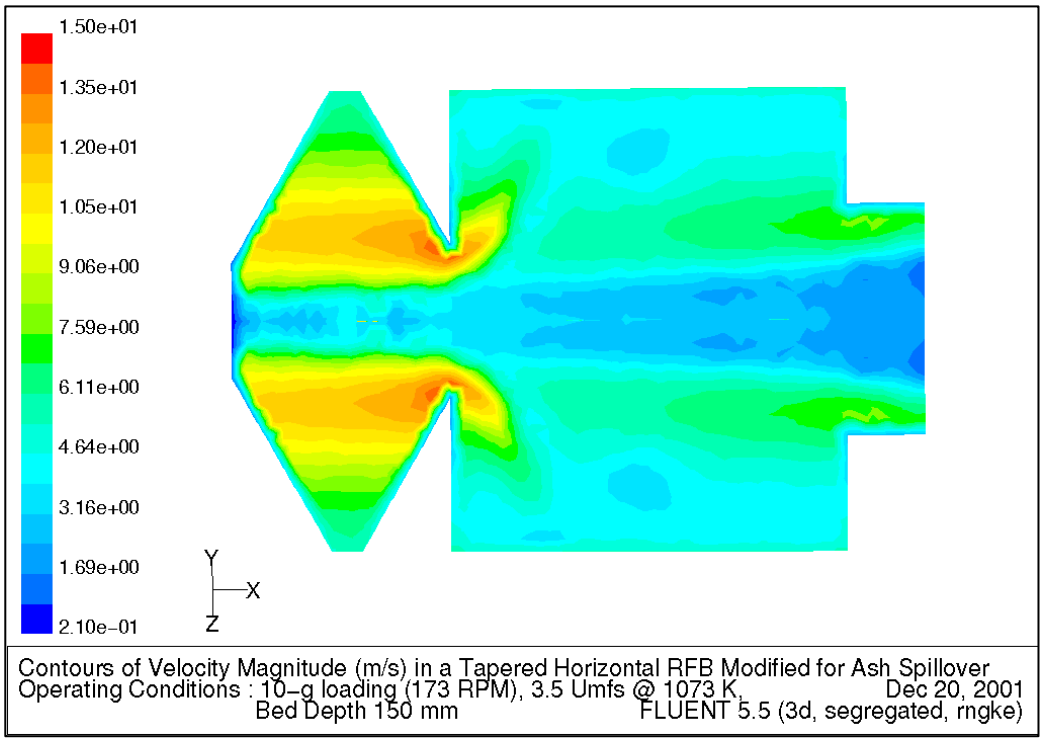

Figure 5.34

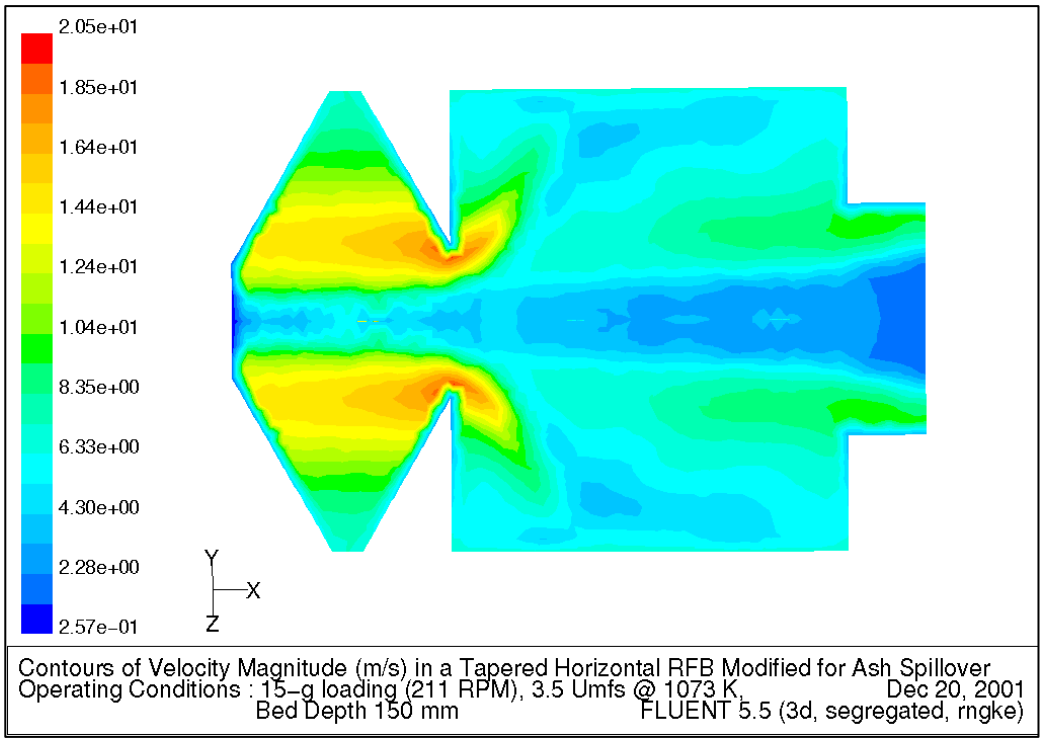

Figure 5.35

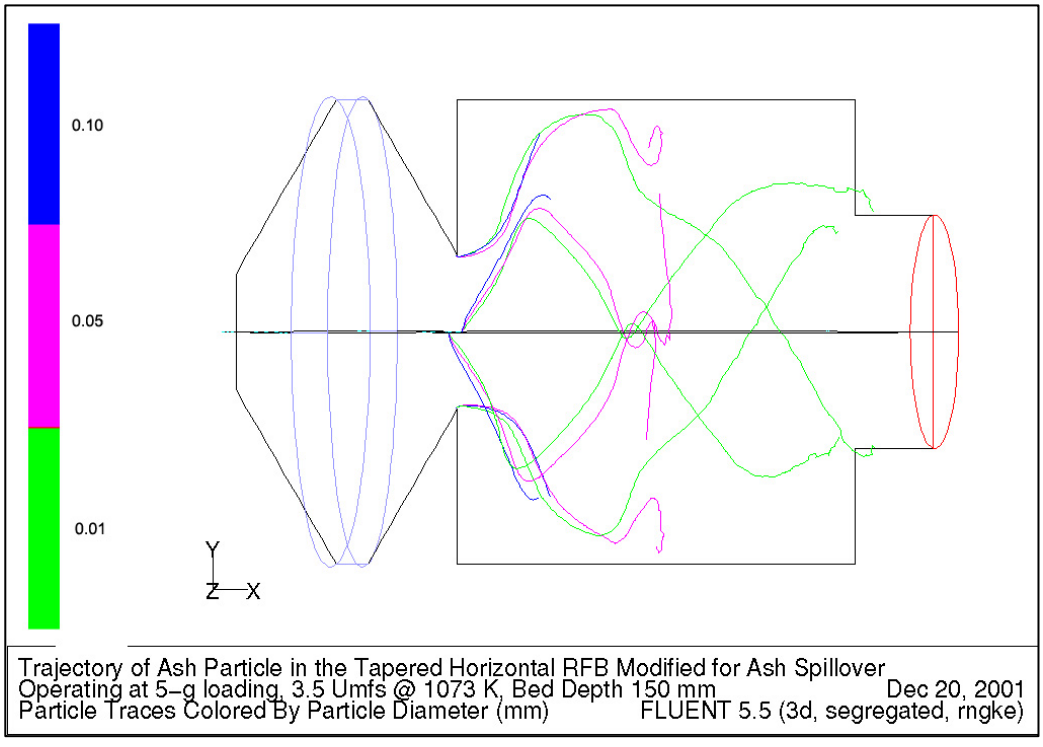

Figure 5.36

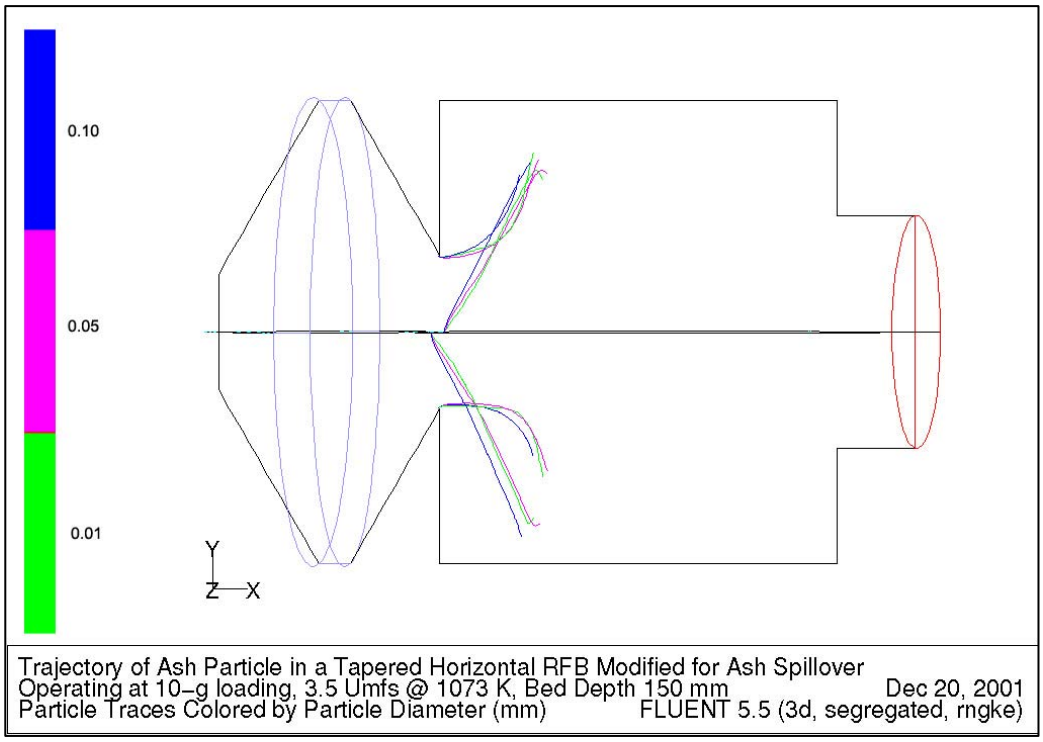
0.10
0.05
0.01
Y
Z
X
Trajectory of Ash Particle in a Tapered Horizontal RFB Modified for Ash Spillover
Operating at 10–g loading, 3.5 Umfs @ 1073 K, Bed Depth 150 mm
Dec 20, 2001
Particle Traces Colored by Particle Diameter (mm)
FLUENT 5.5 (3d, segregated, rngke)

Figure 5.37

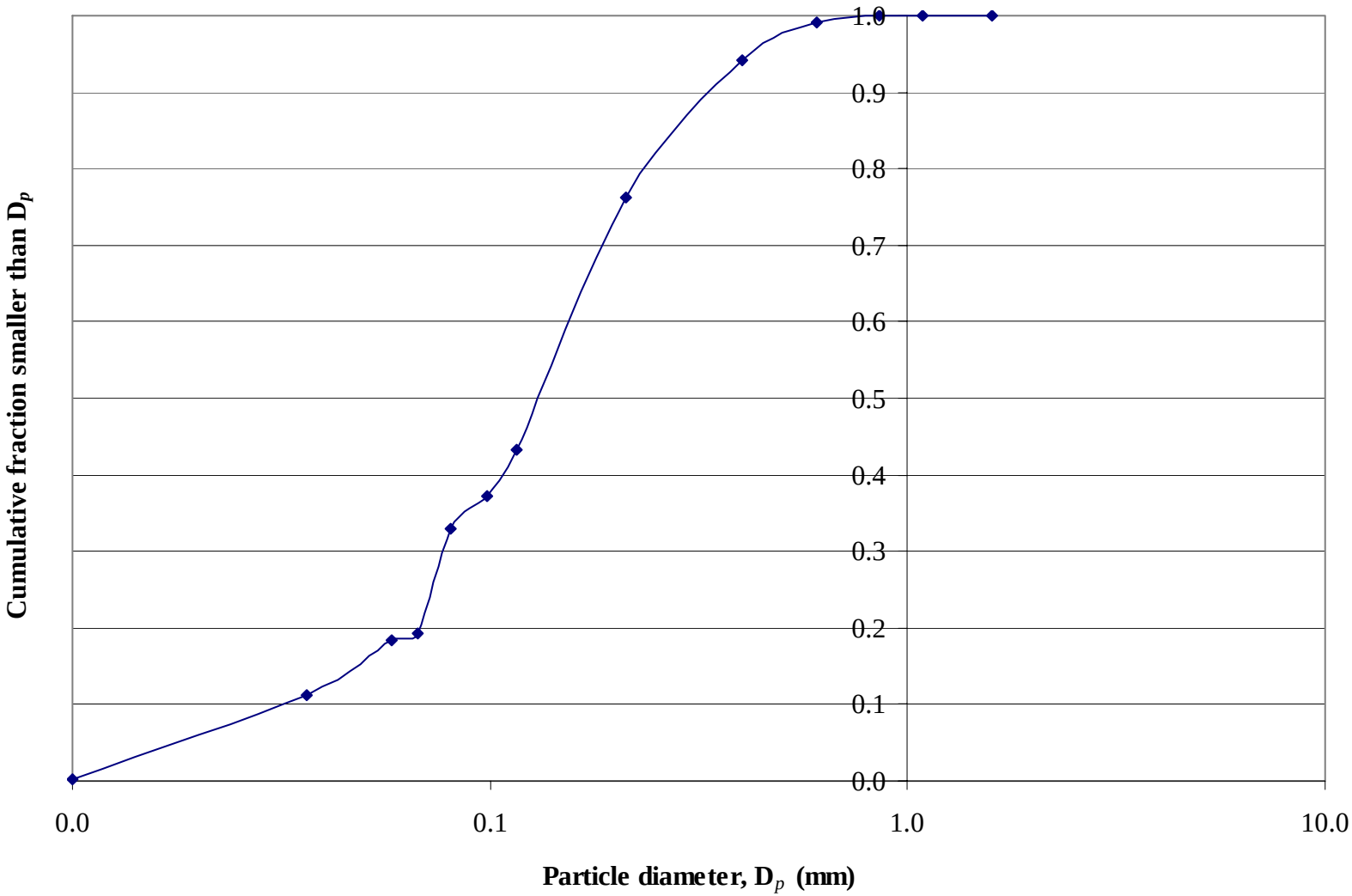

Figure 5.38: Cumulative plot for screen analysis of rice husk ash

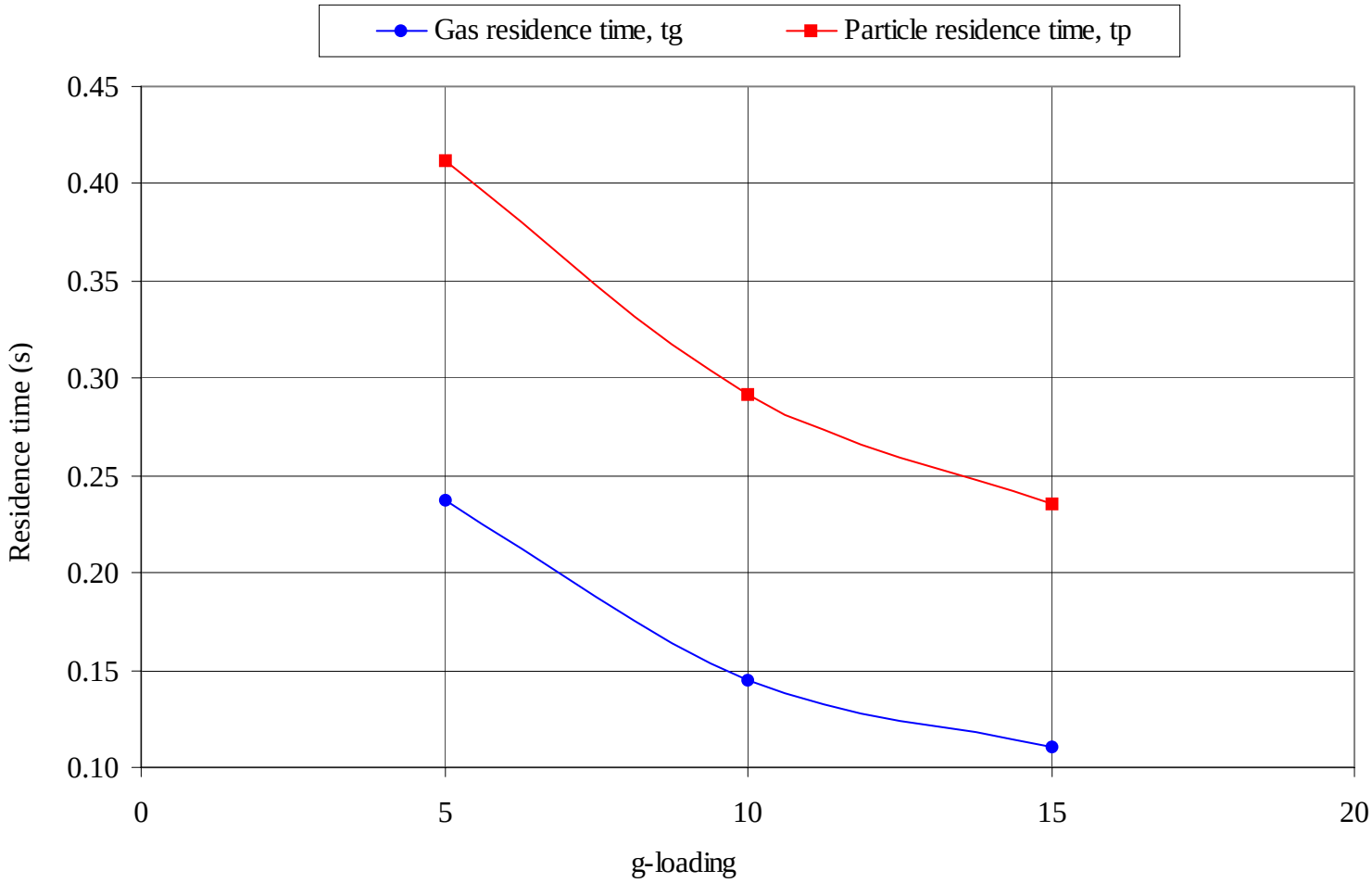

Figure 5.39: Plot of gas/particle residence time versus bed rotating speed (g-loading)

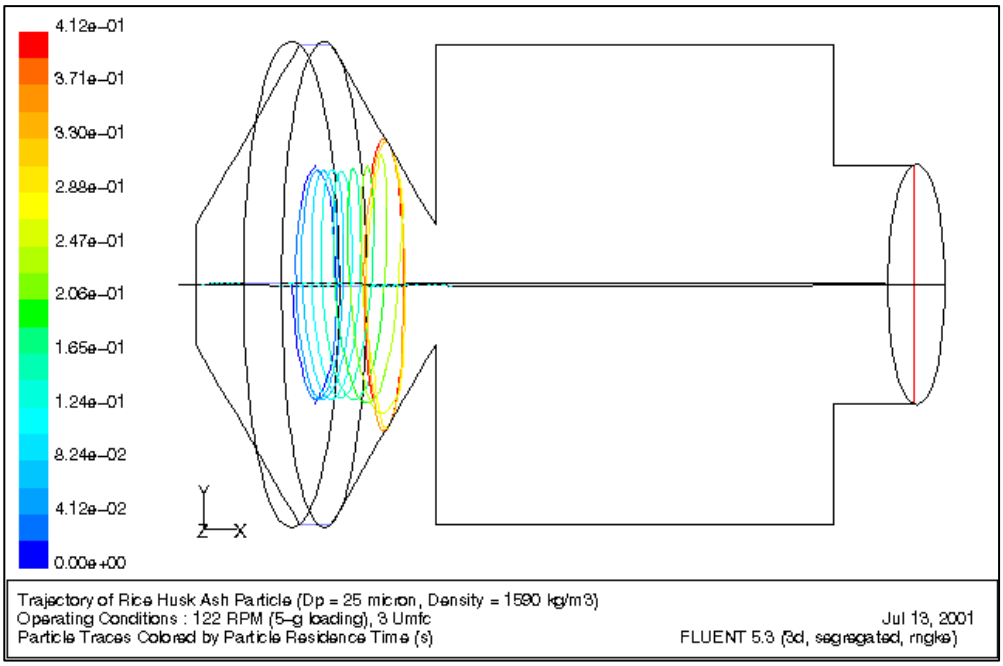

Figure 5.40

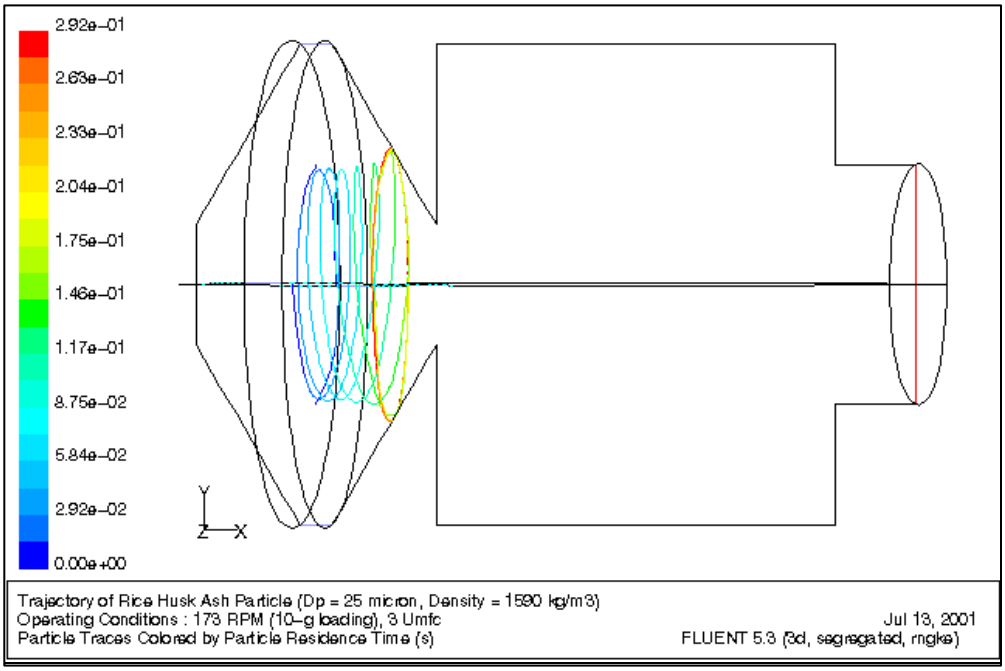

Figure 5.41

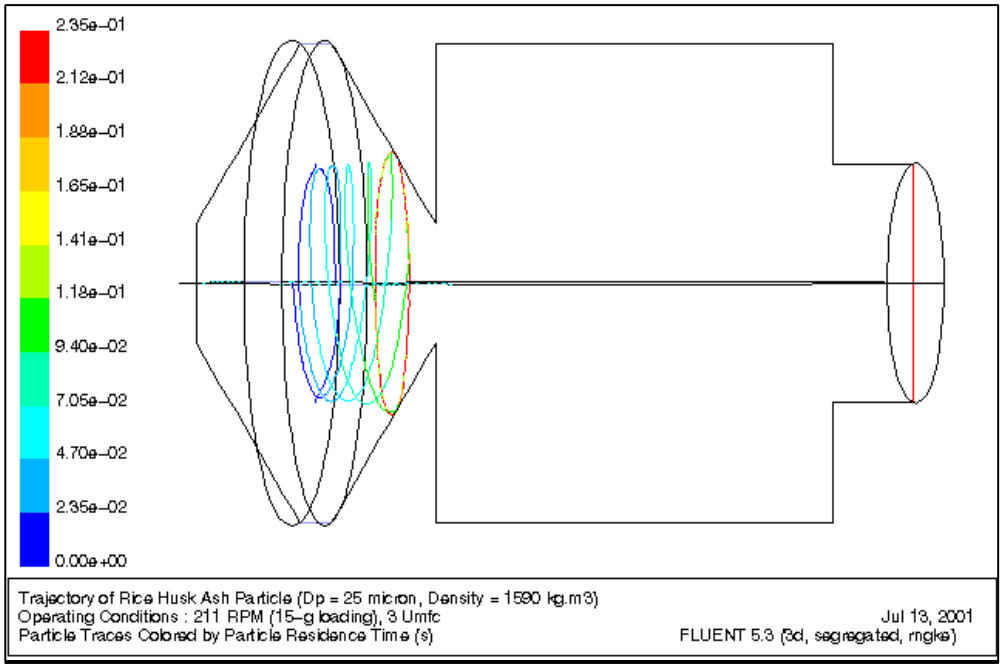

Figure 5.42

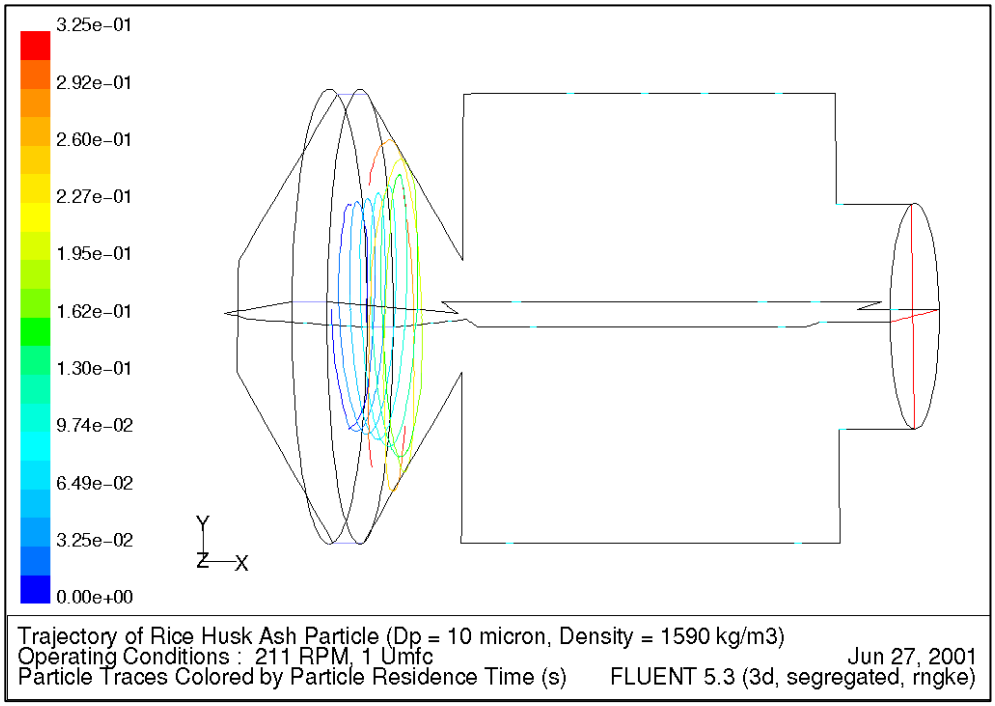

Figure 5.43

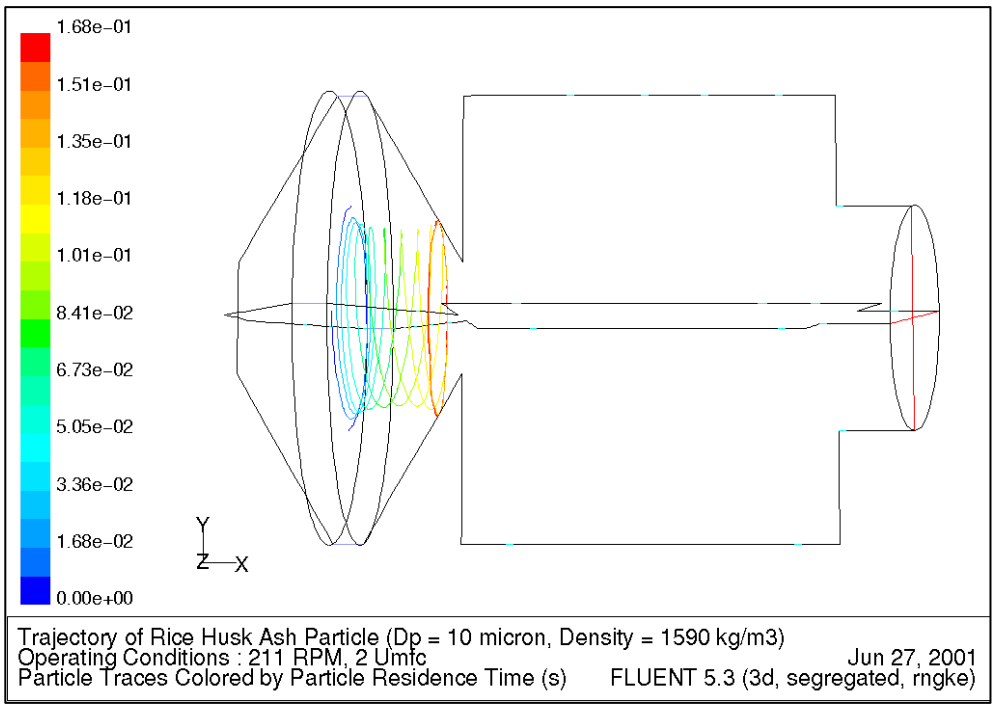

Figure 5.44

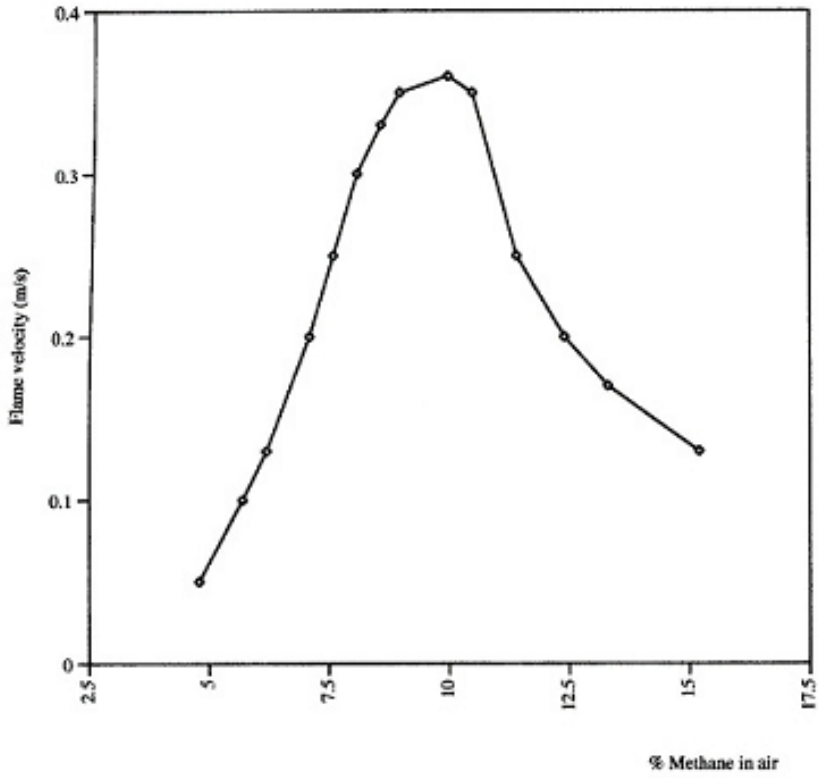

Figure 5.45: Normal flame velocities for different methane concentrations in air (Sarkar, 1990)

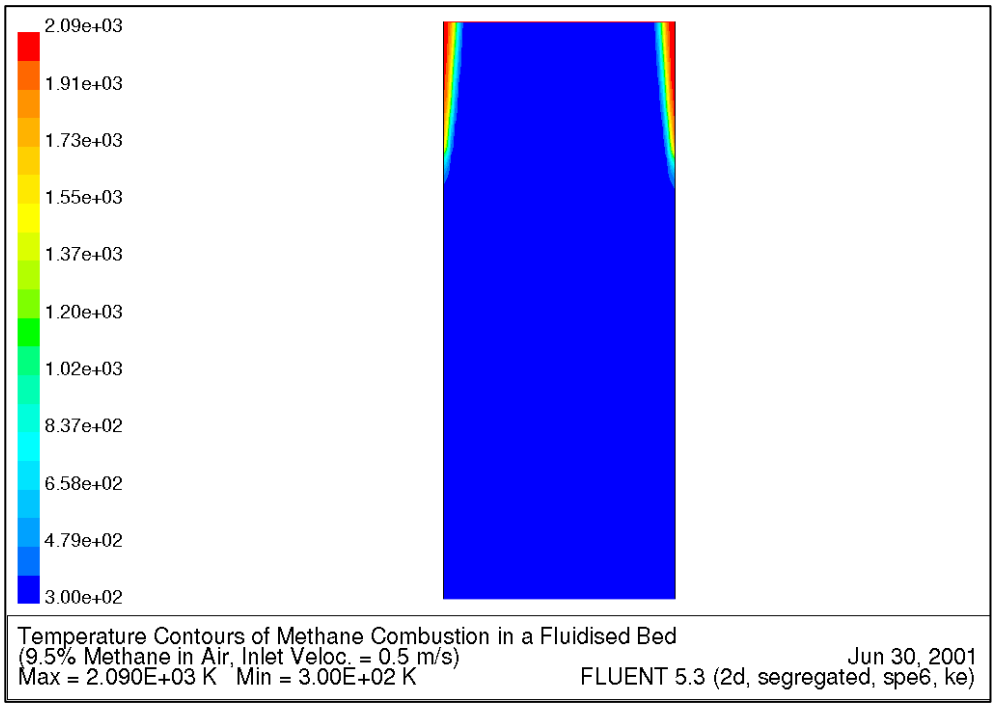

Figure 5.46

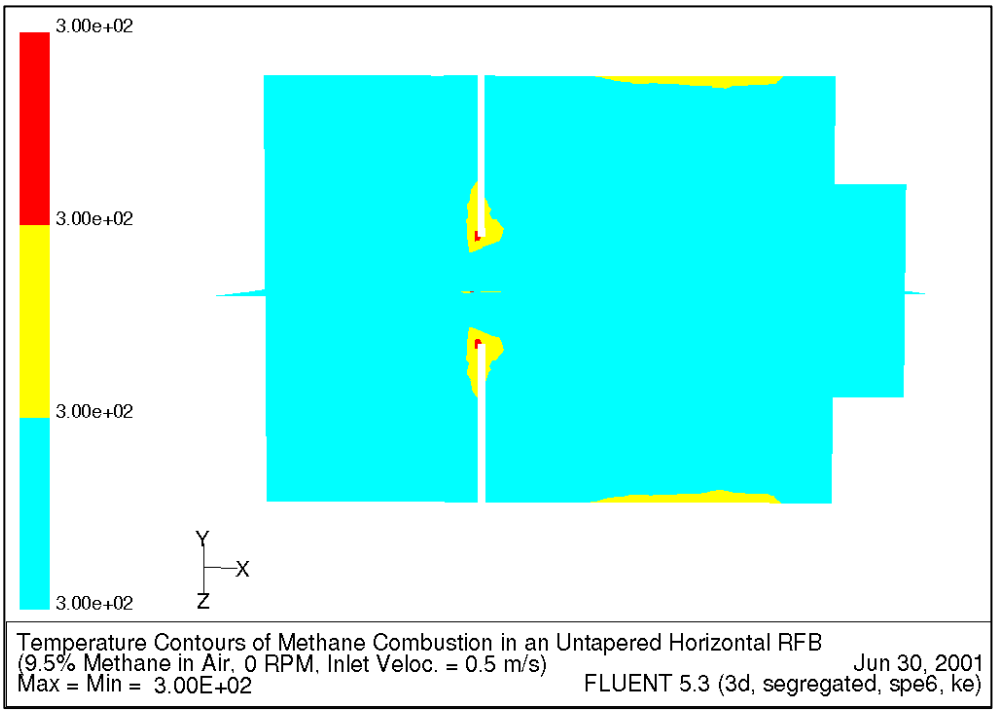

Figure 5.47

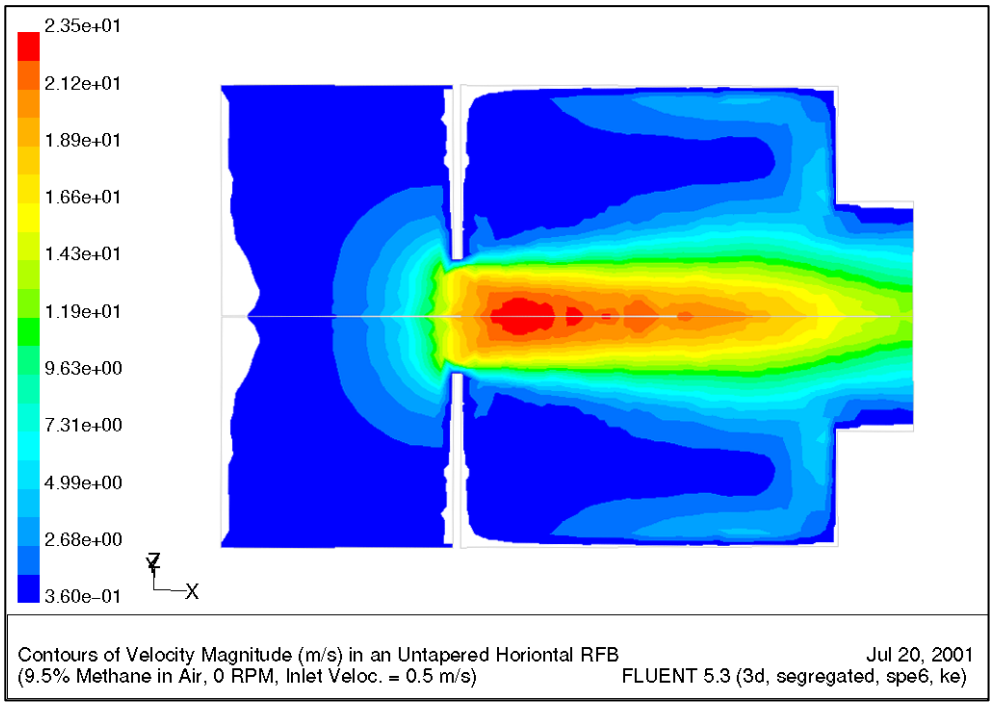

Figure 5.48

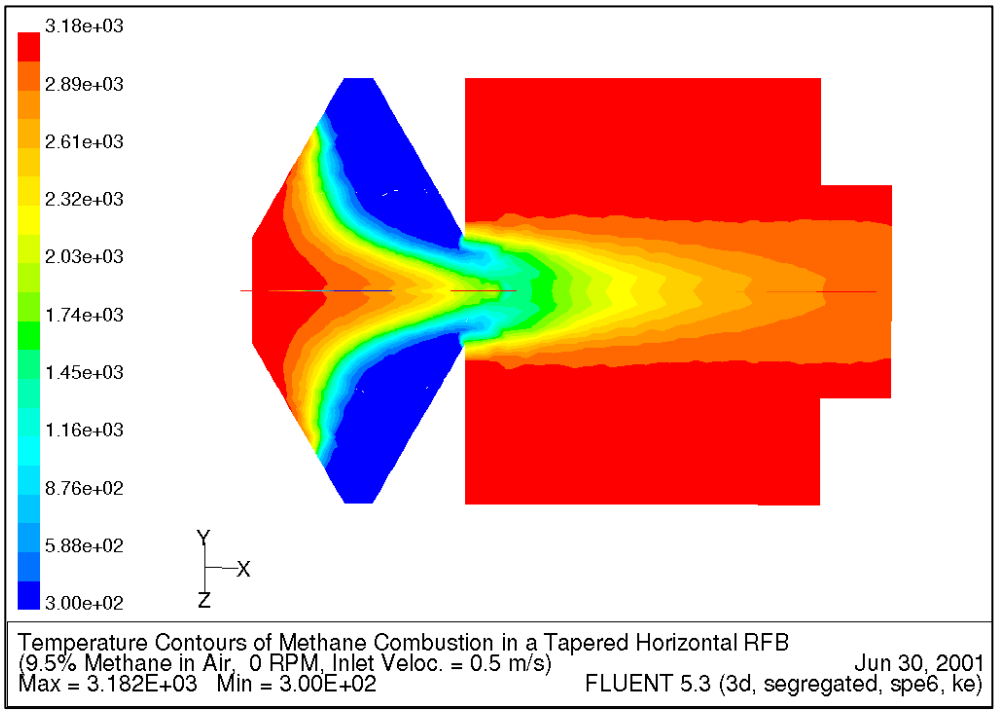

Figure 5.49

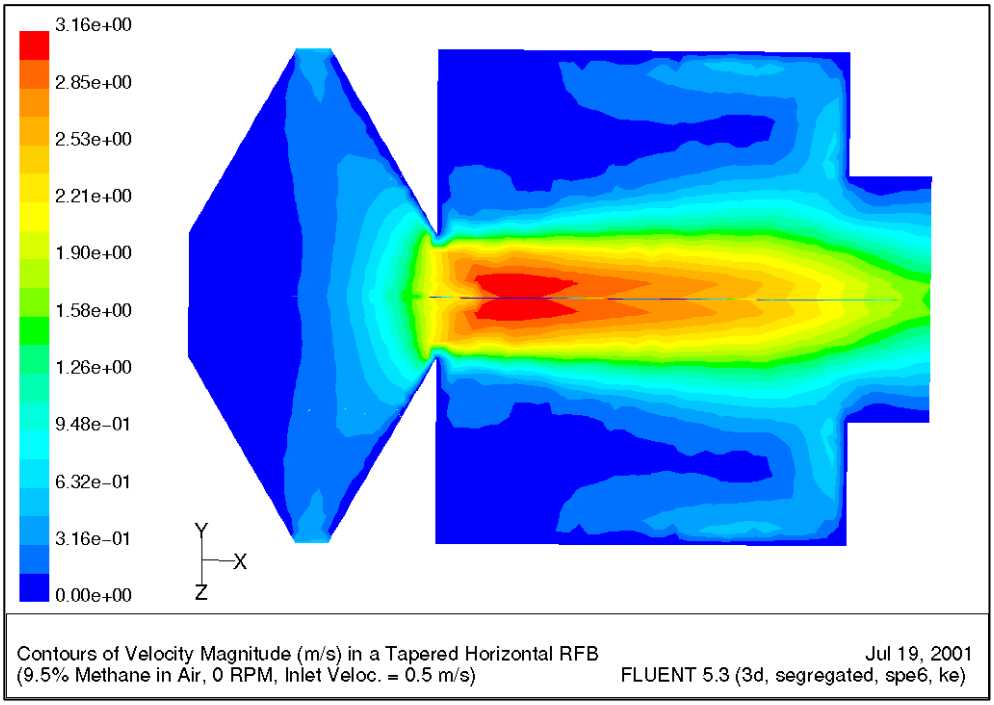

Figure 5.50

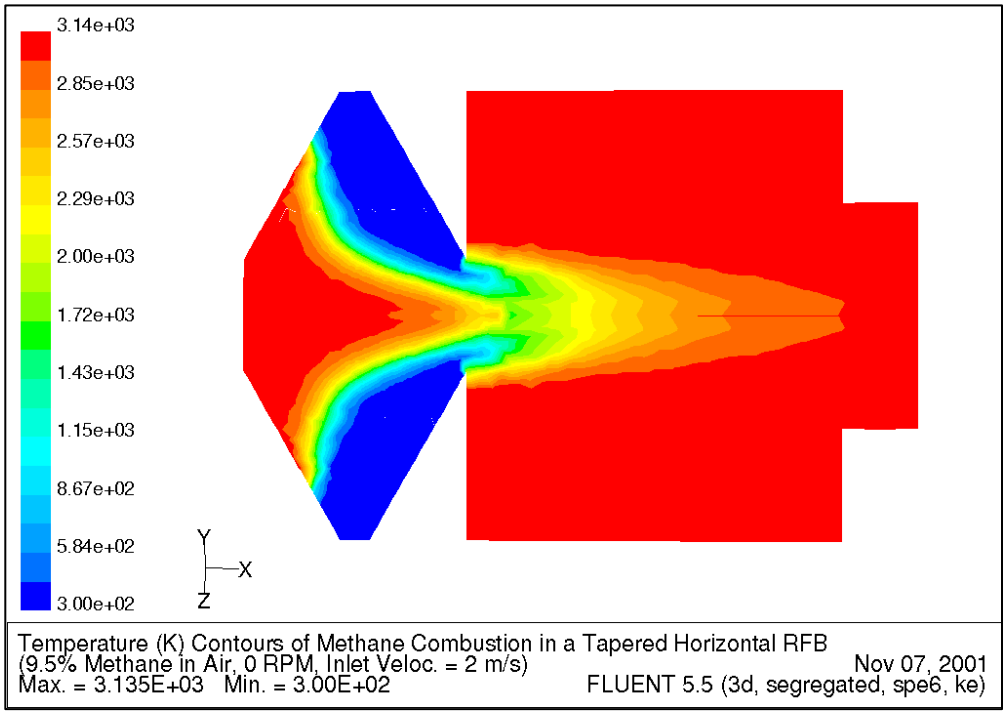

Figure 5.51

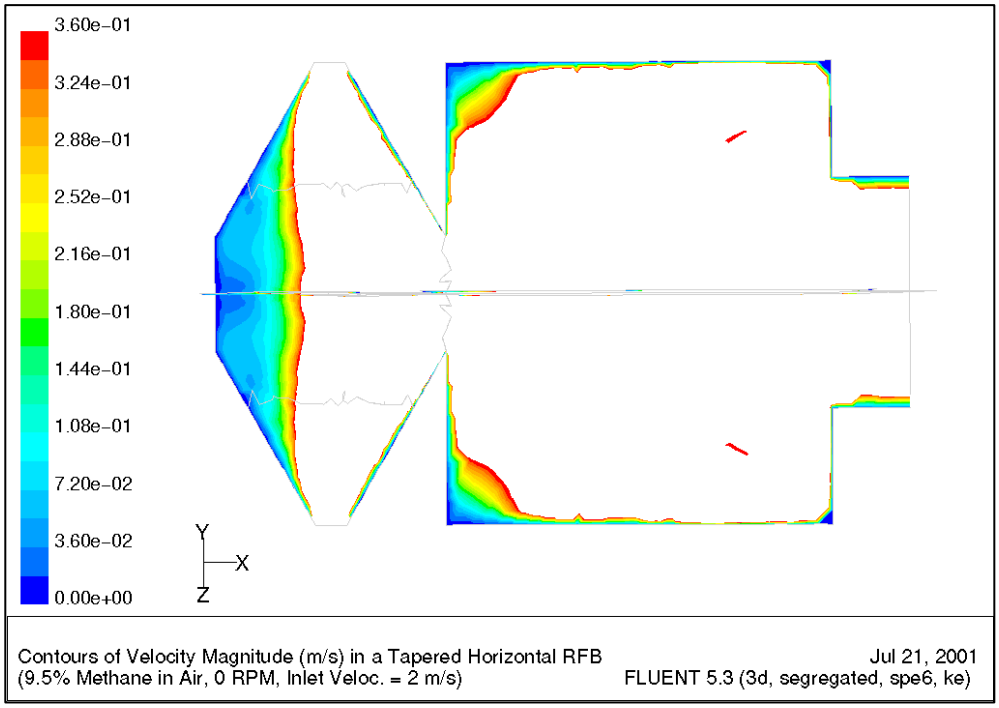

Figure 5.52

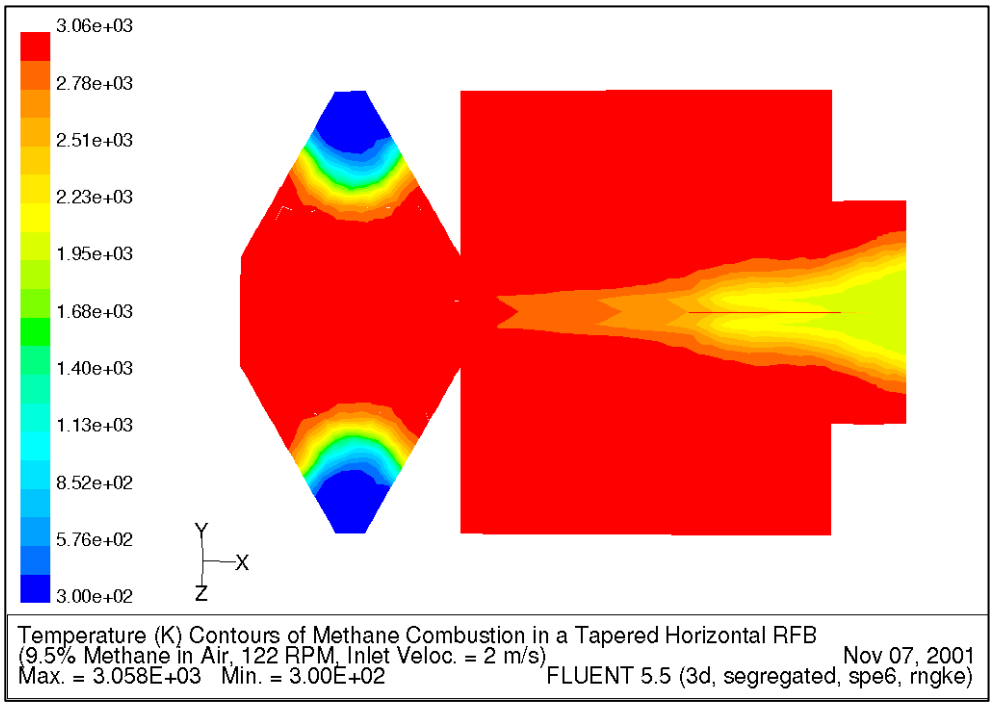

Figure 5.53

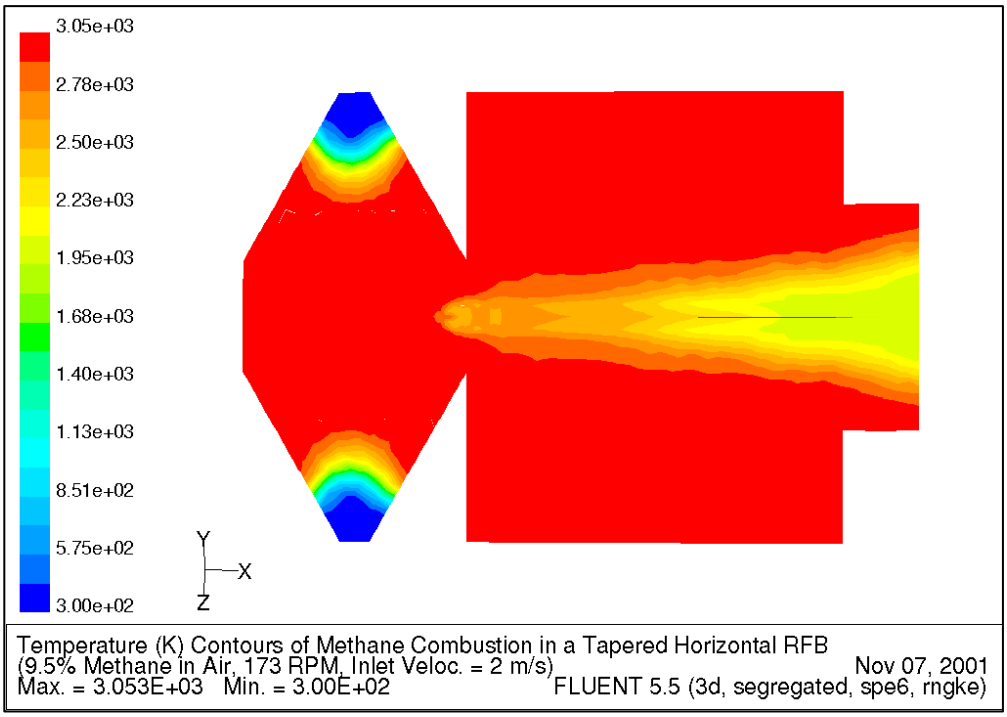

Figure 5.54

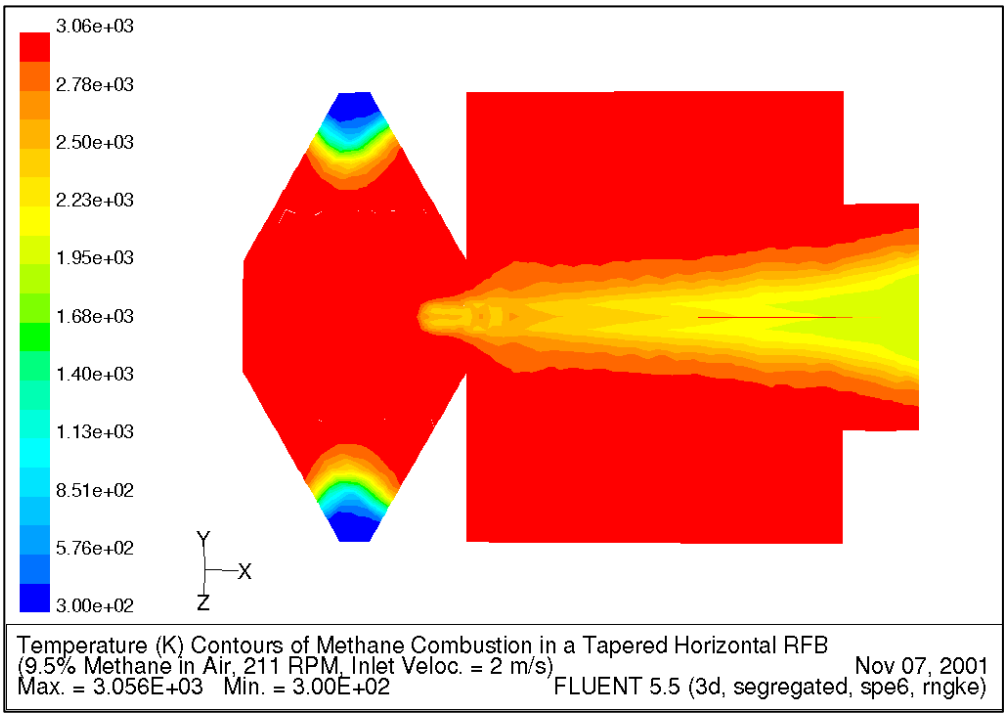

Figure 5.55

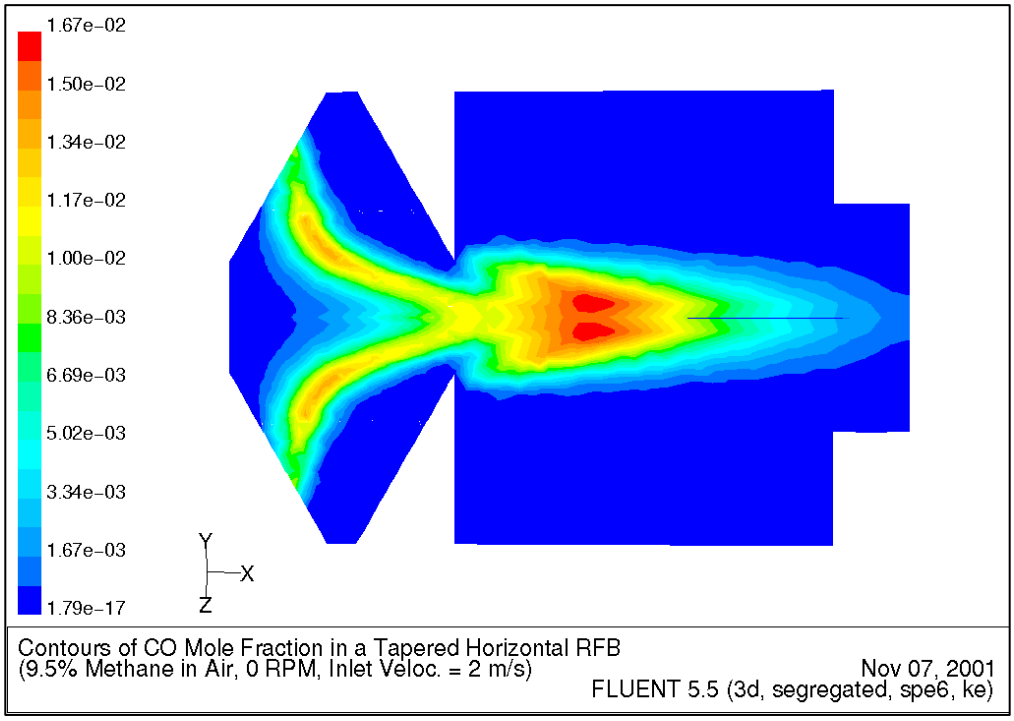

Figure 5.56

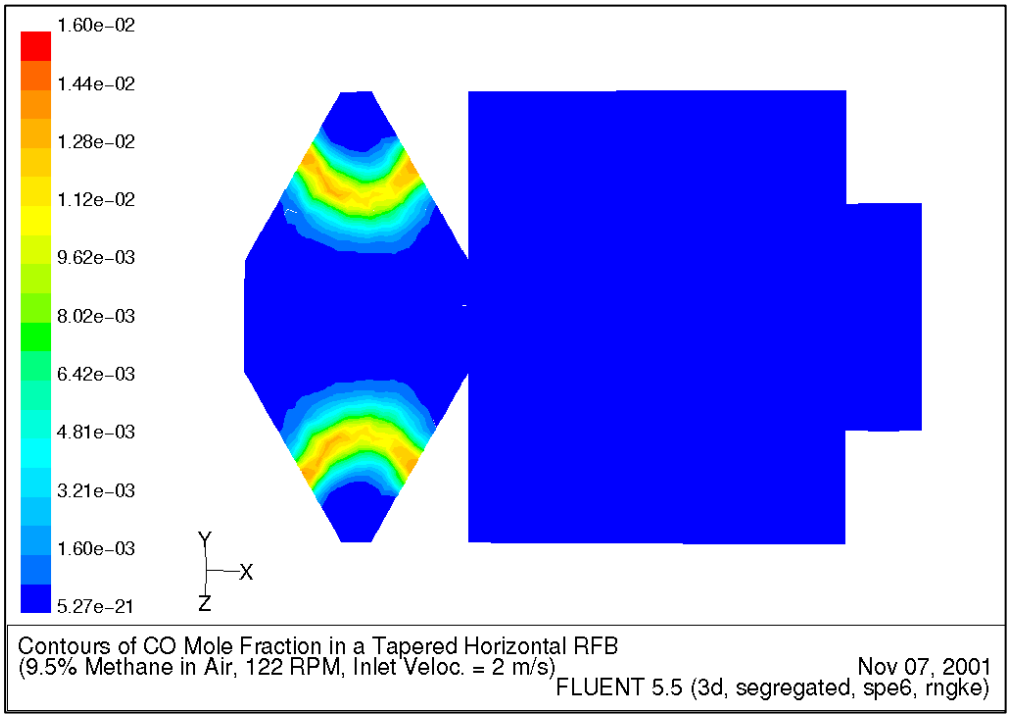

Figure 5.57

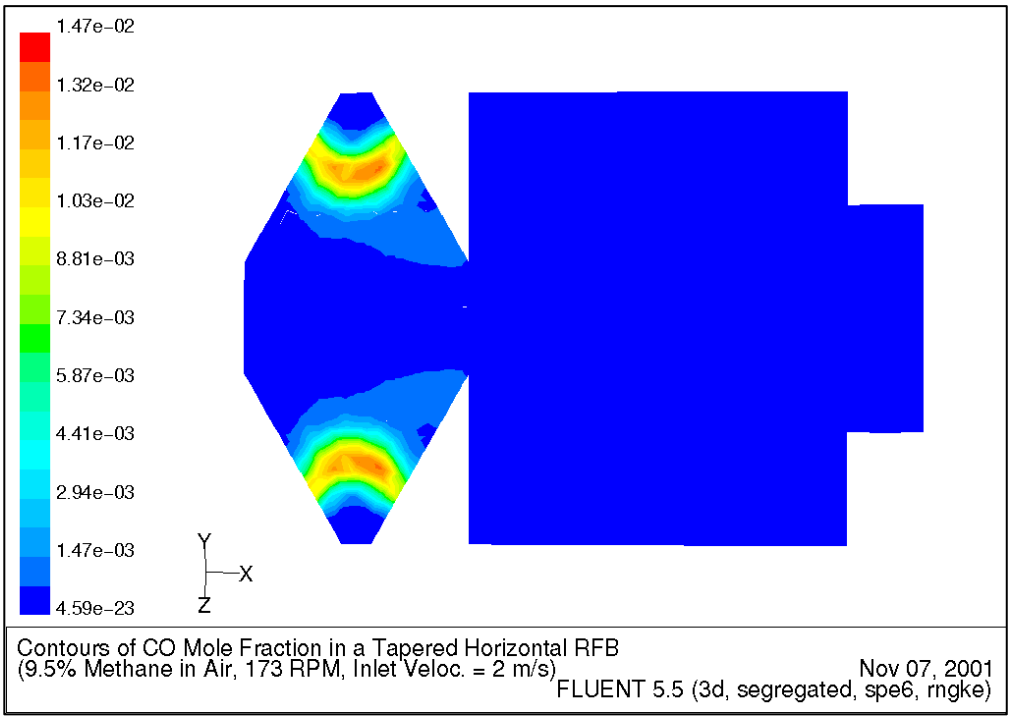

Figure 5.58

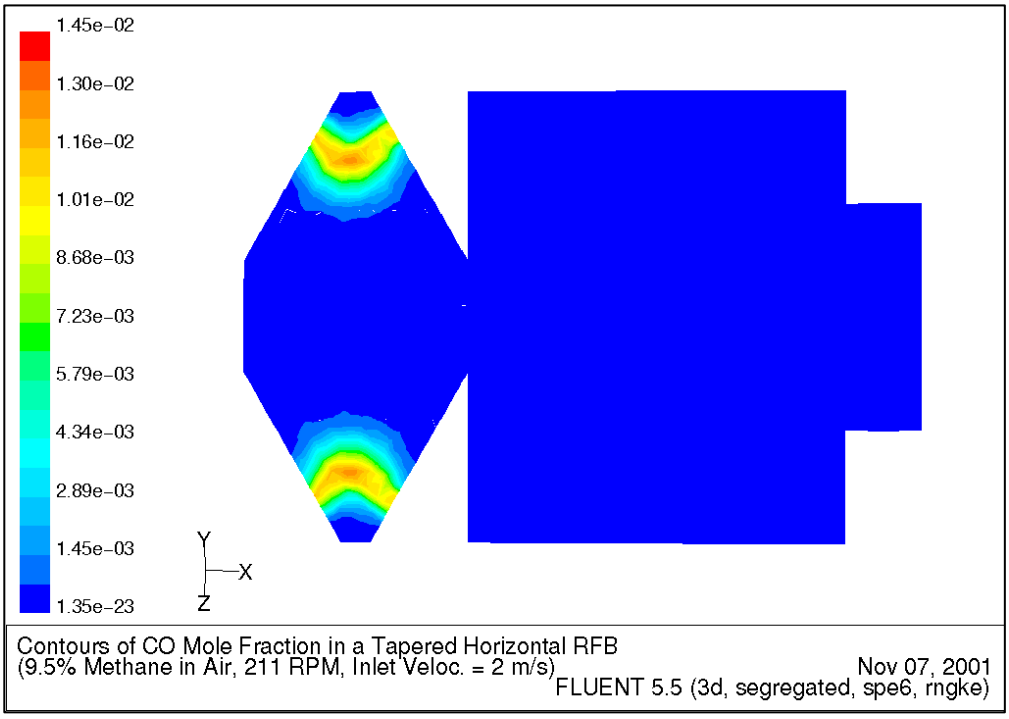

Figure 5.59

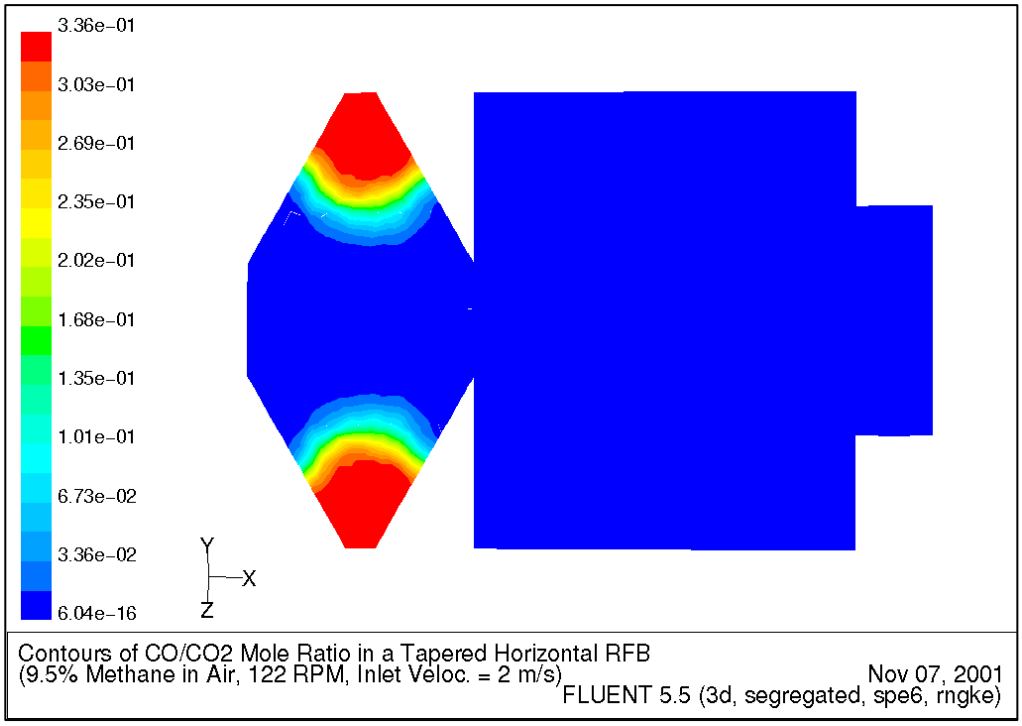

Figure 5.60

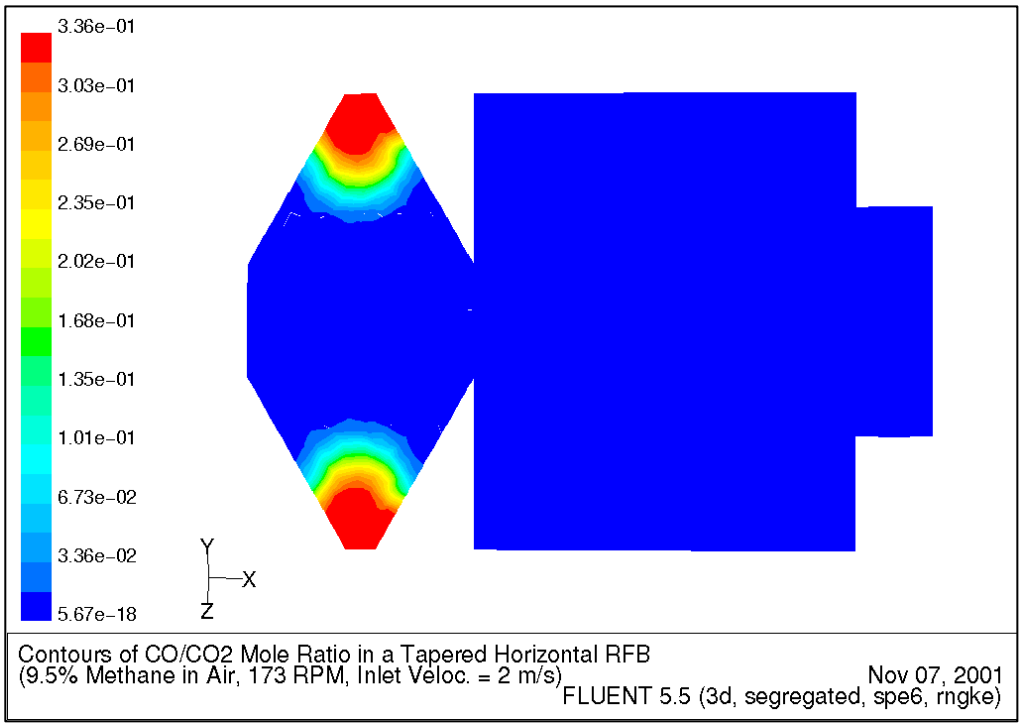

Figure 5.61

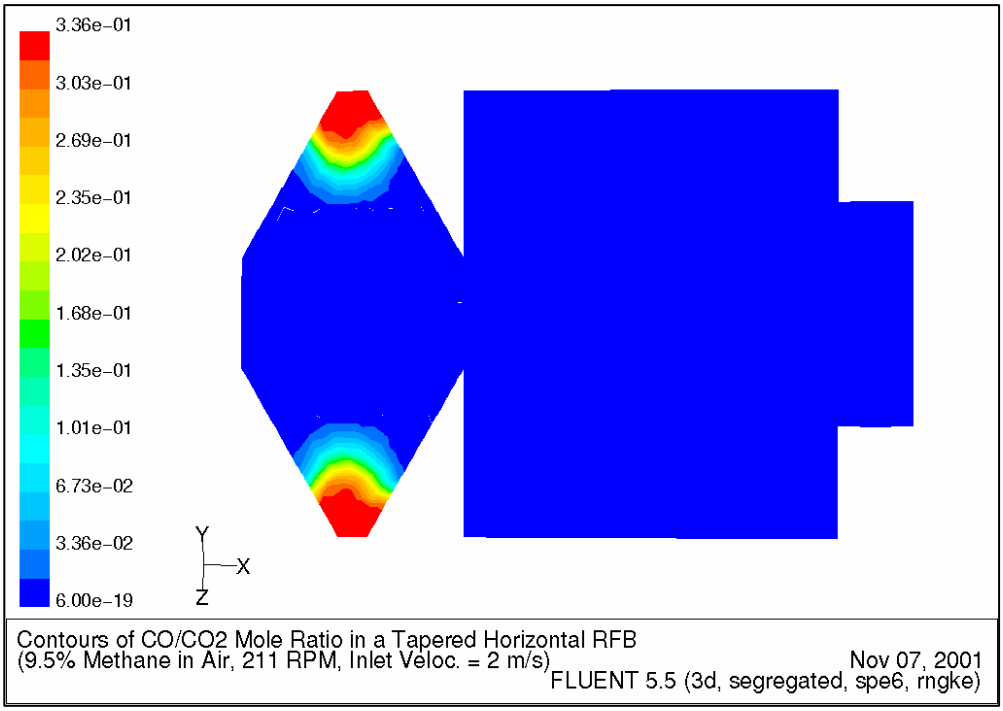

Figure 5.62

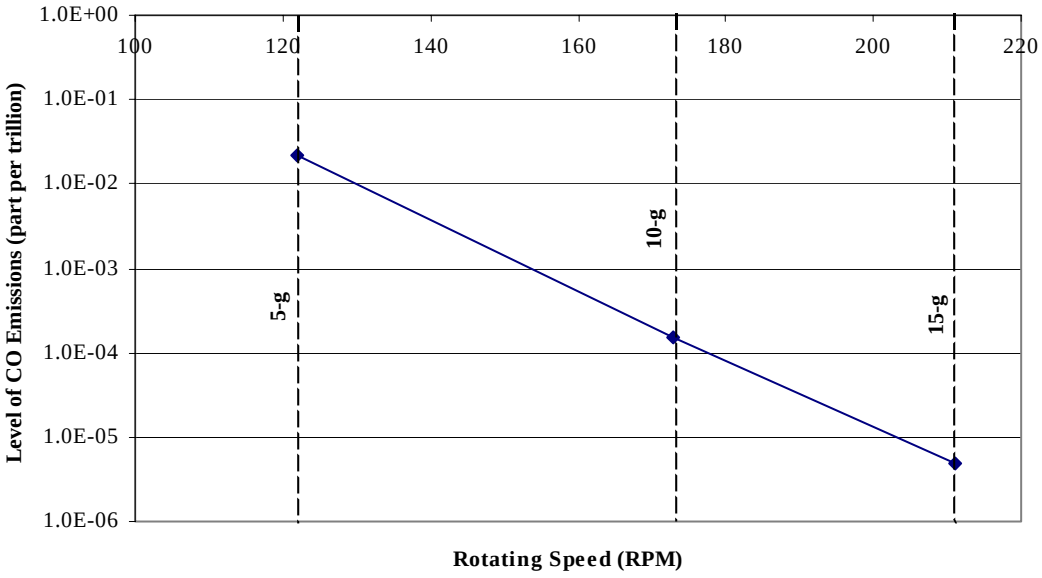

Figure 5.63: CO emission levels in the exhaust gases from the RFB combustor during the combustion of methane (9.5% methane in air) at different rotating speeds

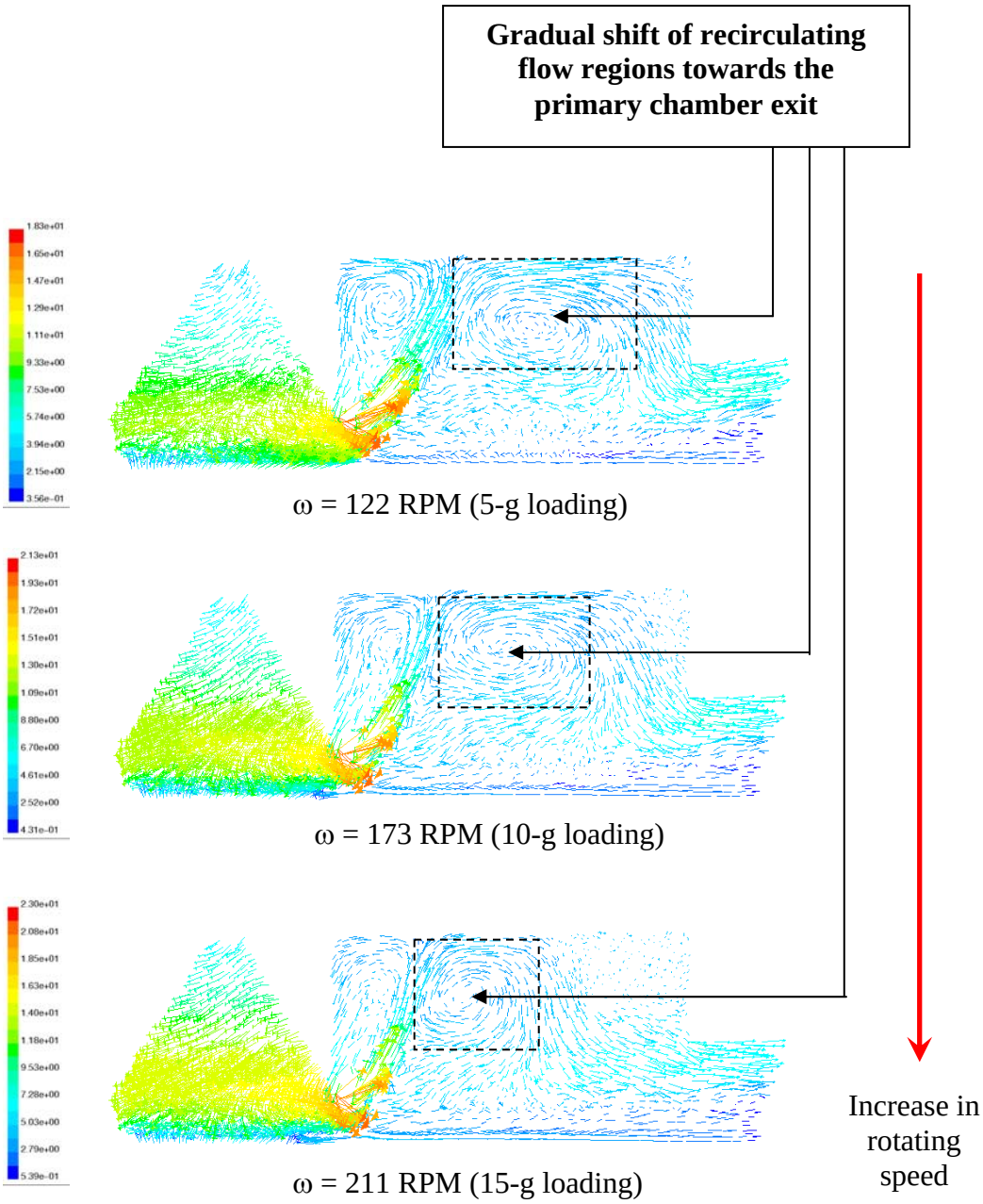

Figure 5.64: Velocity vectors at the axisymmetric plane of the RFB during methane combustion (9.5% methane in air, inlet veloc. = 2 m/s) at different rotating speeds
[Velocity vectors coloured by velocity magnitude (m/s)]

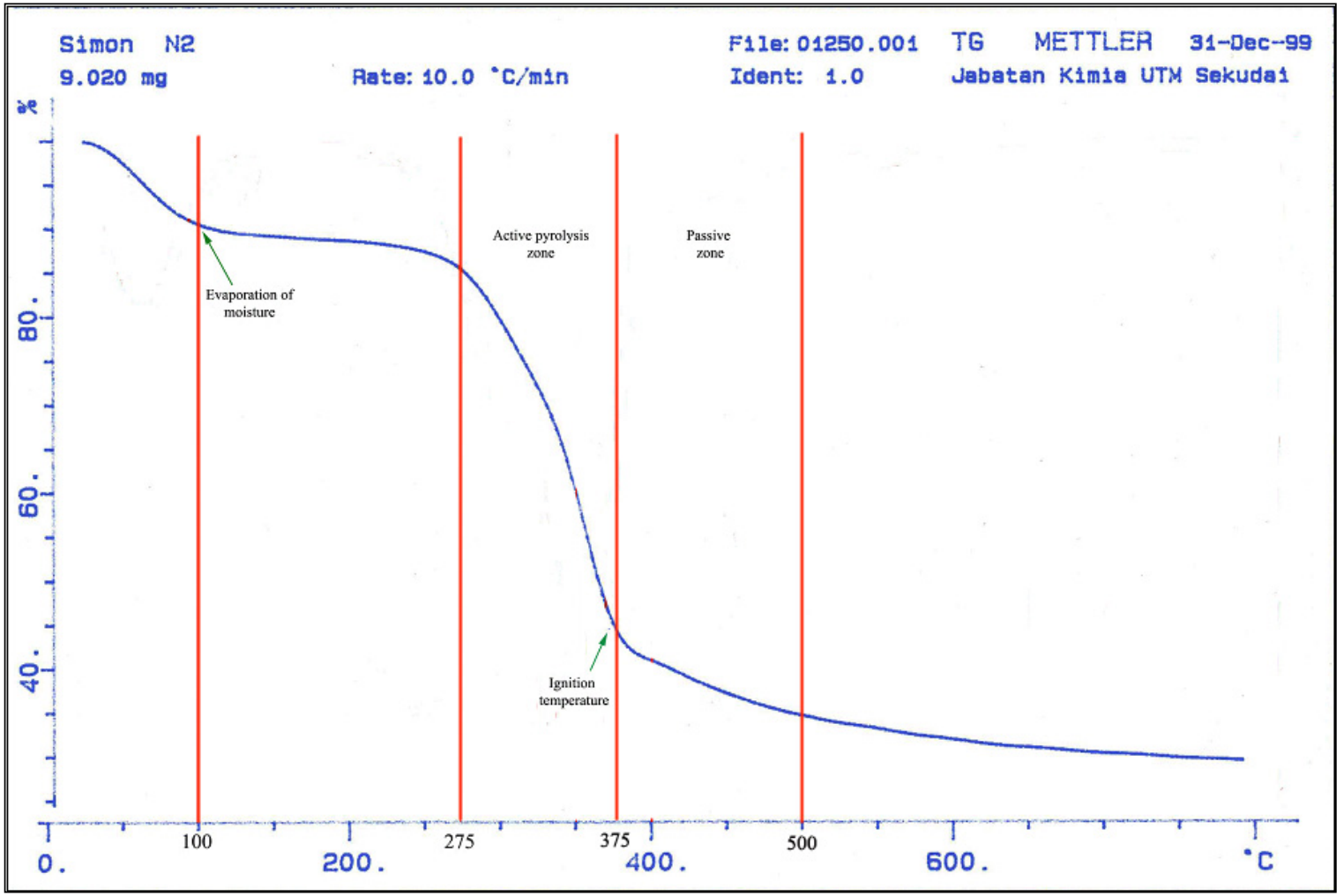

Figure 5.65: Thermogravimetric analysis of rice husk in a reducing environment (N_2) (heating value 10.0^{o}C/min)

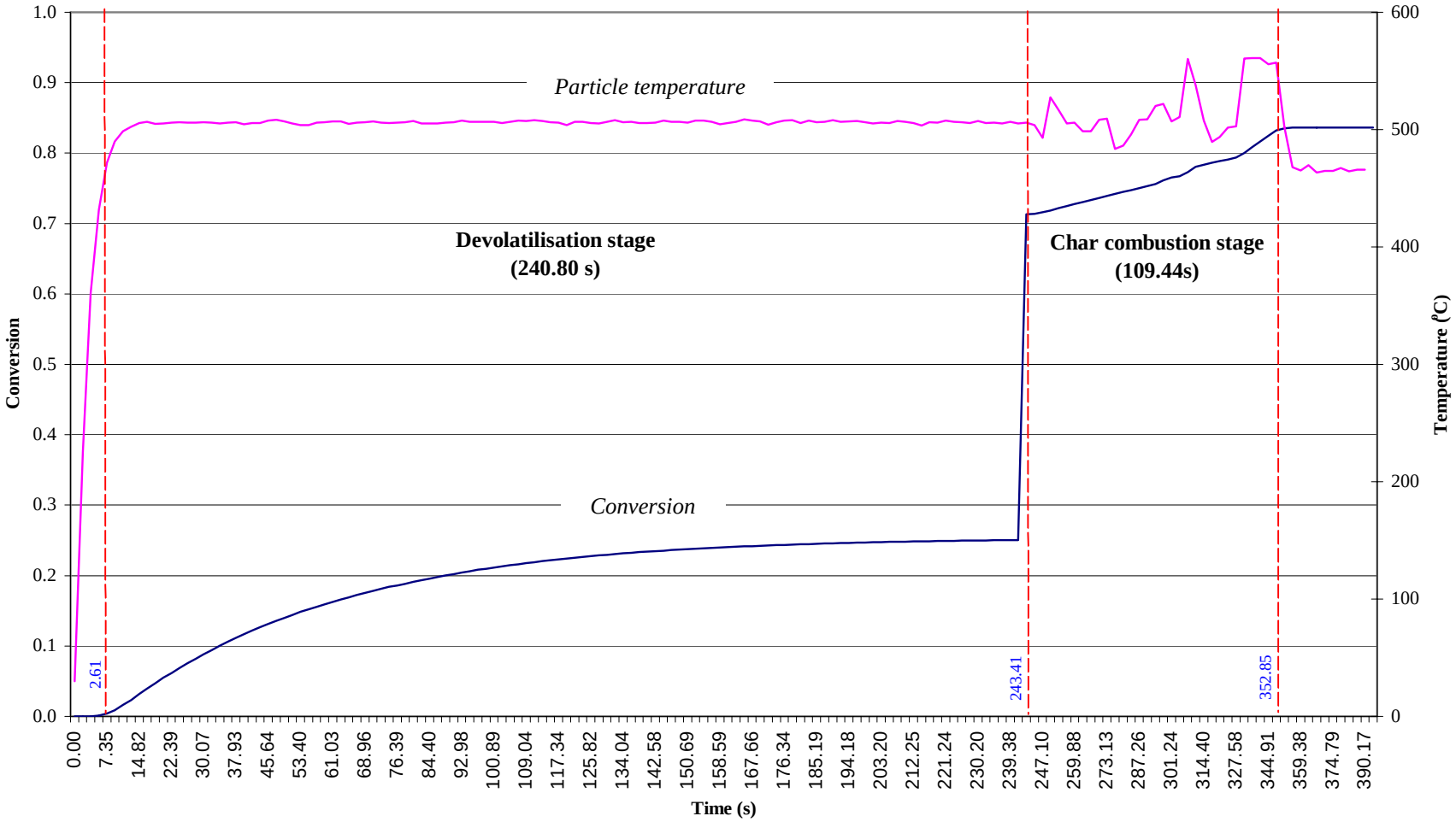

Figure 5.66: Temperature profile and the conversion of rice husk particles in a RFB operating at 5-g loading (122 RPM) and 500^{o}C

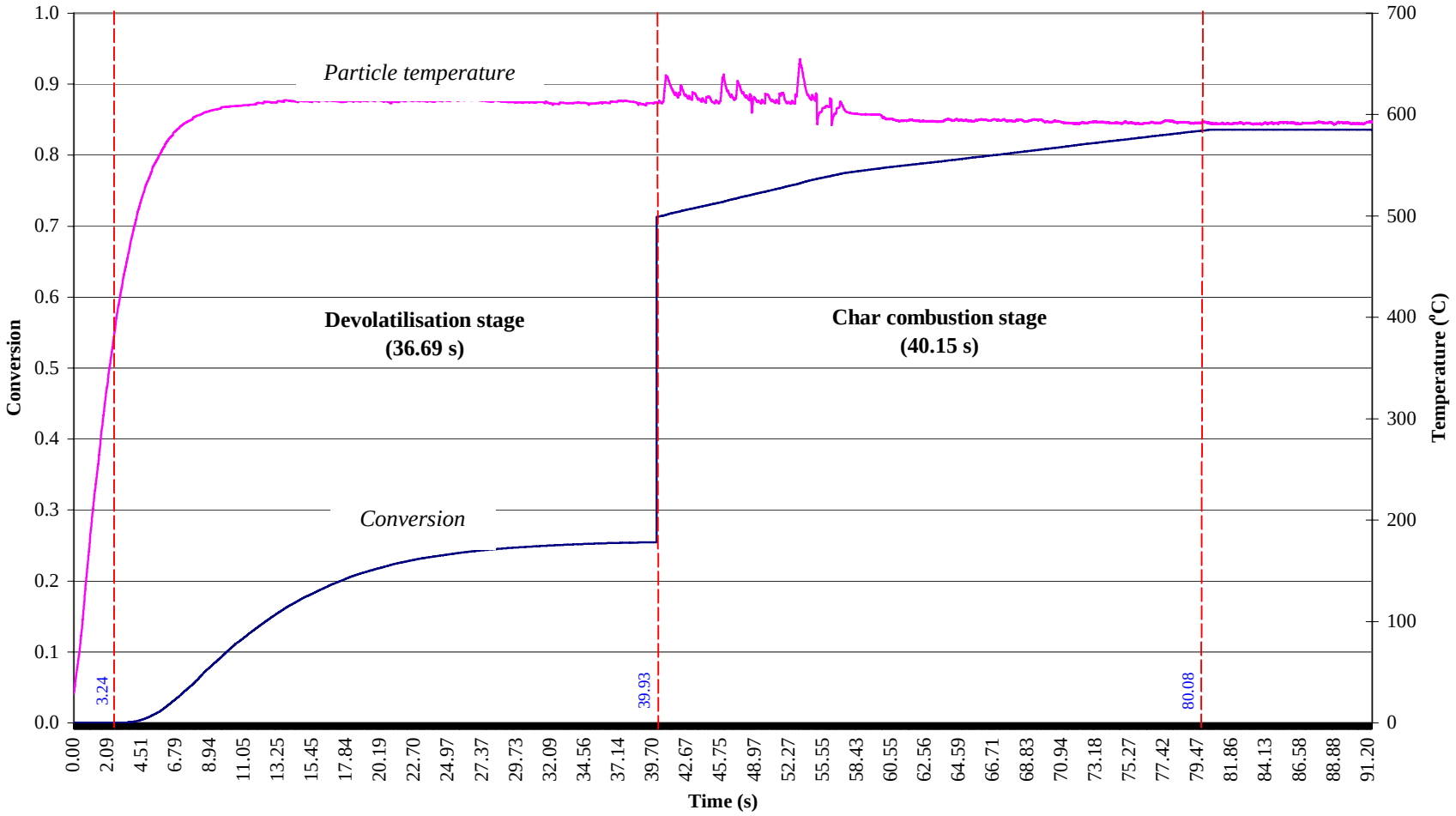

Figure 5.67: Temperature profile and the conversion of rice husk particles in a RFB operating at 5-g loading (122 RPM) and 600°C

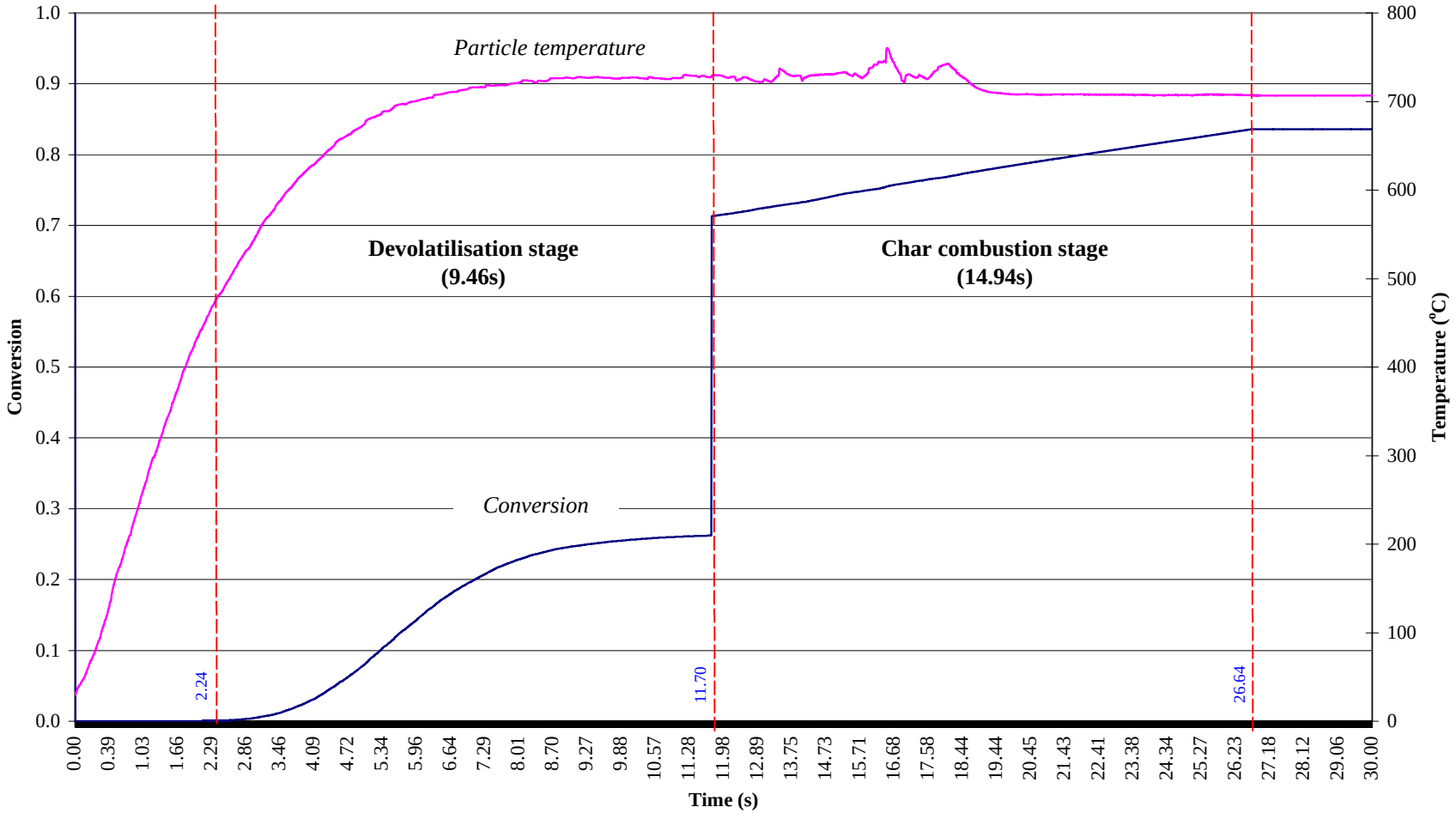

Figure 5.68: Temperature profile and the conversion of rice husk particles in a RFB operating at 5-g loading (122 RPM) and 700^{o}C

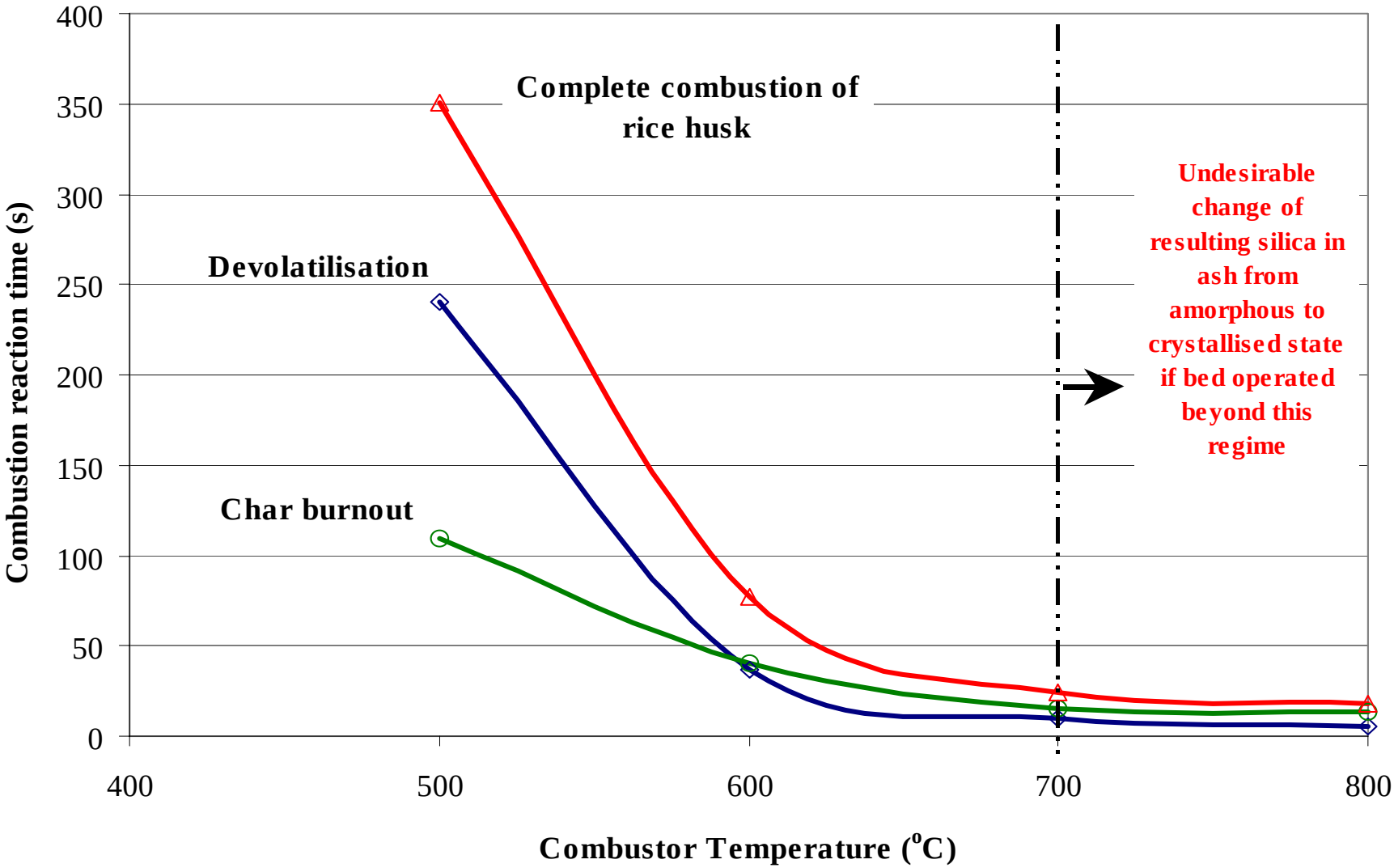

Figure 5.69: Effect of combustor operating temperature [RFB @ 5-g loading (122 RPM)] on the combustion reaction time of rice husk particles

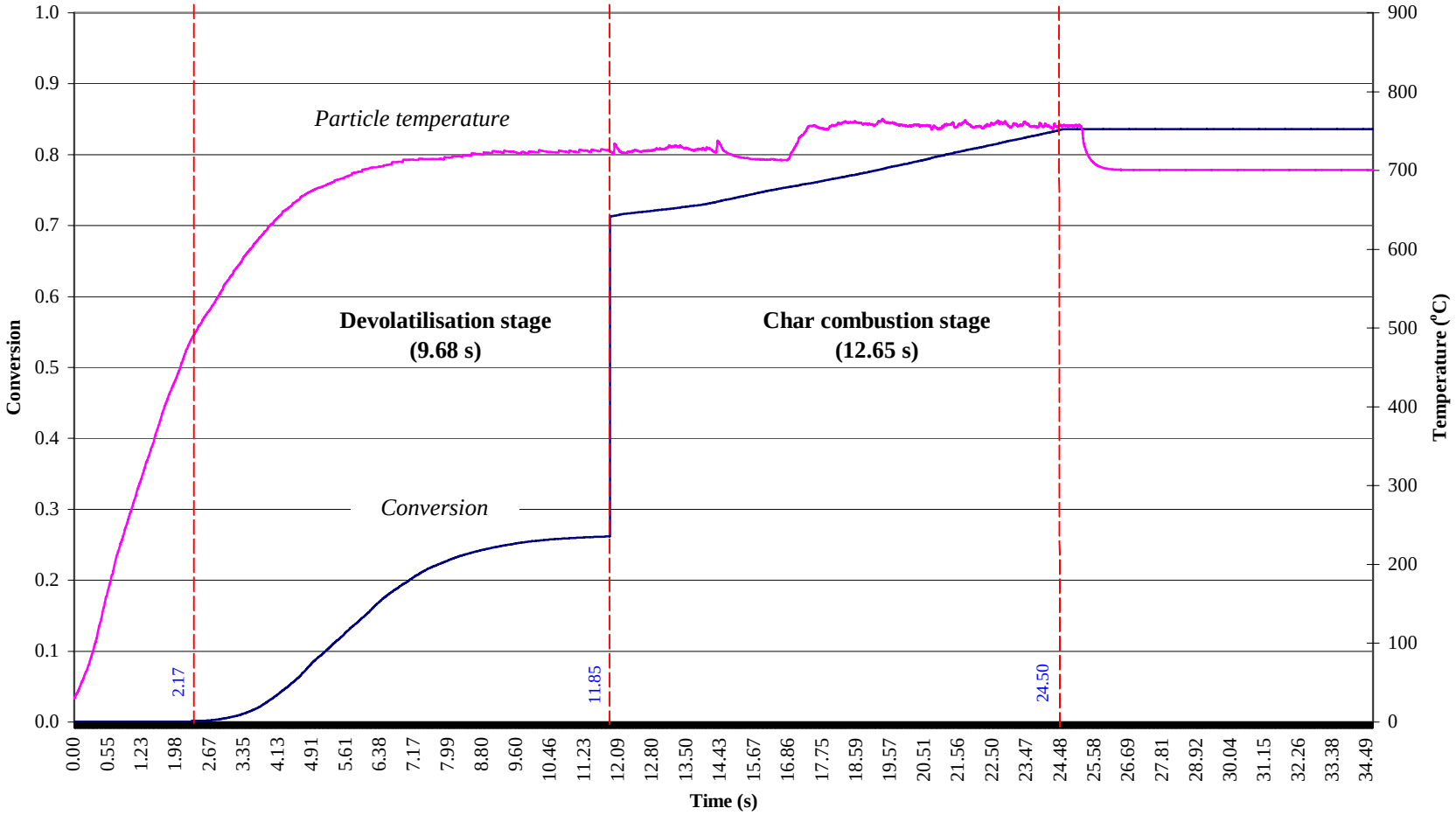

Figure 5.70: Temperature profile and the conversion of rice husk particles in a RFB operating at 10-g loading (173 RPM) and 700°C

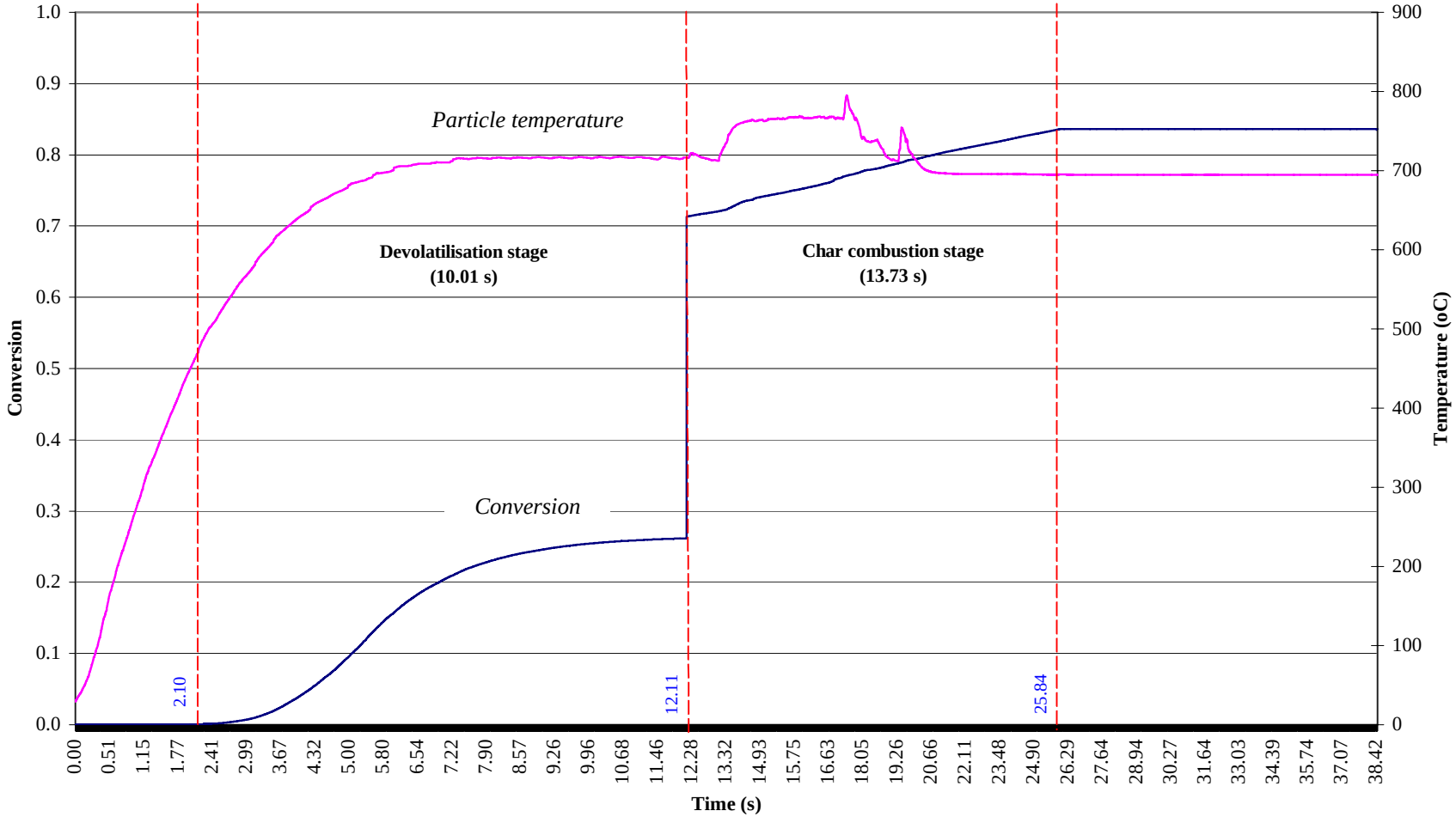

Figure 5.71: Temperature profile and the conversion of rice husk particles in a RFB operating at 12.5-g loading (192 RPM) and 700^{o}C

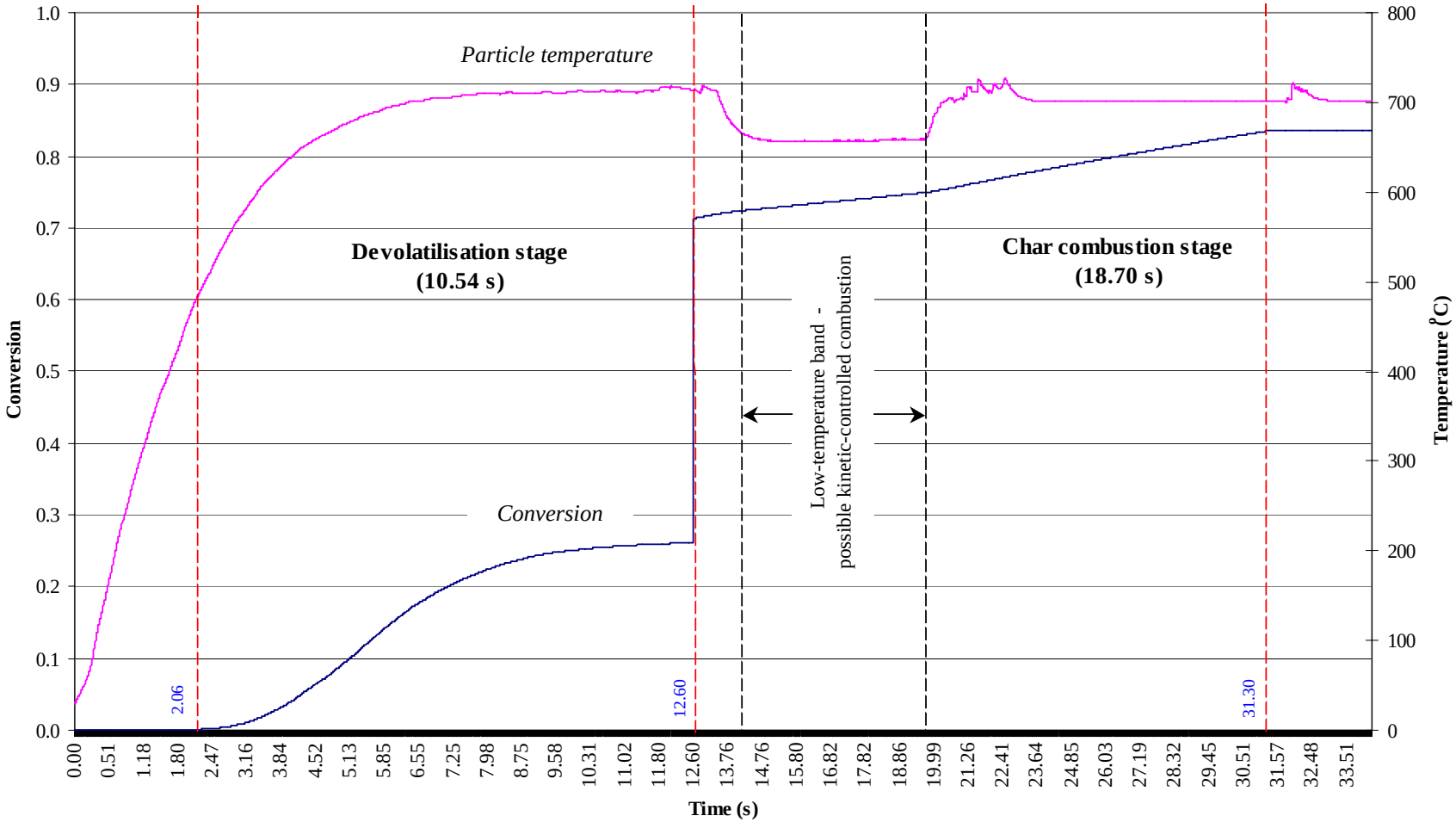

Figure 5.72: Temperature profile and the conversion of rice husk particles in a RFB operating at 15-g loading (211 RPM) and 700°C

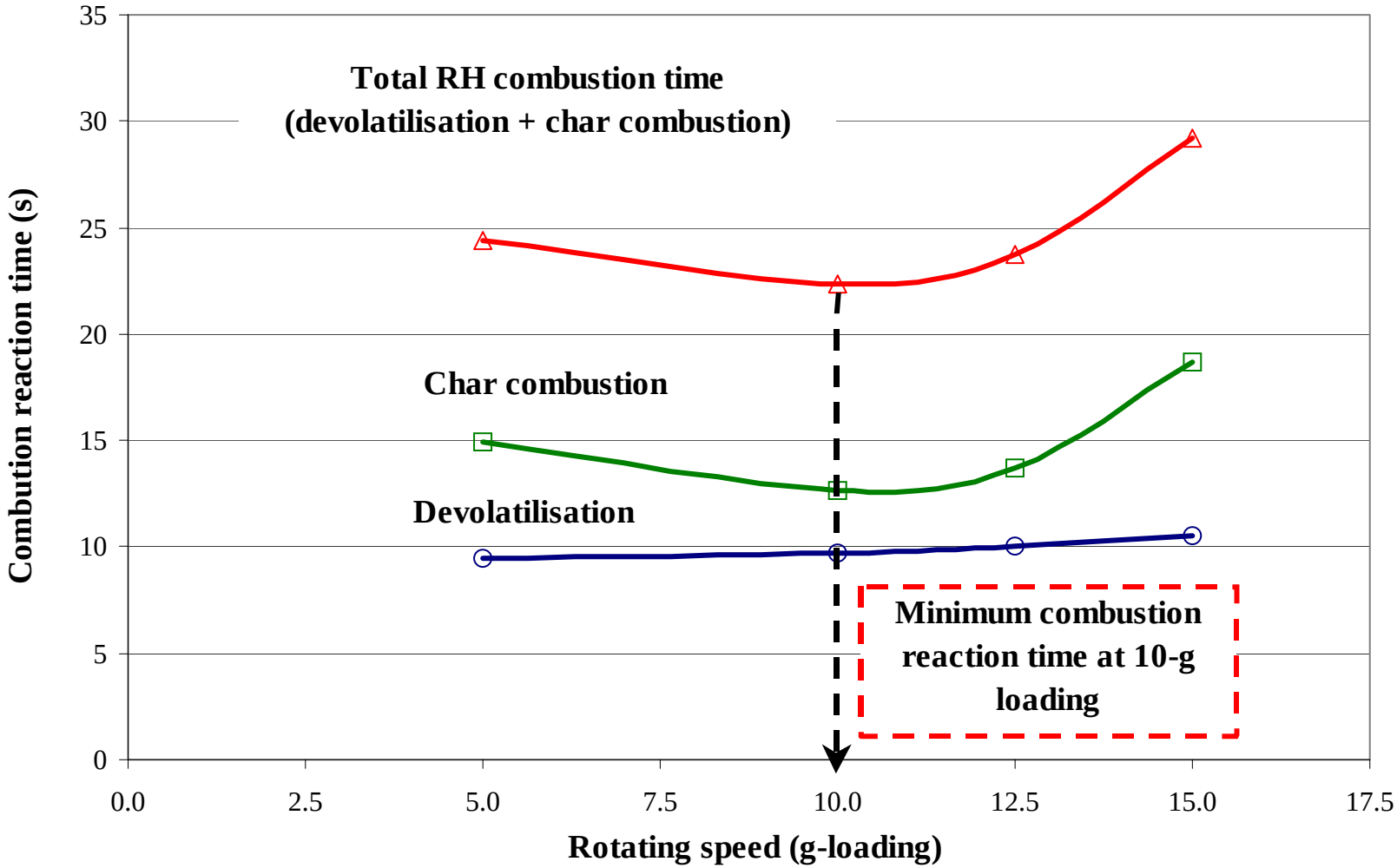

Figure 5.73: Effect of combustor rotating speed (RFB @ 700^{o}C) on the combustion reaction time of rice husk

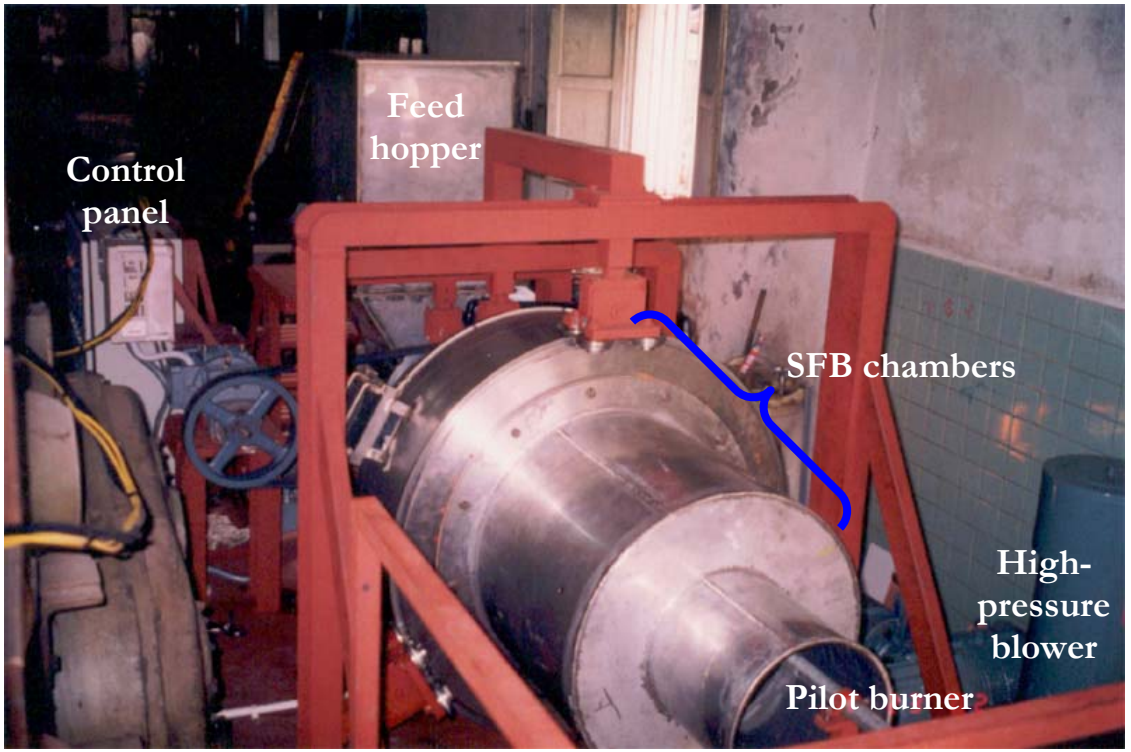

Plate 6.1: The prototype of the Spinning Fluidised Bed (SFB) combustor system

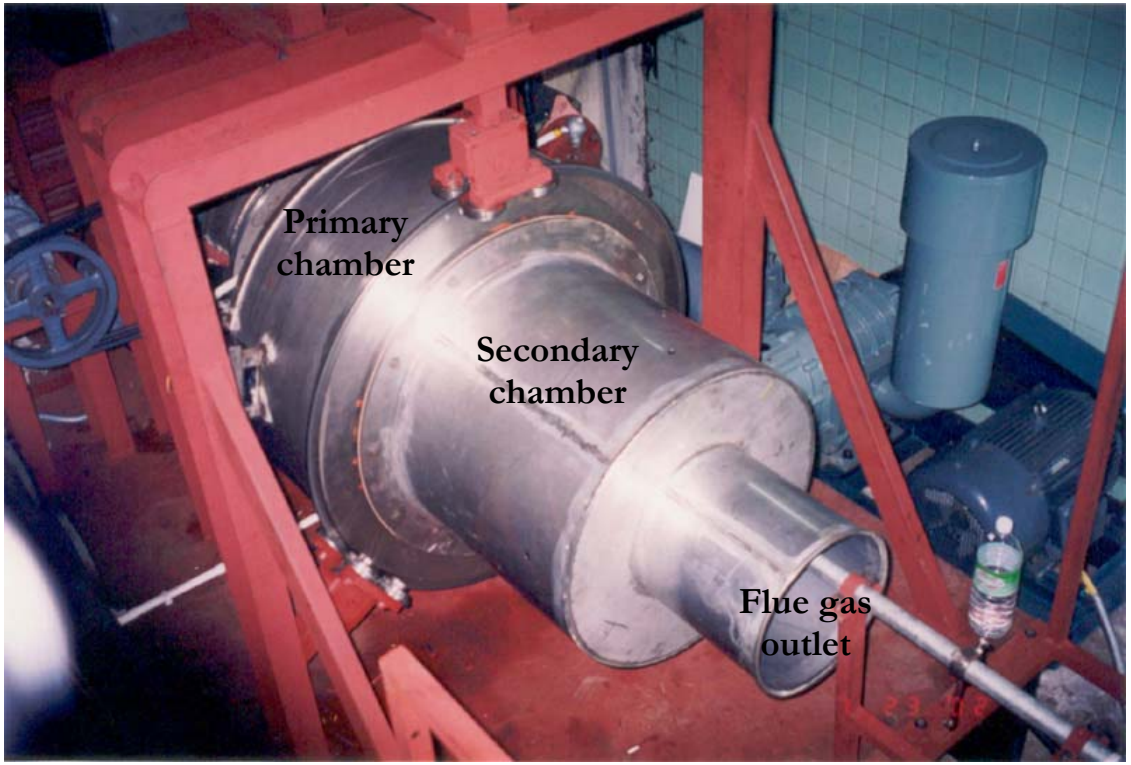

Plate 6.2: Spinning fluidised bed chambers

Plate 6.3: Primary blower unit

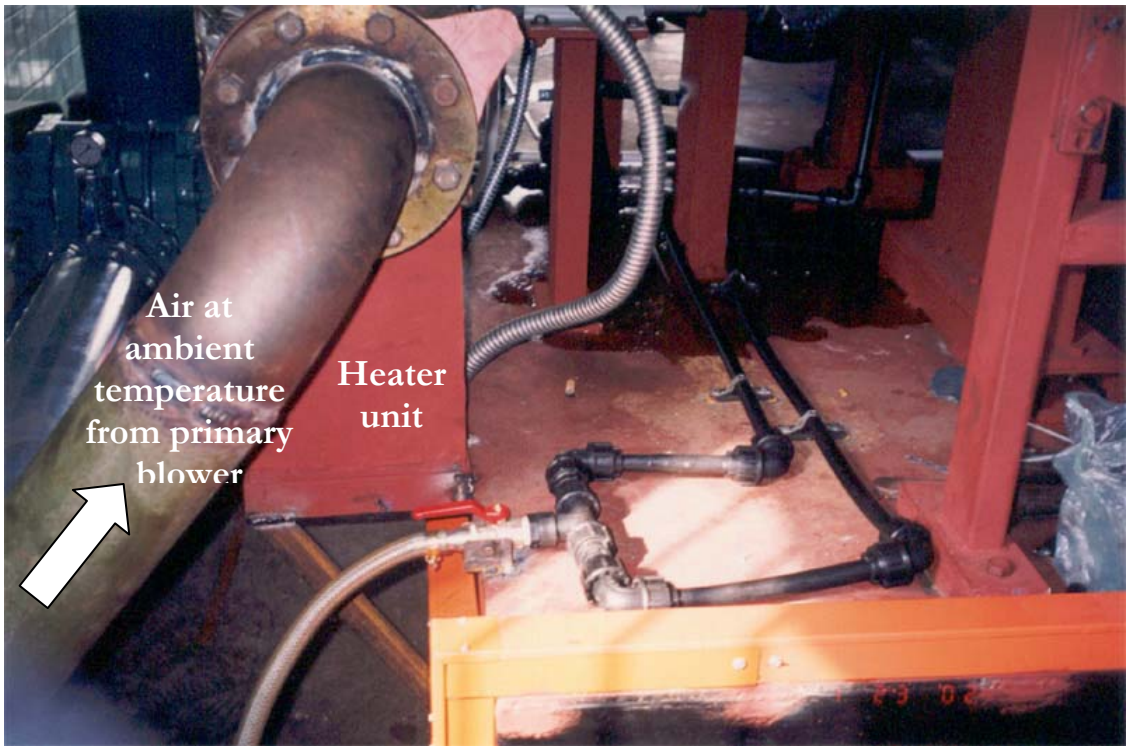

Plate 6.4: Air pre-heating system

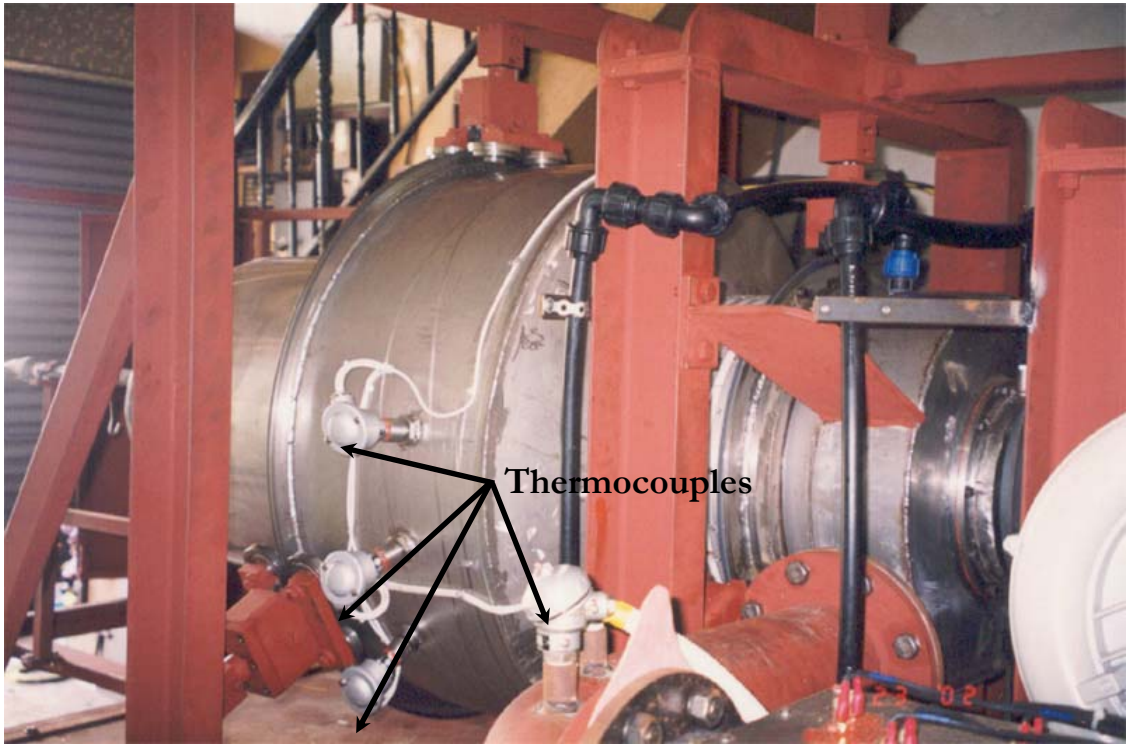

Plate 6.5: Temperature sensors at the SFB primary chamber and pre-heated air supply

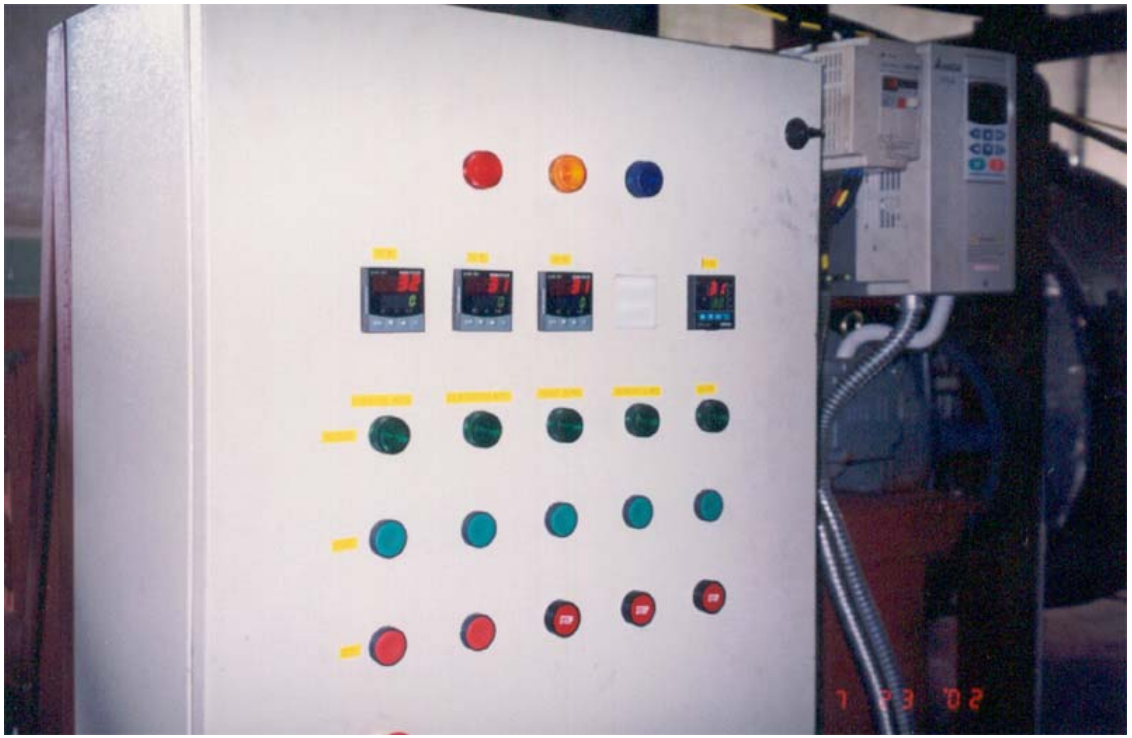

Plate 6.6: Temperature monitoring system of the SFB combustor system

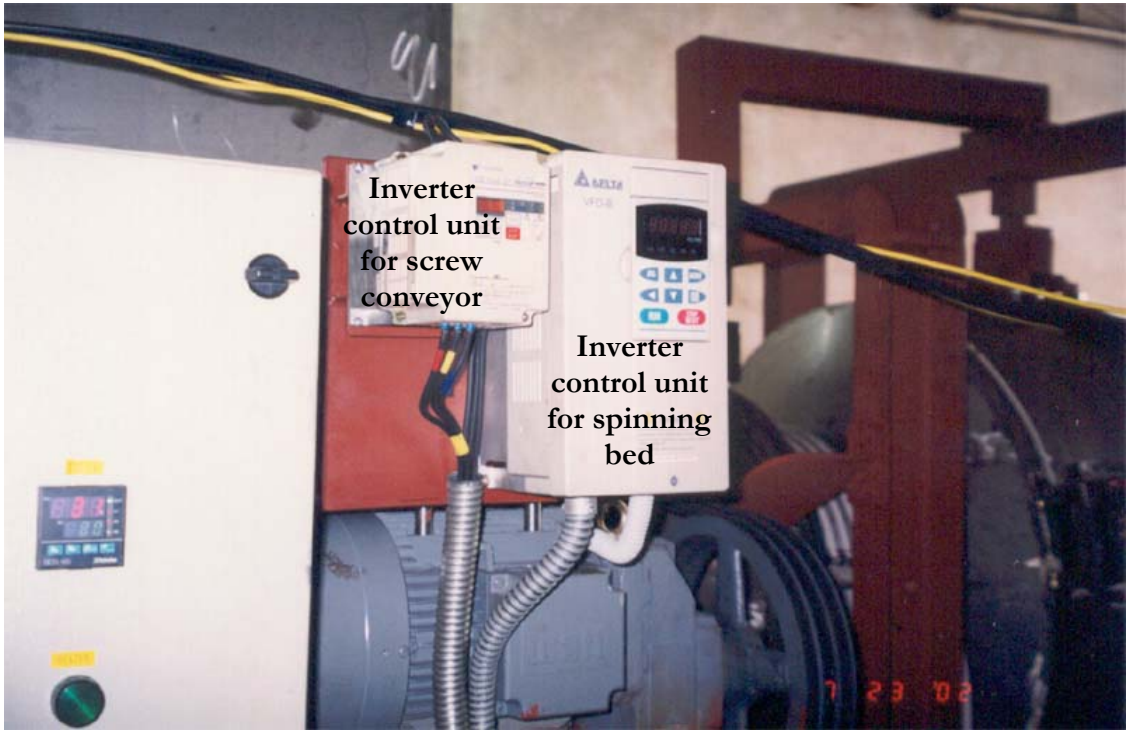

Plate 6.7: Inverter control units for the spinning bed chambers and screw conveyor

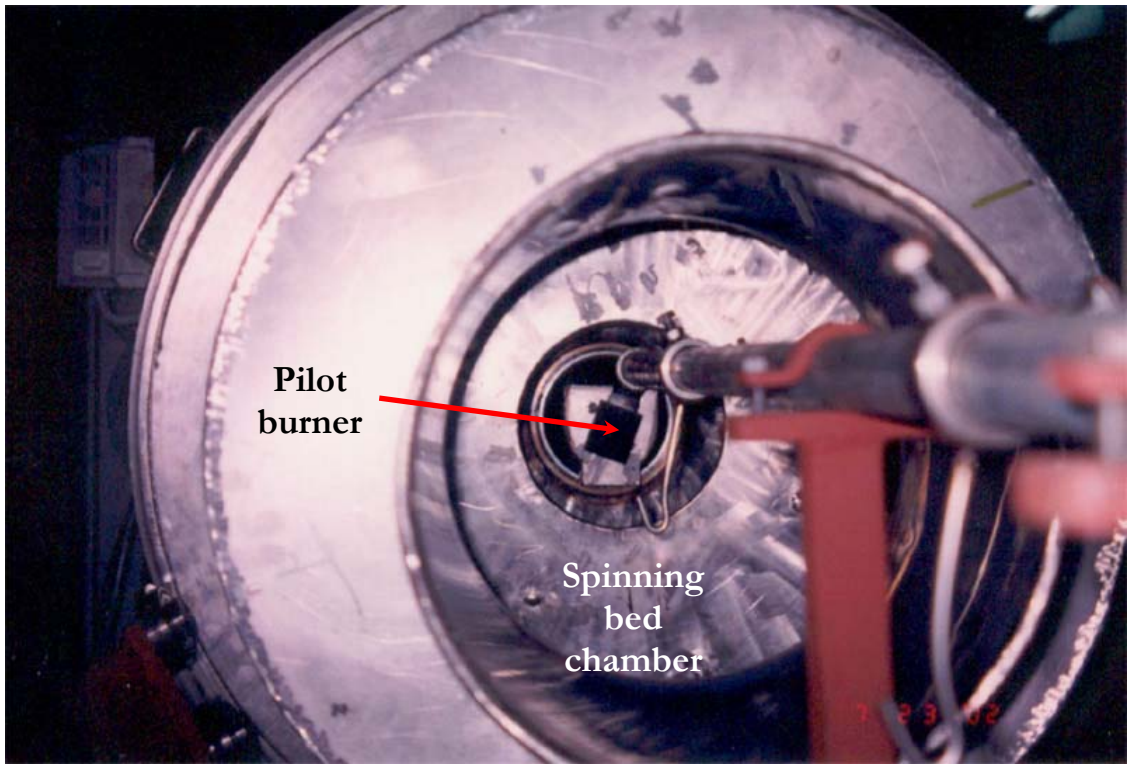

Plate 6.8: Liquefied Petroleum Gas (LPG) Flame Pilot Burner

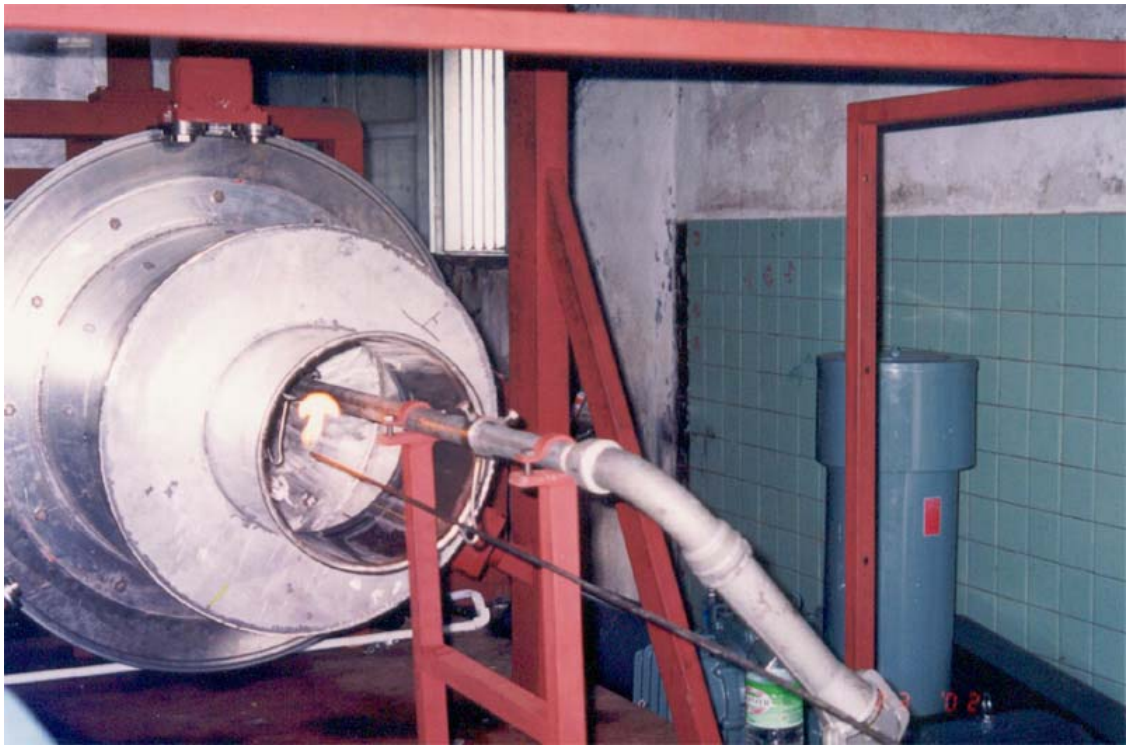

Plate 6.9: Ignition of the pilot burner

APPENDIX A

TENDER DOCUMENT FOR THE DESIGN, DEVELOPMENT, SUPPLY, DELIVERY, INSTALLATION AND COMMISSIONING OF A NOVEL SPINNING FLUIDISED BED COMBUSTOR

ATTACHMENT I

VIDEO FOOTAGE OF THE TEST RUNS ON THE DEVELOPED SFB COMBUSTOR SYSTEM

Note: CD (ID: SFB Test Run) attached at the back cover of report

ATTACHMENT II

VIDEO FOOTAGE OF THE DELIVERY OF THE SFB COMBUSTOR SYSTEM TO UNIVERSITI TEKNOLOGI MALAYSIA

Note: CD (ID: SFB Delivery I & II) attached at the back cover of report

ATTACHMENT III

PAPERS PRESENTED AT SEMINARS/SYMPOSIUMS UNDER THE RESEARCH FUND

ATTACHMENT IV

USER'S MANUAL FOR THE SFB COMBUSTOR SYSTEM

FAKULTI KEJURUTERAAN KIMIA DAN KEJURUTERAAN SUMBER ASLI
UNIVERSITI TEKNOLOGI MALAYSIA
JADUAL PENENTUAN TEKNIKAL

JABATAN : KEJURUTERAAN KIMIA, FAKULTI KEJURUTERAAN KIMIA DAN KEJURUTERAAN SUMBER ASLI

Bil.	Nama dan Alat-alat Penentuan	Spesifikasi Penender
	TITLE: TENDER FOR THE DESIGN, DEVELOPMENT, SUPPLY, DELIVERY, INSTALLATION AND COMMISSIONING OF A NOVEL SPINNING FLUIDISED BED FOR THE DEPARTMENT OF CHEMICAL ENGINEERING, FACULTY OF CHEMICAL ENGINEERING& NATURAL RESOURCES ENGINEERING, UNIVERSITI TEKNOLOGI MALAYSIA, SKUDAI, JOHOR. **SCOPE:** In order to cope with the increasing demand for waste incineration technologies, the Department has embarked on a project utilising the spinning fluidised bed technology. The experimental rig is needed to conduct research activities to determine the effectiveness and suitability of the system to cater for various types of wastes while conforming to stringent environmental regulations. Once proven, the system has the potential to be commercialised to cater for small-scale on-site waste disposal.	

FAKULTI KEJURUTERAAN KIMIA DAN KEJURUTERAAN SUMBER ASLI
UNIVERSITI TEKNOLOGI MALAYSIA
JADUAL PENENTUAN TEKNIKAL

JABATAN : KEJURUTERAAN KIMIA, FAKULTI KEJURUTERAAN KIMIA DAN KEJURUTERAAN SUMBER ASLI

Bil.	Nama dan Alat-alat Penentuan	Spesifikasi Penender
	SPECIFICATION:	
1.0	**GENERAL**	
1.1	**SUPPLY AND DELIVERY**	
1.1.1	This tender includes the supply, delivery from the tenderer and commissioning on-site at Block N12 of Faculty of Chemical Engineering & Natural Resources Engineering, UTM Skudai, Johor of a Spinning Bed Combustor System.	Comply
1.1.2	Tenderer is requested to specify the earliest delivery and commissioning date. In addition, the tenderer should submit a detail work schedule showing how the project is going to be executed to meet the stipulated time frame.	12 – 24 weeks

FAKULTI KEJURUTERAAN KIMIA DAN KEJURUTERAAN SUMBER ASLI
UNIVERSITI TEKNOLOGI MALAYSIA
JADUAL PENENTUAN TEKNIKAL

JABATAN : KEJURUTERAAN KIMIA, FAKULTI KEJURUTERAAN KIMIA DAN KEJURUTERAAN SUMBER ASLI

Bil.	Nama dan Alat-alat Penentuan	Spesifikasi Penender
1.1.3	If the successful tenderer has not completed the supply, installation, testing and eventual handing over of the equipment within the said time and if UTM have not cancelled the contract under the power conferred on it by the General Tendering Conditions of the specifications, the successful tenderer should pay, as liquidated damages, an amount based on the formula given in the tender condition. The amount so calculated may be deducted from any money payable to successful vendor by UTM.	Comply
1.1.4	UTM reserves the right to accept or reject any extension of the period required for the delivery and/or competion of the work.	Comply
1.1.5	If the tenderer is an equipment supplier and not the manufacturer of the equipment, the supplier and the major manufacturer will be jointly and severally liable for fulfilling all the terms, conditions and guarantees entered into in the contract for supply.	Comply
1.1.6	The tenderer is required to provide an original certified true copy of the manufacturing/supplying warranty certificate for the hardware/software provided.	Comply

FAKULTI KEJURUTERAAN KIMIA DAN KEJURUTERAAN SUMBER ASLI
UNIVERSITI TEKNOLOGI MALAYSIA
JADUAL PENENTUAN TEKNIKAL

JABATAN : KEJURUTERAAN KIMIA, FAKULTI KEJURUTERAAN KIMIA DAN KEJURUTERAAN SUMBER ASLI

Bil.	Nama dan Alat-alat Penentuan	Spesifikasi Penender
1.1.7	The tenderer is requested to justify their competency for executing the job successfully. The tenderer is required to submit the company's past experience in handling this kind of job.	Comply
1.1.8	All government regulations, law pertaining to the importation, supply and delivery of the equipment must be followed by the tenderer.	Comply
1.1.9	Insurance cover costs during the course of executing the job will be borne by the tenderer.	Comply

FAKULTI KEJURUTERAAN KIMIA D AN KEJURUTERAAN SUMBER ASLI
UNIVERSITI TEKNOLOGI MALAYSIA
JADUAL PENENTUAN TEKNIKAL

JABATAN : KEJURUTERAAN KIMIA, FAKULTI KEJURUTERAAN KIMIA DAN KEJURUTERAAN SUMBER ASLI

Bil.	Nama dan Alat-alat Penentuan	Spesifikasi Penender
1.2	**INSTALLATION AND COMMISSIONING**	
1.2.1	All items of equipment shall be installed on site by the successful tenderer at no extra cost to UTM.	Comply
1.2.2	The successful tenderer shall undertake to install and commission the hardware and software on site (Block N12 of Faculty of Chemical Engineering & Natural Resources Engineering, UTM Skudai) by a qualified Engineer. Such commission includes setting of equipment, testing according to an acceptable standards and test run of the softwares. All costs related to the above work shall be borne by the tenderer.	Comply
1.2.3	If the work carried in item 1.2.2 is not satisfactory, UTM has the right **NOT** to accept the handing over. UTM has the right to call other professional parties to complete the job satisfactorily. The cost shall be borne by the tenderer.	Comply
1.2.4	All government regulations and procedures must be followed during the installation and commissioning work. Approval from any government authorities wherever applicable will be under the responsibility of the tenderer.	Comply

FAKULTI KEJURUTERAAN KIMIA DAN KEJURUTERAAN SUMBER ASLI
UNIVERSITI TEKNOLOGI MALAYSIA
JADUAL PENENTUAN TEKNIKAL

JABATAN : KEJURUTERAAN KIMIA, FAKULTI KEJURUTERAAN KIMIA DAN KEJURUTERAAN SUMBER ASLI

Bil.	Nama dan Alat-alat Penentuan	Spesifikasi Penender
1.3	**STAFF TRAINING**	
1.3.1	The successful tenderer shall provide proper and satisfactory on job training at the tenderer's own cost. All cost related to the training i.e. training fees, transportation, appropriate subsistence fees (Malaysian Government rates), accommodation (where applicable), refreshment, courseware etc., will be borne by the tenderer. <u>All related training cost must be separately quoted from the equipment supplied but inclusive in the tender price</u>. The minimum training required are as follows: Training of nominated UTM personnel on-site at UTM. The training period must not be less than <u>three (3)</u> working days or to the specification of UTM and must include, but not limited to the followings: ▪ Training on the proper handling and operation of the spinning fluidised bed testing rig. ▪ Training on routine maintenance, general trouble-shooting and repair. ▪ Training on the use of the auxiliary equipment for a complete system of "field to finish".	Comply

FAKULTI KEJURUTERAAN KIMIA DAN KEJURUTERAAN SUMBER ASLI
UNIVERSITI TEKNOLOGI MALAYSIA
JADUAL PENENTUAN TEKNIKAL

JABATAN : KEJURUTERAAN KIMIA, FAKULTI KEJURUTERAAN KIMIA DAN KEJURUTERAAN SUMBER ASLI

Bil.	Nama dan Alat-alat Penentuan	Spesifikasi Penender
1.3.2	The medium of instruction, including all training materials which must be provided, during the whole duration of the training period must be in English of Bahasa Malaysia.	
1.4	**WARRANTY PERIOD**	
1.4.1	The tenderer shall state the warranty period of all equipment supplied.	Comply
1.4.2	The warranty period must not be less than one (1) year from the date of complete handing over. Any equipment/material defects or faulty operation due to manufacturer or installation shall be the responsibility of the suppliers who shall immediately make good and/or replace any such defect or faulty components.	Comply (warrant is valid for 1 calendar year under normal operations within the stated manufacturer specification)
1.4.3	All labour and materials needed during the warranty period shall be supplied free of charge. Any exclusion should be clearly specified in the tender.	Comply, except for fragile items such as heater, sensors and motors which will covers for a period of 3 calendar months from date of commissioned)

FAKULTI KEJURUTERAAN KIMIA DAN KEJURUTERAAN SUMBER ASLI
UNIVERSITI TEKNOLOGI MALAYSIA
JADUAL PENENTUAN TEKNIKAL

JABATAN : KEJURUTERAAN KIMIA, FAKULTI KEJURUTERAAN KIMIA DAN KEJURUTERAAN SUMBER ASLI

Bil.	Nama dan Alat-alat Penentuan	Spesifikasi Penender
1.5	**MAINTENANCE**	
	Full maintenance support of the equipment must be available locally. The engineering/maintenance support shall be provided by competent personnel. The tenderer will have to indicate how he intends to meet this requirement, including naming the facilities available at their locations.	Comply with technical staff and workshop available at manufacturer location
1.6	**MANUALS & DOCUMENTATION**	
	The successful tenderer must provide at least two (2) sets (Comprising of one (1) set of original & one (1) set of duplicate) of the following items: a) User's Guide for the combustor system b) Maintenance/ Technical Manual c) Other manuals available (please specify) The tenderer must clearly specify the relevant manuals for each individual element of the system. All documents listed above must be in English or Bahsa Malaysia.	Comply with English manuals

FAKULTI KEJURUTERAAN KIMIA DAN KEJURUTERAAN SUMBER ASLI
UNIVERSITI TEKNOLOGI MALAYSIA
JADUAL PENENTUAN TEKNIKAL

JABATAN : KEJURUTERAAN KIMIA, FAKULTI KEJURUTERAAN KIMIA DAN KEJURUTERAAN SUMBER ASLI

Bil.	Nama dan Alat-alat Penentuan	Spesifikasi Penender
1.7	**OTHERS** The tenderer shall guarantee the availability of a good after sales service for all the equipment supplied. UTM reserves the right not to consider and automatically reject tenderer's offer which fails to show any of the above mentioned items.	Comply

FAKULTI KEJURUTERAAN KIMIA DAN KEJURUTERAAN SUMBER ASLI
UNIVERSITI TEKNOLOGI MALAYSIA
JADUAL PENENTUAN TEKNIKAL

JABATAN : KEJURUTERAAN KIMIA, FAKULTI KEJURUTERAAN KIMIA DAN KEJURUTERAAN SUMBER ASLI

Bil.	Nama dan Alat-alat Penentuan	Spesifikasi Penender
2.0	**TECHNICAL SPECIFICATIONS OF TOTAL SPINNING FLUIDISED BED COMBUSTOR SYSTEM**	The general construction of the combustor will follow closely to the drawings attached in the tender documents with modifications as and when in accordance to engineering safety requirements.
2.1	The combustor system comprises the following features and subassemblies:-	
	▪ stainless steel rotating fluidised bed as per illustrated attached drawings. The combustion chambers of the spinning bed shall be able to withstand temperatures of up to 1200^{o}C.	Comply with stainless steel construction. The unit is expected to have a core temperature of 1200^{o}C with graduated temperature gradient towards the stainless steel walls. Generally, the unit walls are expected to experience a temperature range of 600 – 800^{o}C.
	▪ rotating jacketed body c/w insulation	Comply
	▪ monitoring thermocouples with jacketed sleeving to the fluidised bed	Comply
	▪ customized inlet assembly for heated air	Comply
	▪ bearing assembly for the spinning bed assembly	Comply
	▪ screw conveyor inside the spinning bed c/w jacketed pipe for secondary air. The screw conveyor system shall be suitable for feeding different types of sludge and solid waste.	Comply for certain sludge and solids as informed but not for all types
	▪ customized insulation clamper for rotary motion and shall be able to seal the air, so that pressurised air of up to 4 m H_2O could be supplied into the spinning combustion chamber.	Comply
	▪ primary burner for high pressure air (up to 4 m H_2O)	Comply

FAKULTI KEJURUTERAAN KIMIA DAN KEJURUTERAAN SUMBER ASLI
UNIVERSITI TEKNOLOGI MALAYSIA
JADUAL PENENTUAN TEKNIKAL

JABATAN : KEJURUTERAAN KIMIA, FAKULTI KEJURUTERAAN KIMIA DAN KEJURUTERAAN SUMBER ASLI

Bil.	Nama dan Alat-alat Penentuan	Spesifikasi Penender
	▪ secondary burner unit for fluidised bed to maintain combustion temperatures of up to 1200^{o}C	Comply
	▪ variable speed motor assembly for the spinning bed assembly capable of rotation up to 1000 rpm	Variable speed motor assembly is capable of only up to 100 rpm
	▪ variable speed motor assembly for the screw conveyor	Comply
	▪ primary high pressure blower with capacity up to 1200 m^3/hr at ambient temperature (30^{o}C) and pressure head of 4 m H_2O	Comply
	▪ secondary air blower	Comply
	▪ the frame and chassis assembly for the spinning bed unit c/w ash pit and weir	Comply
	▪ control panel and electronic housing for the above system	Comply
2.2	The tenderer shall submit detailed design calculations and drawings of the system. The design calculations should illustrate the sizing of the blowers, pumps, burners and motors. The detailed drawings should include the blueprint of the system complete with its three dimensional views.	Comply